

# Numerical Simulation of Diaphragm Rupture

by

Paul Petrie-Repar B.E. (Hons)

Mechanical Engineering Department  
University of Queensland

Submitted for the degree of Doctor of Philosophy

Submitted on December 23, 1997



Paul Petrie-Repar  
7 Havana St  
Ashgrove 4060

Professor J. M. Simmons  
The Dean  
Faculty of Engineering  
The University of Queensland

Dear Sir,

In part fulfilment of the requirements for the award of the Doctor of Philosophy, I hereby submit, for your consideration, this thesis entitled "*Numerical Simulation of Diaphragm Rupture*". I declare that the work presented in this thesis is, to the best of my knowledge and belief, original, except as acknowledged in the text; and that this material has not been submitted, either in whole or in part, for a degree at this or any other university.

Yours sincerely

Paul Petrie-Repar



# Acknowledgements

Firstly and primarily I would like to thank my wife Barbara, for her support, faith, encouragement, patience, sacrifices and love.

The assistance from my supervisor, Dr. Peter Jacobs was beyond the call of duty, and for that I am most grateful. I would also like to thank my associate supervisor Dr. Richard Morgan for his guidance.

I would like to thank the University of Queensland for the Australian Postgraduate Research Award and the Mechanical Engineering Department for the Research Scholarship.

I would like to thank my parents, Laurence and Mary Petrie for their encouragement and enthusiasm during my formal education.

I would like to thank the CFD group (Ian Johnston, Andrew McGhee, and Chris Craddock) at the University for their help in developing the codes for this thesis.

I would like to thank Mark Kendall for his experimental work, Dr. Michael Macrossan for his insight into EFM, and Olga Sudnitisin for translating a Russian paper.

The author would also like to thank Wilfred Brimblecombe, Kevin Austin, Adrian Smith, Steve Kimball, Barry Daniel, Barry Allsop, Dr. Greg Wilson, Dr. David Bogdanoff, Prof. Klaus Bremhorst, Mijo Repar, Cvita Repar, Sean Charleson, Allan Paull, Sam Overton, Dr. Brett Watson, and Michael Cheng for their contributions.



# Abstract

The results from computer simulations of the gas-dynamic processes that occur during and after the rupture of diaphragms within shock tubes and expansion tubes are presented. A two-dimensional and axisymmetric finite-volume code that solves the unsteady Euler equations for inviscid compressible flow, was used to perform the simulations. The flow domains were represented as unstructured meshes of triangular cells and solution-adaptive remeshing was used to focus computational effort in regions where the flow-field gradients were high.

The ability of the code to produce accurate solutions to the Euler equations was verified by examining the following test cases: supersonic vortex flow between two arcs, an ideal shock tube, and supersonic flow over a cone. The ideal shock tube problem was studied in detail, in particular the shock speed. The computed shock speed was accurate when the initial pressure ratio was low. When the initial pressure ratio was high the flow was difficult to resolve because of the large density ratio at the contact surface where significant numerical diffusion occurred. However, solution-adaptive remeshing was used to control the error and reasonable estimates for the shock speed were obtained.

The code was used to perform multi-dimensional simulations of the gradual opening of a primary diaphragm within a shock tube. The development of the flow, in particular the contact surface was examined and found to be strongly dependent on the initial pressure ratio across the diaphragm.

For high initial pressure ratios across the diaphragm, previous experiments have shown that the measured shock speed can exceed the shock speed predicted by one-dimensional models. The shock speeds computed via the present multi-dimensional simulation were higher than those estimated by previous one-dimensional models and were closer to the experimental measurements. This indicates that multi-dimensional flow effects were partly responsible for the relatively high shock speeds measured in the experiments.

The code also has the ability to simulate two-dimensional fluid-structure interactions. To achieve this the Euler equations are solved for a general moving frame of reference. Mesh management during a simulation is important. This includes the ability to automatically generate a new mesh when the current mesh becomes distorted (due to the motion of the structures) and the transfer of the solution from the old mesh to the new.

The shock induced rupture of thin diaphragms was examined. Previous one dimensional models are flawed because they do not simultaneously consider the diaphragm mass and allow the upstream gas to penetrate the diaphragm mass. Two multi-dimensional models which allow the upstream gas to penetrate are described. The first model assumes the diaphragm vaporises immediately after the arrival of the incident shock. The second model assumes the diaphragm shatters into a number of pieces which can be treated as rigid bodies. The results from both models are compared with experimental data.



# Publications relating to the thesis

Petrie PJ, Jacobs PA. Numerical simulation of diaphragm rupture. In: *International Symposium on Shock Waves*, Pasadena, California, 1995.

Petrie-Repar PJ, Jacobs PA. A computational study of shock speeds in ‘high-performance’ shock tubes. *Shock Waves*, 8(2):79–91, April 1998.

Kendall MA, Morgan RG, and Petrie-Repar PJ. A study of free-piston double-diaphragm drivers for expansion tubes. In: *35th Aerospace Sciences Meeting & Exhibits*, Reno, 1997.

Kendall MA, Morgan RG, and Petrie-Repar PJ. Heat losses and shock-diaphragm interactions within double-diaphragm drivers. Submitted to the *AIAA Journal*.



# Contents

<b>1</b>	<b>Introduction</b>	<b>1</b>
1.1	A brief description of an expansion tube . . . . .	3
1.2	Scope of this thesis . . . . .	4
<b>2</b>	<b>Two-dimensional finite-volume code</b>	<b>9</b>
2.1	Governing equations . . . . .	10
2.2	Initial mesh generation and data storage . . . . .	12
2.3	Numerical techniques . . . . .	18
2.3.1	Reconstruction . . . . .	18
2.3.2	Calculation of Fluxes . . . . .	21
2.3.3	Time-stepping . . . . .	22
2.4	Solution-adaptive remeshing . . . . .	23
2.4.1	Error indicator . . . . .	23
2.4.2	Cell refinement - bisection method . . . . .	25
2.4.3	Vertex deletion . . . . .	27
2.5	Ignored cells . . . . .	27
2.6	Summary . . . . .	27
<b>3</b>	<b>Test cases</b>	<b>29</b>
3.1	Supersonic vortex . . . . .	31
3.2	Ideal shock tube problem . . . . .	37
3.2.1	Sod's test case . . . . .	37

3.2.2	Shock tube with high initial pressure ratio . . . . .	40
3.2.3	Axisymmetric shock tube and numerical jetting . . . . .	48
3.2.4	Shock speed . . . . .	53
3.3	Flow over a cone. . . . .	60
3.4	Blast wave flow-field . . . . .	63
3.5	Double Mach reflection . . . . .	68
3.6	Shock wave diffraction over a 90 degree corner . . . . .	72
3.7	Summary . . . . .	74
<b>4</b>	<b>Gradual diaphragm opening</b>	<b>75</b>
4.1	Introduction . . . . .	76
4.1.1	General description of diaphragm opening . . . . .	76
4.1.2	Flow development . . . . .	77
4.1.3	Numerical simulations . . . . .	79
4.1.4	Scope of current work . . . . .	79
4.2	Numerical model of diaphragm opening . . . . .	82
4.2.1	Discretisation of domain . . . . .	83
4.2.2	Opening the diaphragm . . . . .	85
4.3	Flow development within Langley expansion tube . . . . .	85
4.3.1	Shock tube geometry and equation of state . . . . .	92
4.4	Contact surface . . . . .	93
4.4.1	Initial pressure ratio . . . . .	94
4.4.2	Flow development after diaphragm is fully open . . . . .	97
4.4.3	Diaphragm opening time . . . . .	102
4.4.4	Rayleigh-Taylor instabilities . . . . .	110
4.5	Summary . . . . .	110
<b>5</b>	<b>Shock speed</b>	<b>113</b>
5.1	Introduction . . . . .	114

5.1.1	Previous work . . . . .	114
5.1.2	Scope of the current work . . . . .	117
5.2	Langley expansion tube . . . . .	117
5.3	Constant area tube . . . . .	122
5.3.1	Equation of state . . . . .	125
5.3.2	Two-dimensional shock tube . . . . .	125
5.4	Comparison with one-dimensional theories . . . . .	127
<b>6</b>	<b>Fluid-structure interaction</b>	<b>129</b>
6.1	Rigid-body dynamics . . . . .	130
6.2	Flow solver for moving mesh . . . . .	131
6.3	Grid management . . . . .	134
6.4	Test cases . . . . .	140
6.4.1	Random grid motion . . . . .	140
6.4.2	Constant velocity piston . . . . .	141
6.4.3	Gas driving piston . . . . .	149
6.5	Summary . . . . .	149
<b>7</b>	<b>Shock induced rupture of thin diaphragms</b>	<b>151</b>
7.1	Previous work . . . . .	152
7.2	Shock trajectories . . . . .	155
7.3	One-dimensional simulations of PISTL . . . . .	159
7.4	Vaporisation model . . . . .	164
7.5	Fragment model . . . . .	172
7.5.1	Numerical modelling . . . . .	172
7.5.2	Seven piece simulation . . . . .	174
7.5.3	Holding model . . . . .	183
7.5.4	Fourteen piece simulation . . . . .	183
7.6	Summary . . . . .	188

<b>8</b>	<b>Conclusions</b>	<b>191</b>
8.1	Future work . . . . .	195
<b>A</b>	<b>Redlich-Kwong EOS for helium</b>	<b>205</b>
<b>B</b>	<b>One-dimensional Euler solver</b>	<b>209</b>
B.1	Thin diaphragm simulations . . . . .	211
<b>C</b>	<b>Equilibrium Flux Method</b>	<b>213</b>
<b>D</b>	<b>Riemann solver</b>	<b>217</b>
D.1	Stage 1 . . . . .	218
D.2	Stage 2 . . . . .	219
D.3	Stage 3 . . . . .	219
<b>E</b>	<b>Exact one-dimensional flow solver</b>	<b>221</b>
<b>F</b>	<b>Z lines</b>	<b>223</b>

# List of Tables

2.1	Boundary conditions . . . . .	16
2.2	Memory usage . . . . .	16
3.1	Error percentages for supersonic vortex (EFM). . . . .	34
3.2	Error percentages for supersonic vortex (Riemann solver).. . . . .	34
3.3	Comparison of error percentages for supersonic vortex . . . . .	35
3.4	Details of the high pressure shock tube simulations. . . . .	46
3.5	Ideal shock tube test cases . . . . .	53
3.6	Details of double Mach reflection simulations . . . . .	71
4.1	Test condition of Miller & Jones [55] . . . . .	83
6.1	Projectile motion: error of piston velocity versus minimum cell volume.	150
7.1	Experimental conditions of Kendall <i>et al.</i> [44] . . . . .	156
7.2	Details of diaphragm vaporisation simulations. . . . .	164





# List of Figures

1.1	Wave processes within an ideal expansion tube. . . . .	5
2.1	Axisymmetric cell (Jacobs [35]). . . . .	12
2.2	Initial mesh of triangular cells . . . . .	13
2.3	Geometric components of a triangular cell within a domain. . . . .	13
2.4	Example of a structured mesh and how adjacent cells are referenced. . . . .	14
2.5	Data structure for cells. . . . .	15
2.6	Data structure for edges. . . . .	17
2.7	Direction of the unit normal vector at an edge. . . . .	17
2.8	Data structure for vertices. . . . .	18
2.9	Geometry for determining flow data at a vertex from cell-centred data. . . . .	20
2.10	Interpolation geometry. . . . .	20
2.11	Geometry associated with the calculation of the error term for a cell. . . . .	24
2.12	Refinement of triangles using the bisection method. . . . .	26
3.1	Geometry of flow domain for supersonic vortex test case. . . . .	32
3.2	Density contours for supersonic vortex. . . . .	32
3.3	Sequence of meshes used for supersonic vortex. . . . .	33
3.4	Dual mesh. . . . .	36
3.5	Initial flow condition for shock tube problem. . . . .	37
3.6	Unsteady waves within an ideal shock tube after diaphragm breakdown. . . . .	38
3.7	Initial and fixed-grid mesh for Sod's test case. . . . .	38
3.8	Density versus distance for Sod's problem (first-order). . . . .	39

3.9	Density versus distance for Sod's problem (higher-order).	39
3.10	Density versus distance for Sod's problem (adaptive remeshing).	40
3.11	Final mesh for Sod's problem	40
3.12	Ideal shock tube (EFM, $\alpha = 0.1$ ).	41
3.13	Ideal shock tube (EFM, $\alpha = 0.05$ ).	42
3.14	Ideal shock tube (EFM, $\alpha = 0.02$ ).	42
3.15	Ideal shock tube (EFM, $\alpha = 0.01$ ).	43
3.16	Ideal shock tube (Riemann solver, $\alpha = 0.1$ ).	43
3.17	Ideal shock tube (Riemann solver, $\alpha = 0.05$ ).	44
3.18	Ideal shock tube (Riemann solver, $\alpha = 0.02$ ).	44
3.19	Ideal shock tube (Riemann solver, $\alpha = 0.01$ ).	45
3.20	Final mesh for ideal shock tube (EFM).	45
3.21	Final meshes for ideal shock tube (Riemann solver).	47
3.22	Axisymmetric ideal shock tube - axial velocity at axis.	48
3.23	Axisymmetric shock tube - contours and mesh.	49
3.24	2D shock tube - axial flow speed at axis.	49
3.25	Axisymmetric shock tube - axial flow speed away from axis.	50
3.26	Numerical solution by Cambier <i>et al.</i>	51
3.27	Axisymmetric shock tube; first-order solution.	51
3.28	Axisymmetric shock tube - stretched mesh.	52
3.29	Axisymmetric shock tube - contours and mesh for stretched mesh.	52
3.30	Computed shock speed versus distance for various initial pressure ratios.	54
3.31	Shock tube with no contact surface.	55
3.32	Shock speed within shock tube with no contact surface	56
3.33	Computed shock speed versus distance at various mesh resolutions.	56
3.34	Shock speed using different flux calculators	57
3.35	Shock speed for various noise filter coefficients	57

3.36	Shock speed; high resolution EFM compared with Riemann solver . . .	59
3.37	Domain and initial discretisation for flow over a cone. . . . .	60
3.38	Mesh and density contours for cone - 0.5 milliseconds . . . . .	61
3.39	Mesh and density contours for cone - 1.0 millisecond . . . . .	61
3.40	Mesh and density contours for cone - 1.5 milliseconds . . . . .	62
3.41	Flow domain for blast wave at open-ended shock tube. . . . .	64
3.42	Initial discretisation for blast wave at open-ended shock tube. . . . .	65
3.43	Density contours for blast wave flow-field for open-ended shock tube .	66
3.44	Density contours for blast wave flow-field by Wang & Widhopf [89]. .	67
3.45	Double Mach reflection; initial mesh. . . . .	68
3.46	Double Mach reflection; wave configuration. . . . .	69
3.47	Double Mach reflection; EFM solution . . . . .	69
3.48	Numerical solution by Jacobs [34] for Double Mach reflection test case.	70
3.49	Double Mach reflection; Riemann solver solution. . . . .	70
3.50	Double Mach reflection; initial non-aligned mesh. . . . .	71
3.51	Double Mach reflection; Riemann solver solution for non-aligned mesh.	71
3.52	Shock wave diffraction; specified output and initial mesh . . . . .	72
3.53	Density contours for shock diffraction problem . . . . .	73
4.1	Modes of diaphragm rupture (taken from Rothkopf & Low [72]). . . .	77
4.2	Rate of diaphragm opening . . . . .	78
4.3	Numerical Simulation by Cambier <i>et al.</i> [13] . . . . .	80
4.4	Numerical Simulation by Vasil'ev & Danil'chuk [87] . . . . .	81
4.5	Nasa Langley expansion tube . . . . .	82
4.6	Initial mesh for Langley expansion tube. . . . .	84
4.7	Langley expansion tube (condition # 2), flow development. . . . .	87
4.8	Langley expansion tube (condition # 2), flow development. . . . .	88
4.9	Langley expansion tube (condition # 2), flow development. . . . .	89

4.10	Computational mesh at time $t = 20$ microseconds (expansion tube).	90
4.11	Computational mesh at time $t = 240$ microseconds (expansion tube).	90
4.12	Velocity vectors within Langley expansion tube.	91
4.13	Grid convergence for condition #2	91
4.14	Flow development within the Langley expansion tube for condition #1.	92
4.15	Influence of EOS and shock tube geometry	93
4.16	Flow development for constant area shock tube ( $P_4/P_1 = 10$ ).	95
4.17	Flow development for constant area shock tube ( $P_4/P_1 = 100$ ).	96
4.18	Flow development after diaphragm is fully opened ( $P_4/P_1 = 1000$ ).	97
4.19	Grid convergence of contact surface, $P_4/P_1 = 10$	99
4.20	Grid convergence of contact surface, $P_4/P_1 = 100$	100
4.21	Grid convergence of contact surface, $P_4/P_1 = 1000$ .	101
4.22	Contact surface for non-stretched mesh.	102
4.23	Contact surface for 2D shock tube.	103
4.24	Contact surface for different opening times ( $P_4/P_1 = 10$ ).	105
4.25	Contact surface for different opening times ( $P_4/P_1 = 100$ ).	106
4.26	Contact surface for different opening times ( $P_4/P_1 = 1000$ ).	107
4.27	Flow development ( $t_{op} = 157\mu s$ , $P_4/P_1 = 100$ ).	108
4.28	Flow development ( $t_{op} = 300\mu s$ , $P_4/P_1 = 100$ ).	109
5.1	Maximum Mach number versus initial pressure ratio.	115
5.2	Shock speed versus distance for $P_4/P_1 = 1014.5$ .	118
5.3	Shock speed versus distance for $P_4/P_1 = 10145$ .	119
5.4	Shock speed versus distance for $P_4/P_1 = 101450$ .	119
5.5	Grid convergence of computed shock speed for $P_4/P_1 = 1014.5$ .	120
5.6	Grid convergence of computed shock speed for $P_4/P_1 = 10145$ .	120
5.7	Grid convergence of computed shock speed for $P_4/P_1 = 101450$ .	121
5.8	Computed shock speed versus distance ( $P_4/P_1 = 10$ ).	123

5.9	Computed shock speed versus distance ( $P_4/P_1 = 100$ ). . . . .	123
5.10	Computed shock speed versus distance ( $P_4/P_1 = 1000$ ). . . . .	124
5.11	Computed shock speed versus distance ( $P_4/P_1 = 100$ , $t_{op} = 300\mu s$ ). . . . .	124
5.12	Computed shock speed for two-dimensional shock tube. . . . .	126
5.13	Maximum Mach number versus $P_4/P_1$ (computed results included). . . . .	128
6.1	Calculation of effective edge velocity for edge AB. . . . .	133
6.2	Mesh smoothing. . . . .	135
6.3	Diagonal swapping: (a) before and (b) after. . . . .	136
6.4	Vertex deletion. . . . .	136
6.5	Remeshing: (a) before and (b) after. . . . .	137
6.6	Overlapping of new mesh (solid lines) and old mesh (dashed lines). . . . .	138
6.7	Initial (a) and final (b) meshes for random grid motion test case. . . . .	141
6.8	Piston compressing gas: first-order Riemann solver solution. . . . .	142
6.9	Piston compressing gas: higher-order Riemann solver solution. . . . .	142
6.10	Piston compressing gas: (a) initial and (b) final meshes. . . . .	143
6.11	Piston compressing gas: first-order solution from 1D code. . . . .	143
6.12	Piston compressing gas: higher-order ( $\beta = 1.0$ ) solution from 1D code. . . . .	144
6.13	Piston compressing gas: higher-order ( $\beta = 2.0$ ) solution from 1D code. . . . .	144
6.14	Piston compressing gas: first-order EFM solution. . . . .	145
6.15	Piston compressing gas: higher-order ( $\beta = 1.0$ ) EFM solution. . . . .	146
6.16	Piston compressing gas: higher-order ( $\beta = 2.0$ ) EFM solution. . . . .	146
6.17	Piston expanding gas: first-order Riemann solver solution. . . . .	147
6.18	Piston expanding gas: higher-order Riemann solver solution. . . . .	148
6.19	Piston expanding gas: (a) initial and (b) final meshes. . . . .	148
7.1	Pressure traces from PISTL expansion tube ( $6.35\ \mu m$ mylar). . . . .	154
7.2	Pressure traces from PISTL expansion tube ( $127\ \mu m$ mylar). . . . .	154
7.3	Shock trajectories for condition 3A. . . . .	156

7.4	Shock trajectories for condition 3B. . . . .	157
7.5	Shock trajectories for condition 6A. . . . .	158
7.6	Shock trajectories for condition 6B. . . . .	158
7.7	Computed shock trajectories for disappearing diaphragm mass. . . . .	159
7.8	Computed (AEL1D) upstream pressure trace (6.35 $\mu\text{m}$ ). . . . .	160
7.9	Computed (AEL1D) downstream pressure trace (6.35 $\mu\text{m}$ ). . . . .	161
7.10	Computed (AEL1D) upstream pressure trace (127 $\mu\text{m}$ ). . . . .	161
7.11	Computed (AEL1D) downstream pressure trace (127 $\mu\text{m}$ ). . . . .	162
7.12	Grid convergence of solution for 127 $\mu\text{m}$ thick mylar diaphragm. . . . .	162
7.13	Time history of density contours for vapour model (0.00635 $\text{kg}/\text{m}^2$ ). . . . .	165
7.14	Computed (vapour model) upstream pressure trace (6.35 $\mu\text{m}$ ). . . . .	166
7.15	Computed (vapour model) downstream pressure trace (6.35 $\mu\text{m}$ ). . . . .	166
7.16	Time history of density contours for vapour model (0.127 $\text{kg}/\text{m}^2$ ). . . . .	168
7.17	Density contours (higher resolution) for vapour model (0.127 $\text{kg}/\text{m}^2$ ). . . . .	169
7.18	Computed (vapour model) upstream pressure trace (127 $\mu\text{m}$ ). . . . .	170
7.19	Computed (vapour model) downstream pressure trace (127 $\mu\text{m}$ ). . . . .	170
7.20	Computed (2D vapour model) downstream pressure trace (127 $\mu\text{m}$ ). . . . .	171
7.21	Initial mesh for diaphragm fragment model. . . . .	173
7.22	Seven piece fragment model: density contours (0-200 $\mu\text{s}$ ). . . . .	175
7.23	Seven piece fragment model: diaphragm pieces (0-200 $\mu\text{s}$ ). . . . .	176
7.24	Seven piece fragment model: density contours (240-400 $\mu\text{s}$ ). . . . .	177
7.25	Seven piece fragment model: diaphragm pieces (240-400 $\mu\text{s}$ ). . . . .	177
7.26	Mesh at 120 microseconds for seven piece fragment simulation. . . . .	178
7.27	Computed (seven piece) upstream pressure trace (0.00635 $\text{kg}/\text{m}^2$ ). . . . .	178
7.28	Computed (seven piece) downstream pressure trace (0.00635 $\text{kg}/\text{m}^2$ ). . . . .	179
7.29	Computed (seven piece) upstream pressure trace (0.127 $\text{kg}/\text{m}^2$ ). . . . .	179
7.30	Computed (seven piece) downstream pressure trace (0.127 $\text{kg}/\text{m}^2$ ). . . . .	180

7.31	Density contours for elastic collisions. . . . .	181
7.32	Motion of diaphragm pieces for elastic collisions. . . . .	181
7.33	Computed (elastic) upstream pressure trace (0.127 kg/m <sup>2</sup> ). . . . .	182
7.34	Computed (elastic) downstream pressure trace (0.127 kg/m <sup>2</sup> ). . . . .	182
7.35	Computed (hold model) upstream pressure trace. . . . .	184
7.36	Computed (hold model) downstream pressure trace. . . . .	184
7.37	Fourteen piece fragment model: density contours. . . . .	185
7.38	Fourteen piece fragment model: diaphragm pieces. . . . .	186
7.39	Computed (fourteen piece) upstream pressure trace. . . . .	186
7.40	Computed (fourteen piece) downstream pressure trace. . . . .	187
A.1	Heat capacity of helium. . . . .	207
A.2	Comparison of various equations of state for helium. . . . .	208
B.1	One-dimensional interpolation. . . . .	210
B.2	Schematic of thin diaphragm simulations. . . . .	211
D.1	Interpolation logic for the Riemann solver . . . . .	220
F.1	Two $Z$ lines (dashed) starting from the same edge. . . . .	224
F.2	Direct and indirect segments of $Z$ lines. . . . .	225





# Nomenclature, Units

$A$	: cell area in the $x$ - $y$ plane, $\text{m}^2$
$\mathbf{a}$	: acceleration, $\text{m}/\text{s}^2$
$a$	: speed of sound, $\text{m}/\text{s}$
$C$	: specific heat, $\text{J}/\text{kg}\cdot\text{K}$
$E$	: total specific energy (internal + kinetic), $\text{J}/\text{kg}$
$e$	: specific internal energy, $\text{J}/\text{kg}$
$\mathbf{F}$	: array of flux terms
$\mathbf{F}$	: force, $\text{N}$
$\mathbf{F}$	: vector function
$I$	: moment of inertia, $\text{kg}\cdot\text{m}^2$
$\hat{\mathbf{i}}$	: unit vector in $x$ direction
$\hat{\mathbf{j}}$	: unit vector in $y$ direction
$\hat{\mathbf{k}}$	: unit vector in $z$ direction
$\kappa$	: MUSCL interpolation parameter
$k$	: Boltzmann's constant, $1.38 \times 10^{-23} \text{ J}/\text{K}$
$L$	: error
$L$	: length, $\text{m}$
$M$	: moment, $\text{N}\cdot\text{m}$
$M$	: Mach number
$m$	: mass, $\text{kg}$
$m$	: mass flux/area/time, $\text{kg}/\text{m}^2\cdot\text{s}$
$\hat{\mathbf{n}}$	: unit normal vector
$N$	: total number of molecules
$n$	: component of unit normal vector
$n$	: order of convergence
$n$	: number of molecules per unit volume
$P$	: pressure, $\text{Pa}$
$p$	: momentum/area/time, $\text{kg}/\text{m}\cdot\text{s}^2$
$\mathbf{Q}$	: array of source terms
$q$	: cell quality, $0 < q \leq 1.0$

$\mathbf{r}$  : position vector, m  
 $r$  : radial co-ordinate, m  
 $\bar{r}$  : radial co-ordinate of centroid  
 $S$  : characteristic surface  
 $S$  : area of characteristic surface, m<sup>2</sup>  
 $T$  : temperature, K  
 $t$  : time, seconds  
 $\mathbf{U}$  : array of conserved flow quantities  
 $\mathbf{u}$  : flow velocity, m/s  
 $u$  : flow speed in the  $x$  direction, m/s  
 $\mathbf{V}$  : velocity, m/s  
 $V$  : speed, m/s  
 $v$  : flow speed in the  $y$  direction, m/s  
 $\mathbf{w}$  : grid velocity, m/s  
 $w$  : grid speed, m/s  
 $w$  : weighting  
 $w$  : wave speed, m/s  
 $x$  : x co-ordinate, m  
 $y$  : y co-ordinate, m  
 $z$  : z co-ordinate, m  
 $\alpha$  : noise filter coefficient  
 $\beta$  : compression parameter (MUSCL interpolation)  
 $\epsilon$  : energy flux/area/time, J/m<sup>2</sup>·s  
 $\gamma$  : ratio of specific heats  
 $\rho$  : density, kg/m<sup>3</sup>  
 $\sigma$  : Courant number  
 $\theta$  : angle of rigid body  
 $\vartheta$  : cell volume, m<sup>3</sup>  
 $\vartheta'$  : volume per radian for axisymmetric cell, m<sup>3</sup>

## Subscripts

$c$  : critical  
 $f$  : flow  
 $f$  : fragment  
 $g$  : grid  
 $L$  : left

min : minimum  
n : normal direction  
op : opening  
p : piston  
R : right  
R : reduced  
s : solid (rigid) body  
t : tangential direction  
v : constant volume  
x :  $x$  direction  
y :  $y$  direction  
1 : driven gas  
4 : driver gas

# Chapter 1

## Introduction

The design of an aerospace vehicle requires accurate and reliable data estimating the aerodynamic pressures and heating loads on the proposed vehicle. This data, with varying degrees of accuracy, can be obtained from the following sources: theoretical methods, physical flow simulations on subscale models in ground-based test facilities, flight experiments on full-scale or sub-scale models, and computational fluid dynamics simulations. The most reliable source of data is full-scale flight experiments, however, the other approaches are attractive because they are cheaper and a number of design variations can be explored easily.

In the past, data from wind tunnels has been extensively used to design aerospace vehicles. For example, in the mid-1970's the primary source of data for the aerodynamic design of the shuttle Orbiter was 60000 hours of wind tunnel testing. Currently, reflected shock tubes and expansion tubes, are used to generate high-energy, hypersonic flows for the ground testing of aerospace vehicles. These facilities have been able to emulate some of the real-gas effects (high temperature, chemistry related effects such as dissociation) which have been found to be important in determining the centre of pressure of gliding re-entry vehicles [90].

A problem with both reflected shock tubes and expansion tubes is that the details of the gas-dynamic processes within these facilities (particularly those at diaphragm rupture) are not well understood and there is considerable uncertainty in the properties of the test flow [53, 15].

Computational Fluid Dynamics (CFD) involves the use of computers to solve the non-linear equations governing fluid motion. These equations can be applied to complex geometries, such as a proposed aerospace vehicle. The main limitations of CFD (those of requiring fast computational speeds and large memory for accurate simulations) have improved rapidly over the last thirty years and continue to improve. Hence, the utility of CFD has increased to the point where it has become a necessary tool in the design processes of all current aerospace plane programs [54]. Indeed, some consider that the role of CFD has recently become more important than hypersonic wind tunnels [16]. This is because the limitations of wind tunnels (such as limited model size, pressure, velocity, Reynolds number, temperature, and type of atmosphere that can be simulated) cannot be improved upon without the expenditure of large amounts of money. The advantages of CFD methods over ground-based testing are: the reproduction of flight conditions, the use of full scale models, the availability of global field information, versatility, and the lower uncertainty associated with results [52]. However, the quality of any CFD analysis is no better than the underlying theoretical model. Difficulties include uncertainties in chemistry and turbulence models.

Both CFD and experimental techniques have a role in current aerospace design. Sometimes data from one technique is used to help improve the other. For example, the validation of CFD codes using the data from high quality experimental facilities is presently a priority activity [54, 40]. Conversely, when we consider the design and construction of ground-based test facilities, the roles of CFD are to: (i) reduce the dependence on building prototypes, (ii) improve the performance of the facility in terms of both increasing the magnitude of flow quantities (such as velocity and pressure) and increasing flow quality, and (iii) assist with the analysis of experimental data by providing more detailed flow information (surface pressures rather than point measurements) and information that cannot be directly or conveniently measured (field pressures, densities, temperatures and velocities).

The focus of this thesis is the use of computational fluid dynamics to assist in understanding the gas-dynamic processes that occur during the rupture (opening) of diaphragms within ground-based facilities.

## 1.1 A brief description of an expansion tube

For a description of experimental facilities capable of producing high-enthalpy hypersonic flows the reader is referred to Stalker [78]. A brief description of the expansion tube is given here, because the two different types of diaphragm rupture examined in this thesis, occur during its operation.

An expansion tube is an impulse wind tunnel that is capable of producing high-enthalpy test gas. The concept was first proposed by Trimpi [85]. It consists of three sections: driver, intermediate, and acceleration tubes. The wave processes that occur during the ideal operation of an expansion tube are shown in Figure 1.1. A heavy diaphragm (the primary diaphragm) separates the driver and intermediate tubes, while a light diaphragm (the secondary diaphragm) separates the intermediate and acceleration tube. The initial pressure is highest in the driver tube and lowest in the acceleration tube. Flow is initiated when the primary diaphragm separating the driver and intermediate tubes bursts. This causes a shock wave to process the test gas in the intermediate tube. When the shock wave arrives at the light secondary diaphragm, the increased upstream pressure causes the diaphragm to rupture. The test gas then undergoes an unsteady expansion which increases its velocity and enthalpy. The test time commences when the acceleration-test gas interface arrives at the test section and terminates when either the downstream edge of the unsteady expansion or the reflection of its upstream edge from the driver-test gas interface arrives at the test section. Test times within expansion tubes are short, for example

the test time (in air at 11 km/s) within X2 at the University of Queensland is approximately 40 microseconds.

## 1.2 Scope of this thesis

The data presented in this thesis are results from numerical simulations of: (i) the relatively slow rupture of the primary diaphragm in a shock tube, and (ii) the faster rupture of the light secondary diaphragm in an expansion tube. The intention of this study is to examine, in detail, the gas-dynamic processes associated with the opening (or rupture) of both types of diaphragm.

The primary tool in the investigation will be the simulation code U2DE, which solves the unsteady Euler equations for compressible inviscid flow. In Chapter 2, the features of U2DE which are used to perform simulations with stationary flow domains are described. Within U2DE, the flow domain is represented as an unstructured mesh of triangular cells, and solution-adaptive remeshing is used to focus computational effort in regions where the flow-field gradients are high. In Chapter 3 the ability of the code to produce accurate solutions to the Euler equations is verified.

Multi-dimensional simulations of primary diaphragm rupture within experimental facilities have been performed previously. Satofuka [74] performed a numerical study of shock formation in cylindrical and two-dimensional shock tubes. The computed shock speed was examined and compared with theory. Cambier *et al.* [13] performed two-dimensional axisymmetric simulations of a gradually opening diaphragm and made observations about the structure of the developing flow. Vasil'ev & Danil'chuk [87] performed an inviscid two-dimensional simulation of flow formation in a shock tube with transverse diaphragm removal.

The operation of a reflected shock tunnel differs from an expansion tube in that the test gas is stagnated at the secondary diaphragm and then undergoes a steady expansion through a nozzle (for more information on reflected shock tunnels the reader is referred to Stalker [77]). It has been speculated that one possible cause of contamination of the test gas by the driver gas within reflected shock tubes is the jetting of the driver gas into the test gas when the reflected shock from the end of the intermediate (shock) tube interacts with the contact surface (CS) between the driver and test gas [17]. The shape of the CS is determined by the gas-dynamic processes that occur during the diaphragm opening. It is postulated that the shape of this CS at shock reflection has a significant effect upon the subsequent mixing and contamination of the test gas. In Chapter 4, axisymmetric simulations of a shock

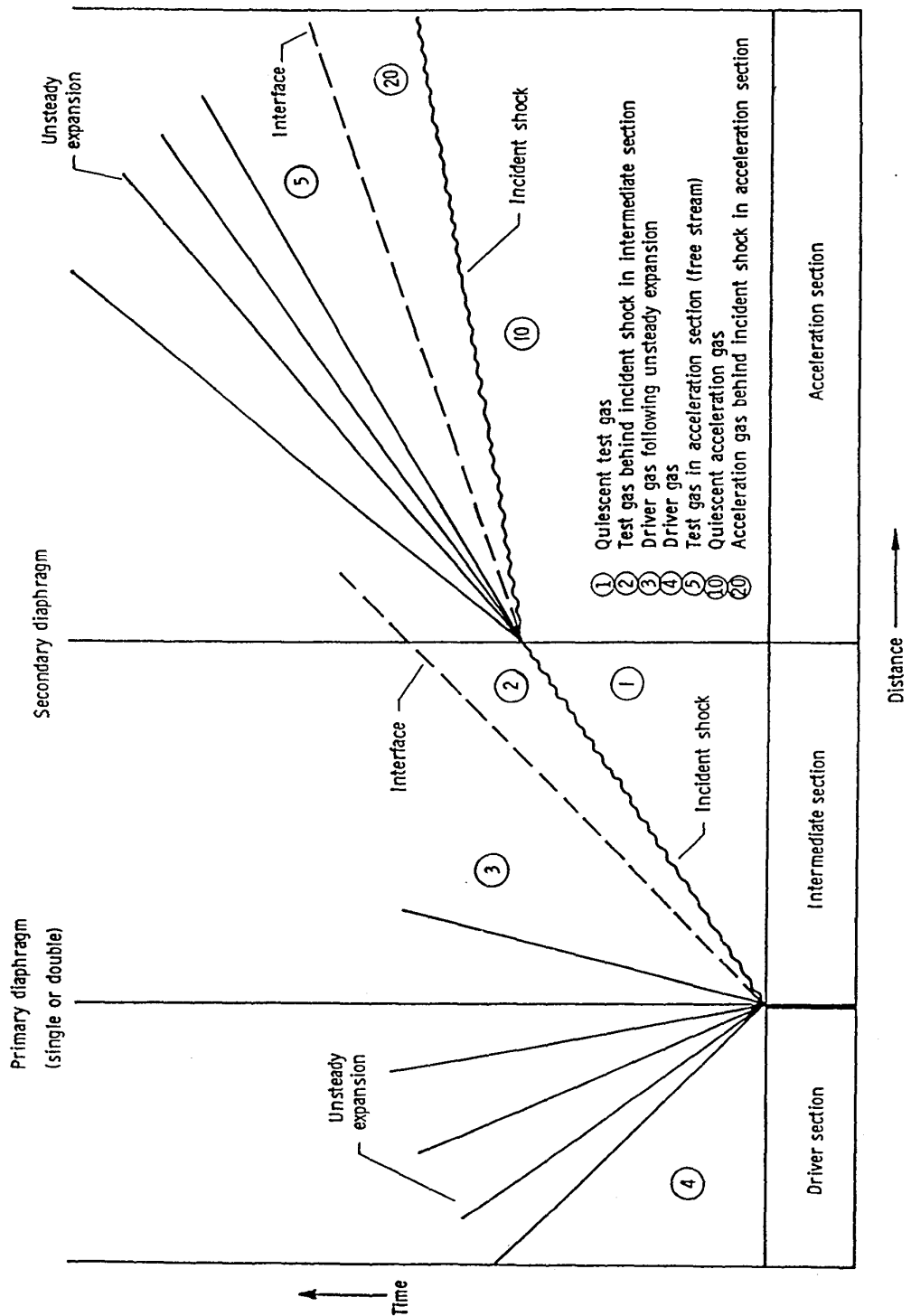


Figure 1.1: Wave processes within an ideal expansion tube (taken from Miller & Jones [55]).



tube with a gradually opening diaphragm are presented. Unlike the previous work, the main factors that influence the development of the CS are identified.

For high initial pressure ratios across the diaphragm, previous experiments have shown that the measured shock speed can exceed (by up to 20%) the shock speed predicted by one-dimensional models. In Chapter 5, the computed shock speeds from the axisymmetric simulations presented in Chapter 4 are compared with shock speeds measured in experiments [55] and estimates from previous one-dimensional models [91, 33]. The current work differs from the previous work in that shock speeds from high resolution multi-dimensional simulations have been compared with experimental data and estimates from one-dimensional theory.

Chapter 6 describes the features of U2DE used to perform simulations of two-dimensional fluid-structure interactions. These features include the ability to solve the Euler equations for a general moving frame of reference. The management of the mesh during the simulations is also described. This includes the ability to automatically generate a new mesh when the current mesh becomes distorted (due to the motion of the rigid bodies) and the transfer of the solution from the old mesh to the new.

The influence of the mass of the secondary diaphragm within an expansion tube, after it has been struck by the incident shock will be examined. Morgan (private communication) has indicated that the mass of the secondary diaphragm is equivalent to 2 km of acceleration gas. Recent flow visualisations by Sutcliffe & Wegener at the University of Queensland (unpublished) show that the diaphragm fragments into many solid pieces and acts as a piston for at least one diameter (38 mm) downstream. By the time the test flow emerges from the acceleration tube the diaphragm mass has been removed from the test flow, although some fragments may appear in the flow after the test time. Just how quickly the diaphragm mass is removed from the flow is of interest.

Wilson [95] performed axisymmetric simulations of the HYPULSE expansion tube to examine the level of dissociation in the test gas after it had been partially processed by the reflected shock and expanded into the acceleration tube. The diaphragm was assumed to hold for a finite time and then disappear. It was concluded that the accuracy of the predictions could be improved by modelling the rupturing of the secondary diaphragm. Bakos & Morgan [8] also predict the levels of dissociation in the test gas using the one-dimensional finite-volume code of Jacobs [38] to solve the unsteady Euler equations for the flow near the diaphragm, assuming that the diaphragm acted like a piston.

In Chapter 7, two different multi-dimensional models describing the shock induced rupture of thin diaphragms are examined. These models differ from the previous work as they consider the influence of the diaphragm mass while allowing the upstream gas to penetrate the diaphragm mass. The first model assumes the diaphragm vaporises immediately after the arrival of the incident shock. The second model assumes the diaphragm shatters into a number of pieces which are treated as rigid bodies. The results from both models are compared with experimental data.



# Chapter 2

## Two-dimensional finite-volume code

U2DE is a cell-centred finite-volume code which integrates, in time, the unsteady Euler equations for inviscid compressible flow. Reviews of methods used to solve the Euler equations have been written by Anderson [5] and Hirsch [30]. U2DE was used to simulate the gas-dynamic processes that occur within shock tubes and expansion tubes during and after diaphragm rupture. These flows exhibit strong shocks and contact discontinuities, and so two upwind shock-capturing schemes: Equilibrium Flux Method (EFM) [64] and Riemann solver [36], were used. Many CFD techniques for compressible flow will simply fail to give answers in these situations [83, 30, 66]. The trade-off between accuracy and robustness, and the desire to have both, has driven much of the development of this code.

In this chapter, the features of U2DE which are used to solve unsteady, compressible flow problems with stationary domains, are described. The numerical techniques used by U2DE are not new and come from many different sources which are referenced throughout the chapter. The first section of this chapter describes the governing equations for two-dimensional planar and axisymmetric geometries. The flow domain is represented as an unstructured mesh of triangular cells. The initial mesh generation, the data structures used by the code to store the mesh and flow data, and the cell geometry are described.

The integral Euler equations are applied directly to each cell, ensuring that mass, momentum, and energy are conserved at the discrete level. Known initial conditions are sequentially advanced in time, step by step, by a time marching scheme. The numerical techniques employed to solve the governing equations are described (Sec. 2.3).

The code uses solution-adaptive remeshing to focus computational effort, in regions where the flow-field gradient is high and thus captures shock waves and shear layers, at a greater mesh resolution and accuracy than possible with fixed grid simulations. This technique is also described.

## 2.1 Governing equations

Considering a stationary volume  $\vartheta$ , bounded by a control surface  $S$ , the Euler equations for two-dimensional flow can be written as,

$$\frac{\partial}{\partial t} \int_{\vartheta} \mathbf{U} \, d\vartheta + \int_S \mathbf{F} \cdot d\hat{\mathbf{n}} \, dS = 0 \quad (2.1)$$

where  $\mathbf{U}$  is the array of *conserved quantities* and  $\mathbf{F} \cdot d\hat{\mathbf{n}}$  is the array of *fluxes*,

$$\mathbf{U} = \begin{bmatrix} \rho \\ \rho u \\ \rho v \\ \rho E \end{bmatrix}, \quad \mathbf{F} = \begin{bmatrix} \rho \mathbf{u} \\ \rho u \mathbf{u} + P \hat{\mathbf{i}} \\ \rho v \mathbf{u} + P \hat{\mathbf{j}} \\ \rho E \mathbf{u} + P \mathbf{u} \end{bmatrix}. \quad (2.2)$$

The first term represents the temporal change of the integral over the cell volume of the mass, momentum and energy, while the second term represents the fluxes of these quantities through the control surface bounding the volume.

The *primary flow variables* are the density  $\rho$ , components of velocity  $u$  and  $v$ , pressure  $P$ , and specific internal energy  $e$ . The *flow state* of a cell is defined by its primary flow variables.

The equation of state relating pressure, density and total energy allows closure of the equations,

$$P = f(\rho, e) \quad (2.3)$$

where,

$$e = E - \frac{1}{2}(u^2 + v^2). \quad (2.4)$$

For a calorifically perfect gas, the equation of state,

$$P = \rho(\gamma - 1)e \quad (2.5)$$

is used. Other equations of state can be used (Appendix A).

Given the initial flow state within the control volume  $\vartheta$  (and its neighbours), these equations can be used to determine the flow state in the control volume at subsequent times.

The axisymmetric form of the Euler equations is determined by applying the equations to an axisymmetric cell (Fig. 2.1) and can be written as,

$$\frac{\partial}{\partial t} \int_{\vartheta'} \mathbf{U} d\vartheta + \int_S r \mathbf{F} \cdot d\hat{\mathbf{n}} dS = \mathbf{Q} \quad (2.6)$$

where,

$$\mathbf{Q} = \begin{bmatrix} 0 \\ 0 \\ PA \\ 0 \end{bmatrix}. \quad (2.7)$$

The volume of the cell is expressed as volume per radian ( $\vartheta'$ ). The source term completes the momentum equation by considering the pressure force contribution on faces ABCD (Fig. 2.1). Further detail on the development of these equations was described by Jacobs [35].

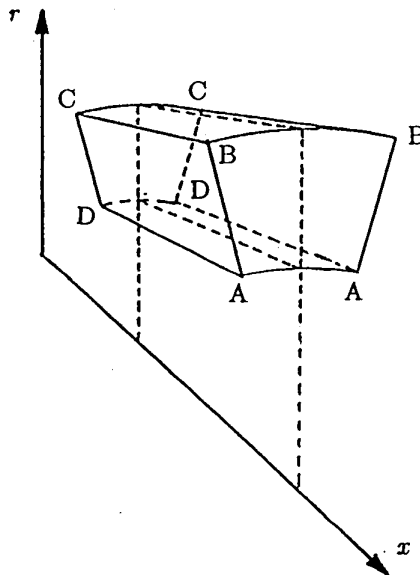


Figure 2.1: Axisymmetric cell (Jacobs [35]).

## 2.2 Initial mesh generation and data storage

The flow domain is discretised (divided) into triangular cells (Fig. 2.2). The bounding contour  $S$ , of each triangular cell (Fig. 2.3) consists of three line segments (referred to as edges). Flow and geometric information relating to the cells, edges and vertices are stored in three separate arrays. Memory allocation to these arrays within the program is dynamic because cells, edges, and vertices are continually being added and deleted from their respective lists during the simulations.

The triangular cells are related to each other in an unstructured manner. The main difference between an unstructured and a structured mesh, is the method used to locate adjacent cells. For a structured mesh, an indexing algorithm is used to locate neighbouring cells. For example the adjacent cells to cell  $(i,j)$  within a structured rectangular mesh are  $(i+1,j)$ ,  $(i-1,j)$ ,  $(i,j+1)$  and  $(i,j-1)$  (Fig. 2.4). For an unstructured mesh, there is no relation between the physical location of a cell and its array number (memory location). The array numbers of adjacent cells can be accessed by storing them within the data structure of a cell. The two main advantages of using unstructured meshes are: the easier implementation of solution-adaptive remeshing, and the easier discretisation of complex geometries.

Initial meshes are generated by dividing a rectangular box into  $n \times m$  cells (Fig. 2.2). Each rectangular cell is divided into two triangular cells which are referred to as the top and bottom cells. The triangular cells are assigned an index number depending on their location within the mesh. The top cells are assigned the number

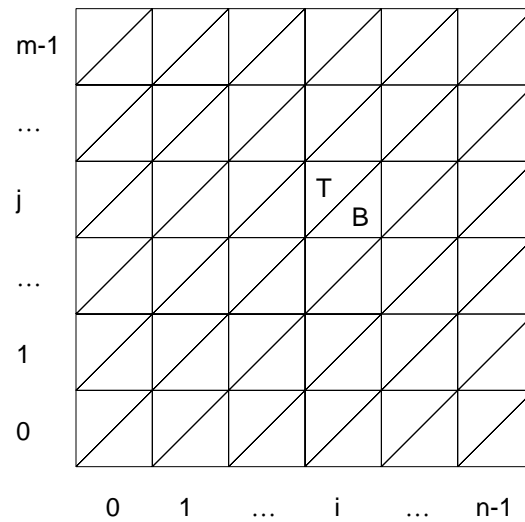


Figure 2.2: Initial mesh of triangular cells, top (T) and bottom (B) cells are marked.

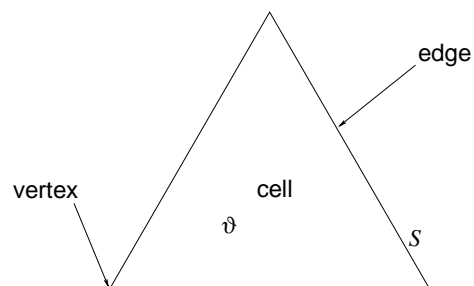


Figure 2.3: Geometric components of a triangular cell within a domain. The cell has volume,  $\vartheta$ , and the boundary,  $S$ , consists of three edges.



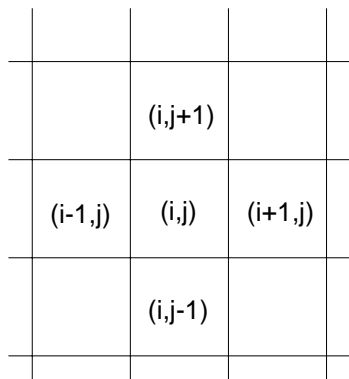


Figure 2.4: Example of a structured mesh and how adjacent cells are referenced.

$$2 \times n \times j + i \text{ where } 0 \leq i < n,$$

and the bottom cells are assigned the number

$$2 \times n \times j + i + 1 \text{ where } 0 \leq j < m .$$

This creates a structured mesh of triangular cells where adjacent cells can be located via the above mentioned indexing scheme. An initial mesh generated in this manner can be treated as a structured mesh, however, the mesh becomes unstructured as extra vertices are inserted during solution-adaptive remeshing. Other geometries can be created by transforming the co-ordinates of the vertices and or by deleting cells. Examples of initial meshes created in this manner can be seen in Chapter 3 (Figs. 3.37, 3.42, 3.45, 3.50, & 3.52b).

The primary flow variables and conserved quantities are associated with the centre of a cell and are assumed to be the cell averaged value. Within the program, these data are stored as part of the data structure for each cell (Fig. 2.5). The array number of the three vertices, the three adjacent cells, and the three bounding edges are also stored within the cell data structure. If a cell is located at the boundary of the domain (i.e. there is no adjacent cell) the integer value -1, is stored as the adjacent cell. The temporal changes in the conserved quantities during time integration (Sec. 2.3.3) are also stored within the cell data structure.

The fluxes of mass, momentum and energy are associated with the midpoint of an edge and are assumed to represent an average along the edge and are stored within the edge data structure (Fig. 2.6). The array numbers of the cells sharing the edge are stored as the left and right cells. The choice of left and right cell is arbitrary and the direction of the unit normal is from left cell to right cell (Fig. 2.7). The flow states (Sec. 2.3.1) on either side of the edge are also stored. If the edge is at the

```

struct cell {
/***** primary variables *****/
    double rho; /* density */
    double velx; /* velocity in global x-direction */
    double vely; /* velocity in global y-direction */
    double pres; /* pressure */
/***** connectivity lists *****/
    int adj_cell[3]; /* array storing array numbers of /*
                    /* adjacent cells */
    int intfc[3]; /* array storing array numbers of */
                    /* bounding edges */
    int vert[3]; /* array string array number */
                    /* of the vertices */
/***** geometry *****/
    double vol; /* volume of cell */
    double scale; /* length of the smallest median */
    double x; /* x co-ordinate of the cell centre */
    double y; /* y co-ordinate of the cell centre */
/***** conserved variables per unit volume *****/
    double mass;
    double momx; /* momentum in x-direction */
    double momy; /* momentum in y-direction */
    double energy; /* total energy */
/***** 1st change in conserved variables *****/
    double d1mass; /* 1st change in mass */
    double d1momx; /* 1st change in momentum in x-direction */
    double d1momy; /* 1st change in momentum in y-direction */
    double d1energy; /* 1st change in energy */
/***** 2nd change in conserved variables *****/
    double d2mass; /* 2nd change in mass */
    double d2momx; /* 2nd change in momentum in x-direction */
    double d2momy; /* 2nd change in momentum in y-direction */
    double d2energy; /* 2nd change in energy */
/***** error indicator *****/
    int error; /* error status of cell */
                    /* 1 = cell to be refined */
                    /* -1 = cell to be de-refined */
                    /* 0 no action required */
/***** optional *****/
#ifdef (AXISYMMETRIC)
    double cont_area; /* contoured area */
#endif
#ifdef (IGNORED_CELLS)
    int ign; /* ignored status of cell; */
                    /* 0 = flow cell; */
                    /* 1 = ignored cell; */
#endif
};

```

Figure 2.5: Data structure for cells.

boundary of the domain, the right cell is the array number of the flow cell and the integer value of the left cell is negative and specifies the type of boundary (Table 2.1).

left cell	applied boundary condition
-1	wall
-2	in-flow
-3	out-flow

Table 2.1: Type of boundary conditions that can be applied and how they are stored within the edge data structure.

The co-ordinates of a vertex are stored within its data structure (Fig. 2.8). The array numbers of the cells surrounding a vertex and the flow state at the vertex (Sec. 2.3.1) are also stored.

The array numbers of two vertices and a refinement level number are also stored within the data structure of a vertex. The purpose of this data is explained in Sections 2.4.2 and 2.4.3.

Most of the simulations were performed on the Silicon Graphics Power Challenge at the University of Queensland. The available memory of this machine is very large (6 Gbytes). Considering the amount of memory required per cell (Table 2.2), it would have been possible to perform a simulation with ten million cells. The computational time for a simulation of this size can be excessive. The number of cells used for simulations relating to this thesis was limited by processor time and not memory restrictions. For this reason, the data structures were designed to reduce CPU time by storing geometric and flow data instead of re-calculating it.

Data structure	Size of data structure (bytes)	Number per cell	Memory per cell
cell	248	1	248
edge	176	1.5	264
vertex	168	0.5	84
Total memory (per cell)			596

Table 2.2: Calculation of memory used per cell assuming six cells are associated with each node.

The centroid of each triangular cell is equal to the average position vector of its vertices,

$$\mathbf{r}_c = \frac{\mathbf{r}_1 + \mathbf{r}_2 + \mathbf{r}_3}{3}. \quad (2.8)$$

For two dimensional planar simulations, each cell is assumed to have unit depth and  $\vartheta = A$ . The area of a cell is found by calculating half of the vector product of two

```

struct edge{
/***** fluxes *****/
  double mass; /* mass flux */
  double momx; /* flux of momentum in global x-direction */
  double momy; /* flux of momentum in global y-direction */
  double energy /* total energy flux */
/***** left state *****/
  double rhoL; /* left state density */
  double velxL; /* left state velocity in global x-direction */
  double velyL; /* left state velocity in global y-direction */
  double presL; /* left state pressure */
/***** right state *****/
  double rhoR; /* right state density */
  double velxR; /* right state velocity in global x-direction */
  double velyR; /* right state velocity in global y-direction */
  double presR; /* right state pressure */
/***** connectivity *****/
  int vert1; /* array number of vertex no. 1 */
  int vert2; /* array number of vertex no. 2 */
  int cell1; /* array number of cell on left side of edge */
  int cell2; /* array number of cell on right side of edge */
/***** Geometry *****/
  double x; /* x co-ordinate of the mid-point of the edge */
  double y; /* y co-ordinate of the mid-point of the edge */
  double nx; /* x component of normal vector */
  double ny; /* y component of normal vector */
  double length; /* length of edge */
/***** Optional *****/
#ifdef IGNORED_CELLS
  int ign; /* ignored status of edge; */
          /* 0 = normal flow edge; */
          /* 1 = edge between ignored cell and flow cell, */
          /*      treated as a wall; */
          /* 2 = edge between two ignored cells, */
          /*      edge is to be ignored */
#endif
};

```

Figure 2.6: Data structure for edges.

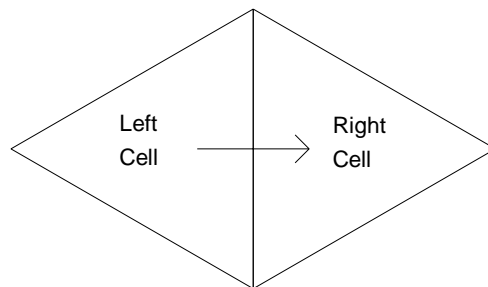


Figure 2.7: Direction of the unit normal vector at an edge.

```

struct point {
    double x;          /* x co-ordinate */
    double y;          /* y co-ordinate */
    int cells[15];     /* list of cells that contain the vertex */
    int level;         /* refinement level of vertex */
    int pt1;           /* the vertices of the edge that was */
    int pt2;           /* split by the current vertex */
/*
 * Note: the primary flow variables are constructed at the vertices
 * before interpolation and the calculation of error for remeshing.
 */
    double rho;        /* constructed density */
    double velx;       /* constructed velocity in x-direction */
    double vely;       /* constructed velocity in y-direction */
    double pres;       /* constructed pressure */
    double e;          /* constructed internal energy */
};

```

Figure 2.8: Data structure for vertices.

edges of the cell,

$$A = \frac{|(\mathbf{r}_2 - \mathbf{r}_1) \times (\mathbf{r}_3 - \mathbf{r}_1)|}{2}. \quad (2.9)$$

For axisymmetrical simulations, a modified cell volume (volume per radian) is used,

$$\vartheta' = \int_{\vartheta} r dx dy = \bar{r} A \quad (2.10)$$

where  $\bar{r}$  is the  $r$  co-ordinate of the centroid of the area projected onto the  $x - r$  plane.

## 2.3 Numerical techniques

Known initial conditions are sequentially advanced in time, step by step, by a time marching scheme. Each *time-step* can be divided into three separate parts. The first part is the *reconstruction* of the left and right edge states (Sec. 2.3.1). The second part is to determine the flux array,  $\mathbf{F} \cdot d\hat{\mathbf{n}}$  at each edge (Sec. 2.3.2). The third part is the update of the cell averaged conserved quantities and the primary flow variables (Sec. 2.3.3).

### 2.3.1 Reconstruction

For a first-order calculation, the left and right edge flow states of an internal edge are set to the left and right cell flow states (Sec. 2.2). If the edge is on the boundary

of the domain, the right-edge state is equal to the flow state of the cell associated with the edge. The left-edge state depends on the applied boundary condition. If out-flow conditions apply at the boundary the left edge flow state is the same as the right edge flow state. This boundary condition assumes that the flow outside the domain does not influence the flow inside the domain. This is true when the flow normal to the boundary is supersonic. If supersonic in-flow conditions apply at the boundary, the left edge state is equal to a pre-defined in-flow condition. If the wall boundary condition applies, the left flow state is set to the mirror reflection of the right flow state where the edge is the reflecting surface,

$$\begin{aligned}
 \rho_L &= \rho_R \\
 (u_n)_L &= -(u_n)_R \\
 (u_t)_L &= (u_t)_R \\
 P_L &= P_R,
 \end{aligned}
 \tag{2.11}$$

where the  $n$  subscript denotes the normal direction, and  $t$  the tangential direction. The flow velocities in these directions are calculated as follows,

$$\begin{aligned}
 u_n &= u n_x + v n_y \\
 u_t &= -u n_y + v n_x.
 \end{aligned}
 \tag{2.12}$$

For a given mesh resolution, the accuracy of the scheme can be improved by reconstructing the flow states either side of the edges from the surrounding cell-centred flow data. This reconstruction is done in two stages. Each primary flow variable is treated independently and in the same manner. Here, density is used as an example. Firstly, the densities at the vertices are determined by summing the densities of the cells surrounding a vertex multiplied by a weight, and then dividing by the sum of the weights [9] (Eqn. 2.13, Fig. 2.9). The weights are equal to the inverse of the distance from the vertex to the cell centre.

$$\rho_v = \frac{\sum_{i=1}^N w_i \rho_i}{\sum_{i=1}^N w_i} \quad \text{where} \quad w_i = \frac{1}{|\mathbf{r}_i - \mathbf{r}_v|}
 \tag{2.13}$$

The second stage is the interpolation of the left and right edge densities ( $\rho_{L0}, \rho_{R0}$ ) from the four pre-interpolation densities ( $\rho_{L2}, \rho_{L1}, \rho_{R1}, \rho_{R2}$ ). If the edge is internal to the flow domain:  $\rho_{L2}$  equals the density at the vertex of the left cell which is opposite the edge,  $\rho_{L1}$  equals the density at the centre of the left cell,  $\rho_{R1}$  equals the density at the centre of the right cell, and  $\rho_{R2}$  equals the density at the vertex of the right cell opposite to the edge (Fig. 2.10). If the edge is external, the far-left

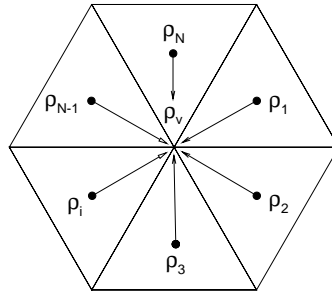


Figure 2.9: Geometry for determining flow data at a vertex from cell-centred data.

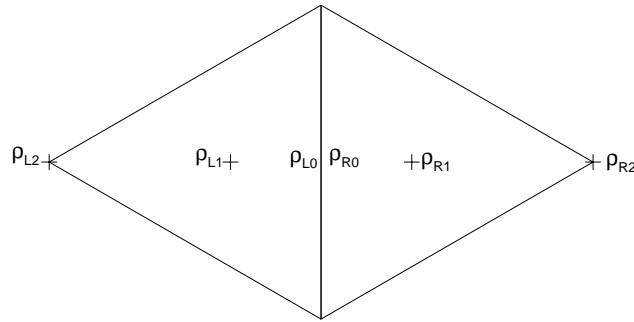


Figure 2.10: Interpolation geometry.

flow state is equal to the mirror reflection of the far-right state with the edge acting as the mirror.

A generalised MUSCL interpolation scheme [4] (shown below) is used to determine the left and right flow states from the pre-interpolation flow states,

$$\begin{aligned}\rho_{L0} &= \rho_{L1} + \Delta_L \\ \rho_{R0} &= \rho_{R1} + \Delta_R\end{aligned}\tag{2.14}$$

where,

$$\begin{aligned}\Delta_L &= \frac{1}{4}[(1 - \kappa)\mathbf{MINMOD}\{(\rho_{L1} - \rho_{L2}), \beta(\rho_{R1} - \rho_{L1})\} \\ &\quad + (1 + \kappa)\mathbf{MINMOD}\{\beta(\rho_{L1} - \rho_{L2}), (\rho_{R1} - \rho_{L1})\}] \\ \Delta_R &= -\frac{1}{4}[(1 + \kappa)\mathbf{MINMOD}\{(\rho_{R1} - \rho_{L1}), \beta(\rho_{R2} - \rho_{R1})\} \\ &\quad + (1 - \kappa)\mathbf{MINMOD}\{\beta(\rho_{R1} - \rho_{L1}), (\rho_{R2} - \rho_{R1})\}].\end{aligned}\tag{2.15}$$

The MINMOD limiter function returns the argument with the minimum magnitude if both arguments have the same sign, and returns zero otherwise. The parameter  $\kappa = 1/3$  is used giving an upwind-biased third-order interpolation scheme. The *compression* parameter is restricted to,

$$1 \leq \beta \leq \frac{3 - \kappa}{1 - \kappa}. \quad (2.16)$$

All simulations presented in this thesis, used the higher-order interpolation scheme with  $\beta = 2$  unless specified otherwise.

### 2.3.2 Calculation of Fluxes

The flux array  $\mathbf{F} \cdot d\hat{\mathbf{n}}$ , in Equation 2.2 is determined from the edge flow states,

$$\mathbf{F} \cdot d\hat{\mathbf{n}} = f(\mathbf{U}_L, \mathbf{U}_R). \quad (2.17)$$

Due to the nature of the flows to be simulated, upwind schemes were used to calculate the flux array. Upwind schemes are designed to account for the direction of propagation of information within the flow-field, and attempt to reduce or eliminate oscillations that may occur using a central difference scheme. Many different types of upwind schemes have been developed such as flux splitting, flux limiting and the Godunov scheme [30]. Depending on the nature of the flow, either an approximate Riemann solver [36] or the equilibrium flux method (EFM) [64] was used to calculate the fluxes. The performance of the various flux calculations is discussed in Chapter 3.

The Riemann solver (described in detail in Appendix D) determines the fluxes by approximately solving the unsteady one-dimensional Euler equations in the direction normal to the edge.

EFM is derived from the kinetic theory of gases and is described in Appendix C. It has been shown [51] that this method solves the Euler equation with added pseudo dissipation, and in the hypersonic limit EFM becomes an upwind scheme. The method is robust due to the extra dissipation.

The flux calculations are performed assuming that the gas behaves as a perfect gas. If the gas behaviour deviates from the perfect gas model, an “effective” ratio of specific heats  $\gamma$ , is used. The effective  $\gamma$  can be calculated from the pseudo left and right edge flow states [24].

$$\gamma_{av} = \frac{\sqrt{\rho_L} \gamma_L + \sqrt{\rho_R} \gamma_R}{\sqrt{\rho_L} + \sqrt{\rho_R}} \quad (2.18)$$



$$\gamma_i = \frac{P_i}{\rho_i \epsilon_i} + 1 \quad (2.19)$$

### 2.3.3 Time-stepping

When the edge fluxes have been determined, the change in the cell averaged conserved quantities, ( $\mathbf{U}$  in Equation 2.2) can be calculated. The rate of change  $\frac{d\mathbf{U}}{dt}$  is obtained from the discretised form,

$$\frac{d\mathbf{U}}{dt} \simeq -\frac{1}{\vartheta} \sum_{k=1}^3 \mathbf{F} \cdot d\hat{\mathbf{n}}S. \quad (2.20)$$

The cell averaged conserved quantities in Eqn. 2.2 are advanced from time level  $n$  to time level  $n + 1$  using the predictor-corrector scheme,

$$\begin{aligned} \Delta\mathbf{U}^{(1)} &= \Delta t \frac{d\mathbf{U}^{(n)}}{dt} \\ \mathbf{U}^{(1)} &= \mathbf{U}^{(n)} + \Delta\mathbf{U}^{(1)} \\ \Delta\mathbf{U}^{(2)} &= \Delta t \frac{d\mathbf{U}^{(1)}}{dt} \\ \mathbf{U}^{(n+1)} &= \mathbf{U}^{(1)} + \frac{1}{2} (\Delta\mathbf{U}^{(2)} - \Delta\mathbf{U}^{(1)}). \end{aligned} \quad (2.21)$$

The superscripts (1) and (2) indicate intermediate results. If a first-order scheme is desired, only the first stage is used and  $\mathbf{U}^{(n+1)} = \mathbf{U}^{(1)}$ .

To maintain stability, the magnitude of the time-step is equal to the minimum allowable  $\Delta t$  (Eqn. 2.22) of all cells as determined by the Courant condition [30]. The length scale of a triangular cell is the smallest median. Wave-speeds are calculated within the flux calculator and are associated with edges. The Courant number,  $\sigma$ , is usually set to 0.5.

$$\Delta t = \sigma \times \text{minimum} \left\{ \frac{\text{length scale}}{\text{highest wave speed}} \right\} \quad (2.22)$$

After the conserved quantities have been advanced to the next time level the primary flow variables for each cell are determined from the updated conserved quantities as,

$$\begin{aligned} \rho &= \rho \\ u &= \frac{\rho u}{\rho} \\ v &= \frac{\rho v}{\rho} \\ e &= E - \frac{1}{2}(u^2 + v^2) \\ P &= f(\rho, e). \end{aligned} \quad (2.23)$$

## 2.4 Solution-adaptive remeshing

Solution-adaptive remeshing concentrates the computational effort at regions of interest within the flow domain. This allows greater resolution of shock waves, discontinuities, and slip lines than possible with fixed-grid simulations at the same (or similar) computational expense. The resolution of the mesh is increased by introducing nodes to the mesh thereby increasing the number of cells in that region. The resolution of the grid can be reduced in regions where the solution has become smooth by removing previously inserted nodes.

The remeshing process comprises three stages. Firstly, the error indicator associated with each cell is calculated and the cells are marked for deletion, refinement or no action. The next step is the deletion of vertices surrounded by cells which have been marked for deletion. Finally, cells marked for refinement are split. The frequency of remeshing is dependent on the Courant number and the number of *protective layers* provided during refinement. A protective layer is formed by marking for refinement all the neighbouring cells of cells marked for refinement. Protective layers allow the flow solution to evolve for a few time-steps without the need for remeshing after each step by ensuring that flow features have not moved into regions where the mesh is coarse. For a Courant number,  $\sigma = 0.5$  and using one protective layer, remeshing was performed every five time-steps.

### 2.4.1 Error indicator

The error indicator for each cell is determined by Equation 2.24. The geometry associated with this equation is shown in Figure 2.11 where  $a_i$  is the density at the centre of an adjacent cell,  $b$  is the density at the centre of the cell and  $c_i$  is the density at the vertex opposite to the adjacent cell.

$$\text{error indicator} = \frac{\sum_{i,j,k} |2b - a_i - c_i|}{\sum_{i,j,k} (|b - a_i| + |c_i - b|) + \alpha \sum_{i,j,k} (a_i + 2b + c_i)} \quad (2.24)$$

The error indicator is based on similar functions developed by Löhner [48] and Probert *et al.* [63] and it is calculated along the same line as the reconstruction. To examine the properties of the error function, consider an equi-spaced one-dimensional data and  $\alpha = 0$ . The error indicator becomes,

$$\frac{|2\phi_0 - \phi_1 - \phi_{-1}|}{|\phi_1 - \phi_0| + |\phi_0 - \phi_{-1}|},$$

where  $\phi_i$  represents the data value. If  $\phi_0$  is an extremum (i.e.  $\phi_0 > \phi_{-1}$  and  $\phi_0 > \phi_1$ , or  $\phi_0 < \phi_{-1}$  and  $\phi_0 < \phi_1$ ) then error equals one. If  $\phi_0$  is not an extremum, it can be shown using Taylor's series that the error indicator equals,

$$\left| \frac{f^{ii}(x) h}{4 f^i(x)} + \frac{f^{iv}(x) h}{8 f^{iii}(x)} + \dots \right|$$

where  $h$  is the spacing between the data points and is assumed to be equal. Neglecting higher-order terms, the error indicator is equal to the second derivative normalised by the first derivative. It is dimensionless and bound between zero and one.

The second term in the denominator of Equation 2.24 ensures that division by zero does not occur in regions where the solution is constant. It also acts as a noise filter, with the amplitude of the filtered waves increasing with  $\alpha$ . The choice of  $\alpha$  depends on the type of flux calculation and the nature of the flow, and generally varies between 0.005 and 0.1. An example of how  $\alpha$  affects the solution is shown in Section 3.2.2.

Cells are marked for refinement if the error function is greater than 0.3, deletion if the error function is less than 0.1, and no action otherwise.

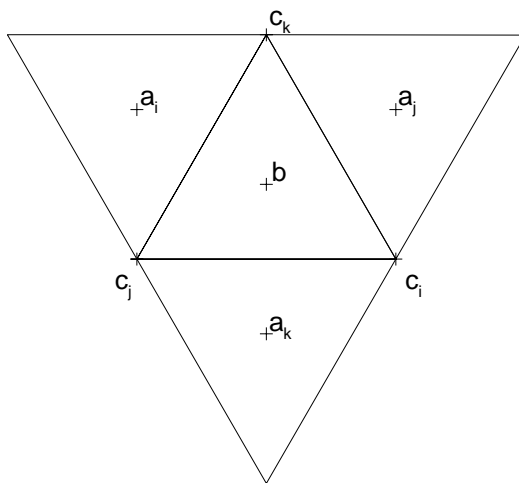


Figure 2.11: Geometry associated with the calculation of the error term for a cell.

### 2.4.2 Cell refinement - bisection method

There are two basic algorithms for the refinement of triangles: the bisection method and regular reflection (h-refinement) [41]. In its simplest form the bisection algorithm bisects the longest edge of a triangle to form two new triangles. The regular reflection algorithm divides a triangle into four similar triangles, or during a cleanup phase, into two triangles. Both algorithms finish with a conforming mesh, in which the edge of a triangle cannot contain a vertex other than its endpoints. The bisection algorithm was chosen to refine the cells because it was easier to implement.

Cell refinement (via bisection) is achieved by inserting a new vertex at the midpoint of an edge and splitting the cells separated by the edge. The edge chosen to be split must have the greatest length of all edges of the cells separated by the edge. For example, suppose  $\triangle ABC$  of Figure 2.12 has been marked for refinement.  $CB$  is the longest edge of  $\triangle ABC$  but not the longest edge of the other cell ( $\triangle BCD$ ) separated by  $BC$ .  $BD$  is the longest edge of  $\triangle BCD$  but, again, is not the longest edge of the adjacent cell ( $\triangle BDE$ ).  $BE$  is the longest edge of  $\triangle BDE$  and is also the longest edge of the other cell ( $\triangle BEF$ ). A vertex (G) can be inserted at the midpoint of edge  $BE$ . Four triangles ( $\triangle BDG$ ,  $\triangle DEG$ ,  $\triangle EFG$  and  $\triangle FBG$ ) now replace the two triangles  $\triangle BEF$  and  $\triangle BDE$ .  $BD$  can now be split as it is the longest edge of  $\triangle BCD$  and  $\triangle BDG$ . Point H is inserted. After the insertion of vertex H, edge  $BC$  can be split and vertex I is inserted. The insertion of vertex I splits  $\triangle ABC$  as required.

A refinement level is assigned to all inserted vertices. This number is equal to the highest refinement level number of surrounding vertices plus one. Initially all vertices are given a refinement level number of zero. For example, if all points of the initial mesh in Figure 2.12 have a refinement level of zero, then the refinement level of vertex G would be one, vertex H would be two and vertex I would be three. The refinement level of a vertex is later used to determine whether it can be removed from the grid.

Sometimes it is necessary to maintain the cell aspect ratio during refinement for an axisymmetric simulation (Sec. 3.2.3). This is achieved by splitting the edge with the lowest sum of refinement level numbers for its vertices. If two or three edges have the same lowest sum, the longest edge is split.

A minimum cell volume (or cell area for axisymmetric simulations) is enforced to prevent the refining of cells ad infinitum. If the volume of a cell is lower than the *nominal* minimum volume, it cannot be marked for refinement. Cells with a volume

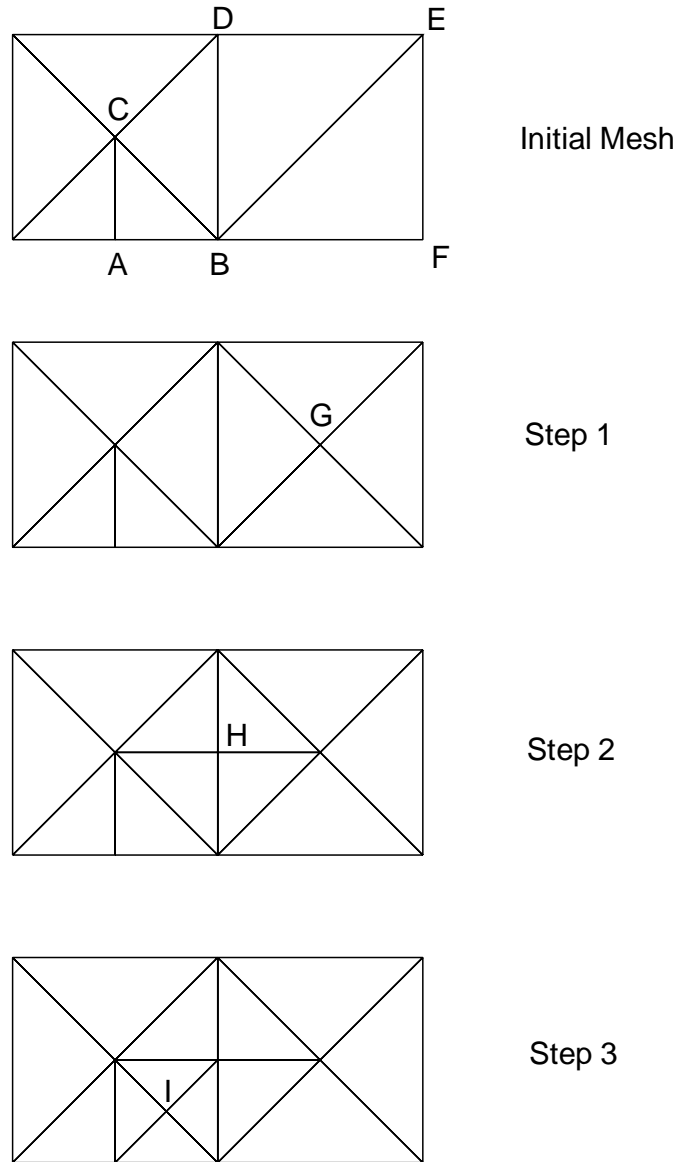


Figure 2.12: Refinement of triangles using the bisection method. To split  $\triangle ABC$ , vertex G then vertex H and finally vertex I are inserted.

less than the nominal minimum value can exist within the mesh but these cells are not split during cell refinement. The minimum cell volume or cell area quoted for any simulation in this thesis refers to this nominal minimum value.

### 2.4.3 Vertex deletion

Only vertices associated with four cells (or two cells for a boundary vertex) are considered for deletion. For a vertex to be deleted, all the cells connected to the vertex must be marked for deletion and the refinement level of the vertex must be higher than all vertices connected to the vertex. When a vertex is inserted, the array numbers of the vertices of the split edge are stored within the data structure of the new vertex. This information is used to ensure that vertex deletion is the reverse of vertex insertion, and allows for further vertex removal.

## 2.5 Ignored cells

To model the gradual opening of a diaphragm, U2DE has the ability to blank out (ignore) parts of the domain. The use of unstructured meshes made the implementation of this feature relatively easy. Ignored cells are simply those which are not considered during the numerical integration. Edges between an ignored cell and a flow cell are treated as a solid wall.

## 2.6 Summary

In this chapter, some of the features of U2DE were described. U2DE is a finite-volume code that solves the unsteady Euler equations for inviscid compressible flow. The flow domain is discretised by an unstructured mesh of triangular cells. The numerical techniques used to solve the equations were described: MUSCL reconstruction, flux calculators (Riemann solver and EFM), and explicit time-stepping. The code also has the ability to adapt the mesh (solution-adaptive remeshing), such that cells are concentrated in regions where solution gradients are high. This feature was also described. The next chapter examines the ability of U2DE to produce accurate numerical solutions by examining some standard test cases. In Chapters 4 and 5, U2DE will be used to perform simulations of the gradual opening of a primary diaphragm. The code described in this chapter is for stationary flow domains.

In Chapter 6, other features of the code, which are used to solve problems with two-dimensional fluid-structure interactions, are described.

# Chapter 3

## Test cases



Blottner [11] identified code validation and code verification, as two items which require investigation to gain confidence in the predictions produced by numerical simulations. Code validation is the demonstration that the governing equations accurately describe the real physical process by comparing numerical results with experimental data. Code verification is the demonstration that the code is numerically solving the governing equations accurately. This can be done by comparing numerical results to analytical solutions for problems where an analytical solution exists. The purpose of this chapter is to verify that the code U2DE, described in the previous chapter, does solve the Euler equations accurately (code validation will be examined in Chapters 5 and 7).

This chapter consists of a set of test cases that exercise the capabilities of the code. Numerical solutions are compared with analytical solutions for the following problems: supersonic vortex flow between two arcs (Sec. 3.1), ideal shock tube flow (Sec. 3.2), and flow over a cone (Sec. 3.3). Particular attention is directed to the ideal shock tube flow and the ability of U2DE to accurately compute the speed of the shock wave.

The ability of U2DE to capture accurately multi-dimensional flow features is verified by examining the following problems: a shock wave exiting an open ended shock tube (Sec. 3.4), transient flow over a wedge (Sec. 3.5), and shock wave diffraction around a 90 degree corner (Sec. 3.6). These test cases were chosen because of the availability and quality of previous experimental and numerical work and they contain flow features similar to those expected within a shock tube with a gradually opening diaphragm. No known analytical solutions exist for these problems, therefore the code is verified by comparing numerical solutions generated by U2DE with previous numerical work. This also acts as an indirect form of code validation because the previous work has validated the use of the Euler equations to describe the flow-field for these test cases.

Various features of U2DE are also examined in this chapter. The value of solution-adaptive remeshing is examined and confirmed. In the previous chapter, two different methods for calculating the fluxes (Riemann solver and EFM) were introduced. This chapter will examine the robustness and accuracy of each of these methods for various test cases.

### 3.1 Supersonic vortex

The first test case is an inviscid supersonic vortex with the flow domain between two circular arcs. The geometry (Fig. 3.1) and flow condition chosen are the same used by Aftosmis *et al.* [1] and Luo *et al.* [50]. The radii of the arcs are chosen so that the flow is supersonic throughout the domain.

The initial flow condition throughout the domain is,

$$\rho = 1.0, P = 1.0, \text{ and } u = v = 0.0.$$

The boundary at  $x = 0.0$  is an in-flow boundary with the flow state at the inner radius,  $r_i = 1.0$  is,

$$\rho_i = 1.0, P_i = 1.0/\gamma, \text{ and } M_i = 2.25.$$

The entropy is assumed to be constant along the in-flow boundary; and the outer radius is 1.384. The ratio of specific heats is  $\gamma = 1.4$ . The boundary at  $y = 0.0$  is an out-flow boundary and the curved boundaries are treated as walls.

Vortex flow can be described as a potential flow and an analytical solution exists with the tangential speed proportional to the inverse of the distance from the centre of the vortex. The density within the domain can be described [1] by,

$$\rho(r) = \rho_i \left[ 1 + \frac{\gamma - 1}{2} M_i^2 \left\{ 1 - \left( \frac{r_i}{r} \right)^2 \right\} \right]^{\frac{1}{\gamma - 1}}. \quad (3.1)$$

This test case was used to examine the accuracy and the order of spatial convergence of U2DE. The order of convergence is dependent on the interpolation scheme. U2DE uses MUSCL interpolation (Sec. 2.3.1) which is effectively switched off in regions where discontinuities (shocks, contact surface) exist due to the action of the MINMOD function. The supersonic vortex is a good test case for evaluating the order of convergence of a scheme because the solution is shock-free and smooth.

The method of References [1] and [50] was used to determine the order of convergence. This method is derived from Richardson extrapolation [69] which assumes that discrete solutions  $f$  can be expressed,

$$f = f[\text{exact}] + C_1 \Delta x + C_2 \Delta x^2 + C_3 \Delta x^3 + \dots \quad (3.2)$$

where  $\Delta x$  is the mesh spacing and the functions  $C_i$  are independent of  $\Delta x$ . If a numerical scheme is second-order accurate,  $C_1 = 0$  and the error is equal to,

$$L = C_2 (\Delta x)^2 + \text{H.O.T.} \quad (3.3)$$

where H.O.T. refers to higher-order terms which are usually considered to be negligible. Thus, for an  $n$ -order method it is assumed that the error of a numerical

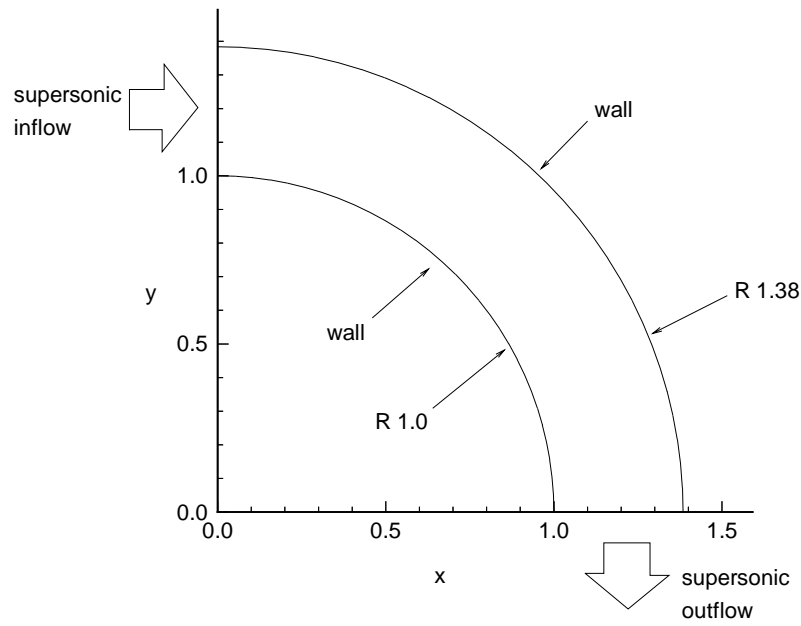


Figure 3.1: Geometry of flow domain for supersonic vortex test case.

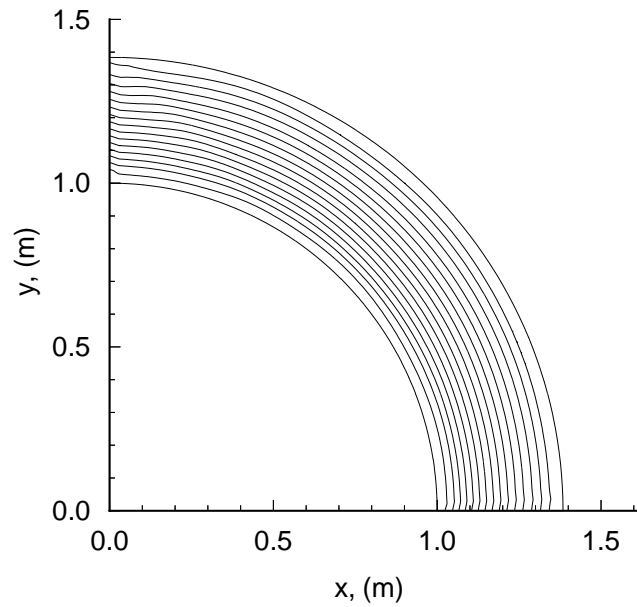


Figure 3.2: Density contours for supersonic vortex. Higher-order EFM solution for the  $60 \times 10$  mesh.

solution is related to mesh spacing by,

$$L = C(\Delta x)^n \quad (3.4)$$

where  $C$  is a constant. The order of convergence can be found by determining the gradient of the log of error with respect to the log of mesh spacing.

The error of a numerical solution can be found by comparing the discrete solution with the analytical solution at all points throughout the domain. For example the  $L_1$  norm of error expressed as a percentage is equal to,

$$L_1 = \frac{\sum_{i=1}^N \frac{|\rho_i - \rho_{exact}|}{\rho_{exact}}}{N} \times 100. \quad (3.5)$$

Steady-state solutions were calculated for three meshes at different resolutions:  $30 \times 5$ ,  $60 \times 10$ , and  $120 \times 20$  (Fig. 3.3). The solution was assumed to be steady state when the maximum relative change in density was,  $\Delta\rho/\rho < 1 \times 10^{-10}$ .

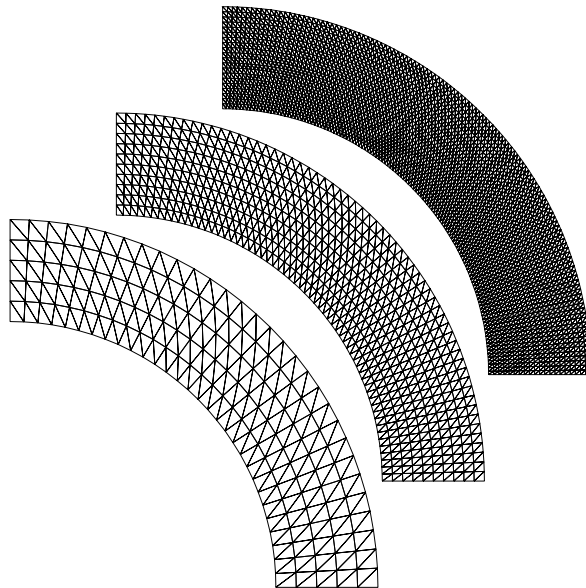


Figure 3.3: Sequence of meshes used for supersonic vortex.

The error percentages for density using EFM and the Riemann solver are shown in Tables 3.1 and 3.2. The Riemann solver was more accurate than EFM for first-order calculations, however, when MUSCL interpolation was used, the EFM solutions were more accurate. This was probably due to the extra diffusivity of EFM damping

numerical oscillations. The improvement gained by increasing the nominal order of the MUSCL interpolation from second-order ( $\kappa = 1/2$ ) to third-order ( $\kappa = 1/3$ ) was found to be small. The highest order of convergence obtained for this test case by U2DE was 1.57, when using EFM.

Mesh	First-order		MUSCL ( $\kappa = 1/2$ )		MUSCL ( $\kappa = 1/3$ )	
	$L_1$	$L_2$	$L_1$	$L_2$	$L_1$	$L_2$
$30 \times 5$	8.6993	11.722	1.9260	2.3736	1.9125	2.3463
$60 \times 10$	4.0316	5.3076	0.6449	0.7838	0.6353	0.7866
$120 \times 20$	1.9929	2.5676	0.2185	0.2997	0.2171	0.2939
$n$	1.06	1.10	1.57	1.49	1.57	1.50

Table 3.1: Error (expressed as percentages) and order of convergence for numerical solutions for supersonic vortex. EFM was used to calculate fluxes.

Mesh	First-order		MUSCL ( $\kappa = 1/2$ )		MUSCL ( $\kappa = 1/3$ )	
	$L_1$	$L_2$	$L_1$	$L_2$	$L_1$	$L_2$
$30 \times 5$	6.8626	8.7407	2.2324	2.6746	2.2653	2.6807
$60 \times 10$	3.4836	4.3873	0.8297	1.0015	0.8273	0.9919
$120 \times 20$	1.8035	2.2921	0.2983	0.4121	0.2966	0.4052
$n$	0.96	0.97	1.45	1.34	1.47	1.36

Table 3.2: Error (expressed as percentages) and order of convergence for numerical solutions for supersonic vortex. Riemann solver was used to calculate fluxes.

The performance of U2DE is compared with a structured MUSCL scheme (quadrilateral grid) and a vertex-based finite-volume scheme [1] in Table 3.3. The fluxes for the other schemes were determined by Roe's approximate Riemann solver. The vertex-based scheme used a least square gradient estimation with no limiters. The comparison indicates that U2DE is more accurate than the structured MUSCL scheme, though the orders of convergence are similar. However, the performance of the vertex-based scheme using a least square gradient estimation is better than U2DE.

As stated by Luo *et al.* [50], the accuracy of a scheme is strongly dependent on the interpolation. The interpolation within U2DE (Sec. 2.3.1) basically applies a one-dimensional structured approach to a multi-dimensional unstructured mesh. A recent paper [1] (November 1995) indicates that multi-dimensional interpolation schemes are more accurate than the current quasi-one-dimensional scheme. A consistent mass reconstruction scheme developed by Luo *et al.* [50] claims even better results.

Mesh	U2DE		structured MUSCL		vertex scheme	
	$L_1$	$L_2$	$L_1$	$L_2$	$L_1$	$L_2$
$30 \times 5$	1.9125	2.3463	8.180	9.820	1.01	1.70
$60 \times 10$	0.6353	0.7866	2.668	3.233	0.29	0.51
$120 \times 20$	0.2171	0.2939	0.964	1.340	0.09	0.17
Slope	1.57	1.50	1.60	1.49	1.80	1.71

Table 3.3: Comparison of error percentages for higher-order EFM solutions with published results from Aftosmis *et al.* [1] for a structured MUSCL Roe solver and a vertex-based scheme using least square gradient estimation with no limiters.

The superior reconstruction schemes recommended by Luo *et al.* [50] and Aftosmis *et al.* [1] are for vertex-based control-volume formulations which apply the Euler equations to the polygonal cells of the dual mesh of a triangular tessellation. A dual mesh can be constructed by connecting centroids of adjacent triangles (Fig. 3.4). The polygonal cells have more edges (typically six), hence the numerical flow approximations are more isotropic with respect to wave orientation [27]. Conversely Aftosmis *et al.* concluded that the extra cell edges for a vertex-based triangular mesh did not enhance the wave propagation, accuracy, or convergence properties because the best numerical results were achieved using a quadrilateral mesh. The better performance of the quadrilateral mesh was probably due to the edges of the mesh being aligned with the flow. This is supported by the fact that a distorted triangular mesh (six sides per cell) gave better results than a distorted quadrilateral mesh (four sides per cell). Also a recent review [88] (1996) of flow solvers for unstructured meshes states that the issue of which method (vertex-based or cell-centred) is better is unresolved.

Most of the simulations relating to this thesis were performed before the better performance of the multi-dimensional schemes was published. However, it will be shown that the accuracy of U2DE is adequate for the purposes of this thesis. For future work, the author recommends the use of a multi-dimensional reconstruction scheme.

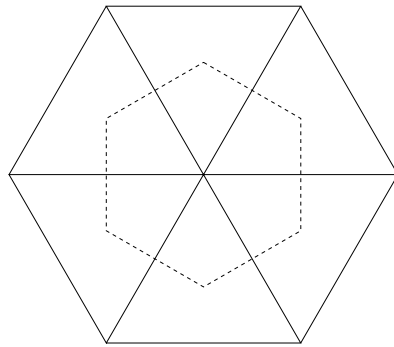


Figure 3.4: A dual mesh (dashed line) of a triangular tessellation (solid line) used for vertex-based schemes.

## 3.2 Ideal shock tube problem

The *ideal* shock tube problem (or Riemann problem) represents the situation where there is a sudden breakdown of a diaphragm in a tube separating two initial gases at different densities and pressures. The initial flow condition at time,  $t = 0$  is,

$$x \leq x_0 : \quad u = u_4, \quad P = P_4, \quad \rho = \rho_4$$

$$x > x_0 : \quad u = u_1, \quad P = P_1, \quad \rho = \rho_1$$

with  $p_4 > p_1$  and the diaphragm is located at  $x = x_0$  (Fig. 3.5). At time,  $t = 0$  the diaphragm bursts. It is assumed that the opening of the diaphragm is instantaneous. Immediately after the removal of the diaphragm the high pressure (driver) gas expands into the low pressure (driven) tube, accelerating and compressing the driven gas. A shock wave develops and propagates through the driven gas; simultaneously an expansion fan propagates through the driver gas. The contact surface which separates the two gas regions propagates to the right at a speed lower than the speed of the shock wave (Fig. 3.6). If viscous effects along the tube walls are neglected, the resulting flow can be described by the one-dimensional Euler equations. If the shock wave or the head of the expansion has not reached the ends of the tube a simple self-similar solution exists.

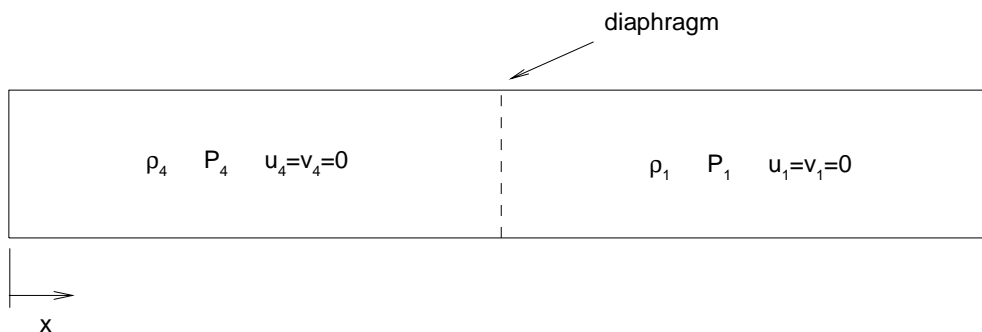


Figure 3.5: Initial flow condition for shock tube problem.

### 3.2.1 Sod's test case

Firstly, a shock tube with a low initial pressure ratio across the diaphragm is examined. The initial condition used here is the same condition used by Hirsch [30] and is similar to the condition used by Sod [76]. This is a simple test case that is commonly used to evaluate the performance of compressible flow codes. The initial state at time,  $t = 0$  is,

$$x \leq 0.5 \text{ m} : \quad \rho_4 = 1.0 \text{ kg/m}^3, \quad P_4 = 10^5 \text{ Pa}, \quad u_4 = 0 \text{ m/s}$$



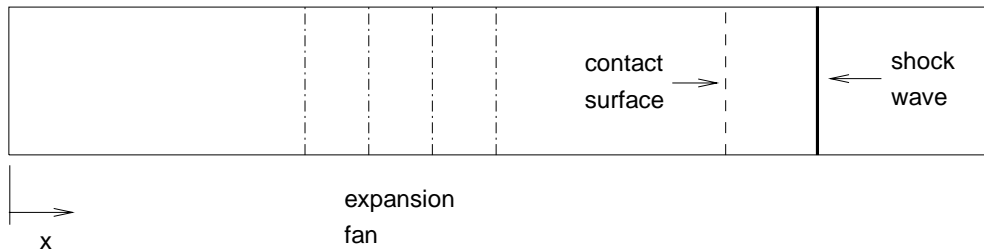


Figure 3.6: Unsteady waves within an ideal shock tube after diaphragm breakdown.

$$x > 0.5 \text{ m} : \rho_1 = 0.125 \text{ kg/m}^3, P_1 = 10^4 \text{ Pa}, u_1 = 0 \text{ m/s.}$$

The domain is a rectangle,  $1.0 \text{ m} \times 0.03 \text{ m}$  ( $100 \times 3 \times 2$  cells). The gas is assumed to be calorically perfect ( $\gamma = 1.4$ ). The initial mesh is shown in Figure 3.7 and the wall boundary condition applies to all boundaries.

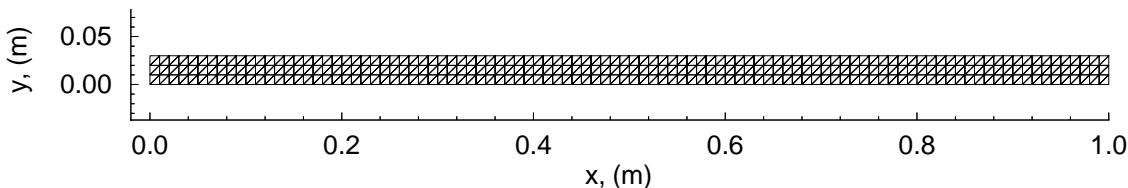


Figure 3.7: Initial and fixed-grid mesh for Sod's test case.

The Euler equations for two-dimensional planar geometry were numerically integrated to  $t = 6.0 \times 10^{-4}$  seconds. The first-order solution and a higher-order solution are compared with the analytical solution in Figures 3.8 and 3.9 respectively. The mesh remained fixed (not adapted) during the numerical integration for these two simulations. As expected, the higher-order solution is better (more accurate). The higher-order solution (119 time-steps) required 6.7 seconds of computational time on the Silicon Graphics Power Challenge (94 microseconds per cell per predictor-corrector time-step) and 29.0 seconds on the IBM Power PC.

The accuracy of the solution can also be improved by using solution-adaptive remeshing (Fig. 3.10). The minimum cell volume<sup>1</sup> for this simulation was  $1.0 \times 10^{-7} \text{ m}^3$ . This simulation required 7239 CPU seconds on the IBM Power PC and the final (and maximum) number of cells was 8572. It is estimated that a fixed-grid simulation with the same minimum cell volume (307200 cells) would take 336000 (3.89

<sup>1</sup>This is the nominal minimum cell volume (Sec. 2.4.2). The actual minimum cell volume for this simulation was  $9.765625 \times 10^{-8} \text{ m}^3$ .

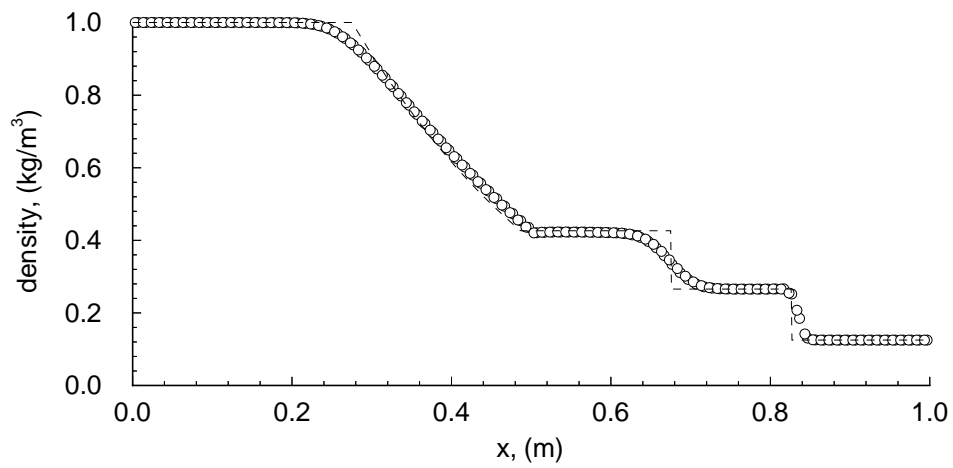


Figure 3.8: Density versus distance for Sod's problem. Comparison of first-order solution (o) with analytical solution (dashed line).

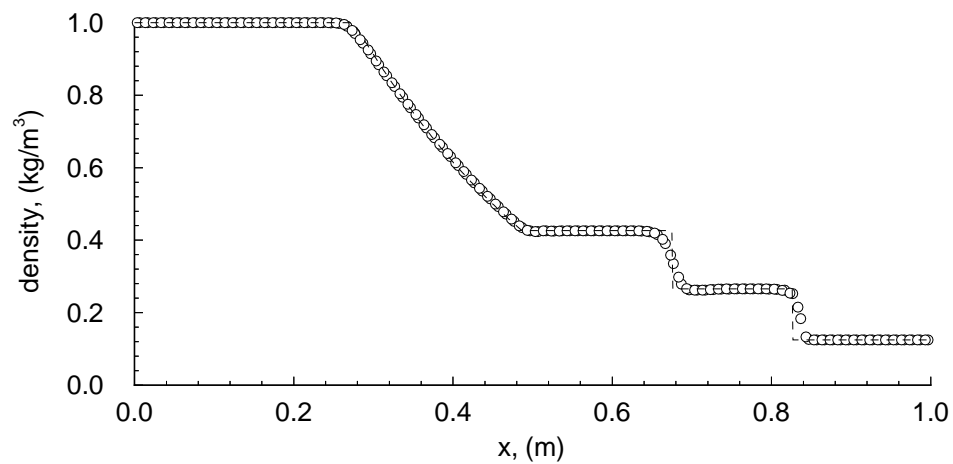


Figure 3.9: Density versus distance for Sod's problem. Comparison of higher-order solution (o) with analytical solution (dashed line).

days) on an IBM. The savings in terms of computational time (97.85%) and memory requirements (97.21%) are significant and increase as the minimum cell volume decreases.

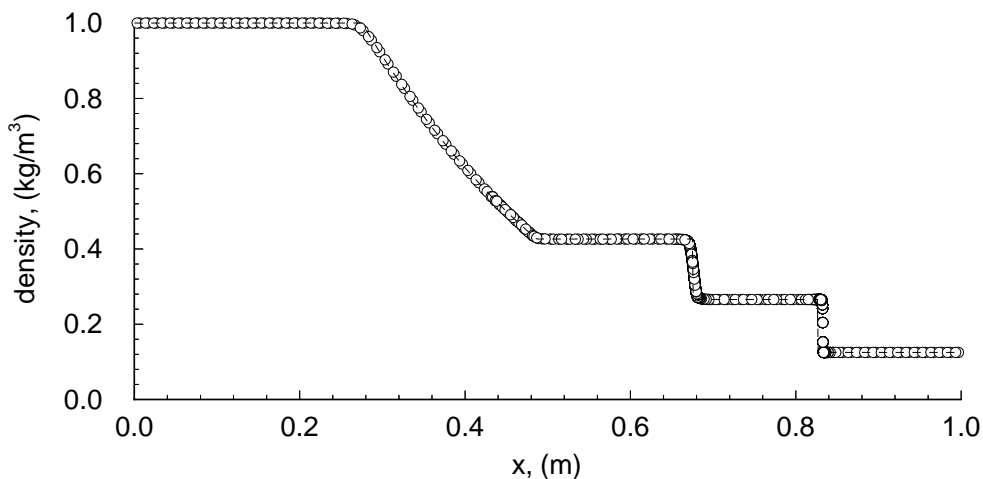


Figure 3.10: Density versus distance for Sod's problem. Comparison of higher-order solution (o) using solution-adaptive remeshing with analytical solution (dashed line). Minimum cell volume =  $1 \times 10^{-7} \text{ m}^3$  and  $\alpha = 0.01$ .

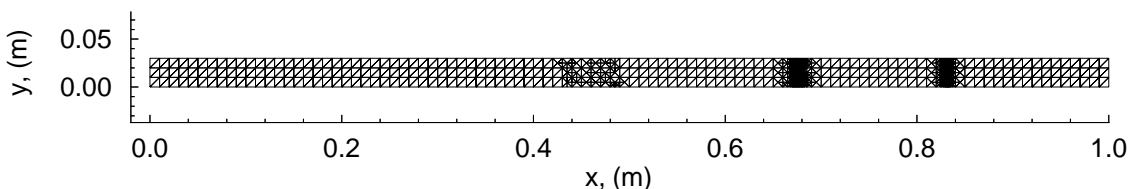


Figure 3.11: Final computational mesh for Sod's test case when solution-adaptive remeshing used. Minimum cell volume =  $1 \times 10^{-7} \text{ m}^3$  and  $\alpha = 0.01$ .

### 3.2.2 Shock tube with high initial pressure ratio

The initial pressure ratio across the primary diaphragm for high-performance shock tubes and expansion tubes is usually greater than 1000, which is considerably higher than for Sod's test problem ( $P_4/P_1 = 10$ ). The ability of U2DE to produce accurate numerical solutions for an ideal shock tube with a large initial pressure ratio ( $P_4/P_1 = 10145$ ) was examined. A test case was chosen with the initial flow condition similar to an experimental condition used by Miller & Jones [55].

The initial state at time  $t = 0$  seconds is,

$$x \leq 5.0 \text{ m} : P = 35 \times 10^6 \text{ Pa}, \quad T = 342 \text{ K}$$

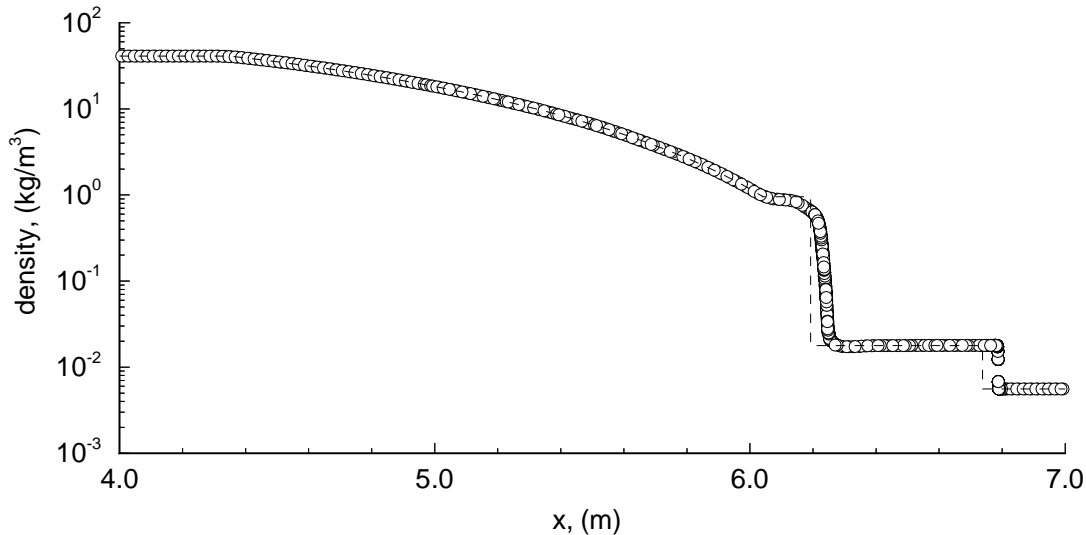


Figure 3.12: Ideal shock tube with high initial pressure ratio. Comparison of numerical solution (o) with analytical solution (dashed line) at  $t = 5.0 \times 10^{-4}$  seconds. EFM used for flux calculations. Minimum cell volume of  $1.0 \times 10^{-6} \text{ m}^3$  and  $\alpha = 0.1$ .

$$x > 5.0 \text{ m} : P = 3450 \text{ Pa}, T = 297.6 \text{ K}.$$

The driver and driven gases are both helium. The domain is a rectangular box ( $10 \text{ m} \times 0.06 \text{ m}$ ,  $500 \times 3 \times 2$  cells) and two-dimensional planar flow is assumed. The driver gas ( $x \leq 5.0 \text{ m}$ ) is at a high enough pressure for van der Waals forces between molecules to be significant and cause deviation from the perfect-gas model. The Redlich-Kwong equation of state (Appendix A) can be used to describe accurately the behaviour of helium for this problem.

Numerical solutions at time,  $t = 5 \times 10^{-4}$  seconds for different values of  $\alpha$  (Eqn. 2.24) and two different flux calculators (Riemann solver and EFM) are compared with the analytical solution (Figs. 3.12 – 3.19). The details of the simulations are listed in Table 3.4. The method for obtaining the analytical solution to the one-dimensional Euler equations for a non-perfect gas is described in Appendix E.

The accuracy of the contact surface for the EFM solutions improves as  $\alpha$  (Eqn. 2.24) decreases due to the increased sensitivity of the error function (Sec. 2.4.1). However, there is no significant difference in the accuracy between the solutions for  $\alpha = 0.02$  and  $0.01$ ; and the solution for  $\alpha = 0.02$  required less computational time.

The location of the shock is closer to the analytical solution for the Riemann solver solutions than the EFM solutions (the error associated with the computed shock location, in particular the shock speed is examined in detail in Section 3.2.4). Un-

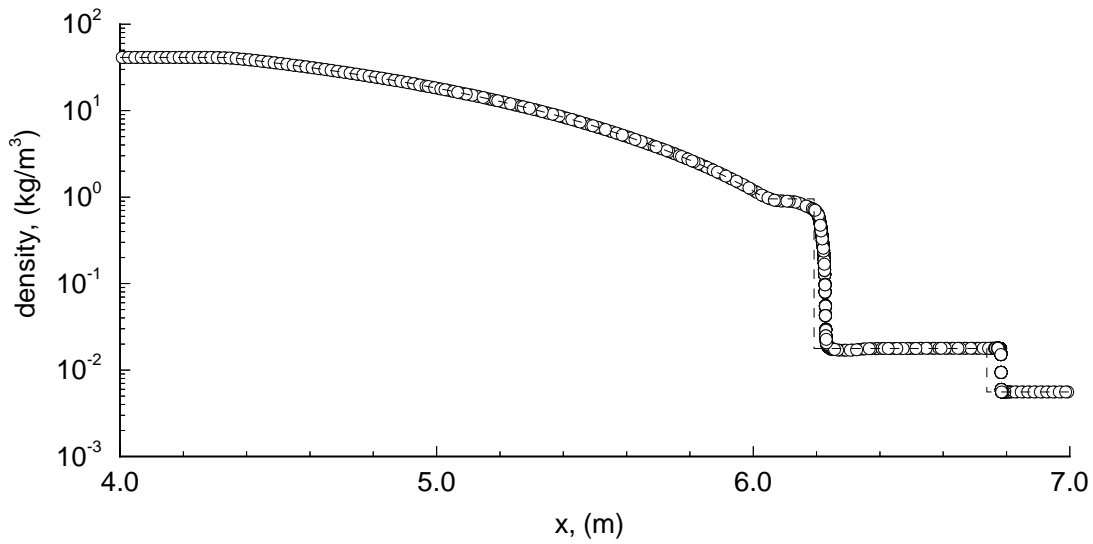


Figure 3.13: Ideal shock tube with high initial pressure ratio. Comparison of numerical solution (o) with analytical solution (dashed line) at  $t = 5.0 \times 10^{-4}$  seconds. EFM used for flux calculations. Minimum cell volume of  $1.0 \times 10^{-6} \text{ m}^3$  and  $\alpha = 0.05$ .

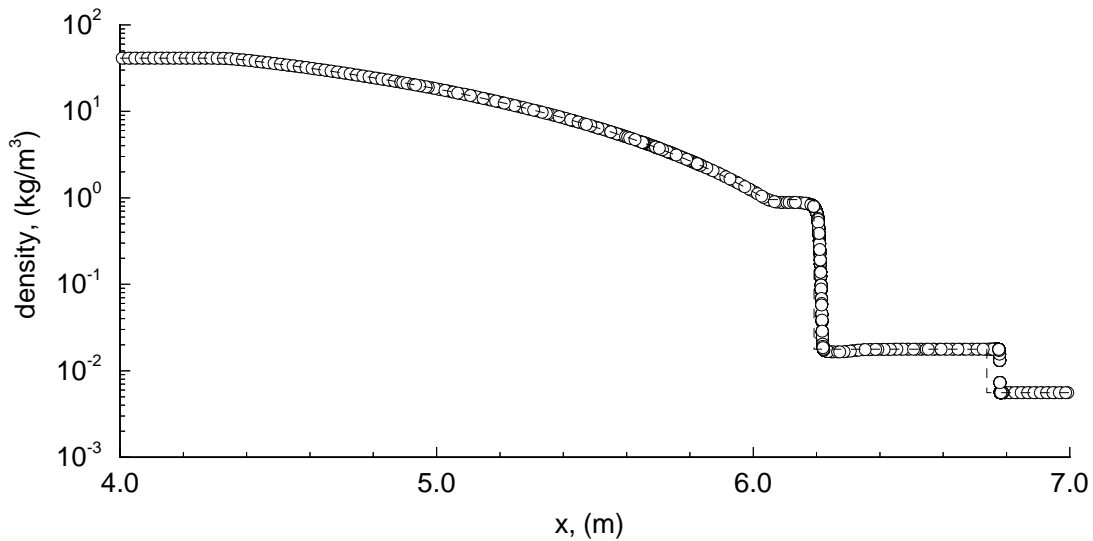


Figure 3.14: Ideal shock tube with high initial pressure ratio. Comparison of numerical solution (o) with analytical solution (dashed line) at  $t = 5.0 \times 10^{-4}$  seconds. EFM used for flux calculations. Minimum cell volume of  $1.0 \times 10^{-6} \text{ m}^3$  and  $\alpha = 0.02$ .

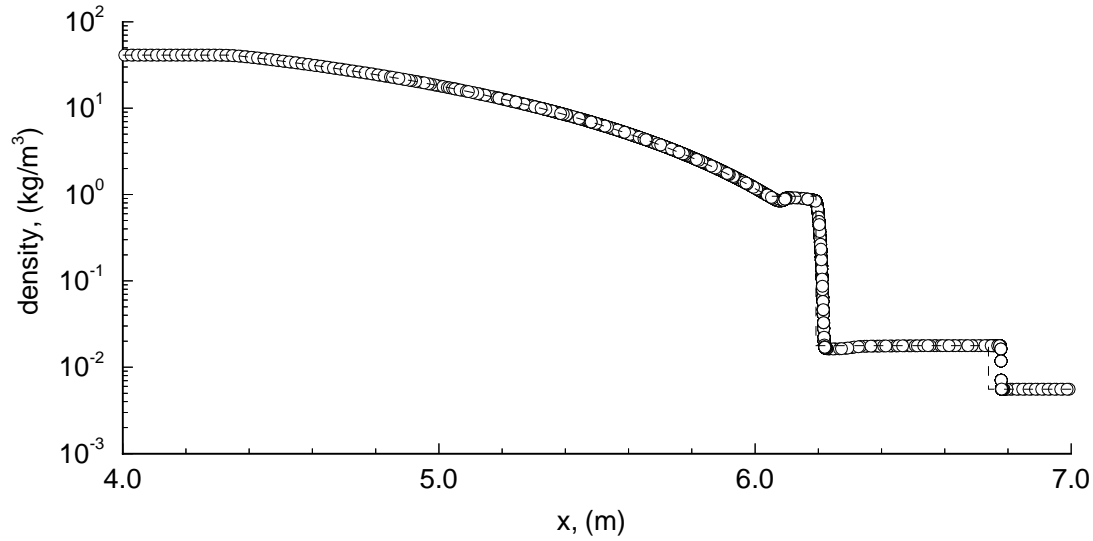


Figure 3.15: Ideal shock tube with high initial pressure ratio. Comparison of numerical solution (o) with analytical solution (dashed line) at  $t = 5.0 \times 10^{-4}$  seconds. EFM used for flux calculations. Minimum cell volume of  $1.0 \times 10^{-6} \text{ m}^3$  and  $\alpha = 0.01$ .

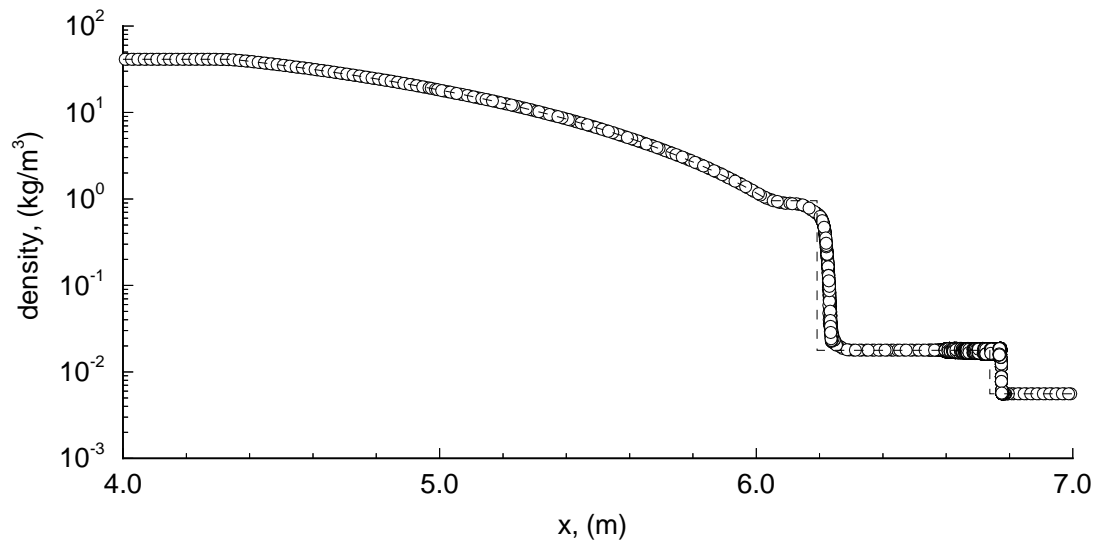


Figure 3.16: Ideal shock tube with high initial pressure ratio. Comparison of numerical solution (o) with analytical solution (dashed line) at  $t = 5.0 \times 10^{-4}$  seconds. Riemann solver used for flux calculations. Minimum cell volume of  $1.0 \times 10^{-6} \text{ m}^3$  and  $\alpha = 0.1$ .

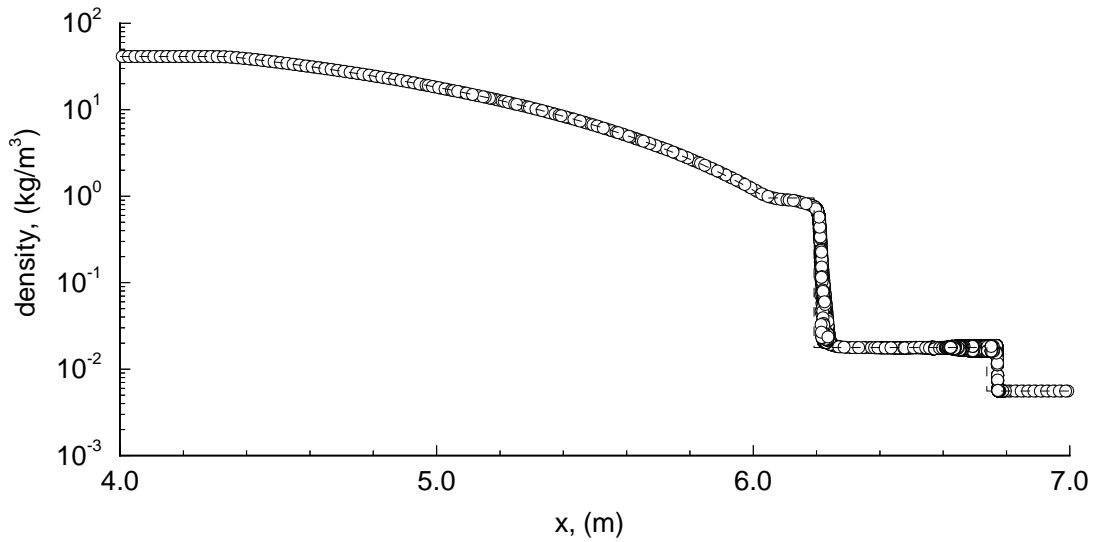


Figure 3.17: Ideal shock tube with high initial pressure ratio. Comparison of numerical solution (o) with analytical solution (dashed line) at  $t = 5.0 \times 10^{-4}$  seconds. Riemann solver used for flux calculations. Minimum cell volume of  $1.0 \times 10^{-6} \text{ m}^3$  and  $\alpha = 0.05$ .

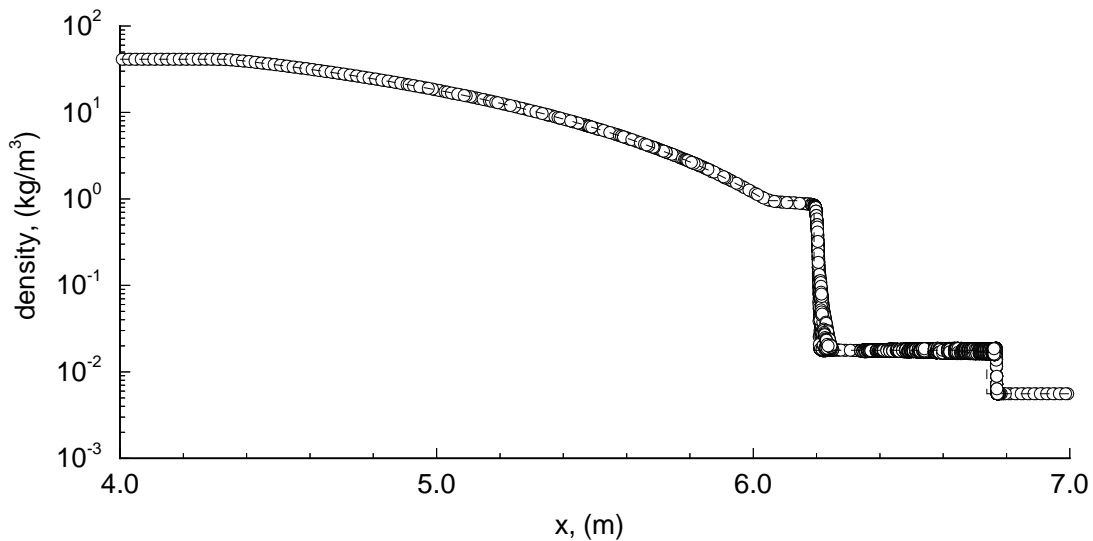


Figure 3.18: Ideal shock tube with high initial pressure ratio. Comparison of numerical solution (o) with analytical solution (dashed line) at  $t = 5.0 \times 10^{-4}$  seconds. Riemann solver used for flux calculations. Minimum cell volume of  $1.0 \times 10^{-6} \text{ m}^3$  and  $\alpha = 0.02$ .

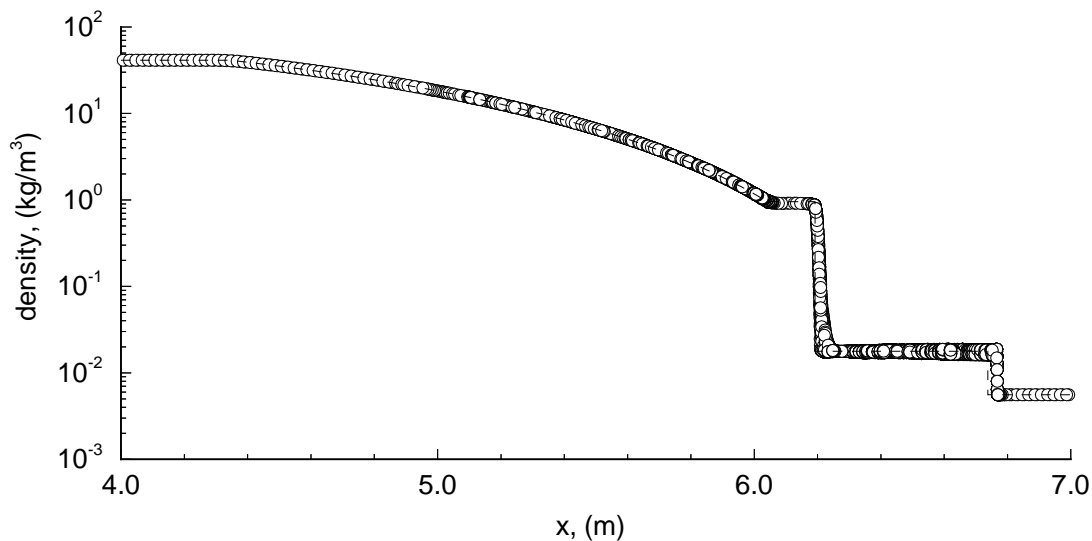


Figure 3.19: Ideal shock tube with high initial pressure ratio. Comparison of numerical solution (o) with analytical solution (dashed line) at  $t = 5.0 \times 10^{-4}$  seconds. Riemann solver used for flux calculations. Minimum cell volume of  $1.0 \times 10^{-6} \text{ m}^3$  and  $\alpha = 0.01$ .

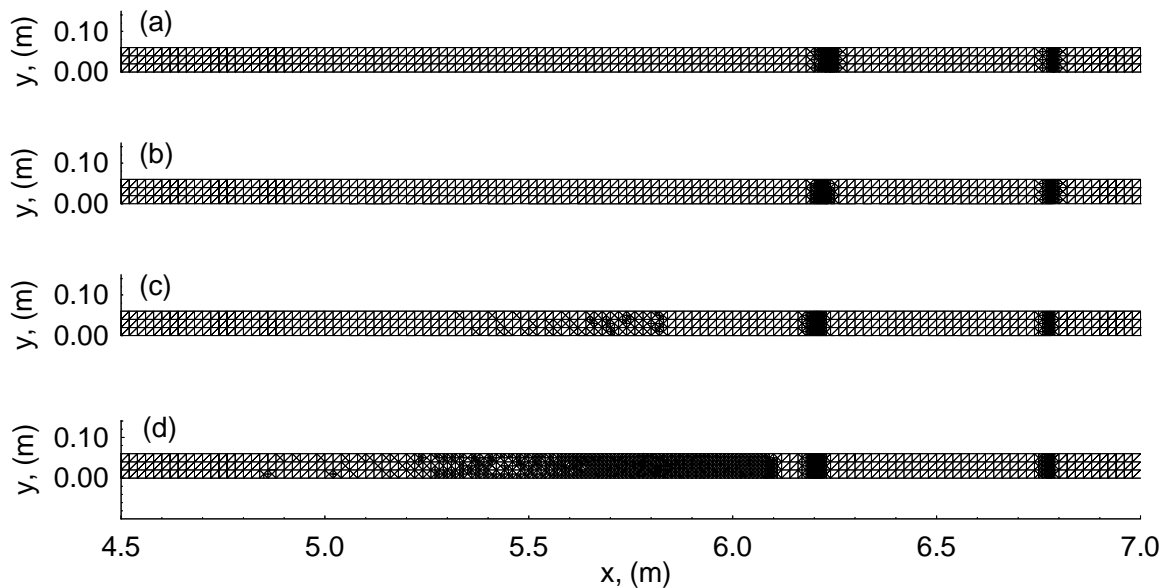


Figure 3.20: Final meshes for ideal shock tube with high initial pressure ratio. EFM was used for the flux calculations. Minimum cell volume is  $1.0 \times 10^{-6} \text{ m}^3$ : (a)  $\alpha = 0.1$ , (b)  $\alpha = 0.05$ , (c)  $\alpha = 0.02$ , (d)  $\alpha = 0.01$ .



fortunately, a significant amount of noise is present in the Riemann solver solutions, particularly behind the shock. This is a well-known failing of the Riemann solver called *odd and even decoupling* [66]. It has been explained [66] that this phenomena occurs because of the lack of inherent dissipation exhibited by Riemann solvers when the normal velocity across the edge is small. This can occur when a planar shock is aligned with the mesh. The solution becomes noisy if the simulation is performed at a high mesh resolution and is subject to systematic perturbations. The perturbations within the current simulations are caused by the cell edges which are at a 45 degree angle to the flow. These edges cause the pressure force in the  $y$ -direction on some cells (especially near the shock) to be non-zero, which generates relatively small velocity components in the  $y$ -direction.

The noise reduces the effectiveness of the solution-adaptive remeshing because it triggers the refinement of cells in regions where it is not required and thus unnecessarily increases the computational effort required to generate a solution at a set minimum cell volume.

Flux solver	$\alpha$	CPU (seconds)	Final number of cells
EFM	0.1	2765	4863
EFM	0.05	3179	5266
EFM	0.02	7698	5923
EFM	0.01	10742	8578
Riemann	0.1	15305	18407
Riemann	0.05	24380	24887
Riemann	0.02	35379	37999
Riemann	0.01	43489	43619

Table 3.4: Details of the high pressure shock tube simulations.

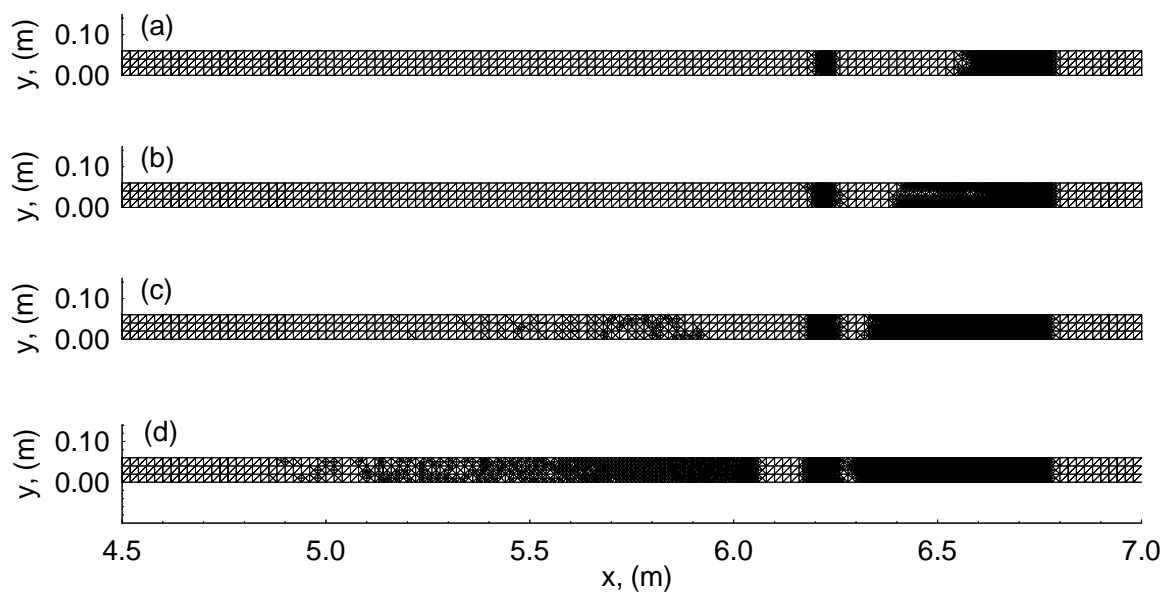


Figure 3.21: Final meshes for ideal shock tube with high initial pressure ratio. Riemann solver was used for the flux calculations. Minimum cell volume is  $1.0 \times 10^{-6}$   $\text{m}^3$ : (a)  $\alpha = 0.1$ , (b)  $\alpha = 0.05$ , (c)  $\alpha = 0.02$ , (d)  $\alpha = 0.01$ .

### 3.2.3 Axisymmetric shock tube and numerical jetting

The ability of U2DE to produce accurate solutions for an ideal shock tube with an axisymmetric geometry was investigated by examining a test case with an initial pressure and density ratio across the diaphragm equal to  $10^4$ . The geometry and flow properties for this problem were treated as non-dimensional values. The flow domain was a rectangle  $9.0 \times 0.18$  ( $150 \times 3 \times 2$  cells), with the diaphragm located at  $x = 4.5$ . EFM was used to calculate the fluxes. Solution-adaptive remeshing was used with the minimum cell area equal to  $4.0 \times 10^{-6}$ .

Three visible *glitches* are present in the higher-order solution shown in Figure 3.22 for cells near the axis ( $0.0 < r \leq 0.2$ ). From right to left the glitches are located immediately upstream of the shock, at the contact surface (Fig. 3.23), and at the tail of the expansion. The glitch at the tail of the expansion is an artifact of the flow solver and is present in the non-axisymmetric solution (Fig. 3.24).

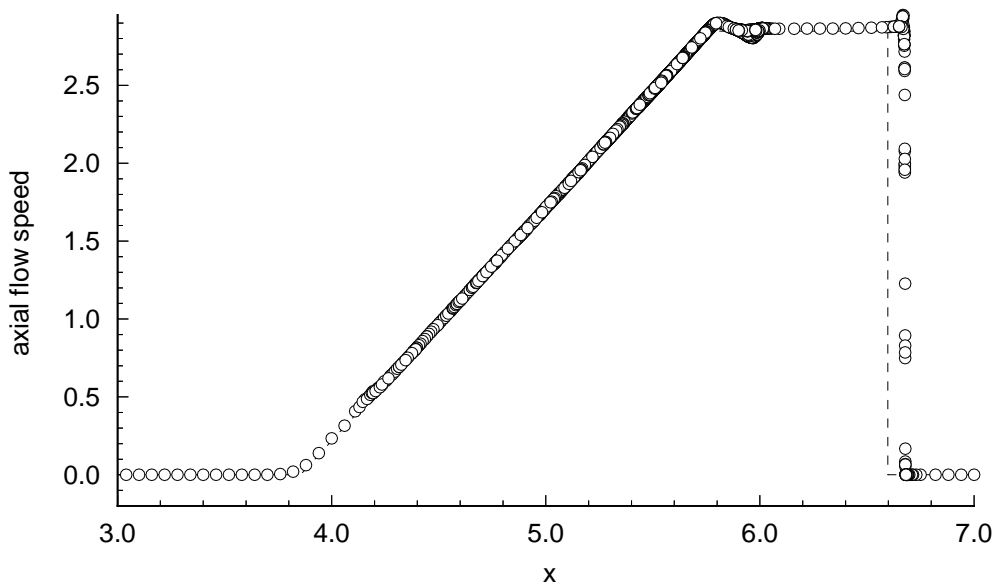


Figure 3.22: Axisymmetric solution to the ideal shock tube problem at  $t = 0.5$ . Axial flow speed versus axial distance for cells,  $0.0 < r \leq 0.02$ .

The glitches at the contact surface and the shock are due to *numerical jetting* at the axis and have significantly lower amplitudes at a distance ( $0.09 < r < 0.11$ ) from the axis (Fig. 3.25).

This phenomena has been observed previously [13, 34] for transient axisymmetric simulations using similar flow solvers on similar problems. Cambier *et al.* [13] suspected the presence of numerical jetting in a simulation of a shock reflection at

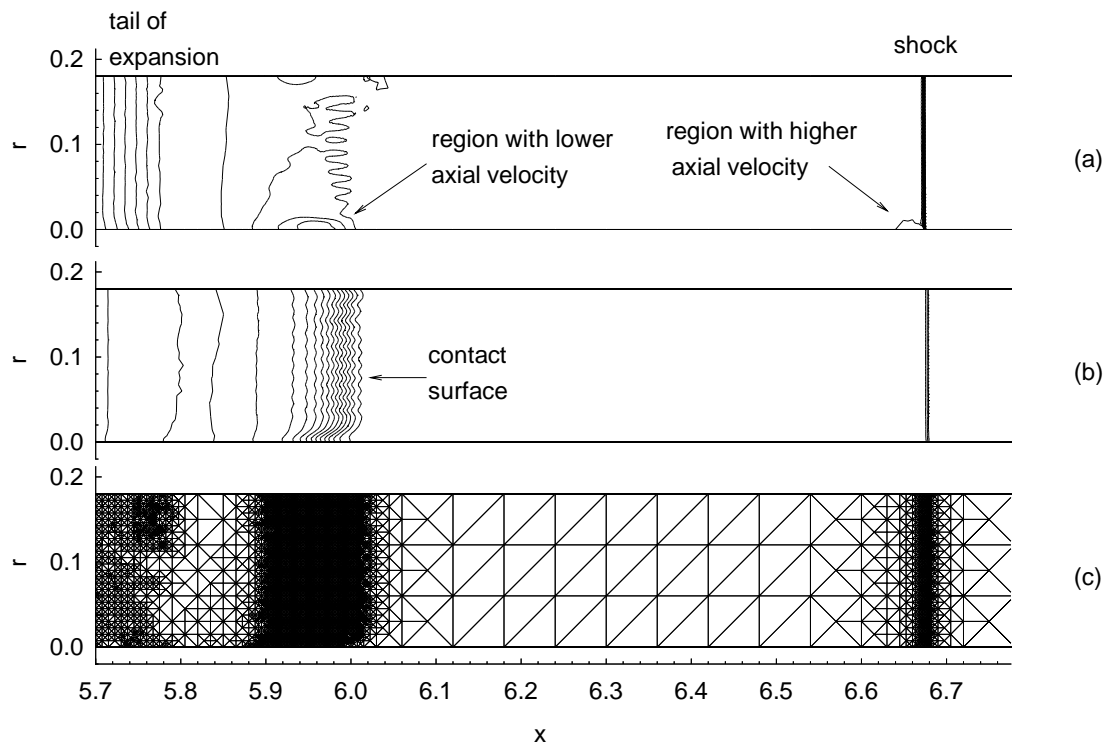


Figure 3.23: Axisymmetric solution to the ideal shock tube problem at  $t = 0.5$ : (a) axial flow speed contours, (b) density contours, and (c) final mesh.

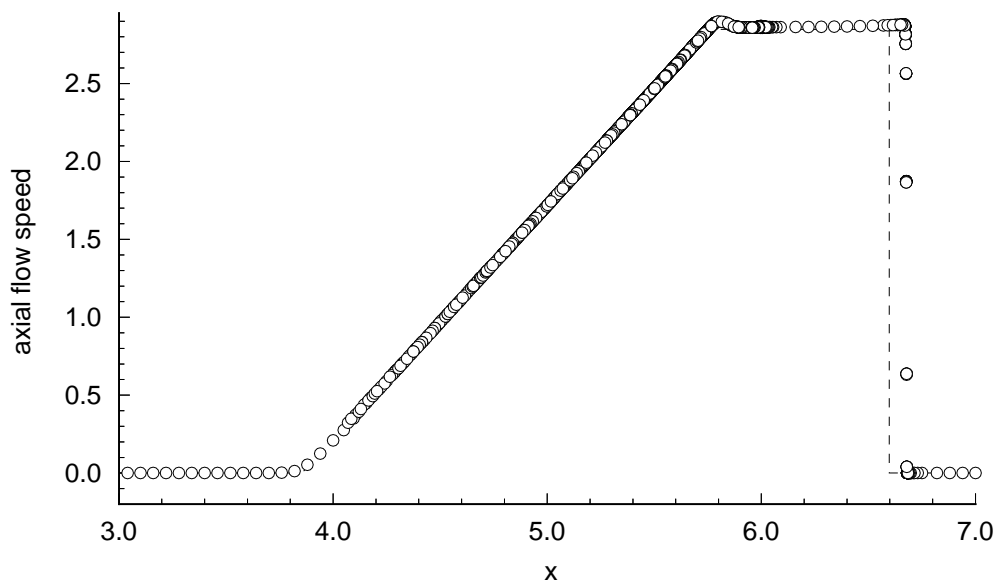


Figure 3.24: Two-dimensional planar solution to the ideal shock tube problem at  $t = 0.5$ . Axial flow velocity versus axial distance for cells  $0.0 < y \leq 0.02$ .

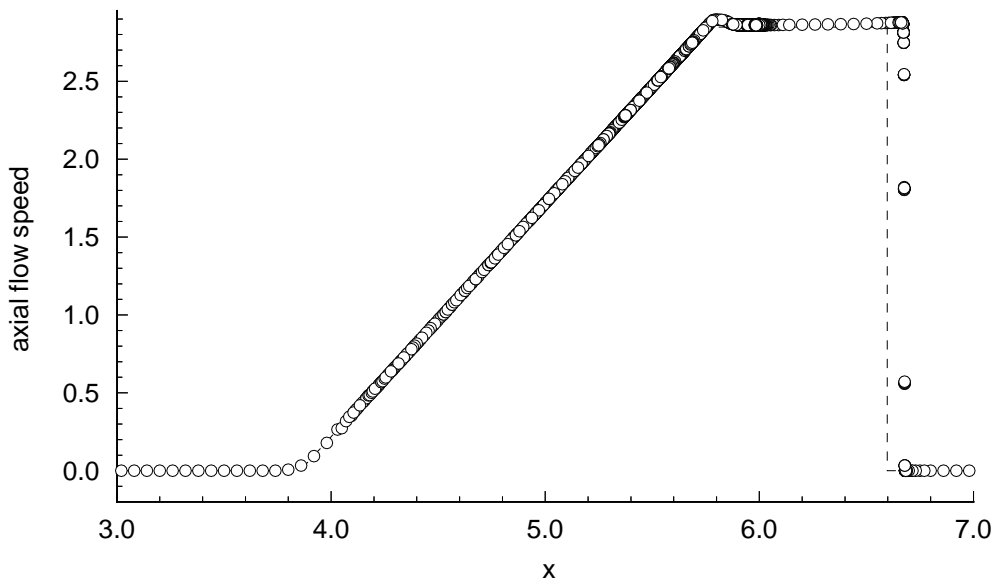


Figure 3.25: Axisymmetric solution to the ideal shock tube problem at  $t = 0.5$ . Axial flow speed versus axial distance for cells,  $0.09 < r < 0.11$ .

the end of a shock tube with a nozzle attached. A conical structure was formed at the axis of the reflected shock (Fig. 3.26). The structure pointed downstream and was in the direction opposite to the flow. Cambier *et al.* observed that numerical jetting only occurred for axisymmetric flows when a second-order accurate scheme (with minimum dispersion) was used. They postulated that the jetting was related to the axisymmetric pressure correction term and could be eliminated by using a grid that was stretched in the radial direction.

To test these ideas, a first-order simulation was performed (Fig. 3.27) and there was no evidence of numerical jetting at the shock along the axis, however, the accuracy of the solution was poor. A higher-order simulation was performed using a stretched mesh with a cell aspect ratio,  $\Delta y/\Delta x = 3.0$  (Figs. 3.28 & 3.29). The initial mesh for this simulation was obtained by increasing the number of grid points in the  $x$ -direction threefold. The solution does not exhibit numerical jetting at the axis (Fig. 3.28) and was more accurate than the solution obtained using a non-stretched grid.

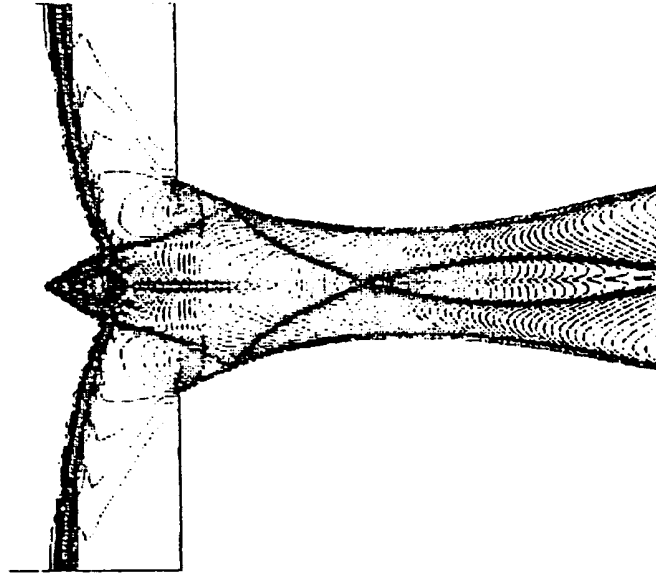


Figure 3.26: Numerical solution by Cambier *et al.* [13] of shock reflection at the end of a shock tube with a nozzle. The conical structure at the axis of the reflected shock is suspected to be due to numerical jetting.

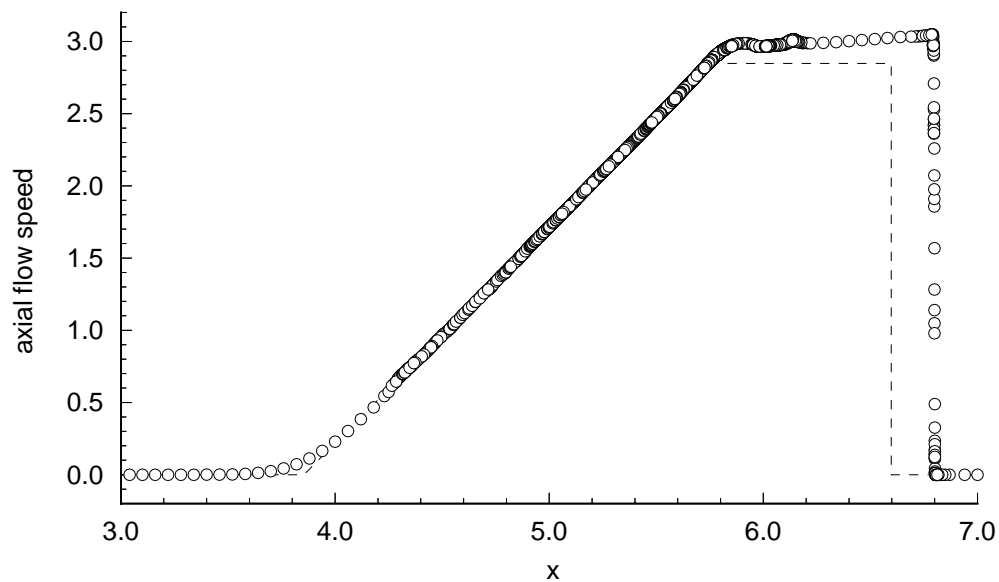


Figure 3.27: First-order axisymmetric solution to the ideal shock tube problem. Axial flow velocity versus axial distance for cells,  $0.0 < r \leq 0.02$ .

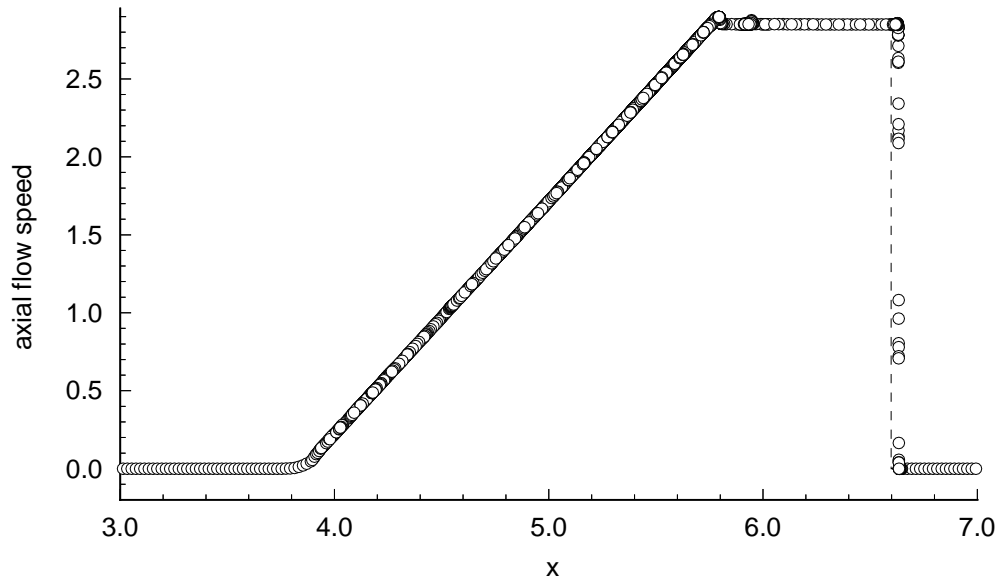


Figure 3.28: Axisymmetric solution to the ideal shock tube problem for a stretched mesh at  $t = 0.5$ . Axial flow velocity versus axial distance for cells,  $0.0 < r \leq 0.02$ .

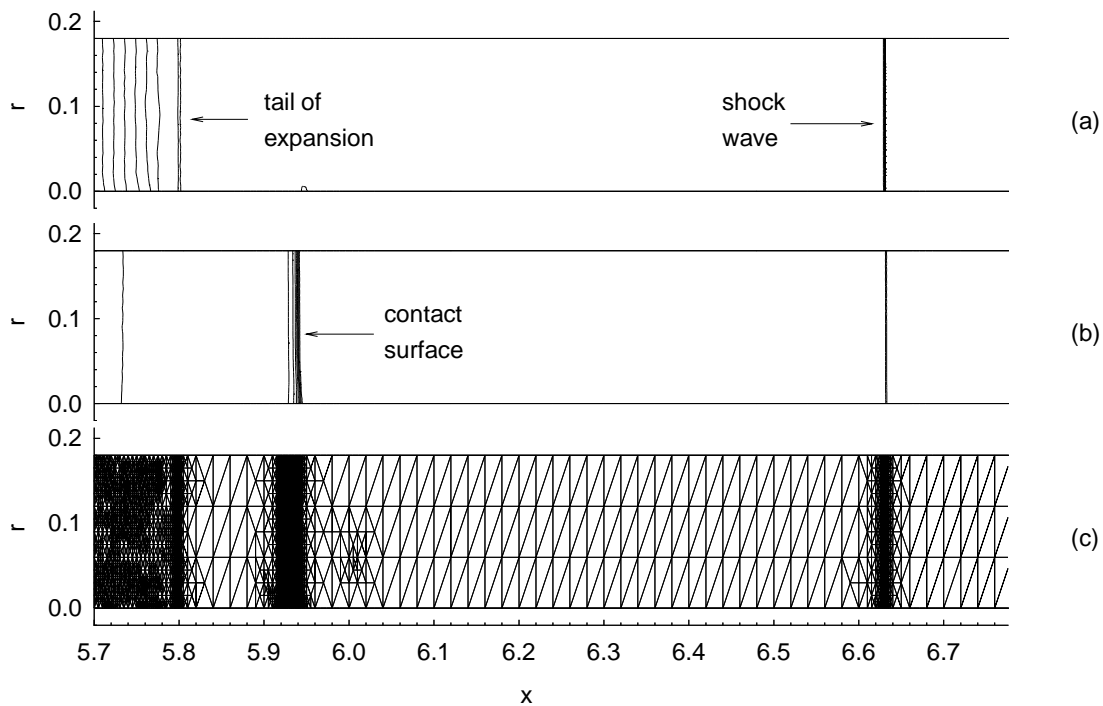


Figure 3.29: Axisymmetric solution to the ideal shock tube problem for a stretched mesh at  $t = 0.5$ : (a) axial flow speed contours, (b) density contours, and (c) final mesh. Note that the contour levels are the same as Figure 3.23.

This section has illustrated that numerical (not physical) jetting can be present in axisymmetric solutions. However, the effects of numerical jetting can be reduced by using meshes stretched in the radial direction.

### 3.2.4 Shock speed

In Chapter 5, the computed shock speed within a shock tube with a gradually opening diaphragm will be examined. However, in some of the previous test cases (Figs. 3.10, 3.15, & 3.28) U2DE overestimated the position of the shock wave. Since this will affect the accuracy of the shock speed measured from the simulations, the overestimation of the shock position in ideal shock tubes is now examined.

The computed shock speed for an ideal shock tube at various initial pressure ratios (10, 100, 1000, and 10000) across the diaphragm was compared with the corresponding analytical shock speeds (Table 3.5). The geometry and flow properties for this problem were treated as non-dimensional values. The initial density and pressure on the right side of the tube were set to unity. The initial temperature of the driver and driven gas were the same for all cases and the gas was assumed to be calorifically perfect ( $\gamma = 1.667$ ). The domain and initial mesh were the same as the shock tube problem described in Section 3.2.1. The minimum cell volume was set to  $1.0 \times 10^{-7}$  ( $\alpha = 0.03$ ).

Pressure ratio	Analytical Mach number	Contact surface density ratio	Flow time	CPU (secs)	Final number of cells	Time steps
10	1.5520	2.5942	0.20	702	2029	3393
100	2.1945	7.3295	0.14	3685	7552	3490
1000	2.7844	21.153	0.11	6615	11089	3517
10000	3.2491	59.473	0.095	9565	16515	3640
10000 <sup>a</sup>	35.611	1.0	$8.7 \times 10^{-3}$	788	1954	3539

<sup>a</sup>Initial temperature ratio is 833.55.

Table 3.5: Summary of ideal shock tube test cases with various initial pressure ratios. The temperatures either side of the diaphragm are equal unless otherwise specified.

The shock speed was computed by recording the position of the shock wave (maximum  $x$  co-ordinate of all cells with  $P > 1.2 P_1$ ) every ten time-steps. This data was smoothed and then differentiated. The computed shock speed was initially higher than the correct value however, the computed shock speed did decay to the correct value for  $P_4/P_1 \leq 1000$  (Fig. 3.30). The shock speed did not converge to the correct



value for  $P_4/P_1 = 10^4$ . The reason for this is discussed later in this section (see Fig. 3.35). The magnitude of the initial overestimation and the distance the shock travelled before the shock speed decayed to the analytical speed increased with the initial pressure ratio.

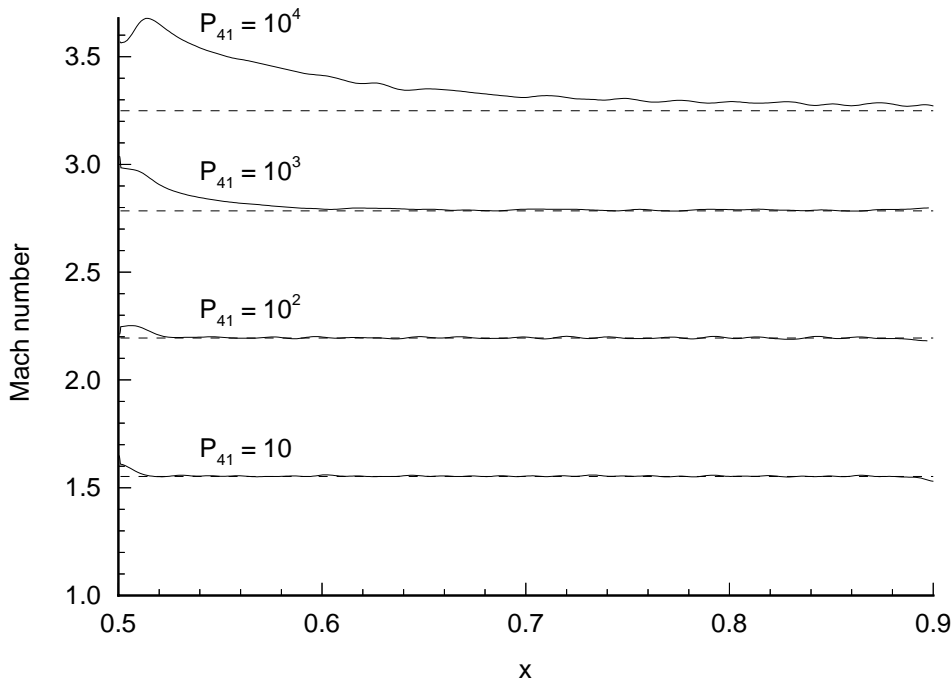


Figure 3.30: Computed shock speed versus distance for various initial pressure ratios. The solid lines represent the computed shock speeds and the dashed lines represent the analytical shock speeds.

The effect of the numerical dissipation (particularly at the contact surface) on the computed shock speed was investigated by designing a test case such that the initial pressure ratio across the diaphragm was high ( $P_4/P_1 = 10^4$ ), but the densities and temperatures either side of the contact surface were equal. The geometry and flow properties for this problem were assumed to be non-dimensional. The domain and initial mesh were the same as the shock tube problem in Section 3.2.1. The initial condition was,

$$\begin{aligned} x \leq 0.5 : & \quad \rho_4 = 11.9969, \quad P_4 = 10^4 \\ x > 0.5 : & \quad \rho_1 = 1.0, \quad P_1 = 1.0. \end{aligned}$$

Note that this initial condition is extreme with a large initial temperature ratio <sup>2</sup> and the large shock Mach number (Table 3.5). Figure 3.31 compares the computed density profile with the analytical solution at  $t = 8.7 \times 10^{-3}$ . The position of the shock wave agrees with the analytical position and the distance required for the

---

<sup>2</sup>  $\frac{P_4}{\rho_4} \frac{\rho_1}{P_1} = 833.55$ . This is the temperature ratio if the driver and driven gases are the same.

shock speed to settle to the analytical speed is significantly reduced (Fig. 3.32). It appears that the numerical diffusion processes at the contact surface determine the accuracy of the shock speed estimation.

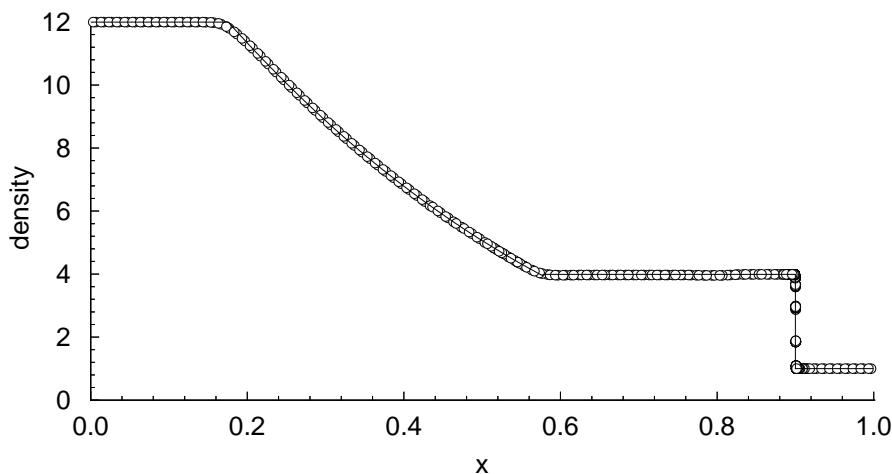


Figure 3.31: Density versus distance for a shock tube problem with a high initial ratio ( $P_4/P_1 = 10000$ ) with no detectable contact surface. The numerical solution (o) is compared with the analytical solution (dashed line) at  $t = 8.7 \times 10^{-3}$ . EFM used for flux calculations and perfect gas assumed. Minimum cell volume of  $1 \times 10^{-7}$  and  $\alpha = 0.01$

Computed shock speeds for the high initial pressure ratio shock tube problem described in Section 3.2.2 are shown in Figure 3.33. It can be seen that the distance travelled by the shock before it decays to the analytical value decreases with increasing mesh resolution (lower minimum cell volume). This emphasises the important role of solution-adaptive remeshing in a scheme designed to produce accurate solutions to shock tube problems with high initial pressure ratios. The overestimation of the primary shock speed by a fixed-grid Navier-Stokes code can be seen in a previous study of the NASA Langley expansion tube by Jacobs (Fig. 7 of Ref. [39]).

Computed shock speeds for EFM and Riemann solver solutions are shown in Figure 3.34. The initial overestimation was lower for the Riemann solver solution, however, the EFM solution converged to the analytic shock speed earlier. The influence of the noise filter coefficient,  $\alpha$  in Equation 2.24 on the computed shock speed is shown in Figure 3.35. It can be seen that the accuracy of the computed shock speed increases as  $\alpha$  decreases. It was shown in Section 3.2.2 that, for higher values of  $\alpha$ , the numerical solution was smeared at the contact surface. It is speculated, that the extra dissipation at the contact surface causes the computed shock to travel faster.

It has been demonstrated that U2DE can accurately compute the speed of the shock wave for an ideal shock tube when the initial pressure ratio is low (Fig. 3.30).

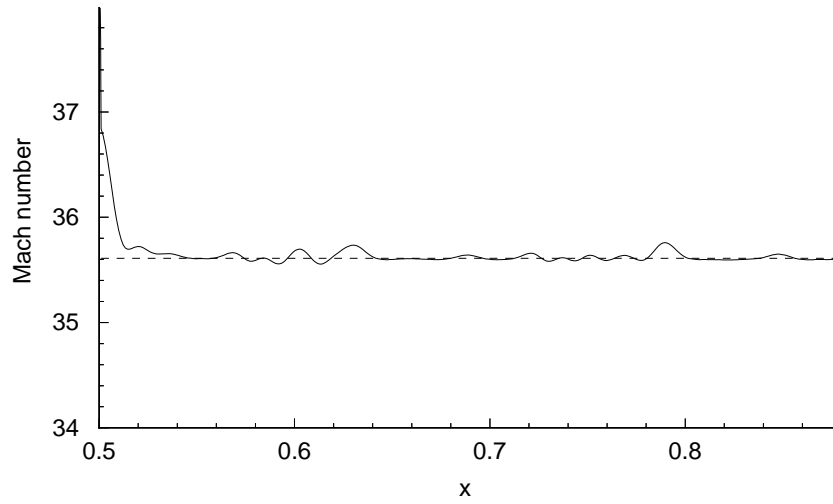


Figure 3.32: Numerical shock Mach number (solid line) versus analytic Mach number (dashed line) for high pressure shock tube with no detectable contact surface.

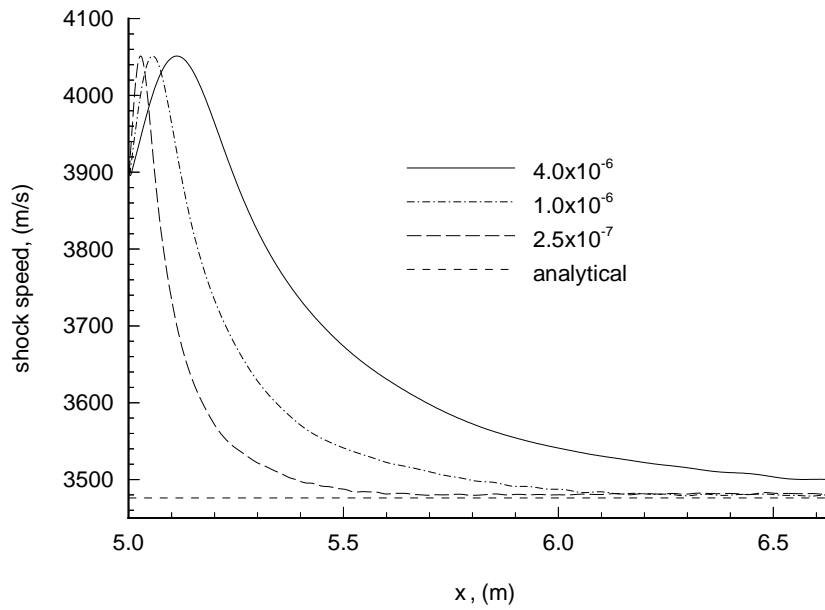


Figure 3.33: Computed shock speed versus distance at various mesh resolutions.

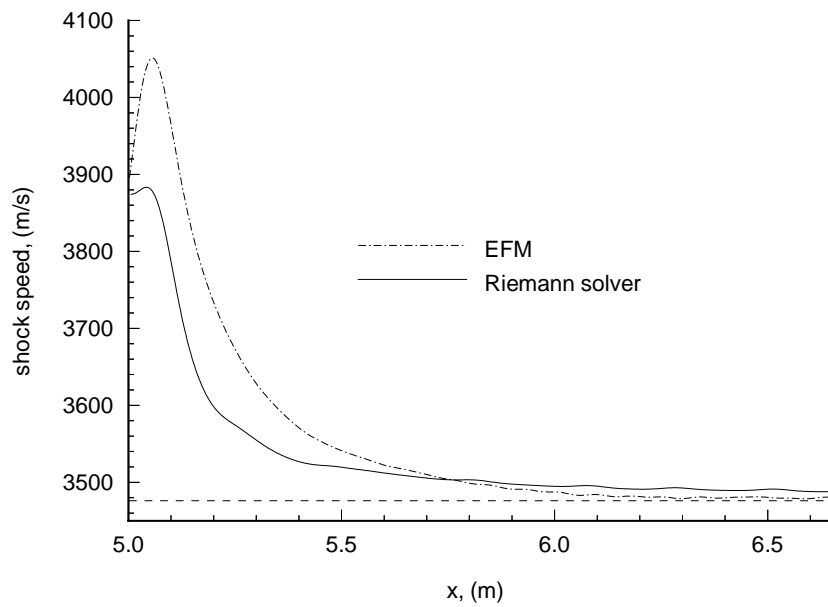


Figure 3.34: Computed shock speed versus distance using different methods to calculate fluxes.

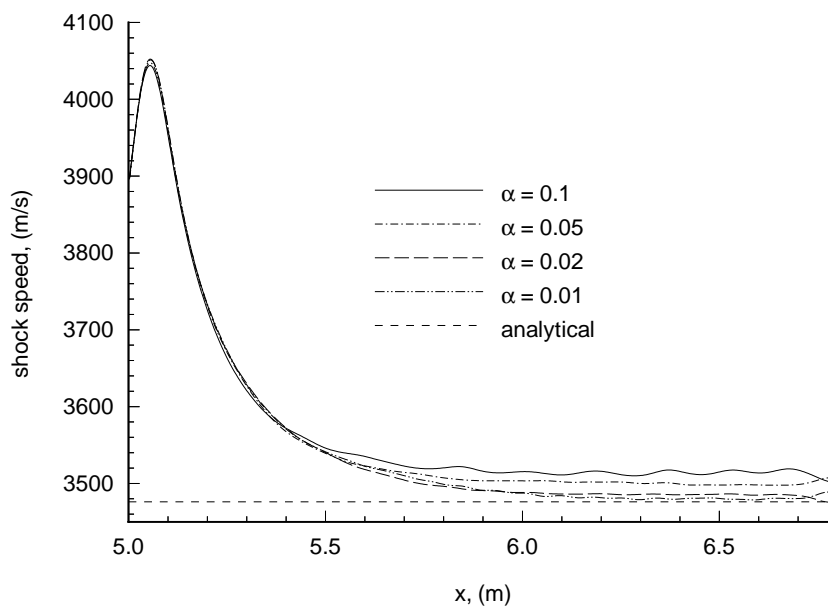


Figure 3.35: Computed shock speed versus distance in a shock tube with high initial pressure ratio. The noise filter coefficient in Equation 2.24 is varied.

Conversely when the initial pressure ratio is high the computed shock speed will be overestimated initially due to numerical dissipation at the contact surface aggravated by the large density ratio (Table 3.5). The noise filter coefficient,  $\alpha$  of Equation 2.24 has to be chosen such that the contact surface is adequately resolved, ensuring that the shock speed converges to the correct value. For simulations of shock tubes with high initial pressure ratios, it would appear that  $\alpha \leq 0.02$  is required to predict accurately shock speed.

In the opinion of the author, EFM is the better flux calculator for shock tube simulations with high initial pressure ratios. EFM solutions contain less noise and require less computational time (Table 3.4). It was not possible to filter the noise from the Riemann solver solutions and at the same time, resolve the important features of the flow (Fig. 3.21). In contrast, the accuracy of EFM solutions can be improved easily by increasing mesh resolution (decreasing minimum cell volume) without excessively increasing CPU time. For example, the shock speed from a high resolution (minimum cell volume =  $2.5 \times 10^{-7} \text{ m}^3$ ) EFM solution (CPU = 36254 seconds) is closer to the analytical value than a medium resolution (minimum cell volume =  $1.0 \times 10^{-6} \text{ m}^3$ ) Riemann solver solution (CPU = 43488 seconds) and required less CPU time (Fig. 3.36).

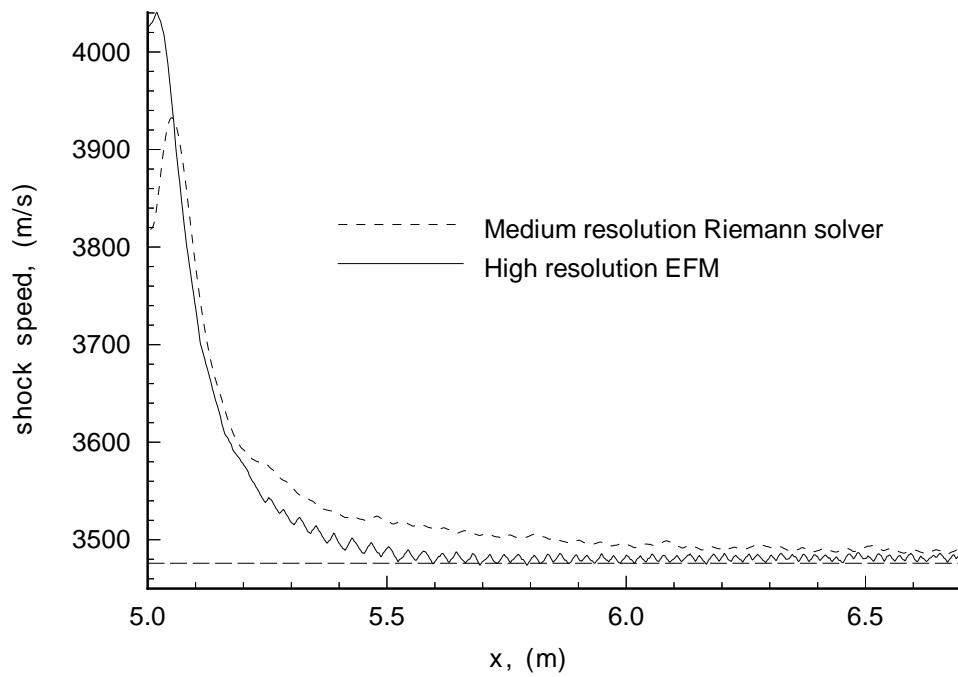


Figure 3.36: Computed shock speed versus distance in shock tube with high initial pressure ratio. High resolution EFM solution (minimum cell volume =  $2.5 \times 10^{-7}$  m<sup>3</sup>) is compared with a medium resolution (minimum cell volume =  $1.0 \times 10^{-6}$  m<sup>3</sup>) Riemann solver solution.

### 3.3 Flow over a cone.

The axisymmetric formulation of the Euler equations (Eqn. 2.6) was tested by examining supersonic inviscid flow over a cone. In the steady-state limit, the shock and other constant property lines are generators from the vertex of the cone. The analytical solution for the angle of the shock wave can be found by using the method of Taylor & Maccoll [81] (Ch. 10, Anderson [5]).

An axisymmetric simulation was performed of flow over a cone with a 20 degree half angle and its axis parallel to the flow. The geometry and initial discretisation are shown in Figure 3.37. The gas was assumed to be calorifically perfect air with  $\gamma = 1.4$  and the initial condition was,

$$\rho = 6.82 \times 10^{-2} \text{ kg/m}^3, P = 6.0 \times 10^3 \text{ Pa}, u = v = 0,$$

throughout the domain. A constant supersonic in-flow,

$$\rho = 0.3028 \text{ kg/m}^3, P = 95.88 \times 10^3 \text{ Pa}, u = 1006 \text{ m/s}, v = 0,$$

was applied at the  $x = 0$  boundary. The out-flow boundary condition was assigned to the  $x = 1.0$  boundary. All other boundaries were treated as walls.

Figures 3.38 – 3.40 show the mesh and density contours at times,  $t = 0.5, 1.0,$  and  $5.0$  milliseconds. The Riemann solver was used to calculate the fluxes; the minimum cell area was  $1.0 \times 10^{-6} \text{ m}^2$ , and  $\alpha = 0.01$ . The total simulation required 87 minutes on the Silicon Graphics Power Challenge. The measured angle of the shock wave relative to the axis in Figure 3.40 is  $48.5^\circ \pm 0.35^\circ$  and the analytical solution is  $48.64^\circ$ . The ability of the code to accurately predict this shock angle suggests that the axisymmetric formulation is correct.

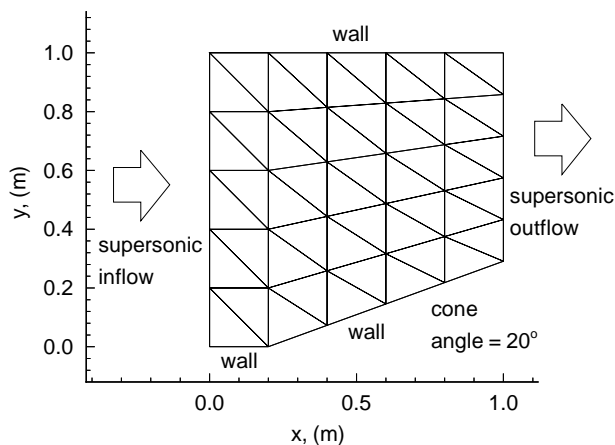


Figure 3.37: Domain and initial discretisation for flow over a cone.

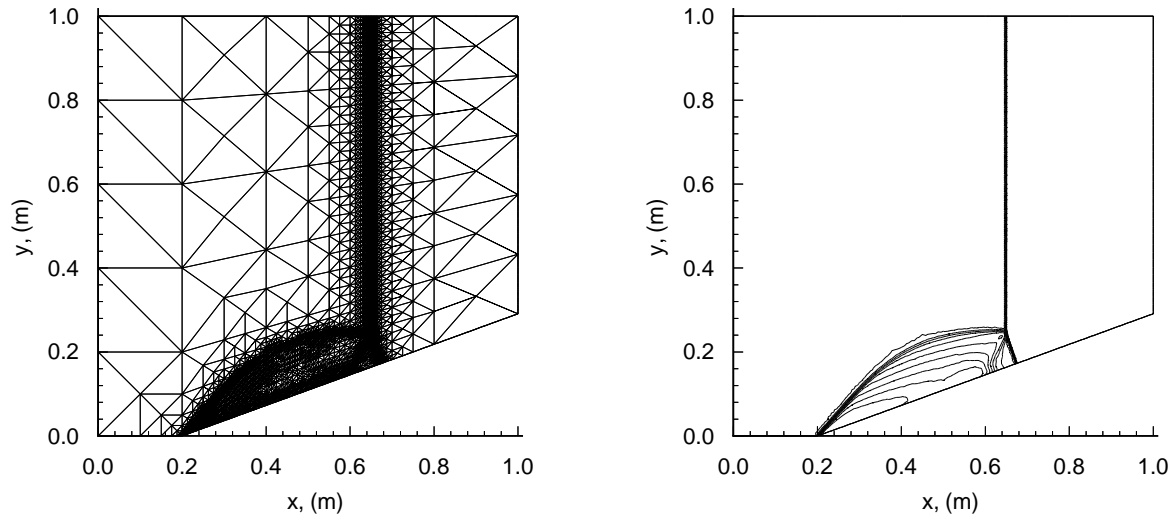


Figure 3.38: Mesh (8099 cells) and density contours for inviscid flow over a cone at time,  $t = 0.5$  milliseconds.

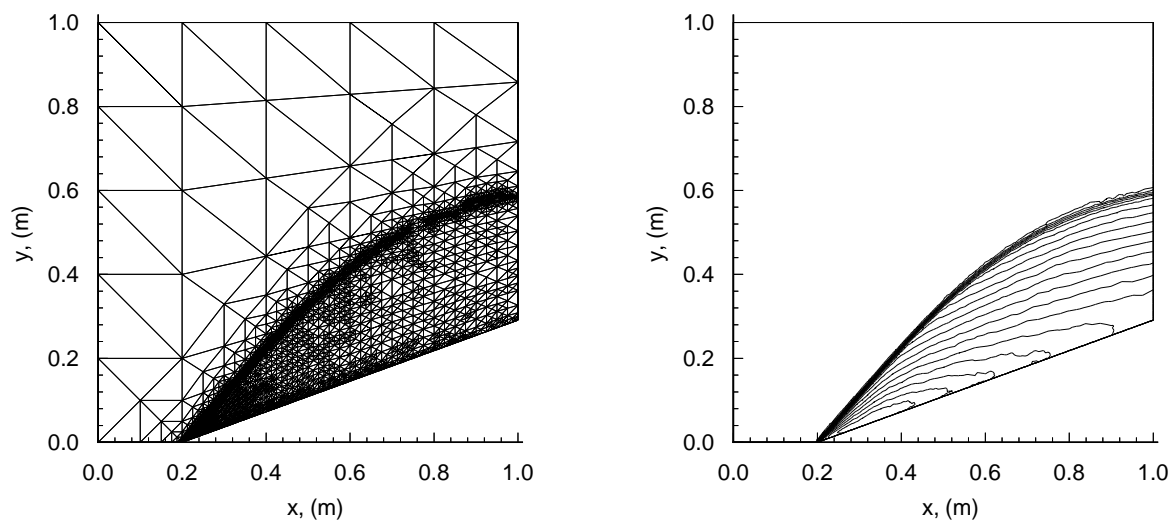


Figure 3.39: Mesh (5541 cells) and density contours for inviscid flow over a cone at time,  $t = 1.0$  millisecond.



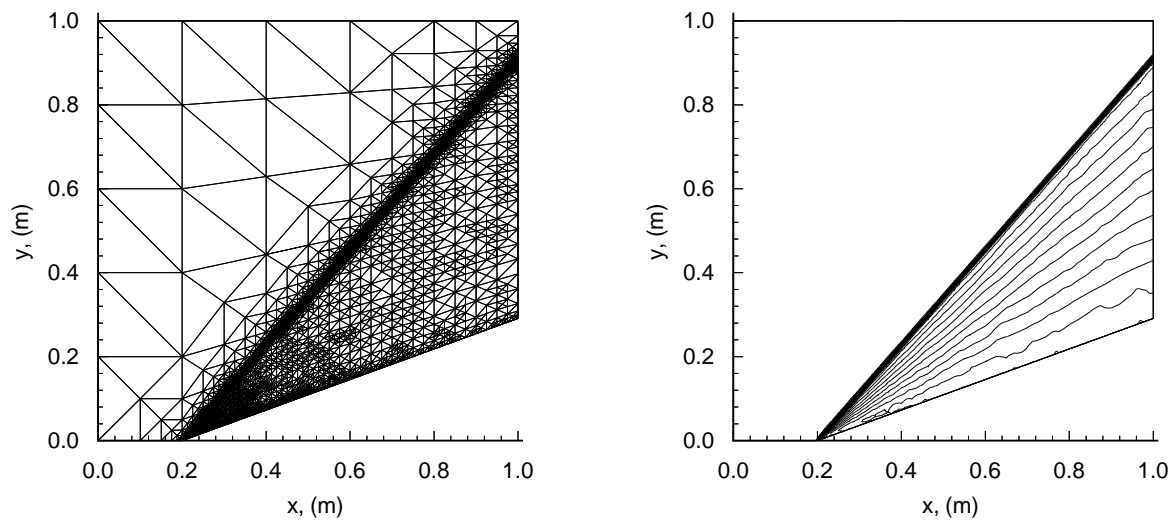


Figure 3.40: Mesh (6431 cells) and density contours for inviscid flow over a cone at time,  $t = 5.0$  milliseconds.

### 3.4 Blast wave flow-field

To verify the ability of U2DE to capture multi-dimensional discontinuities in an axisymmetric flow-field, a blast wave generated by a shock exiting an open-ended shock tube was examined. There is no known analytical solution for this problem, however, numerical simulations have been performed previously by Wang & Widhopf [89] and Cooke & Fansler [19] and can be used for comparison.

The flow domain and initial discretisation are shown in Figures 3.41 and 3.42 respectively. The wall boundary condition applies at the tube walls; the boundary at the entrance of the shock tube is treated as supersonic in-flow. All other boundaries are treated as out-flow even though the flow at these boundaries is never supersonic (Sec. 2.3.1). However, the use of this boundary condition (constant extrapolation) at outer boundaries is considered to be *safe* [42] when the influence of disturbances from outside the domain up until the time of interest is small, which is valid for this test case. The initial condition outside the tube is,

$$\rho = 1.2 \text{ kg/m}^3, P = 101.3 \times 10^3 \text{ Pa}, u = v = 0,$$

and inside the tube,

$$\rho = 2.735 \text{ kg/m}^3, P = 345.05 \times 10^3 \text{ Pa}, u = 337.65 \text{ m/s}, v = 0.$$

The in-flow condition at the entrance to the tube is the same as the initial condition inside the tube.

The density contours and final mesh for a higher-order solution at time,  $t = 1.5 \times 10^{-3}$  seconds is shown in Figure 3.43. EFM was used to calculate the fluxes, the minimum cell area was  $1.0 \times 10^{-6} \text{ m}^2$ , and  $\alpha = 0.005$ . The location and shape of the various flow features agree with previous numerical work (Fig. 3.44) by Wang & Widhopf [89]. This provides confidence, that U2DE is capable of capturing axisymmetric, multi-dimensional, transient flow features.

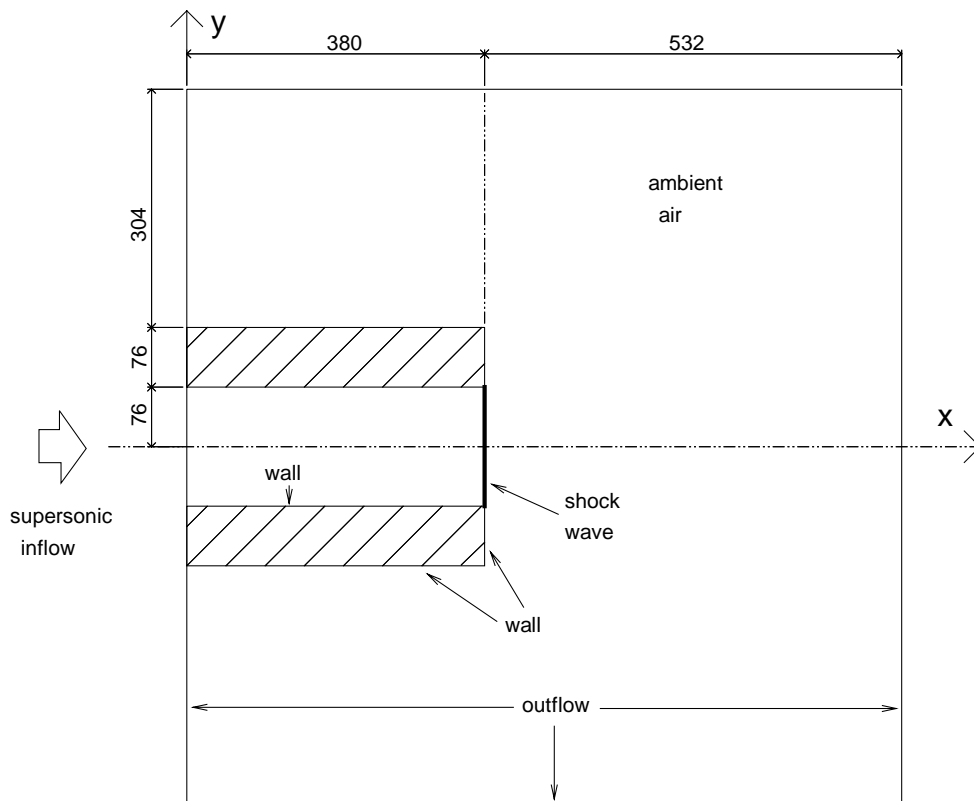


Figure 3.41: Flow domain for blast wave at open-ended shock tube. The geometry is symmetric about the  $x$ -axis. Dimensions are in millimetres.

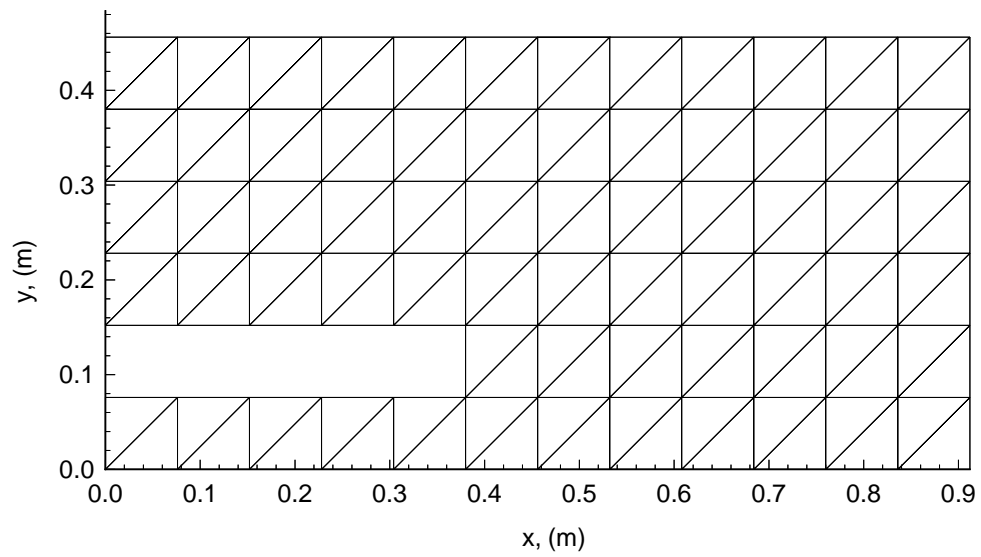


Figure 3.42: Initial discretisation for blast wave at open-ended shock tube.

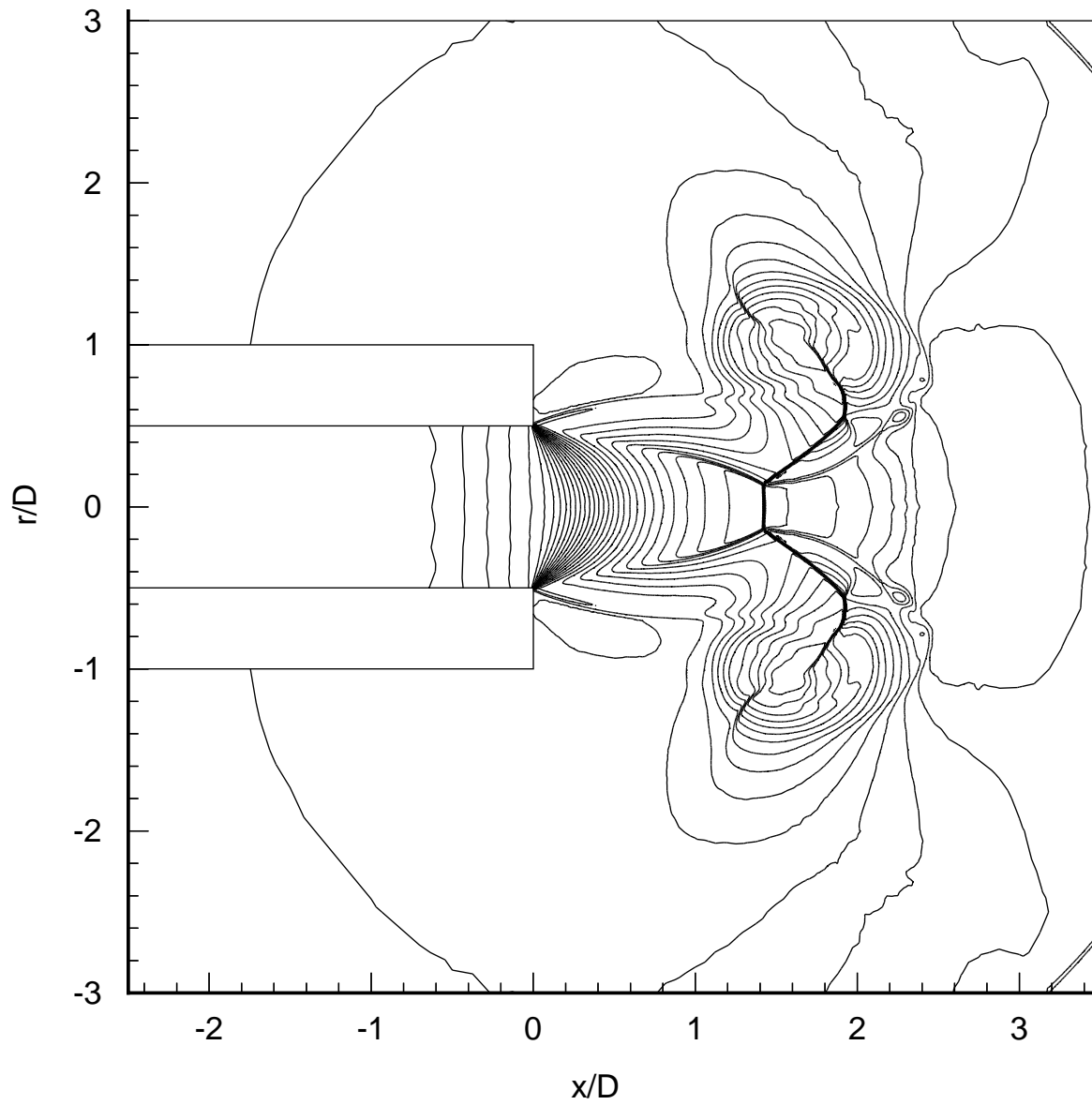


Figure 3.43: Density contours of higher-order solution for the blast wave flow-field for an open-ended shock tube.

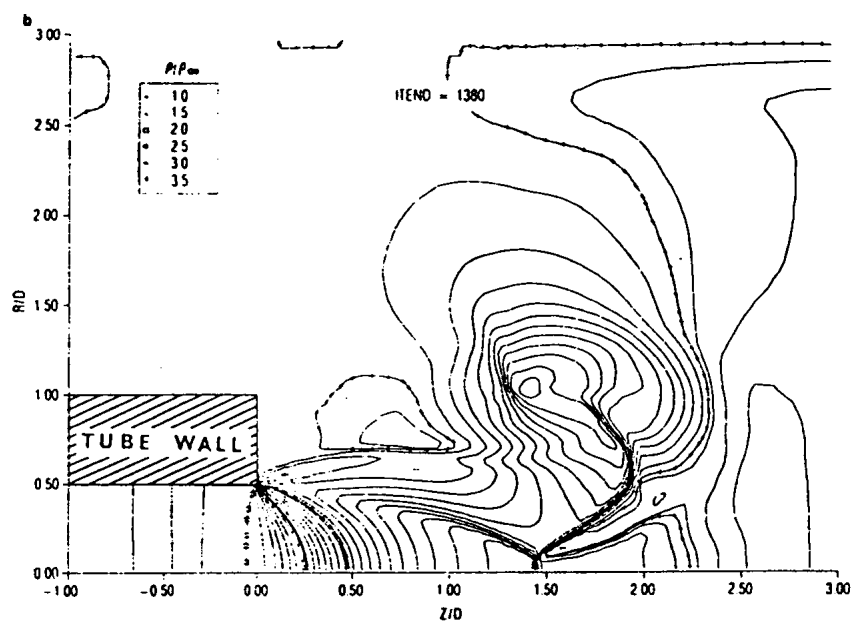


Figure 3.44: Density contours from the simulation by Wang & Widhopf [89].

### 3.5 Double Mach reflection

The double Mach reflection case 10 from Glaz *et al.* [25] was examined. This problem represents inviscid flow over a 40 degree ramp or wedge. The previous numerical work by Jacobs [35] will be used for comparison.

The flow domain is the same as the cone test case but the angle of the ramp is different. The initial flow condition, in-flow condition, and all boundary conditions are the same as the cone test case. The initial mesh is shown in Figure 3.45. Two-dimensional planar flow is assumed. The gas is calorifically perfect air,  $\gamma = 1.4$ .

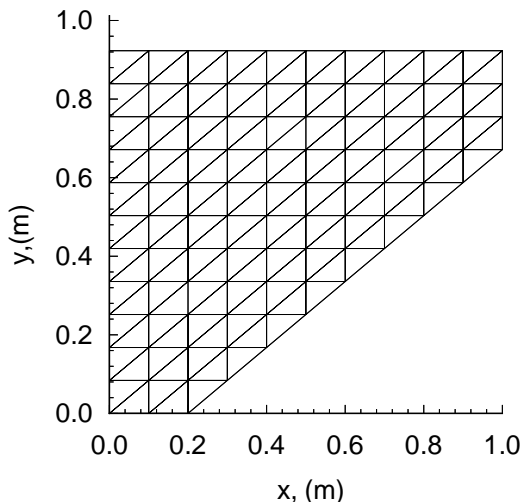


Figure 3.45: Double Mach reflection; initial mesh.

There is no known analytical solution for this problem, however, shock wave reflection phenomena has been well studied [10]. A double Mach reflection (DMR) is expected for the geometry and flow condition stated above. A schematic of the wave configuration for a pseudo-steady DMR is shown in Figure 3.46. The basic flow features are: an incident shock (i), two reflected shocks (r), two Mach stems (m), two slipstreams and (s), two triple points (T). Here the triple point is the intersection of three shock waves and a slipstream. A slipstream is a discontinuity separating gas of different density and velocity, but at the same pressure.

Figure 3.47 shows the density and pressure contours of a high resolution, higher-order EFM solution. This simulation required 21.2 CPU hours on a SUN workstation (66.0 microseconds per cell per corrector-predictor time-step). All of the expected flow features can be seen in the solution except for the second slipstream, because the density difference across it is not large enough to be noticeable on the contour plot. The location of the various flow features do agree with the numerical results of Jacobs [35] (Fig. 3.48).

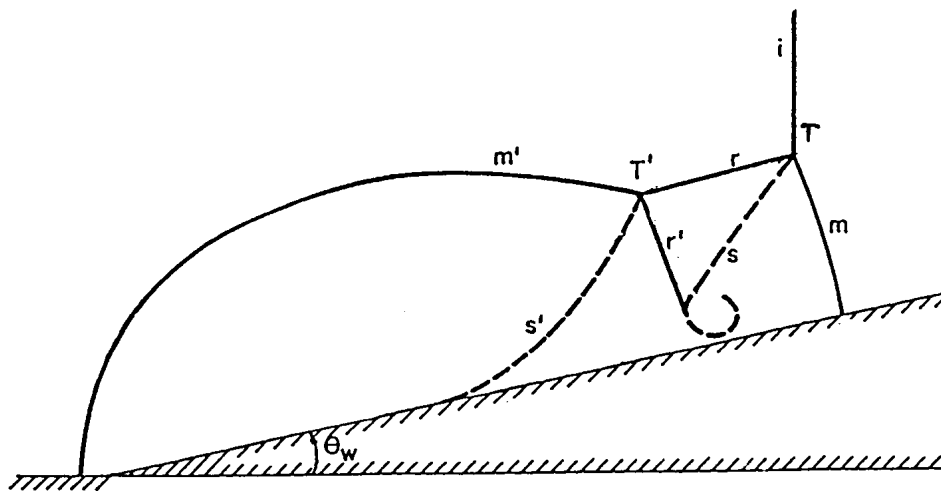


Figure 3.46: Double Mach reflection; wave configuration. Taken from Ben-Dor [10].

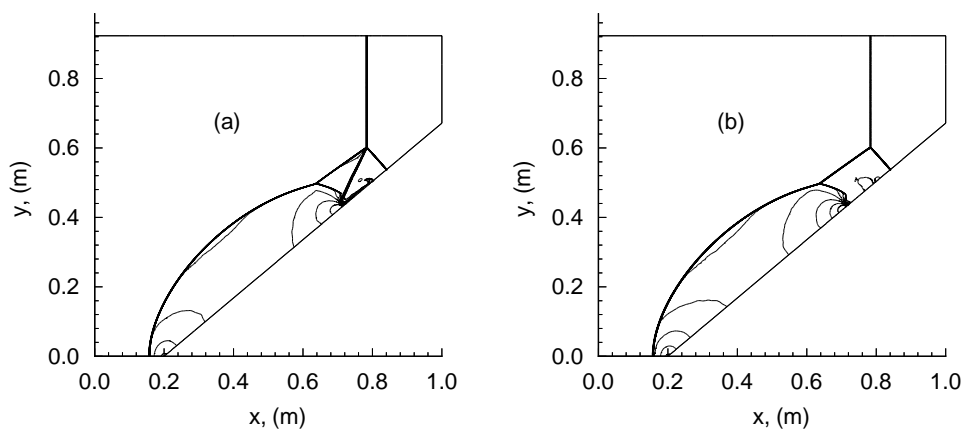


Figure 3.47: Double Mach reflection, density contours and pressure contours for EFM solution with minimum cell volume,  $2.5 \times 10^{-7} \text{ m}^3$ .



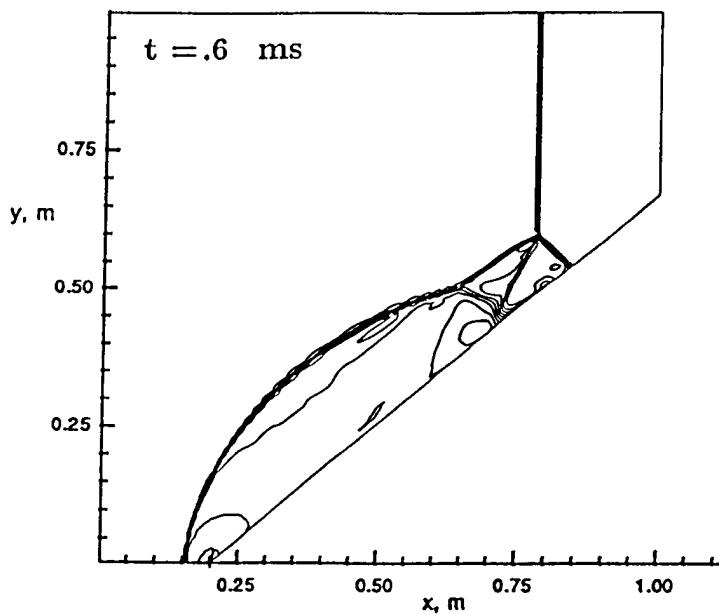


Figure 3.48: Density contours of numerical solution by Jacobs [34] for Double Mach reflection test case.

Noise was found to be present in the Riemann solver solution (Fig. 3.49). This is another example of odd-even decoupling [66] (Sec. 3.2.2). The noise can be reduced if the initial mesh is not aligned to the flow (Figs. 3.50 & 3.51). However, a small amount of noise was still present in the solution near the top boundary ( $y = 1.0$  m) where the mesh was aligned to the shock.

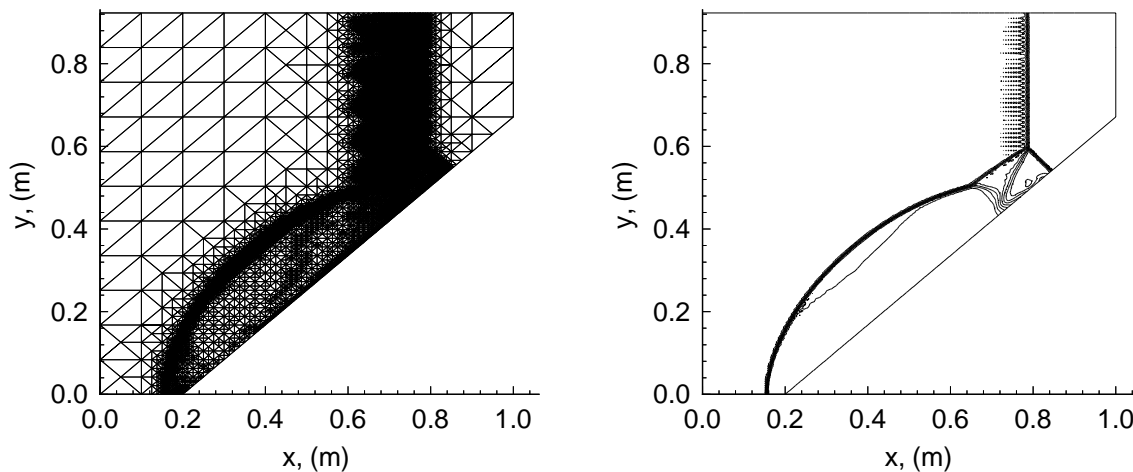


Figure 3.49: Double Mach reflection; density contours and final mesh for a Riemann solver solution with minimum cell volume,  $1.0 \times 10^{-5} \text{ m}^3$ .

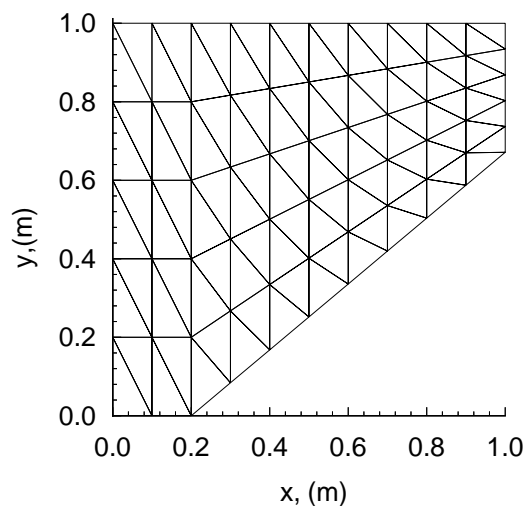
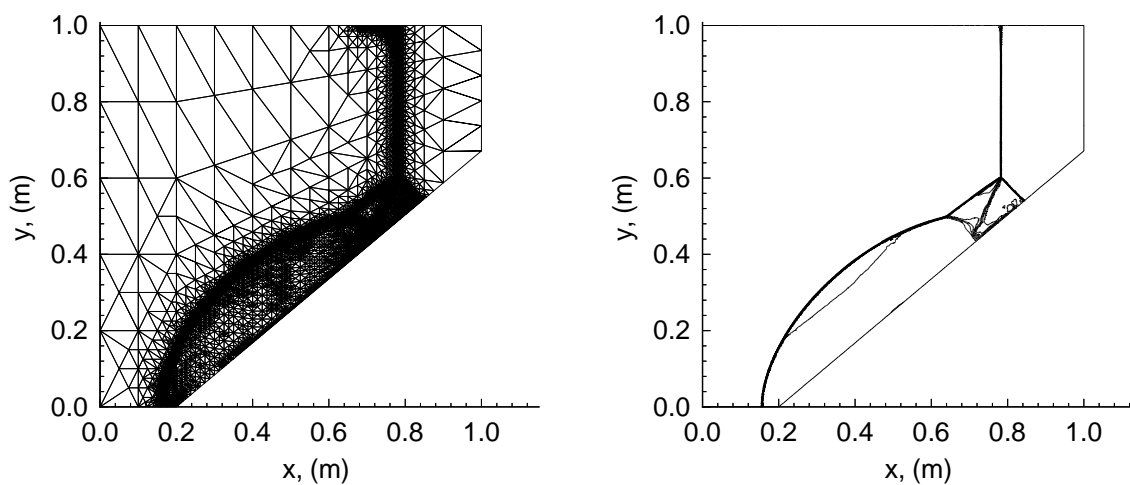


Figure 3.50: Double Mach reflection; initial non-aligned mesh.

Figure 3.51: Double Mach reflection; density contours and final mesh for non-aligned mesh. Riemann solver solution with minimum cell volume,  $2.0 \times 10^{-6} \text{ m}^3$ .

Aligned Mesh	Minimum cell volume ( $\text{m}^3$ )	Flux solver	Final number of cells
yes	$1.0 \times 10^{-5}$	Riemann	16446
yes	$2.5 \times 10^{-7}$	EFM	71945
no	$2.0 \times 10^{-6}$	Riemann	27767

Table 3.6: Details of double Mach reflection simulations. For all simulations,  $\alpha = 0.01$ .

### 3.6 Shock wave diffraction over a 90 degree corner

The problem of a two-dimensional planar shock wave diffracting over a 90 degree sharp corner (Fig. 3.52) was selected as a bench mark problem for the Eighteenth International Symposium on Shock Waves (ISSW) [79]. Sixteen separate numerical solutions using various flow solvers and three separate experimental flow visualisations were presented at the symposium.

The Mach number of the incident shock is 1.5. The ambient gas is ideal air at room temperature and pressure. A numerical solution generated by U2DE is shown in Figure 3.53. The Riemann solver was used to calculate the fluxes. The minimum cell volume was set to  $5.0 \times 10^{-7} \text{ m}^3$ . A low noise filter coefficient,  $\alpha = 0.001$  was necessary to cause the solution-adaptive remeshing to capture some of the weaker flow features.

Note that all the flow-features present in the numerical solutions by Uchiyama & Inoue [86] (Fig. 3.53) appear to have been captured in the current work. These features include: a shear layer (SL) instability and roll-up ( $x \approx 0.54, y \approx 0.50$ ), a Prandtl-Meyer expansion fan (EF), two weak shocks (SW1 and SW2) terminating the expansion fan, two distinctive vortex shocks (VSL and VSR) near the core of the vortex, and a contact surface (CS) emanating from a point on the diffracted shock.

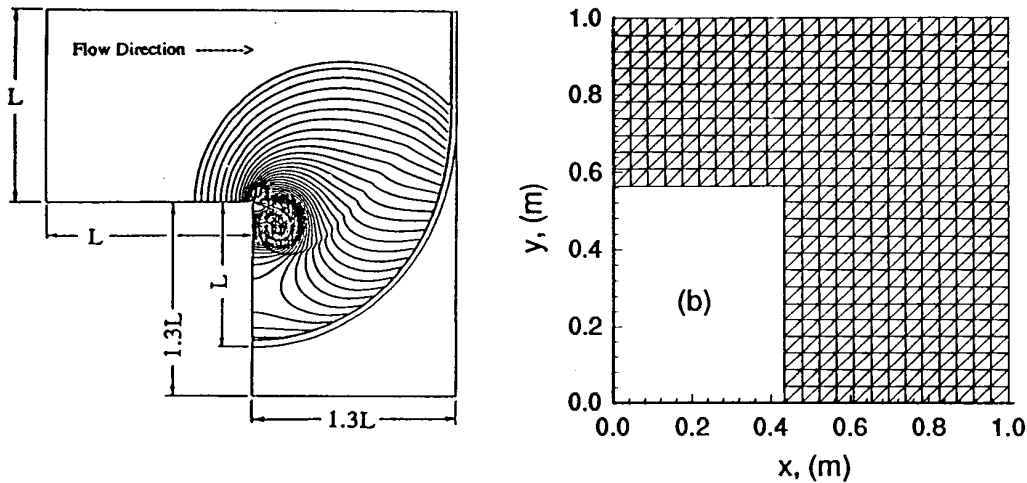


Figure 3.52: Shock wave diffraction: (a) output format specified by ISSW (taken from Takayama & Inoue [79]), (b) initial mesh.

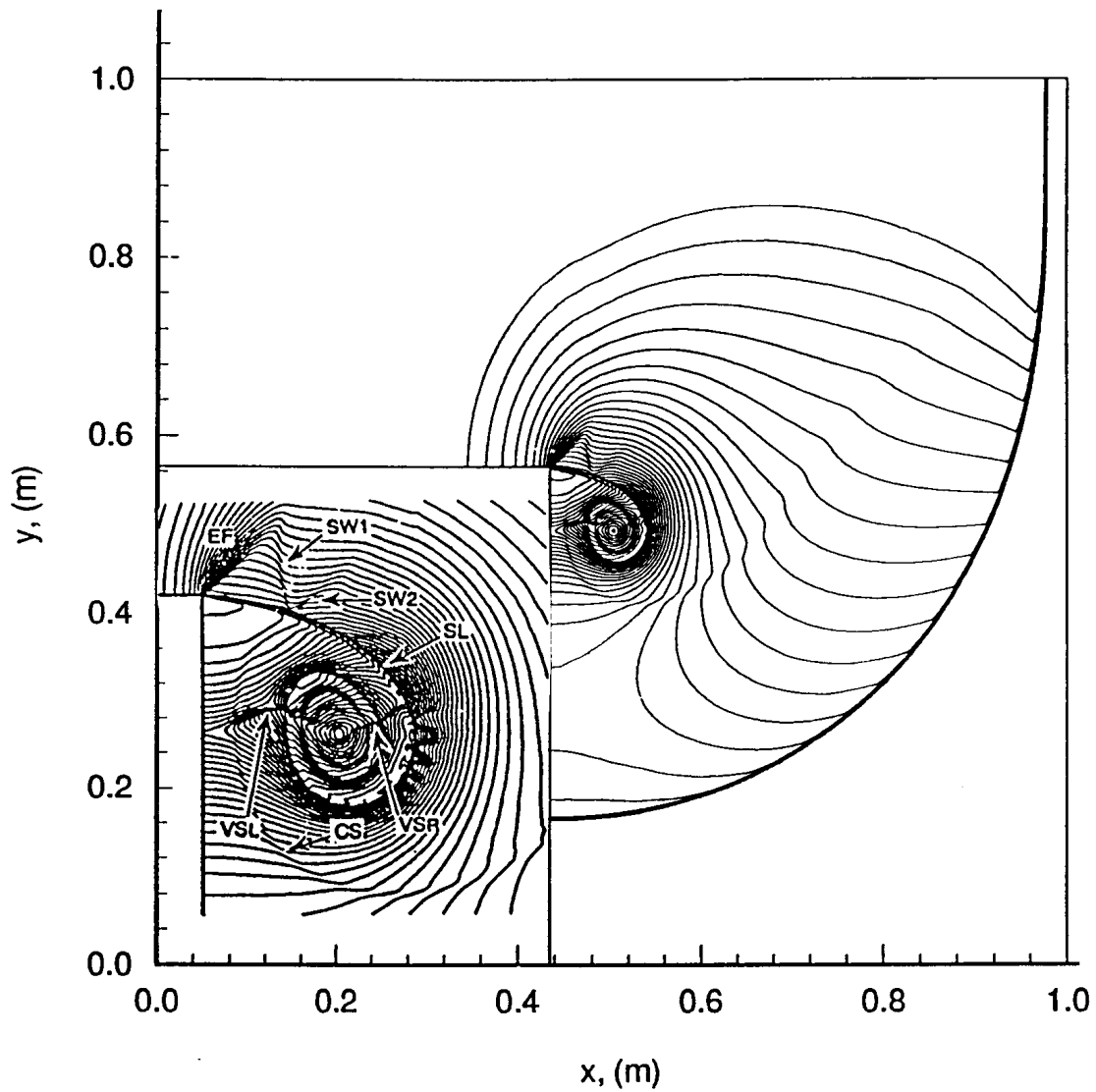


Figure 3.53: Density contours in ISSW format for shock diffraction over a 90 degree sharp corner. Insert: solution from Uchiyama & Inoue [86] with the following flow features labelled: a shear layer (SL), a Prandtl-Meyer expansion fan (EF), two weak shocks (SW1 and SW2), two distinctive vortex shocks (VSL and VSR), and a contact surface (CS).

## 3.7 Summary

The ability of U2DE to produce accurate solutions of the Euler equations has been confirmed by comparing numerical solutions to analytical solutions for a supersonic vortex, an ideal shock tube, and flow over a cone. The spatial order of convergence of U2DE (EFM) for the supersonic vortex test case was found to be 1.57.

The value of solution-adaptive remeshing was confirmed, with large savings in terms of computation time (46.1 times faster) and memory requirement (35.8 times less) for a simulation of an ideal shock tube.

The ability of U2DE to compute accurately shock speeds when the initial pressure ratio is low was demonstrated. When the initial pressure ratio is high the flow is difficult to resolve, because of the large density ratio at the contact surface where significant numerical diffusion occurs. However, solution-adaptive remeshing can be used to control the error and obtain reasonable estimates for the shock speed.

Two different methods for calculating fluxes, the Riemann solver and EFM were examined. The performance of each method was dependent on the problem, with each method performing better for different test cases. For the simulation of a shock tube with a high initial pressure ratio, EFM was found to be the better choice, and will be used for the simulations in the following chapters.

The ability of U2DE to capture multi-dimensional flow features was also confirmed by examining a blast wave flow-field and a shock diffraction test case.

# Chapter 4

## Gradual diaphragm opening

## 4.1 Introduction

This chapter examines the flow development within shock tubes considering the gradual opening of the primary diaphragm. Previous work is examined. The results of axisymmetric simulations of the Langley expansion tube and a constant area tube are presented. The diaphragm was modelled as an opening iris. The simulations were performed by U2DE, the finite-volume code described in Chapter 2. The influence of the initial pressure ratio and diaphragm opening time on the flow development is examined in detail.

### 4.1.1 General description of diaphragm opening

Many researchers [46, 91, 71, 14, 75, 20, 72, 29, 73] have performed experimental investigations of the opening of the primary diaphragm within shock tubes. From this body of work, a general description of the diaphragm opening process can be developed.

Consider the case of a 1 mm aluminium diaphragm separating the high and low pressure gas within a 54 mm square shock tube (Rothkopf & Low [72]). As the pressure in the high pressure (driver) section increases, the diaphragm bulges into an approximately spherical shape. The amount of bulging depends on the ductility of the diaphragm material [72]. The initial tearing occurs along lines of natural or enforced weakness and produces a small aperture near the centre of the diaphragm [14]. The time taken for the diaphragm material to tear accounts for a large portion of the diaphragm opening time [14, 72]. As the diaphragm material tears, petals are formed. The shape of the petals is dependent on the diaphragm material (ductility) and whether lines of weakness have been introduced. Scoring of diaphragms is common practice as it encourages a more repeatable rupture.

High pressure driver gas pushes the petals open and out against the tube wall. As a basic approximation, the motion of a diaphragm petal after tearing can be modelled as a rigid body rotating about an axis (the base of the petal) as described by the equation,

$$I \frac{d^2 \theta}{dt^2} = M \quad (4.1)$$

where  $I$  is the moment of inertia of the diaphragm petal about the hinge axis and  $M$  is the moment due to pressure forces [20]. For thicker diaphragms it may be necessary to consider the resistance moment due to stress within the material [29].

Rothkopf & Low [72] observed the rupture of diaphragms prescribed with an “X”

stamp, and observed that symmetrical tearing occurred for relatively brittle metals while asymmetrical tearing occurred for ductile diaphragm material. Photographs were taken at various stages of the opening (Fig. 4.1). Note the irregular opening of the brass and copper diaphragms. A photomultiplier was also used to determine the projected area of the open aperture as a function of time by continuously monitoring the amount of light transmitted through the aperture. The initial opening process was observed to be slow and accounted for 20% of the opening time. After this time the projected area of the aperture can be considered to be a linear function of time (Fig. 4.2). Rothkopf & Low [72] observed that the opening times for a diaphragm within a tube with a small diameter circular section was longer than a diaphragm within an equivalent square section tube, and irregular petal formation was observed. However, the diaphragm opening times for equivalent circular and square tubes were similar when the diameters (or width) of the diaphragms were large.

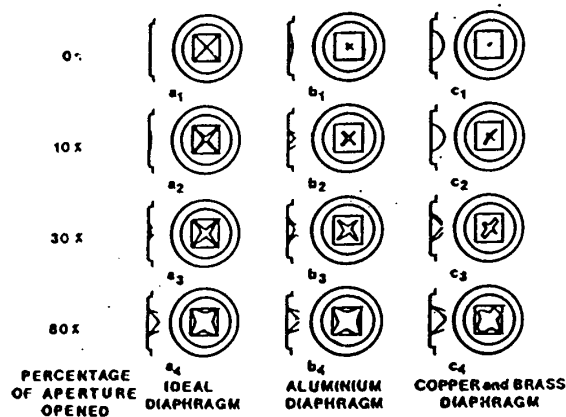


Figure 4.1: Modes of diaphragm rupture (taken from Rothkopf & Low [72]).

## 4.1.2 Flow development

Experimental observations of the development of the flow have been made through the use of flow visualisation techniques such as shadowgraph and Schlieren.

Hickman & Farrar [29] observed that a quasi-steady free jet exists downstream of the ruptured diaphragm and that the presence of the tube walls causes a normal shock wave to process the gas flow to match the driven conditions.

Outa *et al.* [61] observed the presence of oblique shock waves interacting with a



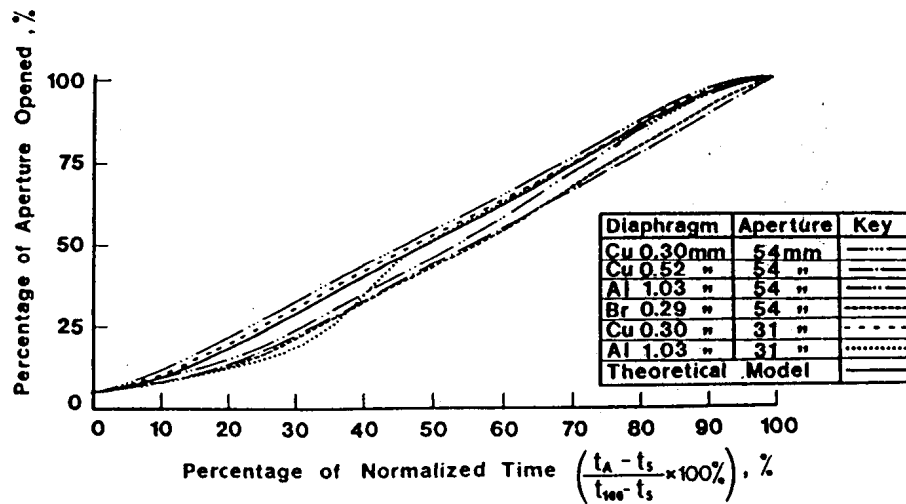


Figure 4.2: Graph illustrating rate of diaphragm opening where  $t_A$  is the actual time during opening, and  $t_5$ , and  $t_{100}$  are the times when the diaphragm is 5% and 100% open (cross-sectional area) respectively. Diagram taken from Rothkopf & Low [72].

multi-dimensional unsteady expansion. It was concluded that the effects of these waves on the flow structure were restricted to one to two diameters downstream.

Henshall [28] described the shock formation process after diaphragm rupture as follows;

when the bowed diaphragm is ruptured, a number of curved compression waves are propagated into the channel. These compression waves quickly coalesce to form a curved shock. Regular reflections of this curved shock will take place at the walls of the tube until the angle of incidence of the shock is such that regular reflection of the shock is impossible and the shock then undergoes Mach reflection. The triple points of the Mach reflection move towards the centre of the tube, until the secondary branches of the Mach configuration are weak and disappear. Finally, an optically flat primary shock propagated down the channel.

Hooker [31] performed experiments in a low pressure shock tube (helium driving argon) where viscous effects were significant. The diameter of the driven section was 39.5 mm. A rake of heat transfer probes was used to determine the shape of the leading edge of the contact surface. “The characteristic turbulent ‘jump’ ... following the region of uniform heat transfer is associated with the arrival of the contact front.” It was concluded that the leading edge of the contact surface was planar at 1.05 m from the diaphragm and was still planar at 4.7 m from the

diaphragm.

### 4.1.3 Numerical simulations

Multi-dimensional simulations of the gradual opening of a diaphragm have been performed previously by Satofuka [74], Outa *et al.* [61], Cambier *et al.* [13], and Vasil'ev & Danil'chuk [87]. This collection of work modelled the diaphragm opening as either a slit for two-dimensional flow or an iris for axisymmetric flow. In each of these simulations the opening commenced in the middle and then progressed towards the tube wall. Most of the work concentrated on the flow development and, in particular, on the structure of the contact surface (CS) and the expansion waves in the driver gas.

Cambier *et al.* [13] performed a two-dimensional axisymmetric simulation (Fig. 4.3) of gradual diaphragm opening and the following observations were made: the primary shock becomes planar very rapidly (within two diameters of the diaphragm), a complex and unsteady flow structure dominated by a Mach disk is formed behind the CS, and the CS itself develops a complex shape. The initial shape of the CS is due to the relatively slow opening time of the diaphragm. The CS does not become planar with time, and it was suggested that its fate could be dominated by Rayleigh-Taylor instabilities.

Vasil'ev & Danil'chuk [87] performed an inviscid two-dimensional simulation (Fig. 4.4) of flow formation in a shock tube with transverse diaphragm removal. Two main observations were made from the simulations: (i) jetting of the CS along the walls due to a system of oblique shock waves, and (ii) fragmentation of the secondary shock which occurred because a pocket of *hot* unexpanded gas at the wall changed the effective area of the tube. The resulting flow is analogous to the flow through a Laval nozzle.

### 4.1.4 Scope of current work

The remaining sections of this chapter study the development of the CS during and after diaphragm rupture within an inviscid shock tube. It is presumed that inviscid simulations will exhibit similar features to the actual flows in situations where the high operating pressures cause boundary layers to be thin. The previous multi-dimensional simulations are extended in the current work by: (i) studying the parameters that affect the shape of the CS, (ii) performing higher resolution

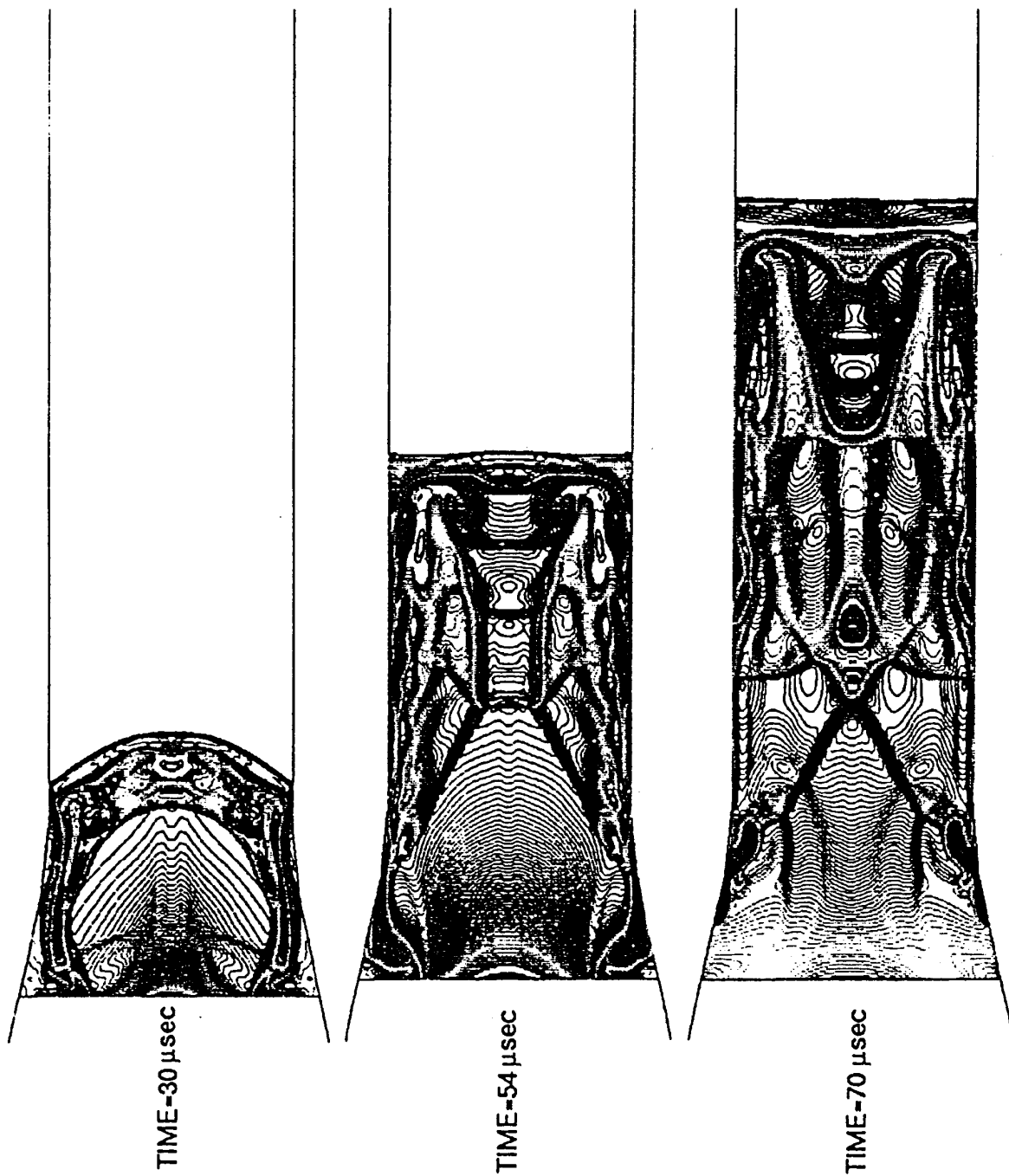
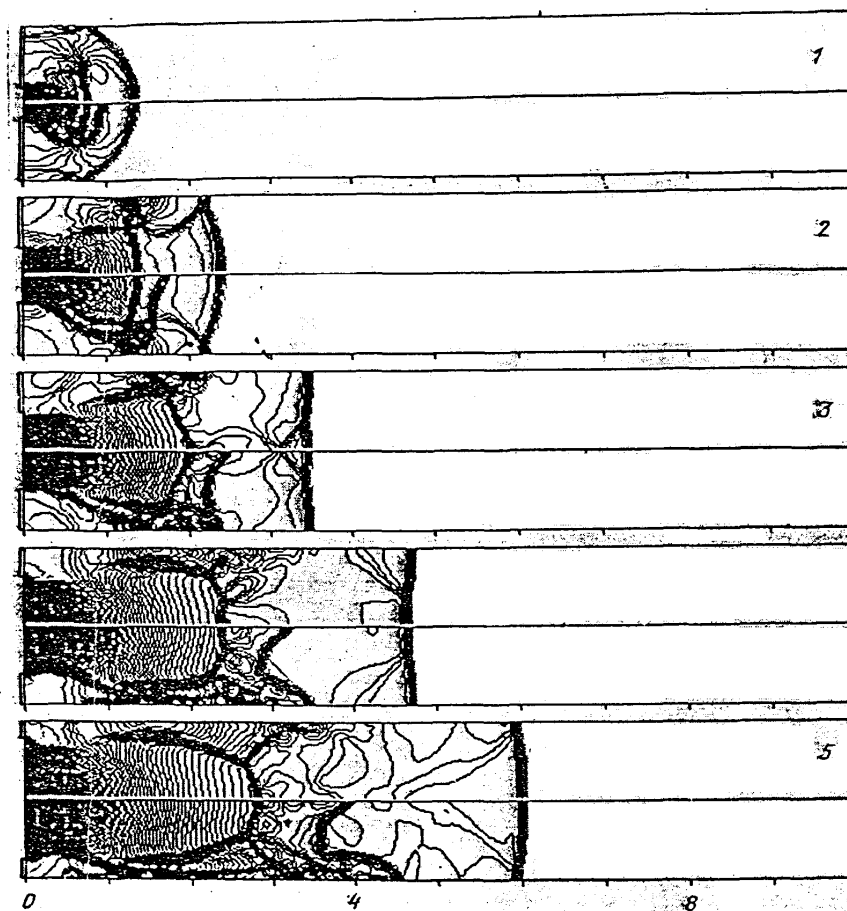


Figure 4.3: Numerical simulation of gradual diaphragm opening by Cambier *et al.* [13]. Temperature contours are shown.



Фиг. 1

Figure 4.4: Numerical simulation of gradual diaphragm opening by Vasil'ev & Danil'chuk [87]. Pressure (top) and density (bottom) contours are shown. The initial pressure ratio was 40.

simulations, and (iii) examining grid convergence.

## 4.2 Numerical model of diaphragm opening

The first set of simulations are of the former NASA Langley expansion tube being used in shock tube mode. This facility was chosen because of the quality and detail of the available experimental data.

The Langley expansion tube consisted of a circular driven section with a diameter of 165.1 mm and a length of 2.44 m. The diameter of the driven tube was 152.4 mm and its length was 29.0 m. The geometry of the computational domain is shown in Figure 4.5. The machine was able to be operated in either double or single diaphragm mode. The experimental results were obtained using the machine in double diaphragm mode because this reduced the “randomness” in the pressure ratio across the diaphragm. However, the effect of the diaphragm mode on shock velocity was minor [55] and to simplify the simulations, single diaphragm mode was assumed. Although the diaphragm section in the experimental machine was square and the transition piece went from square to circular, the geometry for the simulations was assumed to be axisymmetric. The transition from driver diameter to driven diameter occurred after the diaphragm location, and extended over a length of 190.5 mm. Further description of the geometry and operation of the former NASA Langley expansion tube can be found in the report by Miller & Jones [55].

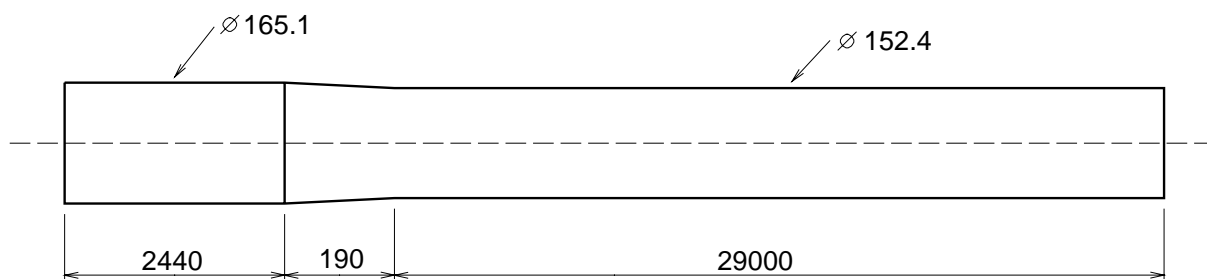


Figure 4.5: Schematic of the axisymmetric domain used to model the former NASA Langley expansion tube. All dimensions shown are in millimetres. The drawing is not to scale.

Four experimental conditions used by Miller & Jones were examined (Table 4.1). The initial driver gas state,

$$x \leq 2.44 \text{ m: } P_4 = 3.5 \times 10^7 \text{ Pa, } T_4 = 342 \text{ K, } u_4 = v_4 = 0,$$

was the same for all conditions. Both driver and driven gases were helium and

the Redlich-Kwong equation of state (Appendix A) was used to describe the gas behaviour.

Condition #	Pressure kPa	Temperature K	Maximum shock speed m/s
1	34.5	297.0	3490
2	3.45	297.6	4206
3	0.345	297.6	4511
4	6.9	297.0	3307

Table 4.1: Pressure and temperature of driven gas of experiments by Miller & Jones [55]. The driver conditions were  $P_4 = 35$  MPa and  $T_4 = 342$  K.

EFM was used to calculate the fluxes for all shock tube simulations with gradual diaphragm opening because the Riemann solver generated noisy solutions when the initial pressure ratio was high (Sec. 3.2.2). Solution adaptive remeshing was used for all the simulations with  $\alpha = 0.02$  or  $0.01$ . It was shown in Section 3.2.4 that  $\alpha \leq 0.02$  is required to resolve the contact surface within shock tubes with high initial pressure ratios.

### 4.2.1 Discretisation of domain

The initial mesh was created from a rectangular grid (Fig. 4.6). Due to the symmetry of the problem, only half of the domain was considered. A simple geometric transformation was applied to increase the driver diameter and create the transition piece. To create the diaphragm the mesh was refined at the diaphragm location and a thin strip of cells, 4.24 mm wide were marked as ignored cells (Sec. 2.5). The ignored cells created a barrier between the driver and driven sections and while it remained intact, the flow throughout the domain was at rest.

When the diaphragm opens, the driver gas jets into the driven tube as a jet centred about the  $x$ -axis. To predict accurately the nature of this jet it was necessary to suppress numerical jetting (Sec. 3.2.3), which can occur along the axis for axisymmetric simulations. It was demonstrated in Section 3.2.3 that numerical jetting can be suppressed if the mesh contains cells which have been stretched in the radial direction. The cell aspect ratio was  $\Delta r/\Delta x = 3.0$  (as recommended by Cambier *et al.* [13]) for all axisymmetric simulations relating to this chapter, unless specified otherwise. Higher aspect ratios were not used because this increases the number of cells in the initial mesh and computational effort. It has also been demonstrated (Löhner [49]) that it is advantageous to use grids with cells stretched in the direction

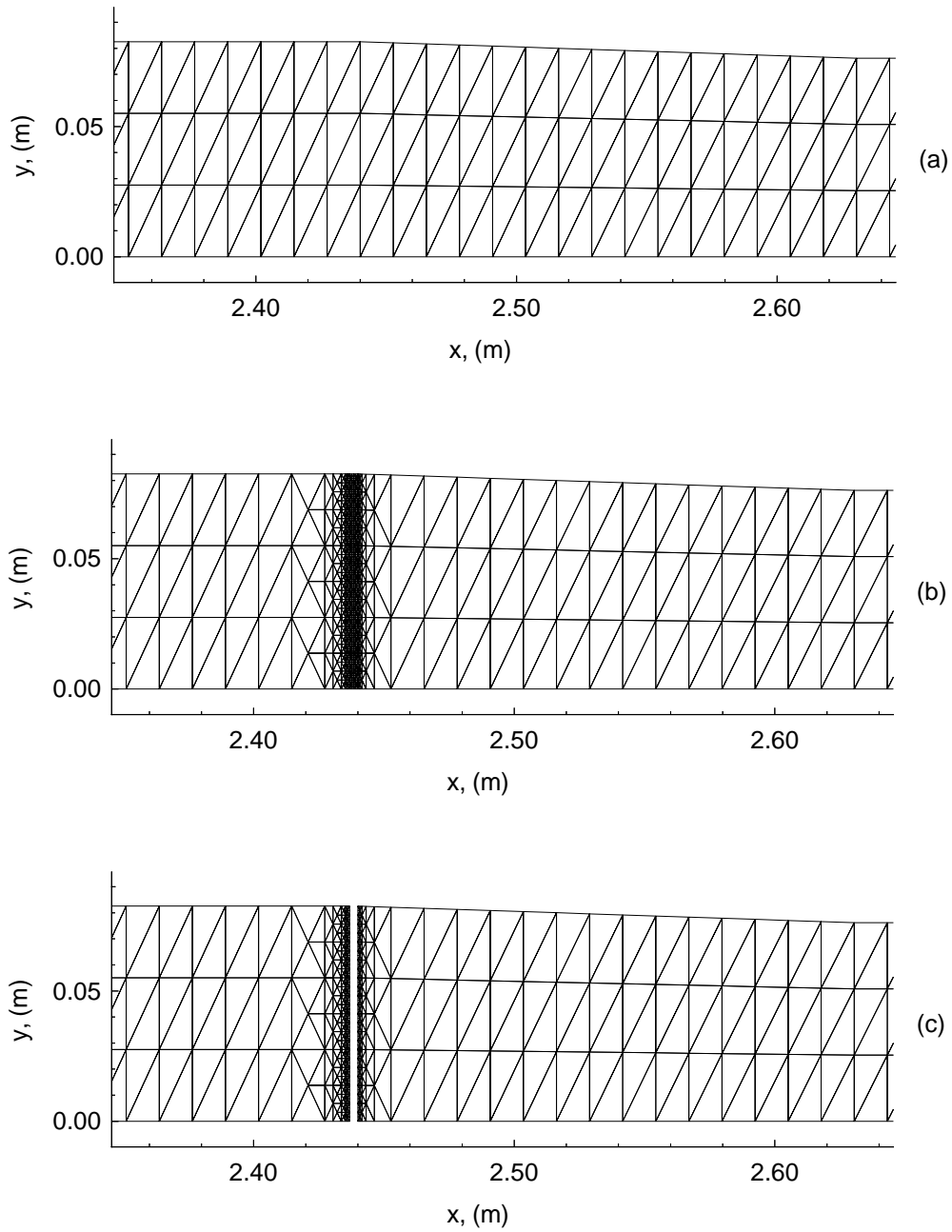


Figure 4.6: Initial discretisation of diaphragm station for the Langley expansion tube.

normal to the flow gradient (directional refinement). This allows the capture of flow features with fewer cells.

## 4.2.2 Opening the diaphragm

At the start of a simulation the status of the cells at the centre of the diaphragm ( $r = 0$ ) is changed from ignored cells to flow cells and given the same initial flow state as the initial driven gas. This effectively creates a circular hole in the centre of the diaphragm causing the two gases to come into contact. The radius of the hole in the diaphragm increases such that the diaphragm area open is proportional to the time since opening. This assumption is based on the experimental work of Rothkopf & Low [72] (Sec. 4.1.1).

It is desirable to have the opening of the diaphragm as continuous as possible. The cells representing the diaphragm were refined until their areas were less than  $5.0 \times 10^{-7} \text{ m}^2$ , which caused the opening to occur in 48 steps. The resolution of the diaphragm opening is significantly higher than in the numerical work of Satofuka [74] (10 cells) and Vasil'ev & Danil'chuk [87] (20 cells).

The opening time of the diaphragm for the Langley expansion tube was not measured by Miller & Jones. However, Miller & Jones did use the method of reference [96] to estimate the opening time to be 500 microseconds. Previous numerical simulations [55] of the experimental conditions used by Miller & Jones found that assuming an opening time of 200 microseconds gave the best agreement with the experimental data for the position where the maximum shock speed occurred (see Fig. 24 of Miller & Jones). The influence of the diaphragm opening time on the shock speed is discussed further in Section 5.1.1. The simulations of the Langley expansion tube presented here assume an opening time of 200 microseconds, but the discussion will return to consider the influence of the opening time on the flow development in Section 4.4.3.

## 4.3 Flow development within Langley expansion tube

Figures 4.7 – 4.9 display the density and pressure contours of the simulated flow within the Langley expansion tube for initial condition #2 to time,  $t = 240$  microseconds at 20 microsecond intervals. The minimum cell area was  $5.0 \times 10^{-7} \text{ m}^2$



for the simulation. The meshes at time,  $t = 20$  and 240 microseconds are shown in Figures 4.10 and 4.11 respectively.

The initial shape of the shock wave in Figure 4.7 is spherical until it reflects at the tube wall at approximately 50 microseconds. The shock front and the reflected (transverse) waves interact causing the shock front to become planar within a relatively short distance and the transverse waves to become weaker. Note that the shock wave is not fully planar after 240 microseconds in Figure 4.9. In Section 4.4.2, the flow development is examined at later times for a different condition ( $P_4/P_1 = 1000$ ), and it can be clearly seen that the shock front has become planar after 400 microseconds (seven tube diameters). These observations of the shock front formation are similar to those made from previous numerical [13, 87] and experimental work [28] (Sec. 4.1.2).

The initial shape of the contact surface is convex when viewed from the downstream end due to the diaphragm initially opening at the centre. At approximately 100 microseconds an oblique upstream-facing shock develops, redirecting the radially expanding driver gas along the tube wall (Fig. 4.12). This causes the pressure of the flow behind the contact surface to be higher at the wall than at the centre. This region of higher pressure gas accelerates the contact surface at the wall relative to the centre. The contact surface eventually becomes concave when viewed from the downstream end. The evolution of the contact surface is similar to that observed in the previous numerical studies. Note that the study of Cambier *et al.* [13] included viscous effects which slowed the contact surface at the walls, but the jetting of the contact surface near the walls relative to the centre of the tube was evident.

The grid convergence of the solution at  $t = 240$  microseconds was studied (Fig. 4.13). The contact surface becomes sharper and finer detail can be seen as the resolution of the simulation increases. Note that there appears to be a small amount of jetting of the CS at the centre of the tube. Unfortunately, at this stage, it is not possible to determine whether this structure is physical due to the possibility that it may be numerical jetting. To determine the nature of this structure it would be necessary to either develop an axisymmetric flow solver which does not exhibit numerical jetting, or perform a three-dimensional simulation. The later option would require a major computational effort. However, the basic shape of the contact surface does not change as the resolution increases. This provides some confidence that the simulation has adequately captured the essential processes driving the development of the flow.

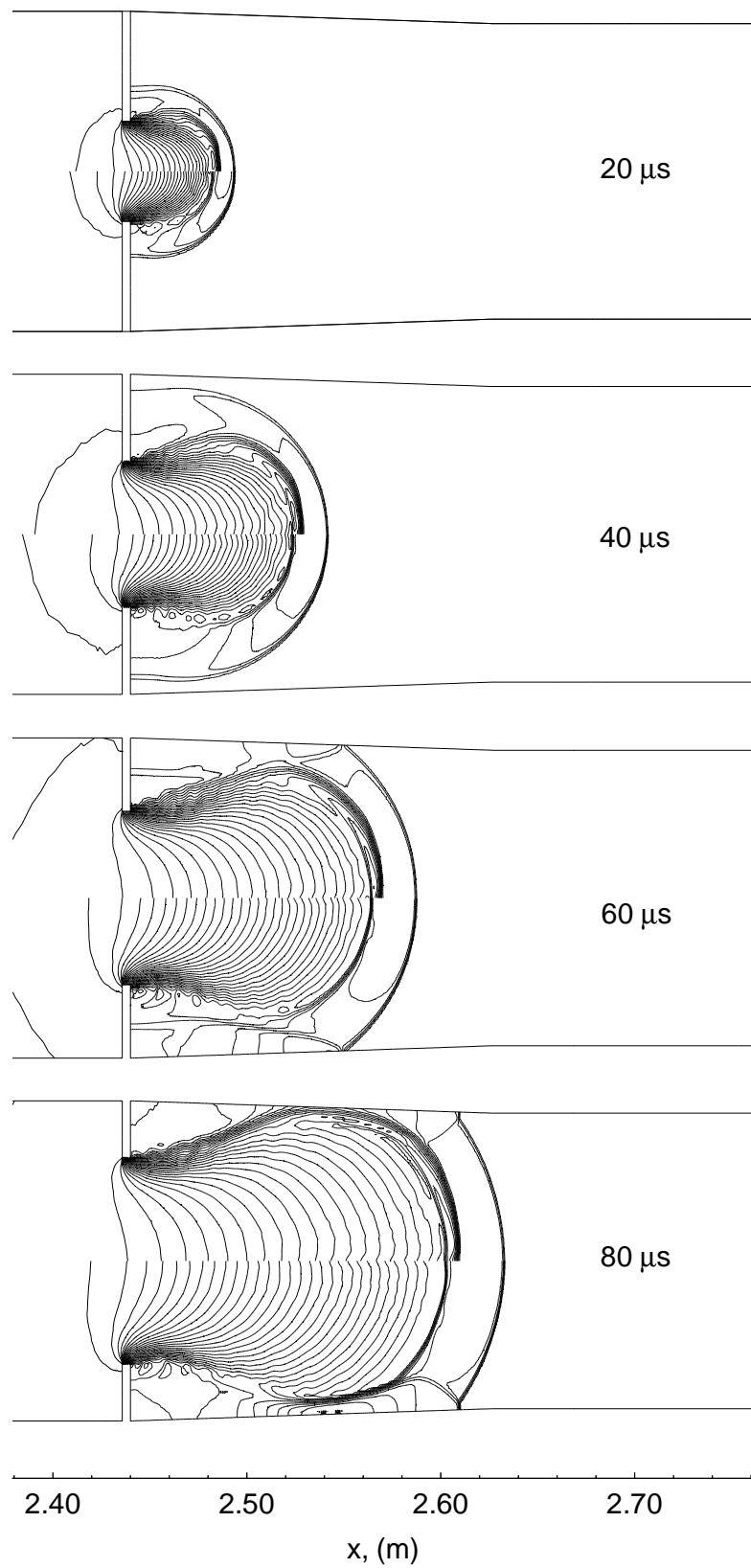


Figure 4.7: Time history of density (top half) and pressure (bottom half) contours for simulation of the Langley expansion tube (condition # 2) from 20 to 80 microseconds.

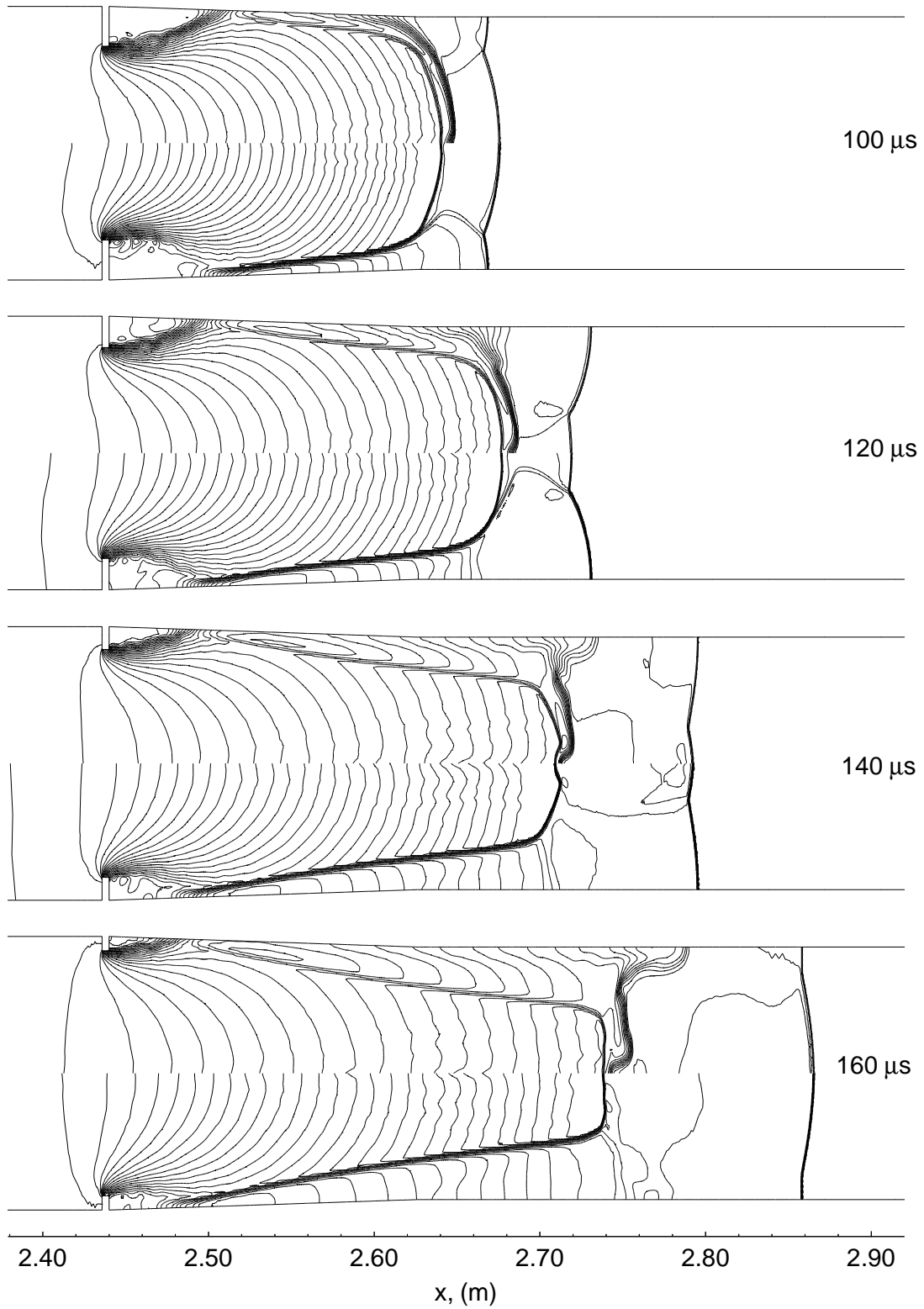


Figure 4.8: Time history of density (top half) and pressure (bottom half) contours for simulation of the Langley expansion tube (condition # 2) from 100 to 160 microseconds.

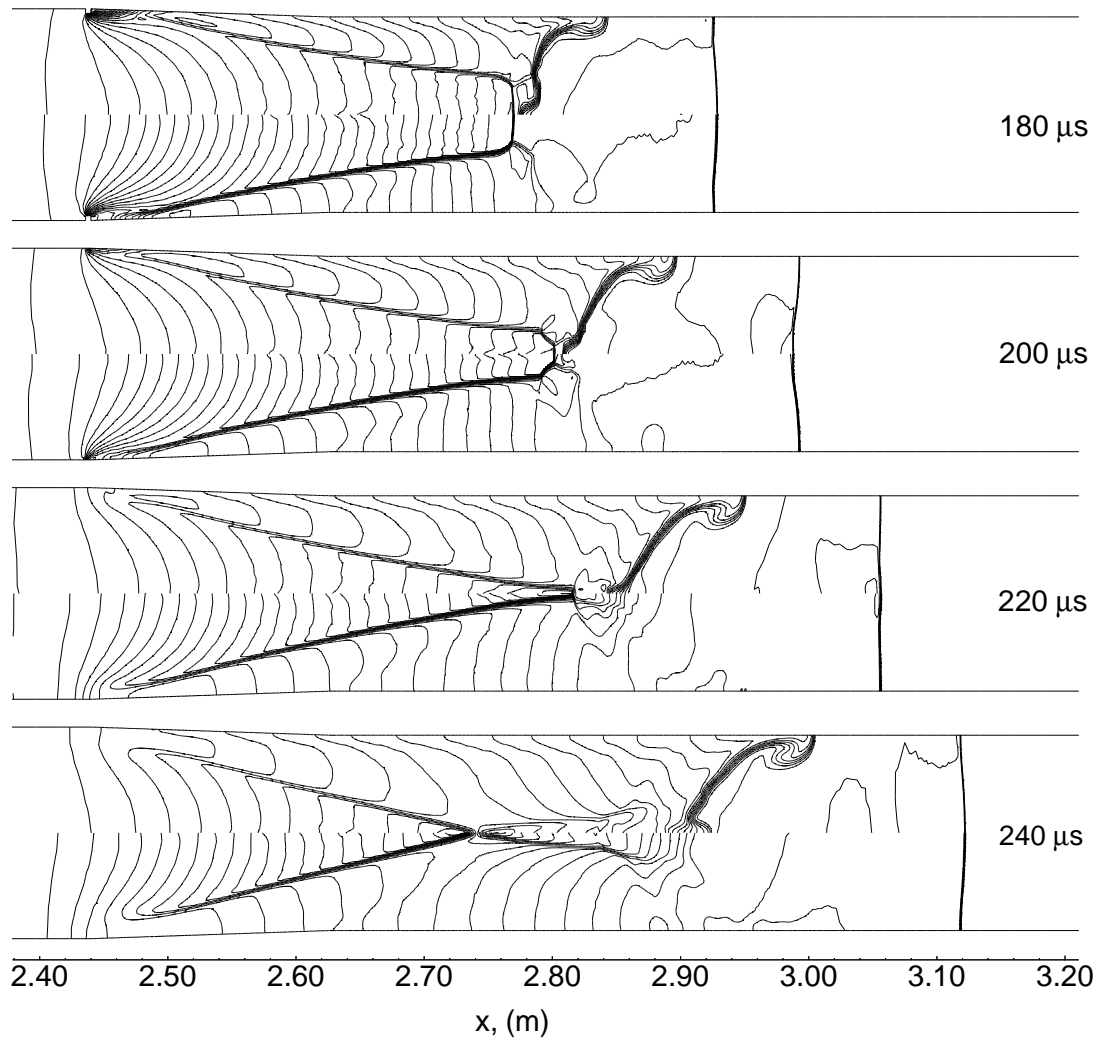


Figure 4.9: Time history of density (top half) and pressure (bottom half) contours for simulation of the Langley expansion tube (condition # 2) from 180 to 240 microseconds.

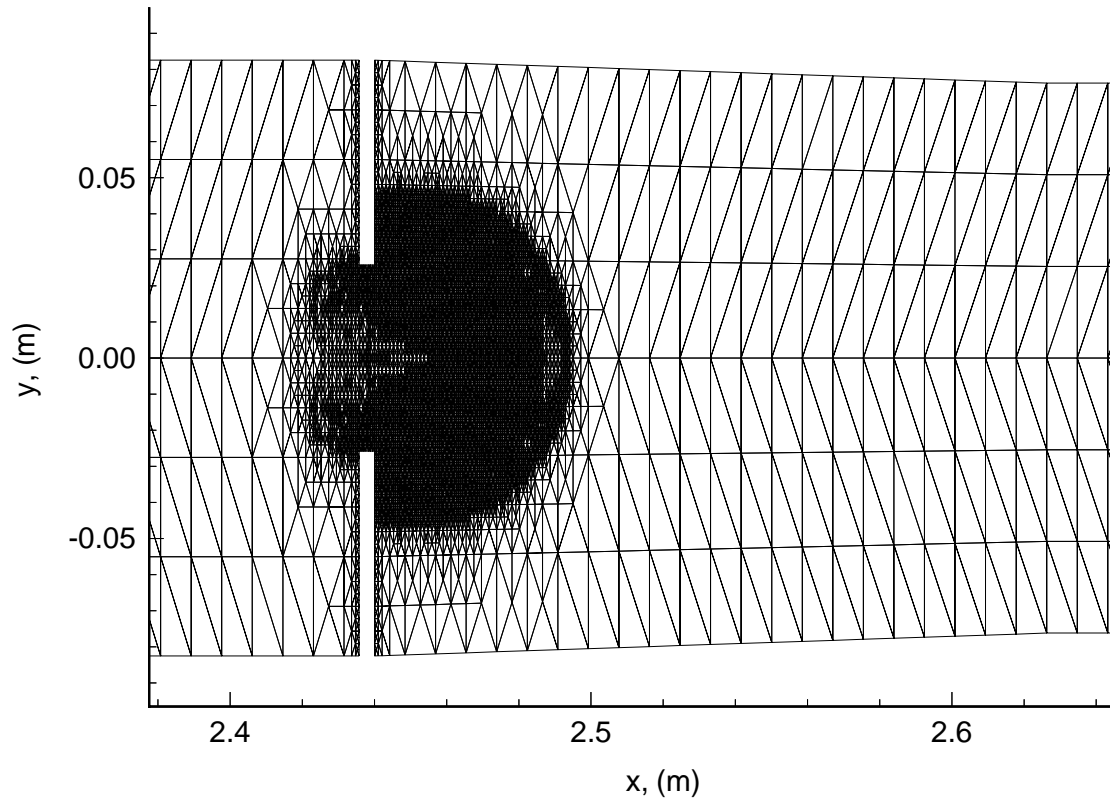


Figure 4.10: Computational mesh from the simulation of the Langley expansion tube at time,  $t = 20$  microseconds.

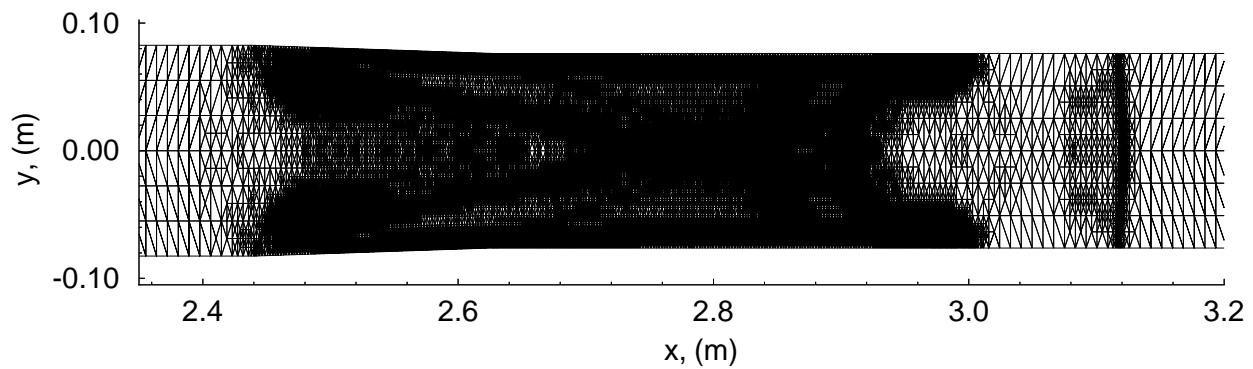


Figure 4.11: Computational mesh from the simulation of the Langley expansion tube at time,  $t = 240$  microseconds.

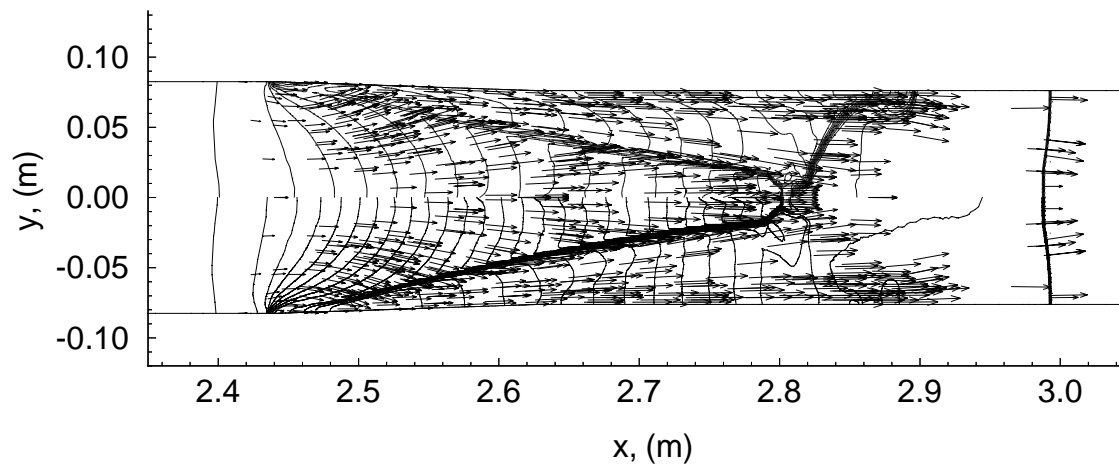


Figure 4.12: Velocity vectors at 200 microseconds for flow within the Langley expansion tube. Density (top half) and pressure (bottom half) contours are also shown.

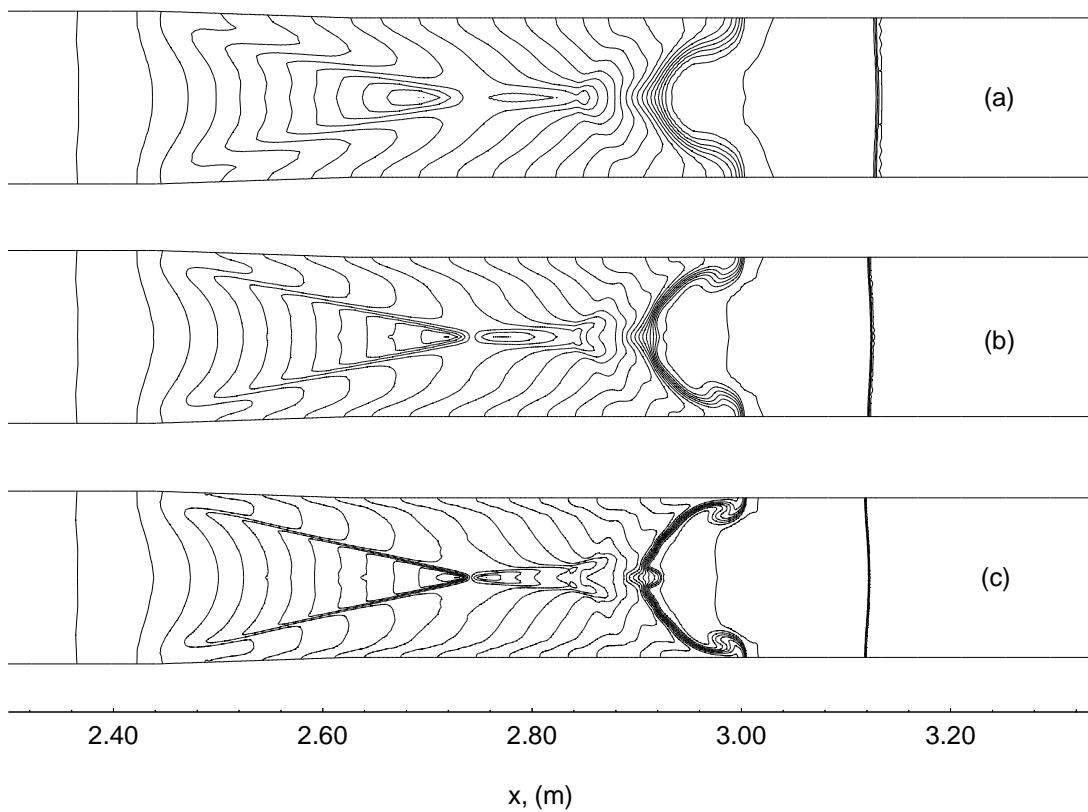


Figure 4.13: Density contours at 240 microseconds for the Langley expansion tube at various mesh resolutions for condition #2. The simulations were performed with a minimum cell area of (a)  $8.0 \times 10^{-6}$ , (b)  $2.0 \times 10^{-6}$ , and (c)  $5.0 \times 10^{-7} \text{ m}^2$ .

The density and pressure contours of the simulated flow within the Langley expansion tube for initial condition # 1 ( $P_4/P_1 = 1014.5$ ) to time,  $t = 240$  microseconds at 20 microsecond intervals are displayed in Figure 4.14. The minimum cell area was  $2.0 \times 10^{-6} \text{ m}^2$  for this simulation. The development of the primary shock wave is similar for both initial conditions, #1 and # 2 ( $P_4/P_1 = 10145$ ), with the shock wave becoming planar earlier for the higher initial pressure ratios. Conversely, the development of the contact surface does vary and is discussed further in Section 4.4.

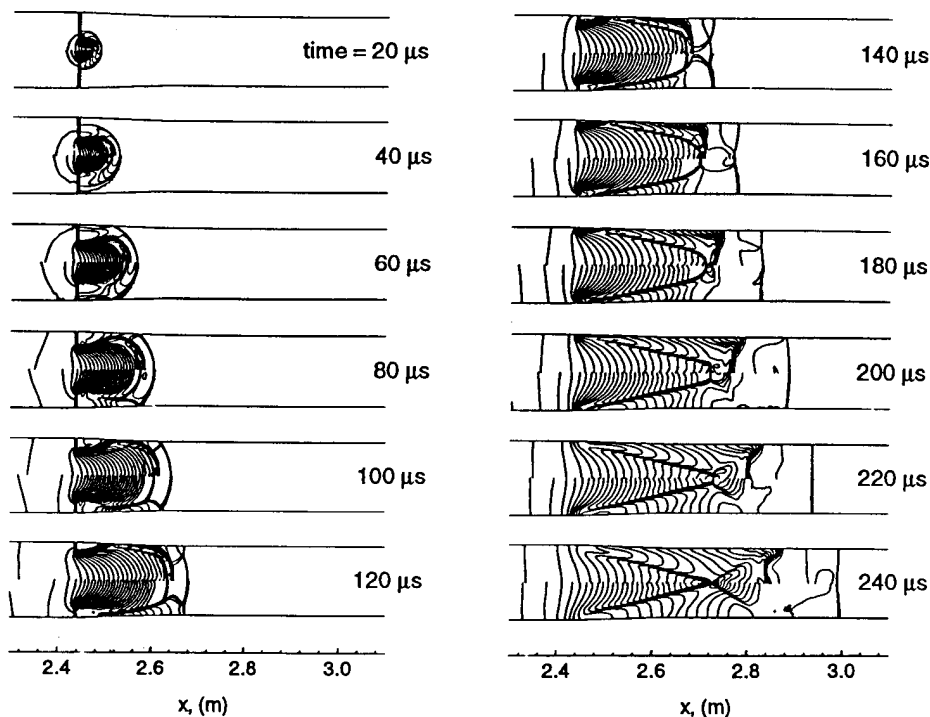


Figure 4.14: Flow development within the Langley expansion tube for initial condition #1. The diaphragm opening time is 200 microseconds. Minimum cell area was  $2.0 \times 10^{-6} \text{ m}^2$  for the simulation. The upper half of each frame shows density contours, the lower half shows pressure contours.

### 4.3.1 Shock tube geometry and equation of state

Solutions for a constant area shock tube for initial condition #2 at 200 microseconds are shown in Figure 4.15. The Redlich-Kwong equation of state was assumed for the solution (a), and perfect gas for the solution (b). The minimum cell area was  $1.0 \times 10^{-6} \text{ m}^2$ . It can be seen that the qualitative differences in the solutions are small, that is, the choice of equation of state had little effect on the flow development. The two solutions are almost identical to the solution for the Langley expansion tube (Fig. 4.9) at the same time.

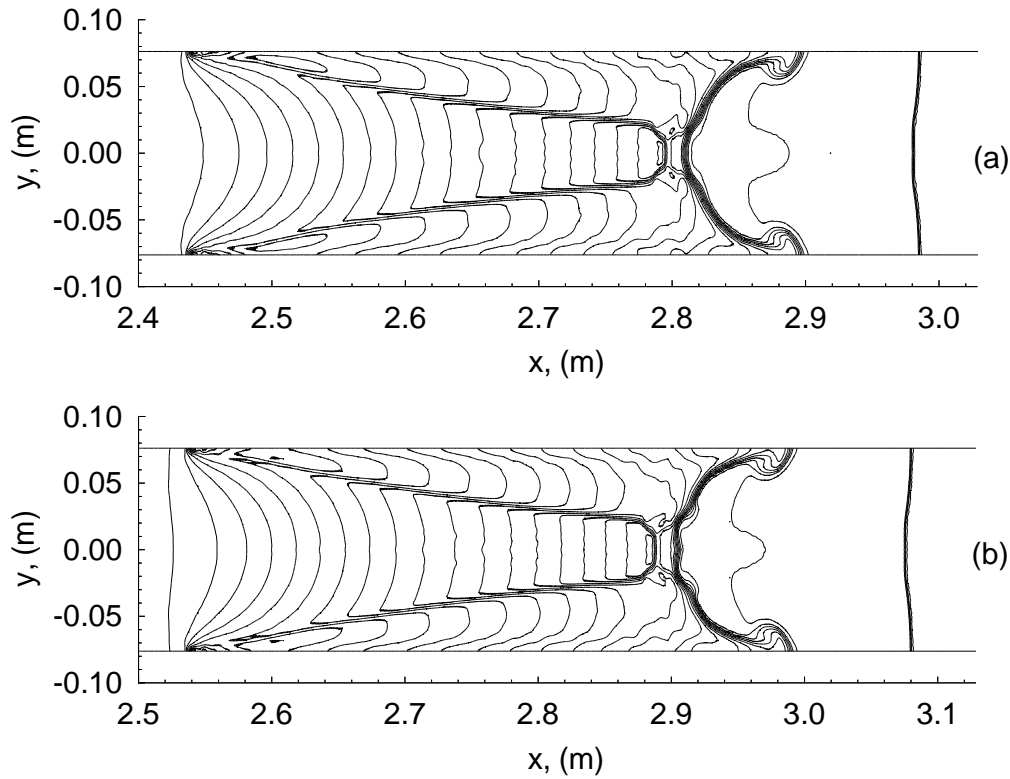


Figure 4.15: Constant area shock tube with initial condition #2, (a) Redlich-Kwong equation of state used, and (b) perfect gas assumed. Density contours only.

## 4.4 Contact surface

In this section, the development of the contact surface (CS) as a function of the operating condition is examined. The shape of the contact surface is important for shock tube and expansion tube operation because it marks the boundary between the driver gas and the test gas. The operation of a reflected shock tunnel differs from an expansion tube in that the test gas is stagnated at the secondary diaphragm and then undergoes a steady expansion through a nozzle (for more information on reflected shock tunnels the reader is referred to Stalker [77]). It has been speculated that one possible cause of contamination of the test gas by the driver gas within reflected shock tubes, is the jetting of the driver gas into the test gas when the reflected shock from the secondary diaphragm interacts with the CS between the driver and test gas [17]. Chue & Itoh [17] and Wilson *et al.* [94] performed simulations of this process assuming that the CS is planar prior to interaction with the reflected shock, however, the simulations of Cambier *et al.* [13] and Vasil'ev & Danil'chuk [87] demonstrated that the CS is not planar. The effect of the distortion of the CS on its interaction with the reflected shock and the contamination of the test gas is presently unknown but given the strong instabilities that occur upon shock reflection, its shape at shock reflection is assumed to have a significant effect upon



the subsequent mixing and contamination of the test gas.

#### 4.4.1 Initial pressure ratio

The time history of density and pressure contours for the Langley expansion tube for initial condition #2 ( $P_4/P_1 = 10145$ ) is shown in Figures 4.7 – 4.9, and for initial condition #1 ( $P_4/P_1 = 1014.5$ ) in Figure 4.14. The development of the flow within a constant area shock tube for initial pressure ratios of 10 and 100 are shown in Figures 4.16 and 4.17. Note that, in the previous section, it was demonstrated that there is little difference between the simulated flow within the Langley expansion tube geometry and for a constant area shock tube. The diameter of the constant area shock tube was 152.4 mm and the diaphragm was located at  $x = 2.54$  m. The initial driven gas condition was,

$$\rho = 0.001 \text{ kg/m}^3, P_4 = 623.1 \text{ Pa}, u_4 = v_4 = 0$$

for all initial conditions. The gas was assumed to be perfect helium ( $\gamma = 1.667$ ) and the initial temperature of the driver gas and the driven gas was 300 K. The minimum cell area was  $2.5 \times 10^{-7} \text{ m}^2$  for these simulations.

From these figures it can be seen, that the higher the initial pressure ratio, the greater the strength of the radial expansion, and the shorter the distance downstream from the diaphragm where the contact surface initially interacts with the tube walls. When the initial pressure is high ( $P_4/P_1 = 10145$ , Figs. 4.7 – 4.9;  $P_4/P_1 = 1014.5$ , Fig. 4.14; and  $P_4/P_1 = 100$ , Fig. 4.17), an oblique upstream facing shock is formed after the contact surface arrives at the tube wall. The presence of the oblique shock causes the jetting of the CS along the tube walls as described in Section 4.3 and, as the strength of the oblique shock increases with the initial pressure ratio, so does the penetration of the CS at the wall.

There is no oblique shock present in the solution for  $P_4/P_1 = 10$  (Fig. 4.16) and consequently there is no jetting of the CS at the walls. Note that Vasil'ev & Danil'chuk [87] performed a similar two-dimensional planar simulation with  $P_4/P_1 = 40$ , and observed oblique shocks and CS jetting at the walls. This suggests that the minimum initial pressure ratio required to establish an oblique shock wave is between 10 and 40.

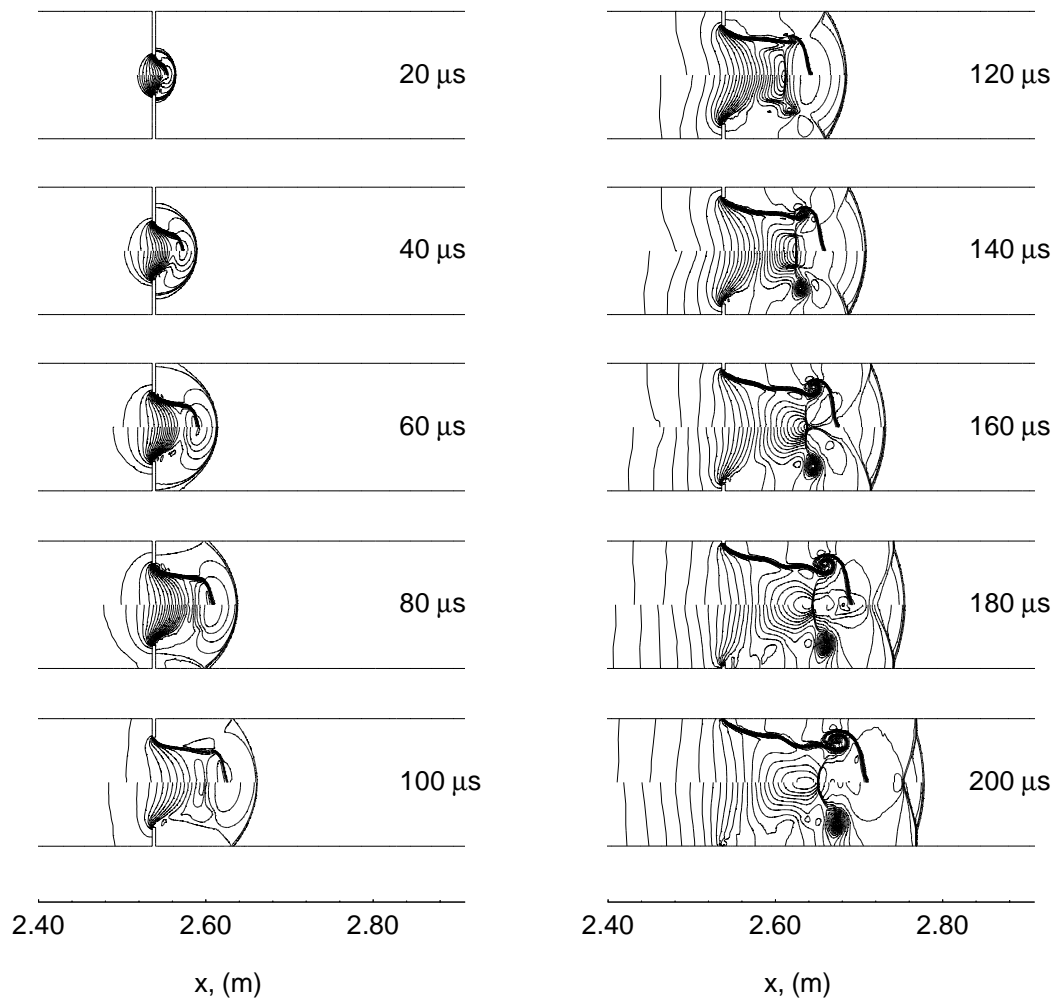


Figure 4.16: Early flow development in a constant area shock tube with gradual diaphragm opening. The initial pressure ratio is 10 and the opening time is 200 microseconds. The upper half of each frame shows density contours, the lower half shows pressure contours.

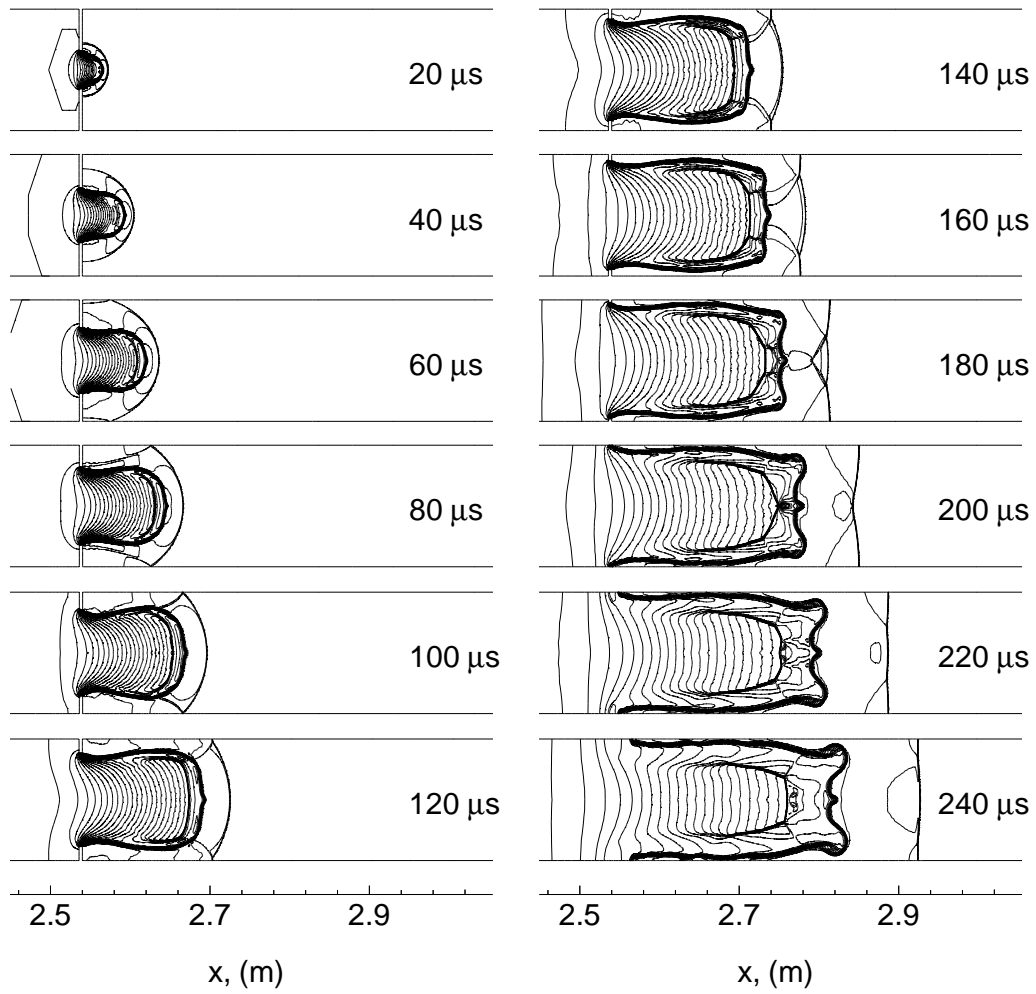


Figure 4.17: Early flow development in a constant area shock tube with gradual diaphragm opening. The initial pressure ratio is 100 and the opening time is 200 microseconds. Density contours only.

### 4.4.2 Flow development after diaphragm is fully open

The development of the flow after the diaphragm was fully opened was investigated for the constant area shock tube with  $P_4/P_1 = 1000$  (Fig. 4.18). While the diaphragm is opening, a pocket of unexpanded gas is trapped immediately upstream of the partially opened diaphragm. When the diaphragm is fully opened, this pocket of heavier gas ( $2.7 \text{ m} < x < 2.9 \text{ m}$ ,  $t = 400 \text{ } \mu\text{s}$ ) accelerates relatively slowly down the tube and acts as a bluff body causing the flow to be similar to a Laval nozzle flow. This observation was also made by Vasil'ev & Danil'chuk [87]. The oblique shock is no longer present in the flow at time,  $t = 400$  microseconds.

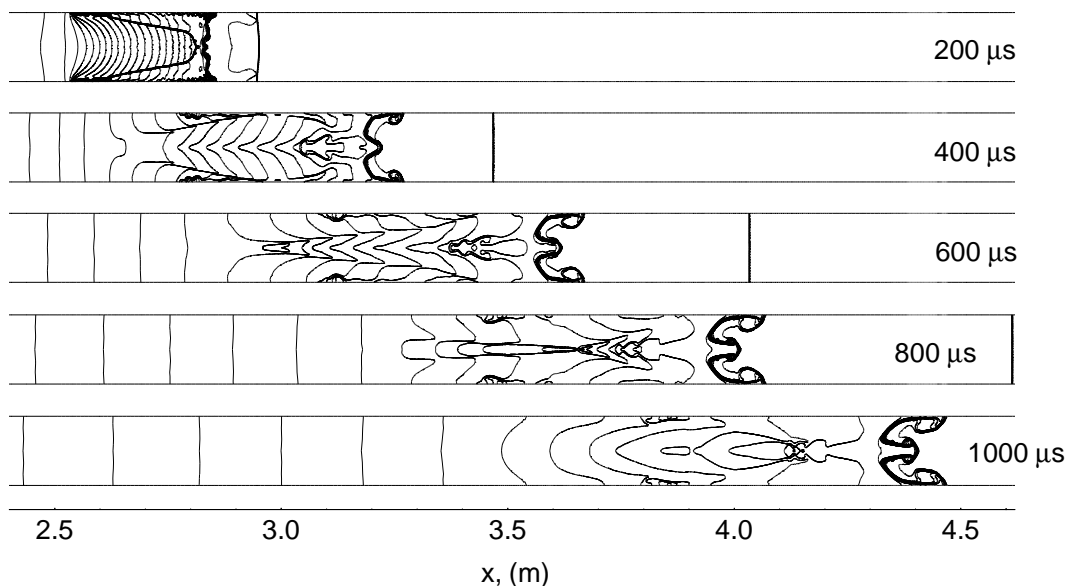


Figure 4.18: Flow development within constant area shock tube after diaphragm is fully opened,  $P_4/P_1 = 1000$ . Diaphragm opening time = 200 microseconds and minimum cell area =  $5.0 \times 10^{-7} \text{ m}^2$ . Density contours only.

The shape of the contact surface 1.0 millisecond after the initial diaphragm opening was investigated. Figures 4.19 – 4.21 display density contours of the CS at various mesh resolutions for the initial pressure ratios 10, 100, and 1000 respectively. The opening time of the diaphragm was 200 microseconds for each case. Grid convergence was achieved for  $P_4/P_1 = 10$  but not for 100 or 1000. The highest resolution simulations for  $P_4/P_1 = 100$  required 71 real days (approximately 24 computational days on a single R8000 processor).

It is interesting to note that it was possible to achieve grid convergence for  $P_4/P_1 = 10145$  at 200 microseconds (Fig. 4.13), but not for a lower initial pressure ratio ( $P_4/P_1 = 100$ ) at 1000 microseconds. It would appear that the error due to numerical

jetting grows with time, hence reducing the accuracy of the numerical solutions at later times.

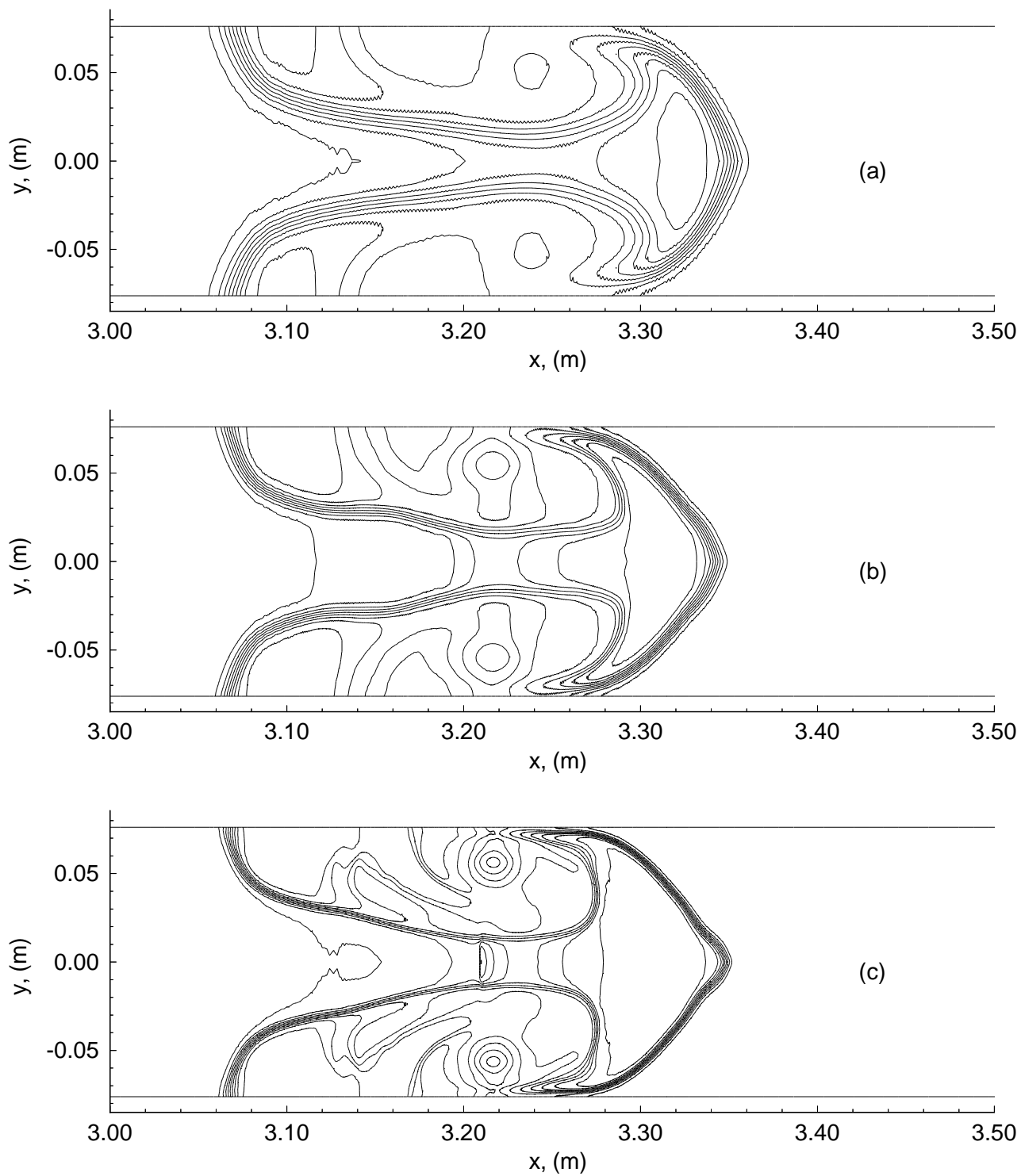


Figure 4.19: Density contours of the contact surface at 1000 microseconds for  $P_4/P_1 = 10$ . The opening time was 200 microseconds. The minimum cell areas for the simulations were: (a)  $4.0 \times 10^{-6}$ , (b)  $1.0 \times 10^{-6}$ , and (c)  $2.5 \times 10^{-7} \text{ m}^2$ .

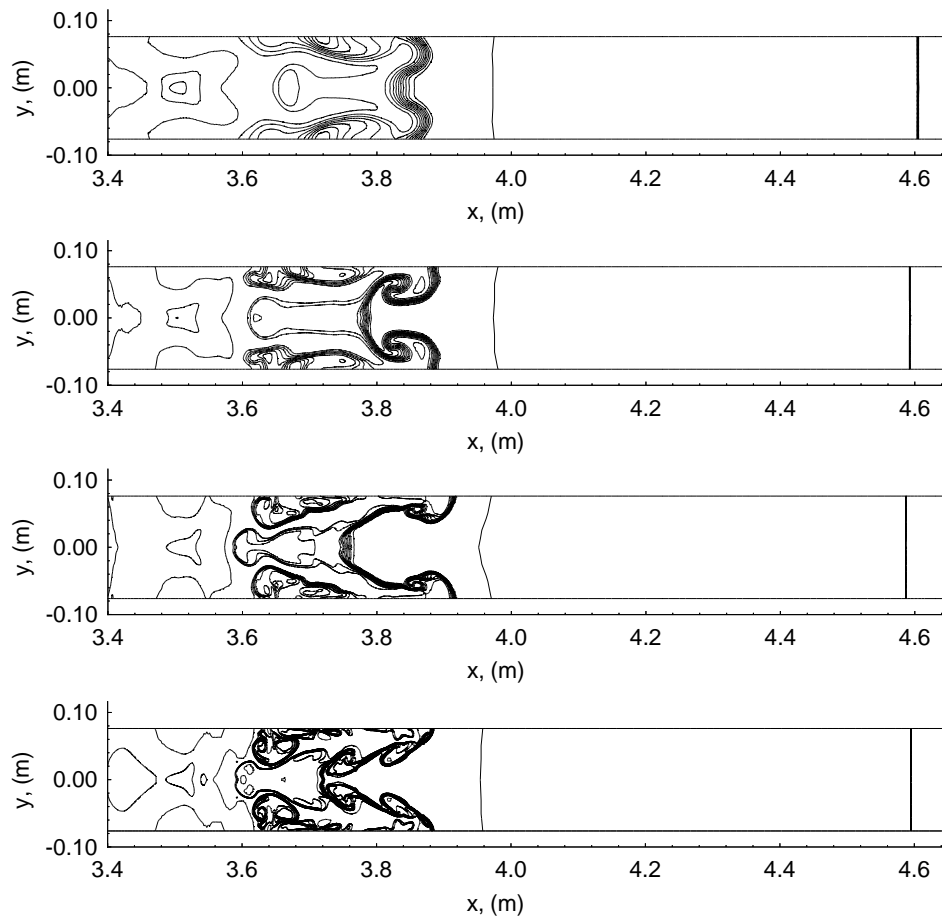


Figure 4.20: Density contours of the contact surface at 1000 microseconds for  $P_4/P_1 = 100$ . The opening time was 200 microseconds. The minimum cell areas for the simulations were: (a)  $4.0 \times 10^{-6}$ , (b)  $1.0 \times 10^{-6}$ , (c)  $2.5 \times 10^{-7}$  and (d)  $6.25 \times 10^{-8}$  m<sup>2</sup>.

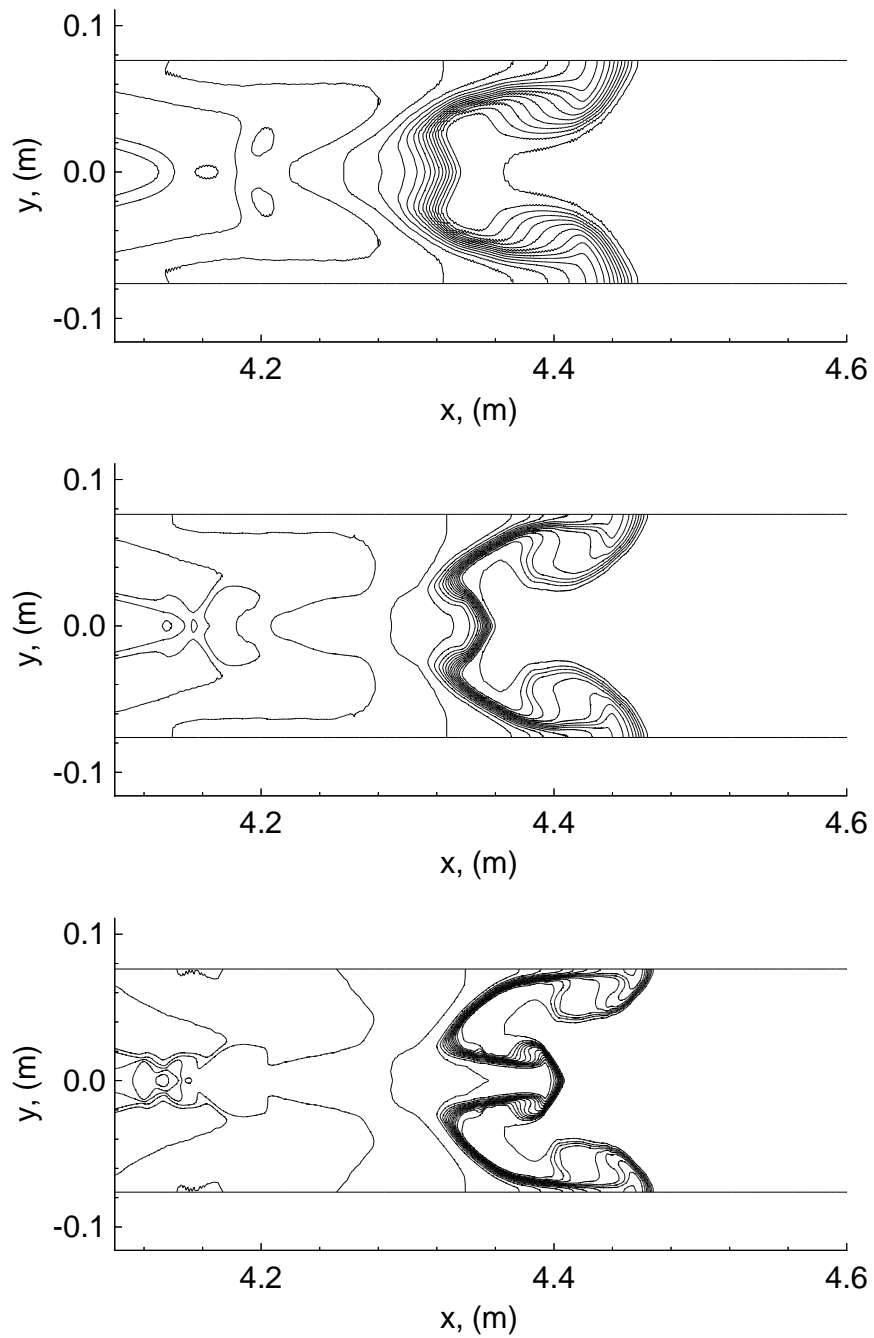


Figure 4.21: Density contours of the contact surface at 1000 microseconds for  $P_4/P_1 = 1000$ . The opening time was 200 microseconds. The minimum cell areas for the simulations were: (a)  $4.0 \times 10^{-6}$ , (b)  $1.0 \times 10^{-6}$ , and (c)  $2.5 \times 10^{-7}$  m<sup>2</sup>.



It is strongly suspected that “numerical jetting” (as opposed to a genuine physical jetting) is present in the solutions at  $t = 1.0$  millisecond for  $P_4/P_1 = 100$  and 1000. A simulation was performed with the cell aspect ratio,  $\Delta r/\Delta x = 1.0$  and the minimum cell of  $1.0 \times 10^{-6} \text{ m}^2$  (Fig. 4.22). The solution is similar to a higher resolution solution with a cell aspect ratio  $\Delta r/\Delta x = 3.0$ . It has been demonstrated [13] that numerical jetting can be aggravated by increasing the mesh resolution or by using cells with a low cell aspect ratio. The presence of numerical jetting in the solutions would explain why the high resolution solution with a cell aspect ratio,  $\Delta r/\Delta x = 3.0$  is similar to the lower resolution solution with a cell aspect ratio,  $\Delta r/\Delta x = 1.0$ .

Note that the jetting at the contact surface for  $P_4/P_1 = 100$  is in the opposite direction to the flow. This was also the case for the ideal shock tube studied in Section 3.2.3. However, the jetting for  $P_4/P_1 = 1000$  (Fig. 4.21) is in the same direction as the flow. This would appear to suggest that it is possible for numerical jetting to occur in either direction. The reason for this unknown.

Two-dimensional simulations of a gradually opening slit ( $P_4/P_1 = 100$ ) were performed. The cell aspect ratio was 1.0. The density contours at the contact surface for three different mesh resolutions are shown in Figure 4.23 where it can be seen that the solution is converging. It can be concluded that the jetting at the axis for the previous solution is enhanced by the axisymmetric formulation.

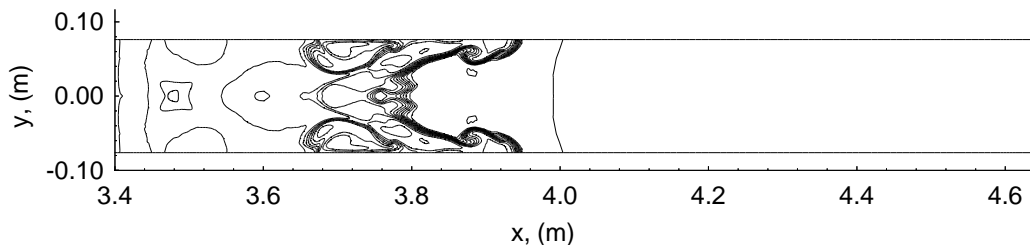


Figure 4.22: Contact surface for constant area shock tube at 1.0 millisecond.  $P_4/P_1 = 100$ , opening time = 200 microseconds, and minimum cell area =  $1.0 \times 10^{-6} \text{ m}^2$ . The cell aspect ratio was 1.0 for the simulation.

### 4.4.3 Diaphragm opening time

Simulations were performed to study the influence of the diaphragm opening time on the shape of the CS (Figs. 4.24 – 4.26). The minimum cell area for these simulations was  $2.0 \times 10^{-6} \text{ m}^2$ .

As discussed in Section 4.4.1, the higher the initial pressure ratio, the greater the

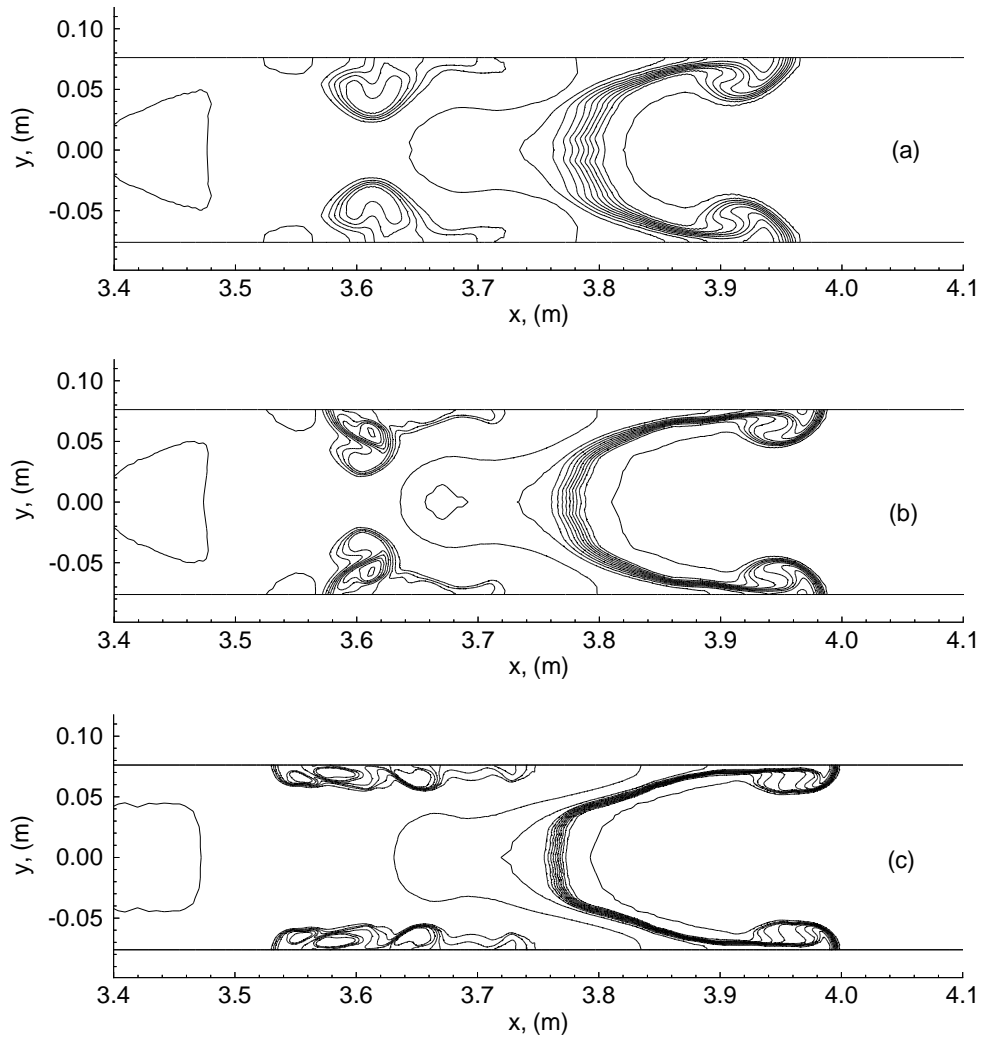


Figure 4.23: Contact surface for constant area *two-dimensional* shock tube at 1.0 millisecond.  $P_4/P_1 = 100$ , opening time = 200 microseconds, at different mesh resolutions: (a)  $4.0 \times 10^{-6}$ , (b)  $1.0 \times 10^{-6}$ , and (c)  $2.5 \times 10^{-7}$ . The cell aspect ratio was 1.0 for the simulation.

radial expansion and the shorter the distance travelled by the CS before it arrives at the tube walls. When the initial pressure ratio is low,  $P_4/P_1 = 10$ , the radial expansion is not strong enough for the CS to reach the tube wall and the CS commences at the partially opened diaphragm and extends downstream into the flow. The area of the CS continues to grow until the diaphragm is fully opened (Fig. 4.24) and the final area increases with opening time.

For higher initial pressure ratios, the arrival of the CS at the tube wall causes the CS to form a surface starting and ending at the tube wall which is not connected to the partially opened diaphragm. Note that some of the driven gas is trapped immediately downstream of the partially opening diaphragm. It is difficult to draw conclusions about how the opening time affects the shape of the CS for  $P_4/P_1 = 100$  and 1000, at time,  $t = 1.0$  millisecond due to the existence of numerical jetting in the solutions. Note that the nature of the jetting that develops as the opening time decreases in Figure 4.26 is similar to the jetting that occurs in Figure 4.21 as the resolution of the simulations increase. This may be due to the stronger physical jetting that occurs at the faster opening times aggravating the numerical jetting in the solution.

Figures 4.27 and 4.28 show the early development of the flow for a constant area shock tube ( $P_4/P_1 = 100$ ) with diaphragm opening times of 157 and 300 microseconds respectively. The minimum cell area for these simulations was  $2.5 \times 10^{-7}$  m<sup>2</sup>. It can be seen that there is little difference in the shape of the CS at time,  $t = 200$  microseconds.

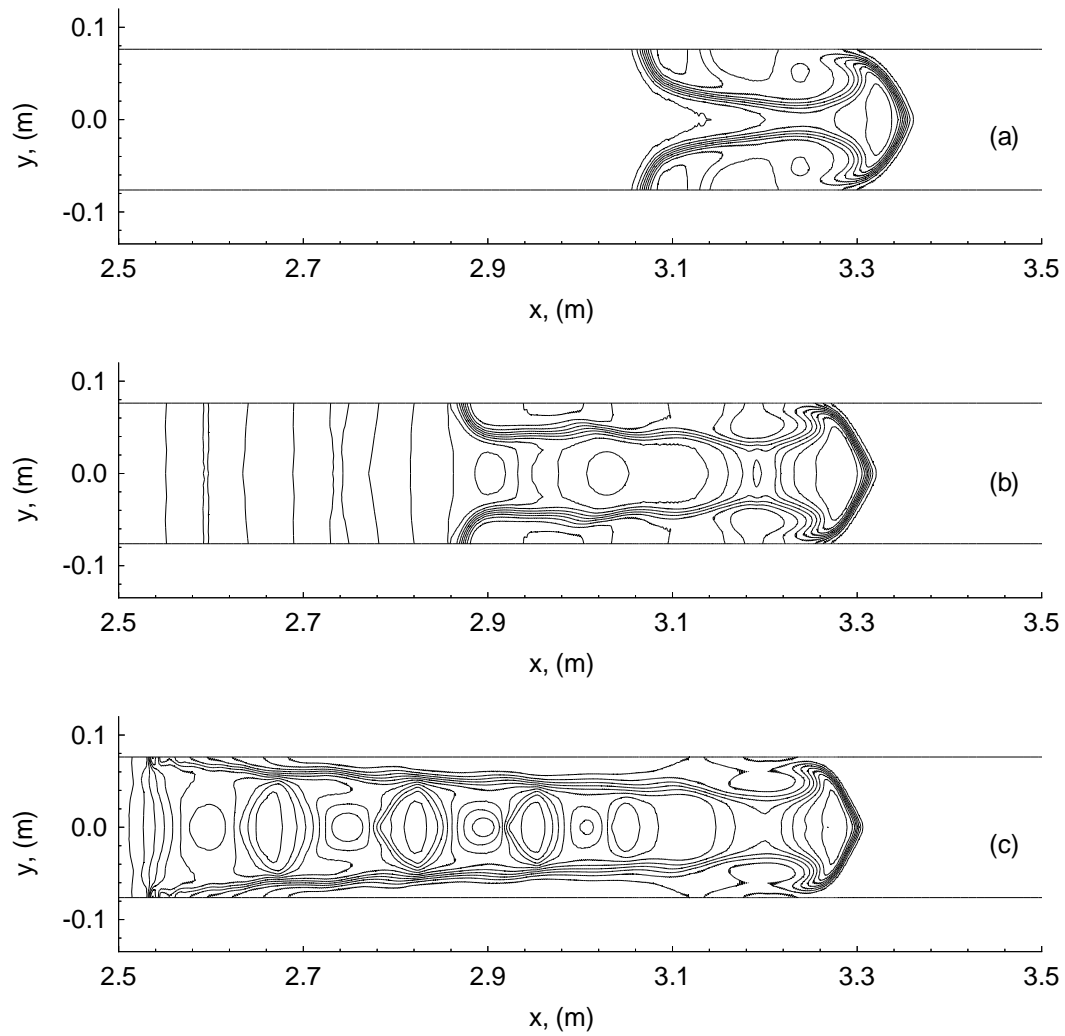


Figure 4.24: Contact surface at 1.0 millisecond for a constant area shock tube ( $P_4/P_1 = 10$ ) for various diaphragm opening times: (a) 200, (b) 500, and (c) 1000 microseconds. Density contours only.

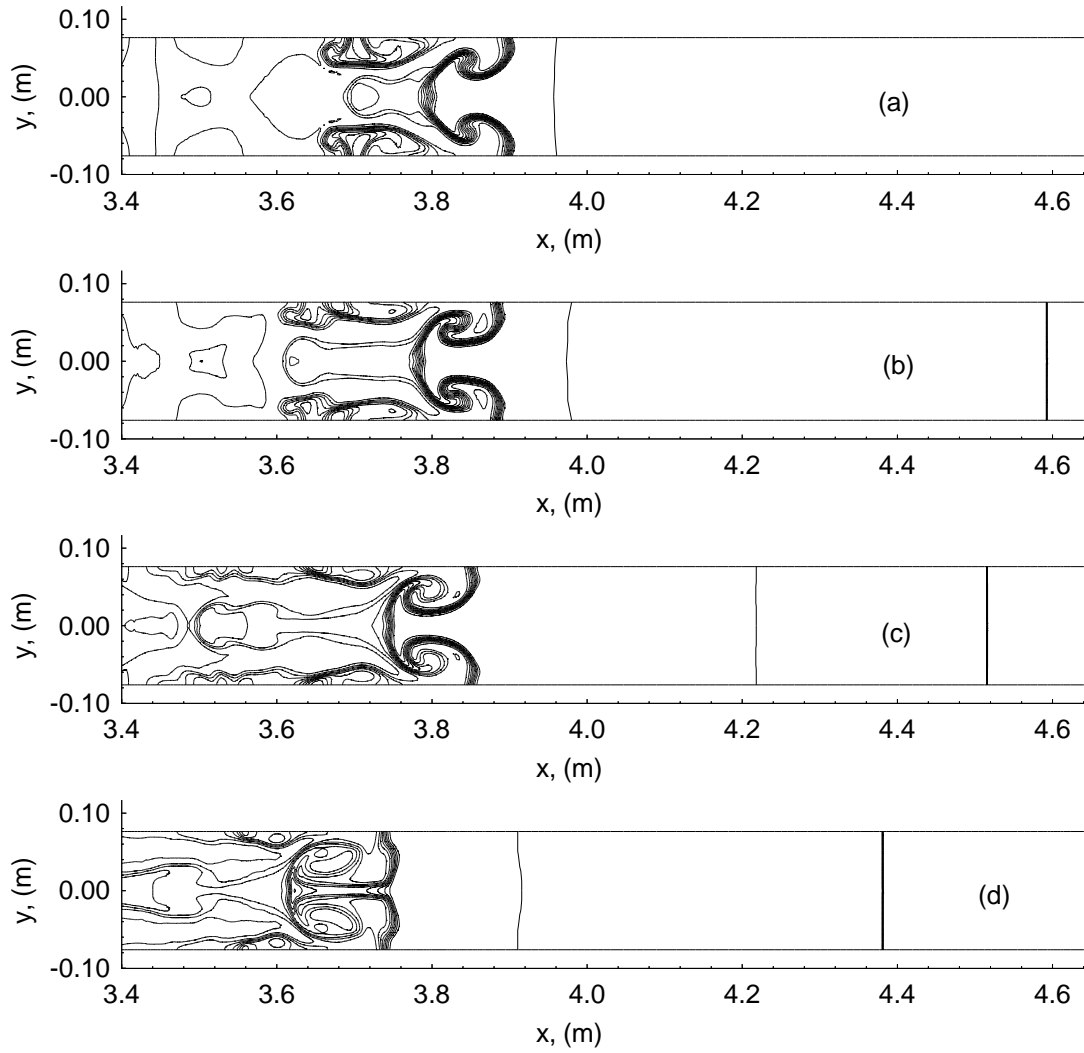


Figure 4.25: Contact surface at 1.0 millisecond for a constant area shock tube ( $P_4/P_1 = 100$ ) for various diaphragm opening times: (a) 157, (b) 200, (c) 300, and (d) 600 microseconds. Density contours only.

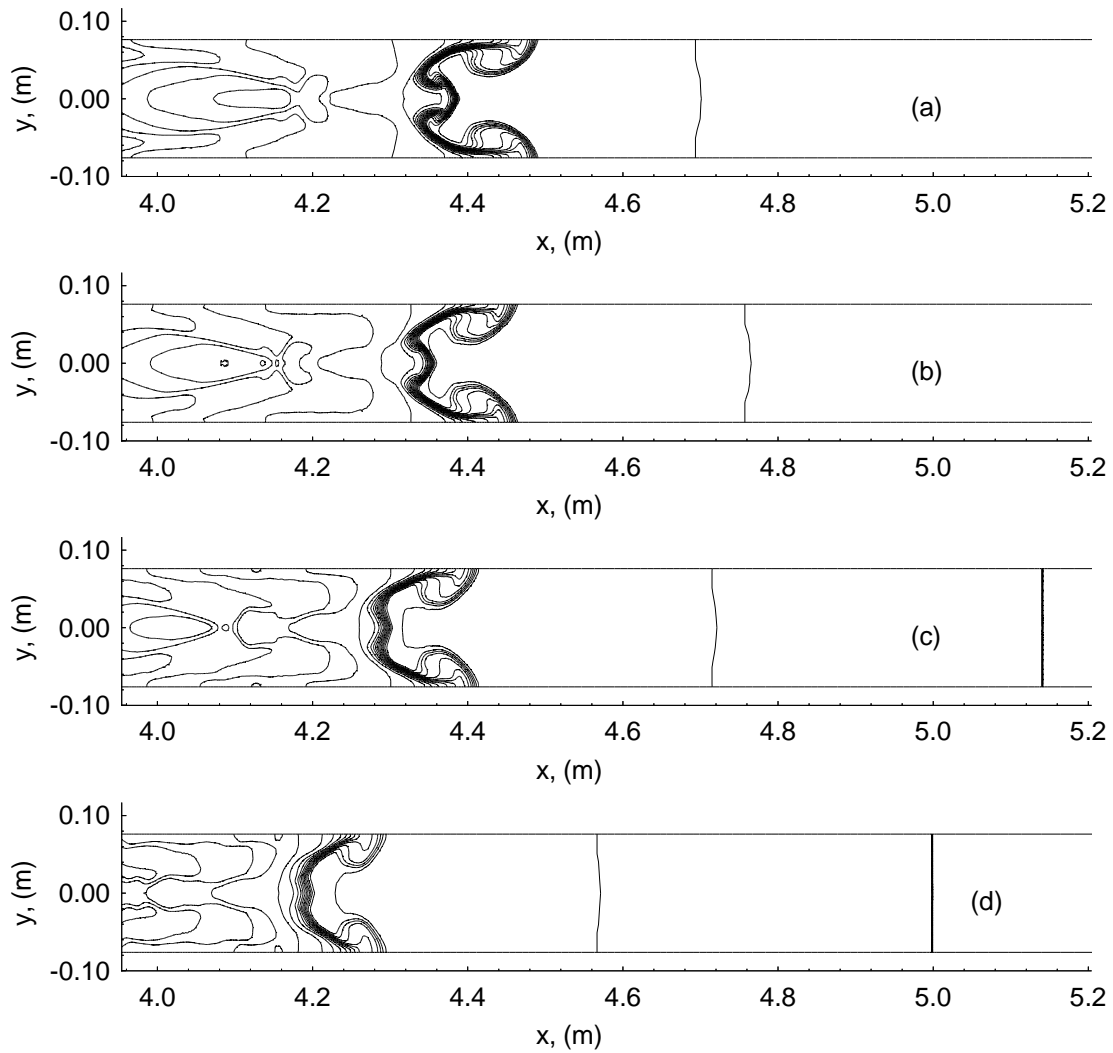


Figure 4.26: Contact surface at 1.0 millisecond for a constant area shock tube ( $P_4/P_1 = 1000$ ) for various diaphragm opening times (a) 150, (b) 200, (c) 300, and (d) 600 microseconds. Density contours only.

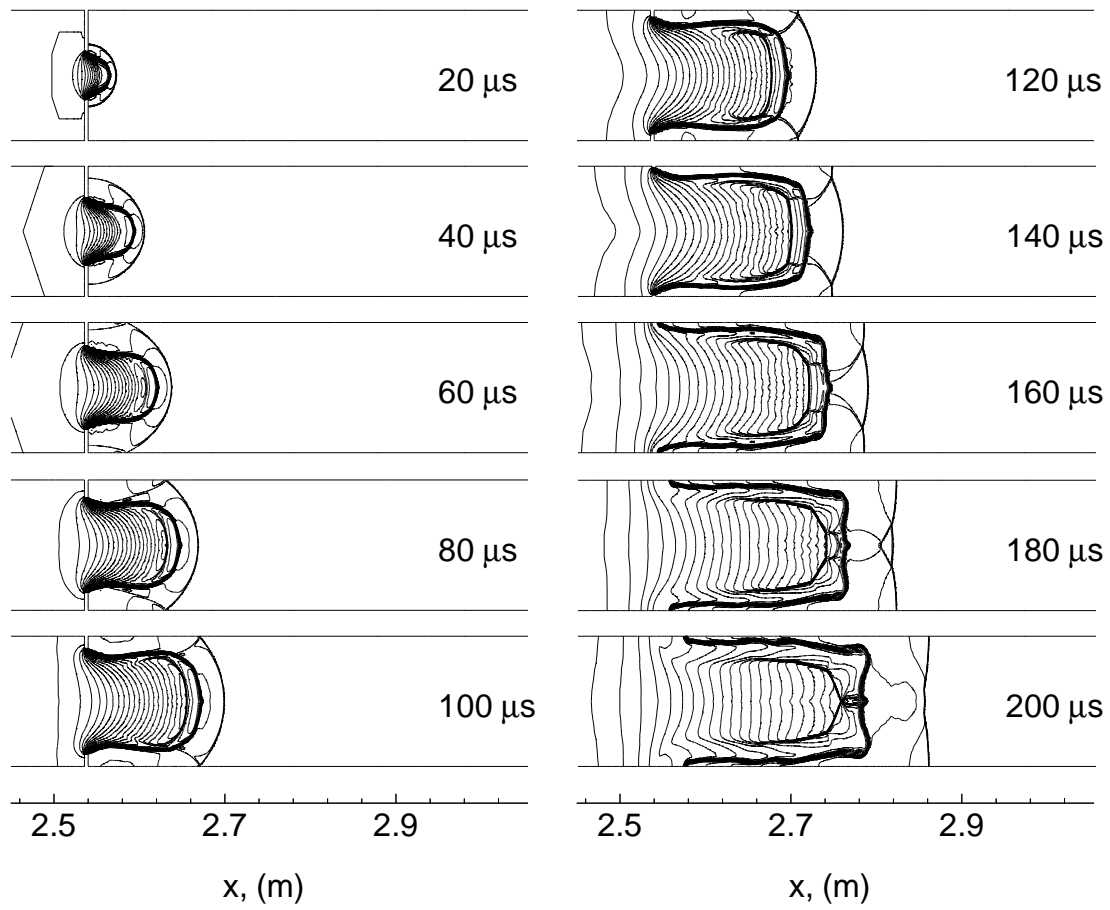


Figure 4.27: Early flow development for a constant area shock tube with  $P_4/P_1 = 100$ . The diaphragm opening time is 157 microseconds. Density contours only.

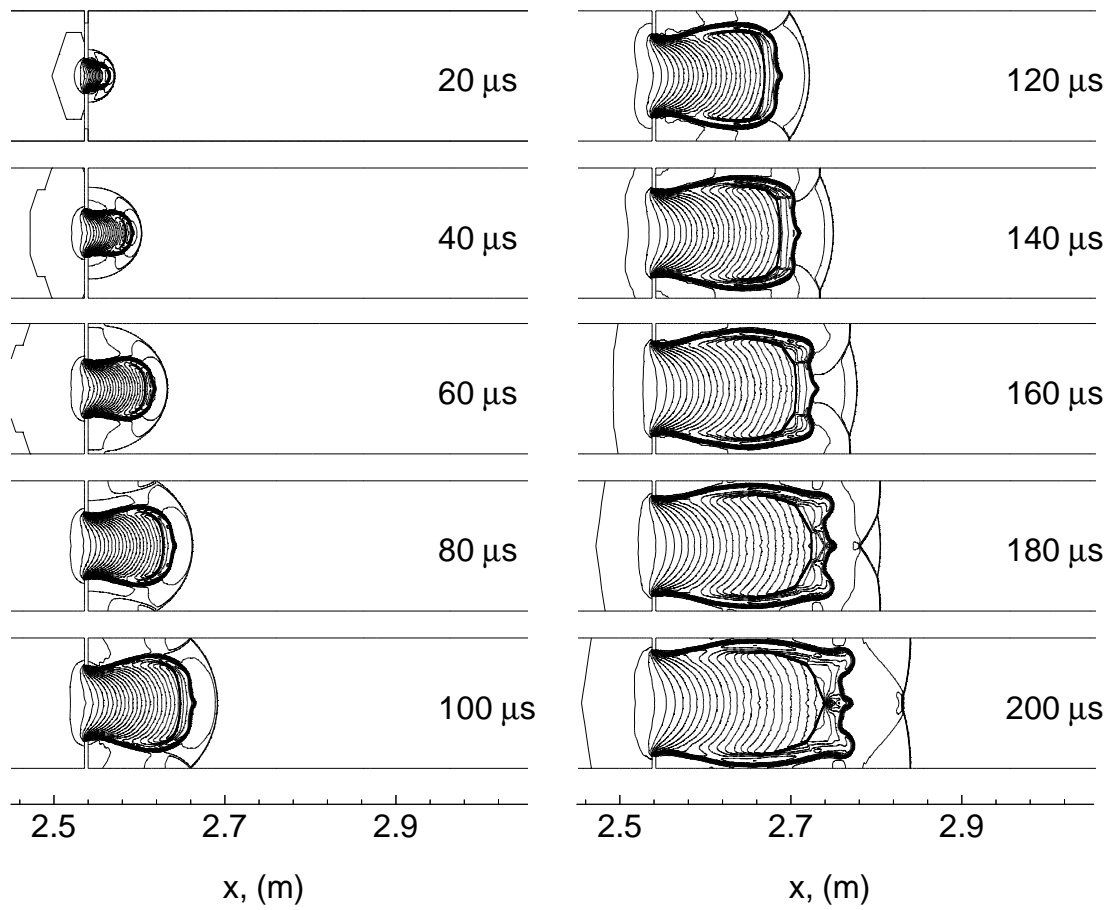


Figure 4.28: Early flow development for a constant area shock tube with  $P_4/P_1 = 100$ . The diaphragm opening time is 300 microseconds. Density contours only.



#### 4.4.4 Rayleigh-Taylor instabilities

Cambier *et al.* [13] discussed the effects that Rayleigh-Taylor instabilities may have on the development of the CS. Taylor [80] showed that a CS between two fluids, experiencing an acceleration perpendicular to their interface is stable if the heavier fluid is *pushing* the lighter fluid and unstable if the opposite is true. Since, for the present conditions, the density of the expanded driver gas, is greater than the shock-processed driven gas, the CS will be stable during an acceleration phase and unstable during a deceleration phase. For an opening time of 200 microseconds the shock wave reaches its maximum speed approximately 1.0 millisecond after the initial opening. It is reasonable to suspect, that for a large percentage of this time the CS is also accelerating, and hence stable.

### 4.5 Summary

Axisymmetric simulations of gas flow within shock tubes with gradually opening diaphragms were performed and the nature of the developing flow was studied in detail. Similar to observations from previous experimental and numerical work, it was observed that the primary shock wave becomes approximately planar and that at high initial pressure ratios ( $P_4/P_1 > 40$ ), an oblique upstream facing shock is formed. This shock redirects the radially expanding flow parallel to the tube walls and causes the CS to jet along the tubes walls.

Unlike previous work, the influence of the initial pressure ratio and diaphragm opening time were examined and found to be important. When the initial pressure was low ( $P_4/P_1 = 10$ ) it was discovered that an oblique shock was not formed, and there was no jetting of the CS along the tube walls. It was also observed that the higher the initial pressure ratio ( $P_4/P_1 \geq 100$ ) the greater the radial expansion, the stronger the oblique shock, and the greater the penetration of the CS along the tube wall.

The diaphragm opening time did not significantly affect the area of the CS for the simulations when  $P_4/P_1 > 10$ . This was because the radially expanding driver gas arrived at the tube walls quickly, separating the CS from the partially opened diaphragm. If the pressure was low,  $P_4/P_1 = 10$ , the radial expansion was not strong enough to separate the CS from the partially opened diaphragm and the area of the CS increased with diaphragm opening time.

Grid convergence was achieved for the shape of the CS at time  $t = 200$  microseconds

for initial pressure ratios of 10, 100, 1014.5, and 10145. At time  $t = 1.0$  millisecond grid convergence was only achieved for  $P_4/P_1 = 10$ . For  $P_4/P_1 \geq 100$ , it is speculated that numerical jetting occurred along the axis, degrading the accuracy of the solutions.



# Chapter 5

## Shock speed

## 5.1 Introduction

In the previous chapter, the results from axisymmetric simulations of shock tubes with gradually opening diaphragm were presented. This chapter examines the speed of the primary shock wave from the same simulations. The computed shock speed is compared with experimental results and estimates from theory.

### 5.1.1 Previous work

The shock speed within an *ideal* shock tube, with instantaneous diaphragm removal and negligible viscous effects, can be determined by solving the unsteady one-dimensional Euler equations. The ideal shock speed has been reported by Duff [23] to overestimate the shock speed within long, thin driven tubes where viscous effects are significant. Conversely, measured shock speeds [91, 55, 32, 59, 92] within “high-performance” (and larger diameter) shock tubes can exceed the ideal shock speed by up to 20% when the initial pressure ratio across the diaphragm is high ( $> 10^3$ ) (Fig. 5.1). The higher than ideal shock speed can be partially explained by considering the wave processes which occur during the gradual opening of a diaphragm.

White [91] developed a theory based on shock formation from compression waves. The model assumes that unsteady isentropic compression waves are formed in the driven gas as the diaphragm gradually opens. The compression waves are then assumed to coalesce into a shock wave some distance downstream from the diaphragm. An upstream-facing expansion is formed to match the flow conditions. This model can predict higher maximum shock speeds than the ideal shock tube model, but it fails to predict the shock front acceleration which has been observed in experiments. As an improvement to the model of White [91], Ikui *et al.* [33] developed a multi-stage model. They assumed that a series of compression waves produced by the gradual opening of the diaphragm, can be divided into a finite number of groups of compressions. A group of compression waves coalesce at the same point and the shock front generated by the first group is successively accelerated by the other groups. This model can predict slightly higher maximum shock speeds than the model of White [91] as shown by the solid line in Figure 5.1.

Zeitoun *et al.* [97] performed a one-dimensional computation using the method of characteristics. The finite opening time of the diaphragm and boundary layer effects were included. The finite opening time of the diaphragm was found to induce a strong shock acceleration followed by a slow deceleration, and the maximum com-

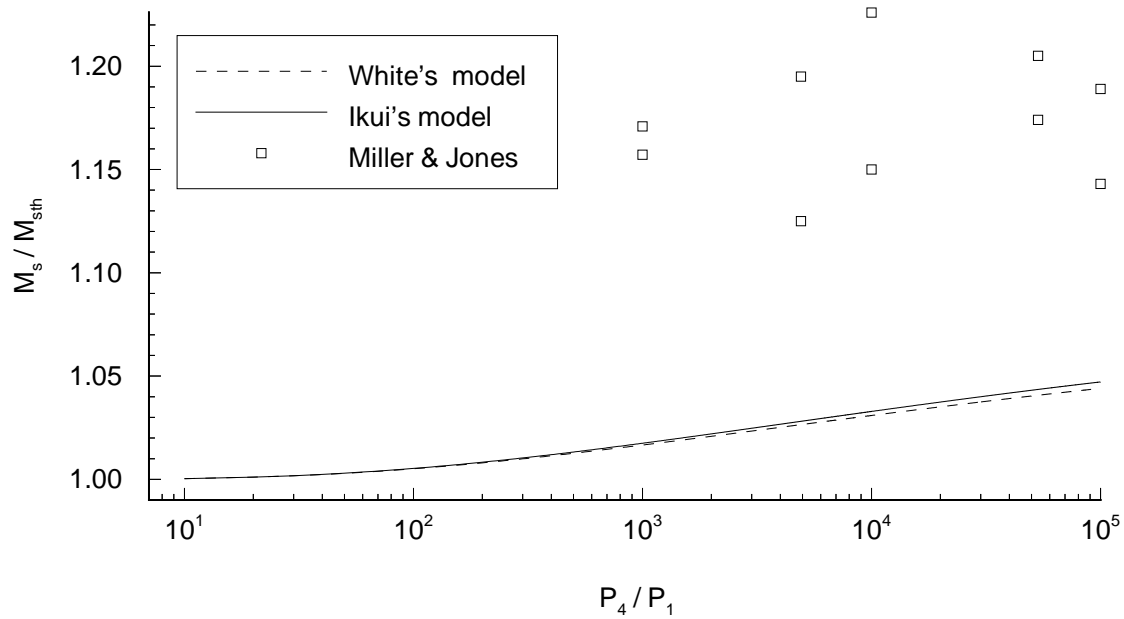


Figure 5.1: Maximum Mach number of developed shock wave within a shock tube versus initial pressure ratio. Experimental data by Miller & Jones [55] is compared with the theories of White [91] and Ikui *et al.* [33]. The Mach number of the shock wave has been normalised by the Mach number of the shock wave within an ideal shock tube for the same initial conditions.

puted shock speed was close to the value predicted by the theory of White. When the effects of the boundary layer were neglected, the shock still decelerated after its initial acceleration but its velocity remained higher than the ideal shock speed. However, the inclusion of boundary layer effects caused a monotonic decrease of the shock speed to values below the ideal shock speed.

Miller & Jones [55] measured shock-wave velocities in the Langley six-inch diameter expansion tube. Air, argon, carbon dioxide and helium were used as test gases. The driver gas was always helium. The shock speed measurements were made using a microwave interferometer and via the response of pressure transducers positioned along the driven section (time of arrival gauges). The maximum shock speeds measured exceeded the maximum speeds predicted by the one-dimensional theories of White [91] and Ikui *et al.* [33] at high initial pressure ratios for all test gases except argon.

Satofuka [74] performed a numerical study of shock formation in cylindrical and two-dimensional shock tubes. Air/Air driver-driven gas combinations were examined at diaphragm pressure ratios of 10, 100 and 1000. The calculated shock speeds were similar to those of White [91] and Ikui *et al.* [33] at the lower initial pressure ratios. However, at the highest pressure ratio of 1000, a slightly higher shock speed (+0.05%) was predicted.

Outa *et al.* [61] performed experiments and two-dimensional simulations (similar to Satofuka) of a gradually opening diaphragm. The maximum experimentally measured shock speed within a 100 mm square shock tube for an initial pressure ratio of 6100 exceeded the ideal shock speed by ten percent and exceeded the maximum shock predicted by the theory of Ikui *et al.* [33] by five percent.

Curzon & Phillips [20] experimentally measured the distance a shock wave travelled in an electric shock tube before reaching maximum velocity by placing several piezoelectric probes spaced along a shock tube. It was concluded that this distance is proportional to the product of the maximum shock speed and the diaphragm opening time. Miller & Jones [55] concluded from numerical simulations that the location of maximum velocity increased linearly with assumed opening time and that the predicted maximum shock velocity did not alter with diaphragm opening time.

### 5.1.2 Scope of the current work

We have chosen the experimental work of Miller & Jones [55] to be our reference point for the present study because of the high quality and detail of the available experimental data. Figure 5.1 compares the normalised maximum Mach number of shock waves (helium as the test gas) with the theories of White [91] and Ikui *et al.* [33] (constant area tube and ratio of specific heats  $\gamma = 1.667$ ). The maximum Mach number of the shock is normalised by the Mach number of the shock wave in an ideal shock tube with the same initial conditions. Two important observations can be made from Figure 5.1: (i) the experimental data points are significantly higher than estimates from the one-dimensional theories, and (ii) the normalised Mach number predicted by the theories of White [91], and Ikui *et al.* [33] increases with initial pressure ratio.

Miller & Jones [55] suggested that the higher shock speeds were caused by a combination of mechanisms including heating of driver gas during pressurisation, effects of the finite opening time, and multi-dimensional effects. We will concentrate on the multi-dimensional nature of the flow resulting from a gradually opening diaphragm to see if it contributes significantly to the higher than expected experimental shock speeds.

The computed shock speed from the axisymmetric simulations of a gradually opening diaphragm presented in Chapter 4 are compared with the experimental data of Miller & Jones [55]. The models of White [91] and Ikui *et al.* [33] fail to predict the maximum shock speed at these conditions. It will be shown that the multi-dimensional nature of flow contributed to the higher than expected maximum shock speed.

## 5.2 Langley expansion tube

Computed shock speeds (as functions of distance downstream from the diaphragm for the initial conditions stated in Table 4.1) are compared with the experimentally measured shock speeds in Figures 5.2 – 5.4. The opening time for these simulations was 200 microseconds. Solution-adaptive remeshing was used for the simulations with  $\alpha = 0.02$  or 0.01. Note that it was shown in Section 3.2.4 that a noise filter coefficient,  $\alpha \leq 0.02$  is required to resolve the contact surface and accurately predict the shock speed within shock tubes with high initial pressure ratios. The maximum experimental shock speeds exceeds the computed speeds for all cases, however, the



experimental and computed profiles are similar in that both exhibit an acceleration phase followed by a deceleration phase. Note that the computed profile has a deceleration phase even though viscous effects are not included (also noted by Zeitoun *et al.* [97]).

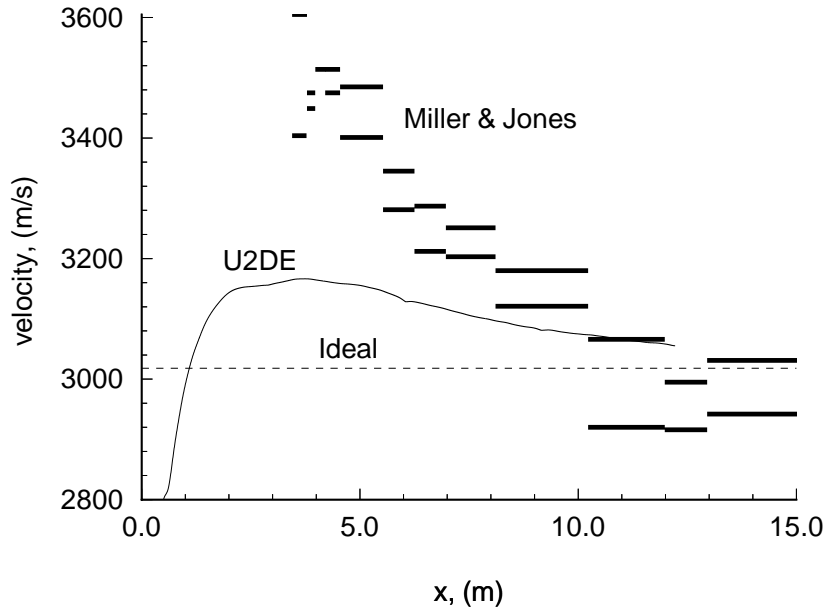


Figure 5.2: Shock speed versus distance for condition # 1 (Table 4.1),  $P_4/P_1 = 1014.5$ .

The grid convergence of the computed shock speeds was examined (Figs. 5.5 – 5.7), and only occurred for  $P_4/P_1 = 1014.5$ . This is similar to results for the ideal shock tube (Sec. 3.2.3), where the computed shock speed converged to the ideal value for  $P_4/P_1 \leq 1000$ . The simulation with the highest mesh resolution for  $P_4/P_1 = 1014.5$  required 22 days of computation time (on a SGI Power Challenge R8000 processor; 85 microseconds per cell per predictor-corrector time-step). A higher resolution simulation could not be obtained with the available computing resources.

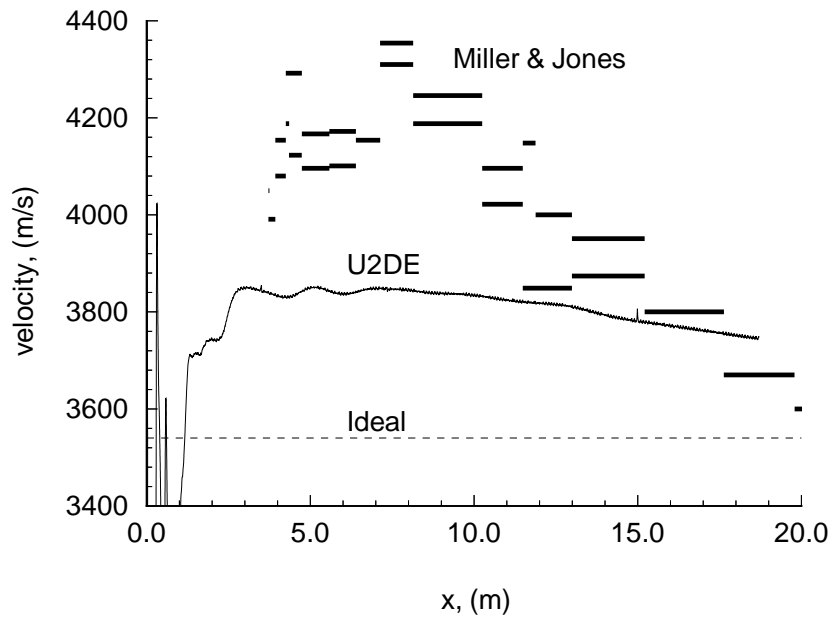


Figure 5.3: Shock speed versus distance for condition # 2 (Table 4.1),  $P_4/P_1 = 10145$ .

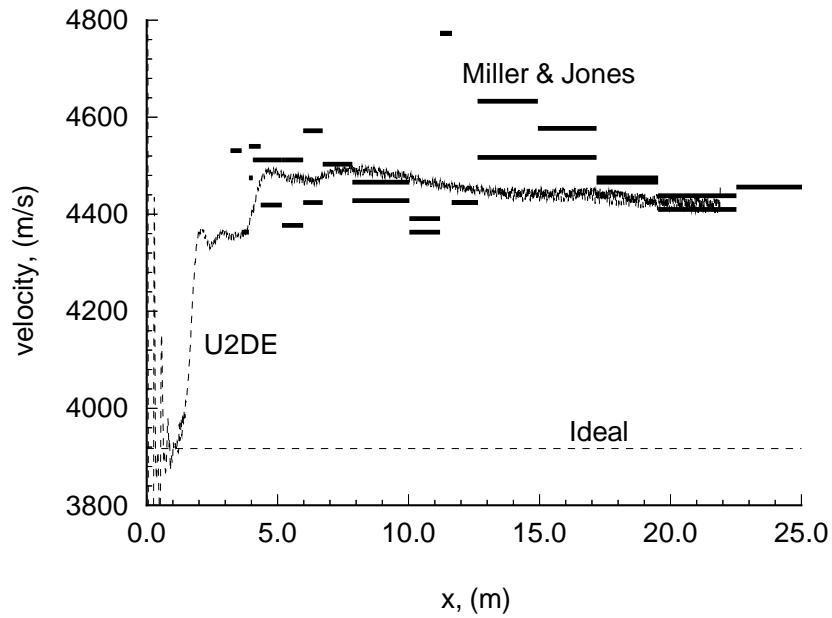


Figure 5.4: Shock speed versus distance for condition #3 (Table 4.1),  $P_4/P_1 = 101450$ .

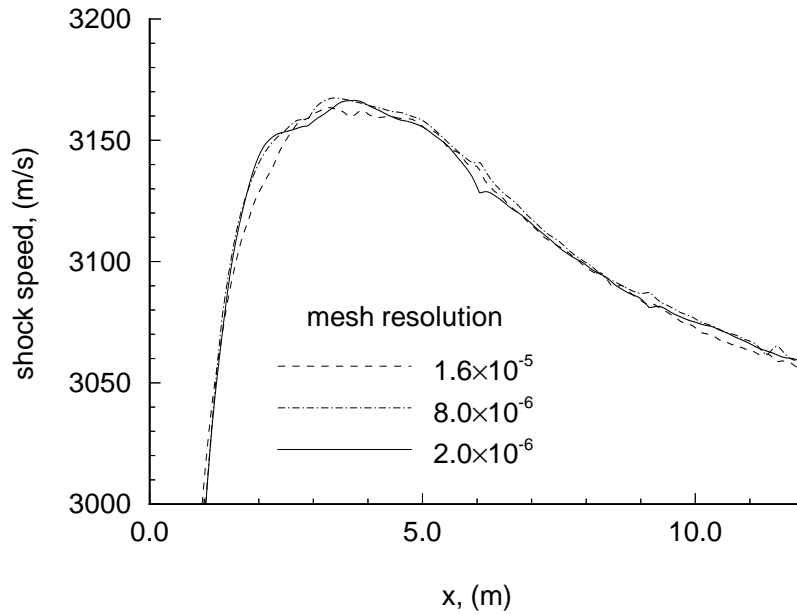


Figure 5.5: Grid convergence of computed shock speed for condition # 1 (Table 4.1),  $P_4/P_1 = 1014.5$ .

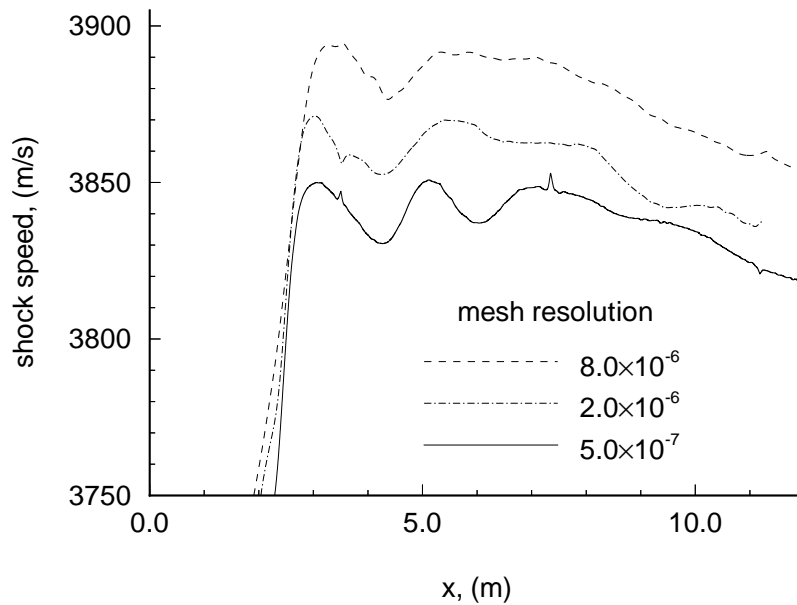


Figure 5.6: Grid convergence of computed shock speed for condition # 2 (Table 4.1),  $P_4/P_1 = 10145$ .

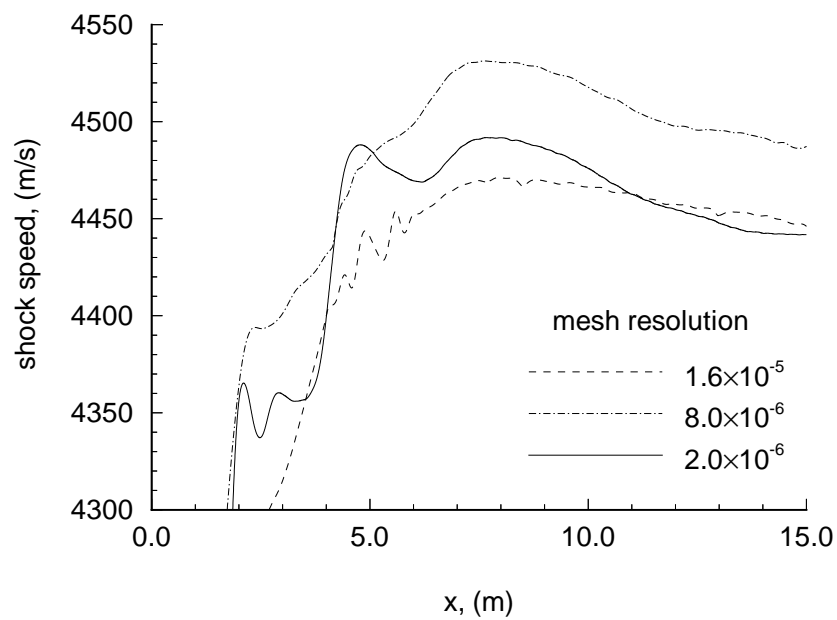


Figure 5.7: Grid convergence of computed shock speed for condition # 3 (Table 4.1),  $P_4/P_1 = 101450$ .

### 5.3 Constant area tube

Due to the uncertainty of the computed maximum shock speed when the initial pressure ratio was high, the shock speeds within a constant area shock tube with gradual diaphragm opening for low initial pressure ratios ( $P_4/P_1 = 10, 100,$  and  $1000$ ) were examined. The computed speeds of the shock waves versus distance downstream from the diaphragm location are shown in Figures 5.8 - 5.10. The opening time for these simulations was 200 microseconds. Grid convergence was only clearly achieved for  $P_4/P_1 = 1000$ . However, for  $P_4/P_1 = 10$ , which is not formally converged (the difference between the highest and middle resolution is greater than the difference between the middle and lowest resolution), the differences between the solutions are small.

The differences between solutions are largest for  $P_4/P_1 = 100$ . However, the changes were significantly less when the diaphragm opening time was 300 microseconds (Fig. 5.11). The reason for this is presently unknown. A possible explanation is that numerical jetting has become aggravated by the nature of the flow that develops for the given geometry when the initial pressure ratio is 100, and when the opening time of the diaphragm is 200 microseconds.

It would appear that grid convergence was achieved for the shock speed (Fig. 5.10) and not the shape of the contact surface (Fig. 4.21) for the case when  $P_4/P_1 = 1000$ . The reason for this is unknown, however, it should be noted, that for an ideal shock tube (Fig. 3.23) the numerical jetting was more pronounced at the contact surface than the shock.

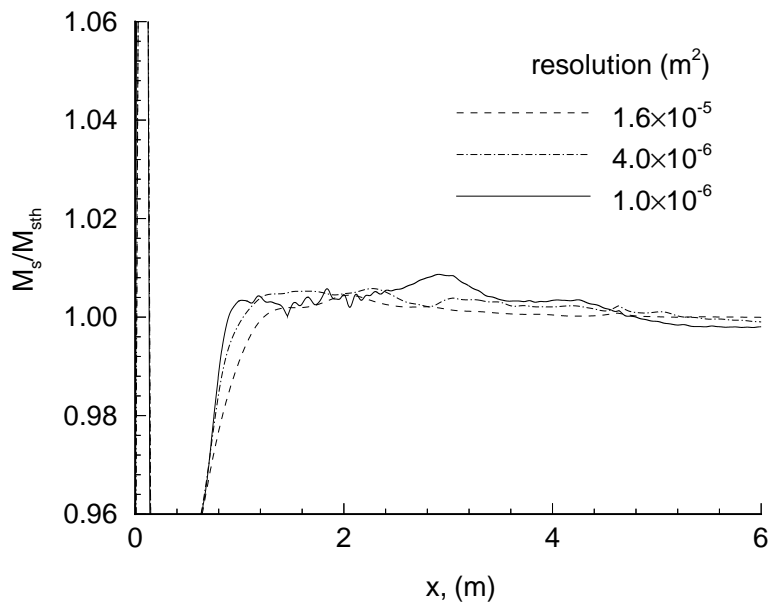


Figure 5.8: Computed shock speed versus distance ( $P_4/P_1 = 10$ ).

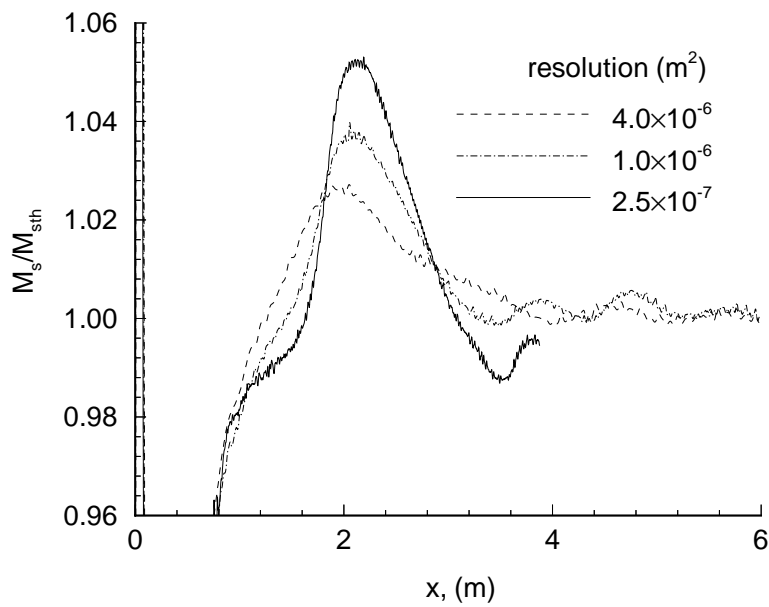


Figure 5.9: Computed shock speed versus distance ( $P_4/P_1 = 100$ ).

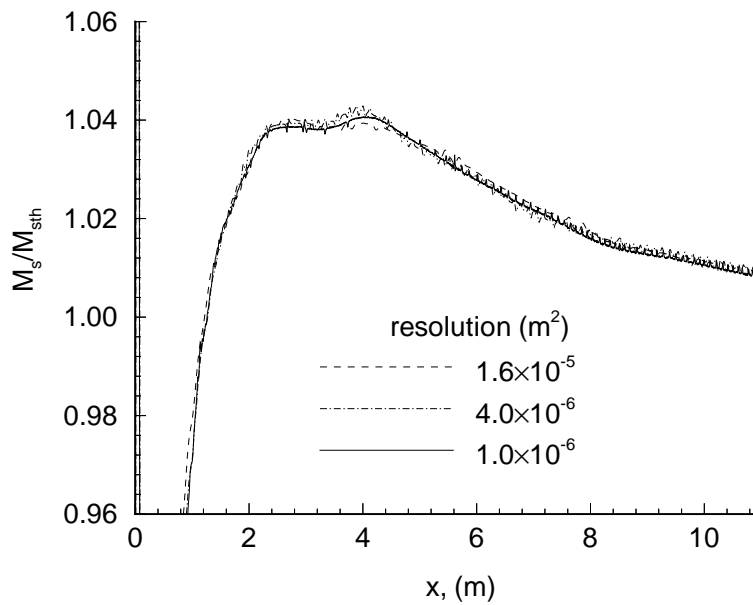


Figure 5.10: Computed shock speed versus distance ( $P_4/P_1 = 1000$ ).

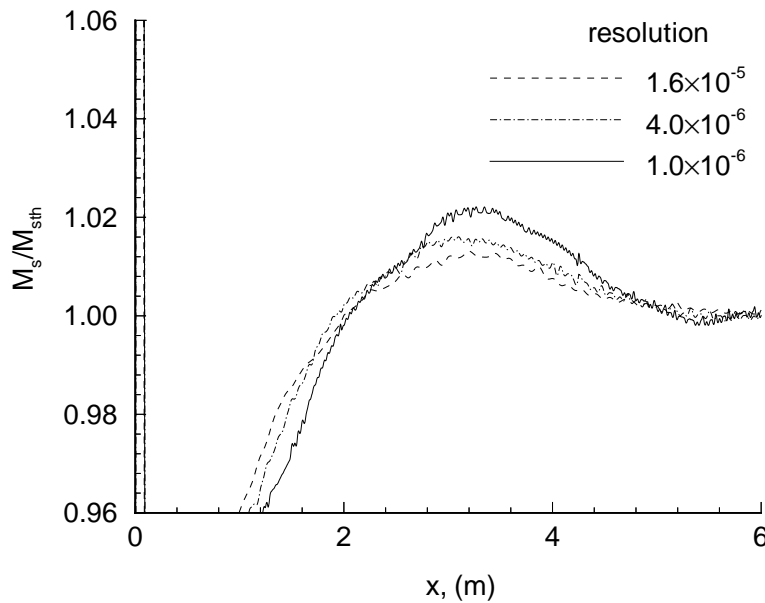


Figure 5.11: Computed shock speed versus distance ( $P_4/P_1 = 100$ ,  $t_{op} = 300\mu s$ ).

### 5.3.1 Equation of state

The pressure of the driver gas for the experiments by Miller & Jones [55] was high enough to cause van der Waals forces to be significant and so cause a deviation from perfect gas behaviour. The Redlich-Kwong equation of state (Appendix A) was used to describe the behaviour of helium for the simulations of these experiments. Initially, it was expected that the use of the Redlich-Kwong equation of state would cause an increase in the computed shock speed because the speed of sound of the driver gas was significantly higher (19.3%). However the difference in the computed shock speeds for the perfect and non-perfect equations of state, was found to be small (0.0233% for initial condition # 2, Table 4.1). The reason for the small difference can be explained by the observation that the higher the ratio of specific heats of the driver gas in an ideal shock tube, the slower the speed of the shock wave (Eqn. 7.94 & 3.57 [5]). This was indeed the case when the Redlich-Kwong equation of state was used. The effective ratio of specific heats (Eqn. 2.19) for the driver gas increased to 1.790 compared with 1.667 for the perfect gas model. It would appear that the effect of increasing the speed of sound was balanced by increasing the ratio of the specific heats of the driver gas for this operating condition.

### 5.3.2 Two-dimensional shock tube

Simulations were performed at different mesh resolutions of a two-dimensional shock tube ( $P_4/P_1 = 100$ ) with a gradually opening diaphragm. The density contours of the contact surface are shown in Fig 4.23. The speeds of the shock waves from these simulations are shown in Fig 5.12. The solutions do not formally converge, but the differences between the solutions is small (similar to  $P_4/P_1 = 10$ ). Unlike the axisymmetric simulations, the maximum shock speed does not increase with mesh resolution. This suggests that the increase in the maximum shock speed with resolution for the axisymmetric solutions is due to the axisymmetric flow solver; most probably numerical jetting.



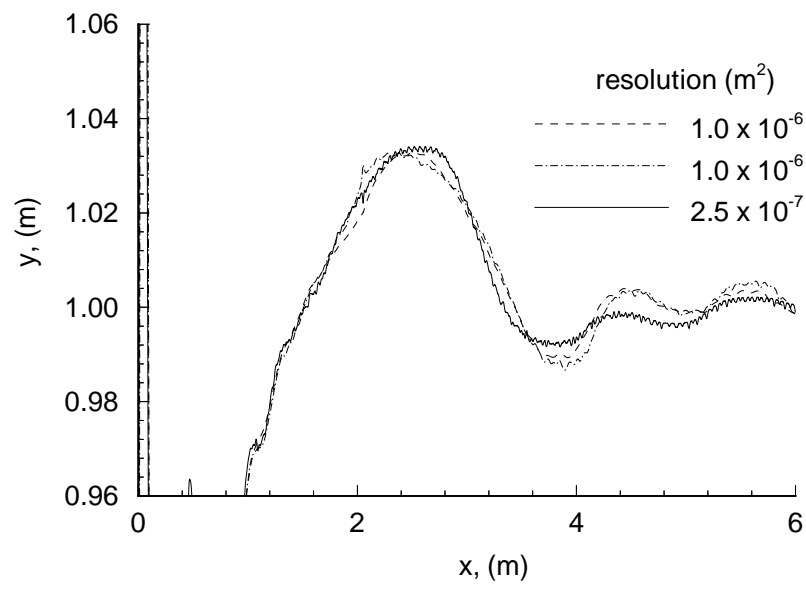


Figure 5.12: Computed shock speed versus distance ( $P_4/P_1 = 100$ ) for two-dimensional shock tube.

## 5.4 Comparison with one-dimensional theories

The maximum shock speeds for the simulations of gradual diaphragm opening are compared with theoretical and experimental shock speeds in Figure 5.13. Grid convergence was only clearly demonstrated for the numerical solutions when  $P_4/P_1 = 1000$  and 1014.5. Despite this, the trends remain consistent: (i) the computed shock speed in an axisymmetric shock tube with a gradually opening diaphragm is greater than the speed predicted by various one-dimensional theories (ideal, White [91], and Ikui *et al.* [33]), and (ii) the normalised shock speed increases with initial pressure ratio.

The first trend is probably due to the oblique upstream facing shock (discussed in Sec. 4.3) that temporarily appears downstream of the diaphragm and raises the entropy of the driver gas processed by it. Using a one-dimensional model, Zeitoun *et al.* [97] showed, that if an upstream facing normal shock exists downstream of the expansion, the speed of the shock wave can transiently exceed the ideal value. The theories of White and Ikui *et al.* do not consider this upstream facing shock. The idea of increasing the entropy of the driver gas to generate faster shocks has been studied by Bogdanoff [12] and Kendall *et al.* [43] and it appears that similar entropy raising mechanisms are operating here.

The second trend, of increasing normalised shock speed with initial pressure, is predicted by the theories of White and Ikui *et al.*. However, the greater the initial pressure ratio at the diaphragm, the greater the strength of the oblique shock (as discussed in Sec. 4.4.1) and the greater the entropy jump across the shock. This mechanism probably contributes to the increase in the normalised computed shock speed with initial pressure ratio.

The normalised maximum Mach number (1.034) for the two-dimensional shock tube is greater than the speed predicted by the one-dimensional models. This indicates that the higher than expected shock speed is not due to numerical jetting caused by the axisymmetric flow solver.

The computed shock speeds obtained via the multi-dimensional model, although higher than the one-dimensional shock speeds, are less than the experimental values of Miller & Jones. There are a number of possible reasons for this. The simulations did not include viscous and turbulent mixing at the contact surface. It was shown in Section 3.2.4 that numerical diffusion at the contact surface can cause higher computed shock speeds. The temperature of the expanded gas can be very low (16 K for  $P_4/P_1 = 1000$ ), and at these temperatures, the behaviour of helium cannot be

accurately described by the Redlich-Kwong equation of state (Appendix A). Also the opening of the primary diaphragm via petalling produces a fully three-dimensional flow and the current simulation is not modelling this process.

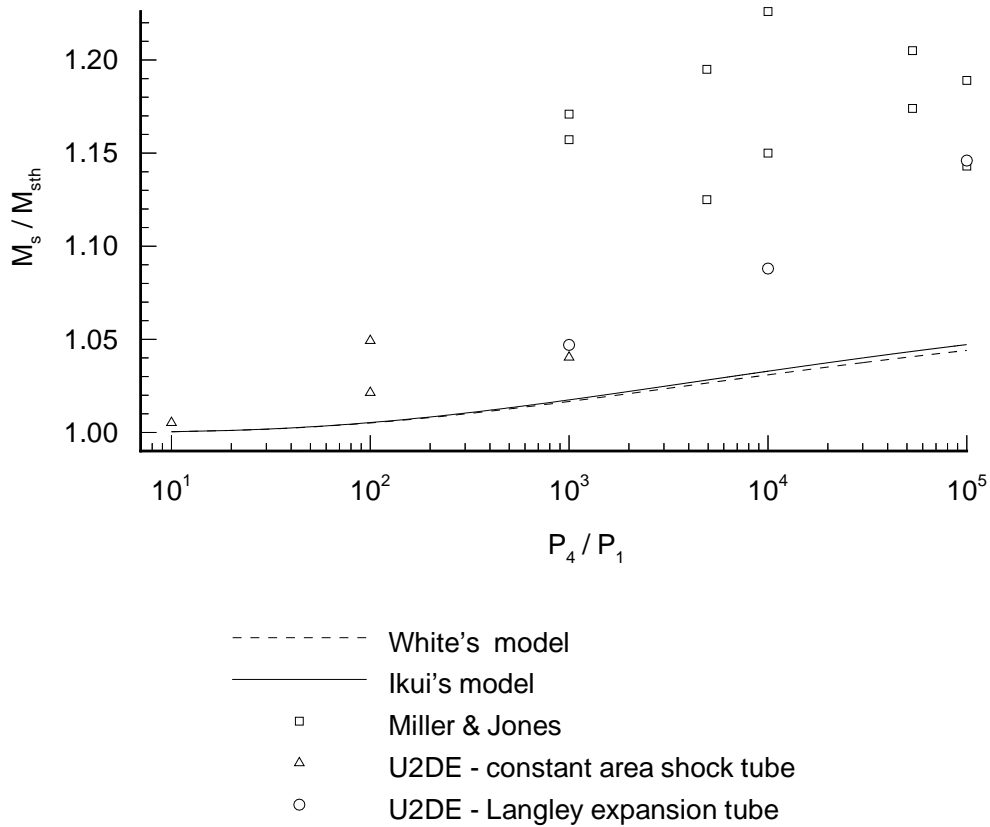


Figure 5.13: Maximum Mach number of developed shock wave within a shock tube versus initial pressure ratio. Experimental data by Miller & Jones [55] is compared with the theories of White [91] and Ikui *et al.* [33]. The Mach number of the shock wave has been normalised by the Mach number of the shock wave within an ideal shock tube for the same initial conditions. The results from simulations by U2DE are included. The two computed shock speeds at  $P_4/P_1 = 100$  are for opening times of 200 (higher shock speed) and 300 microseconds.

# Chapter 6

## Fluid-structure interaction

In Chapter 2, the numerical techniques employed by U2DE to solve compressible flow problems with stationary domains were described. In this chapter, the techniques employed by the code to solve problems with two-dimensional fluid-structure interactions are described.

The structures are assumed to be rigid bodies and their motion, due to fluid pressure, causes the boundary of the flow domain to move. The mesh of the flow domain is allowed to deform while maintaining connectivity. To solve the unsteady Euler equations for a moving domain, a general moving reference frame formulation is used. The techniques required to solve the Euler equations for this formulation are described and vary from the techniques described in Section 2.3.

Sometimes the motion of the rigid bodies cause low quality cells (described in Sec. 6.3) to occur which can reduce the accuracy of the simulation. If this occurs, a new mesh is automatically generated by manipulating the old mesh. The solution is then transferred to the new mesh, and the simulation continues. The methods used to generate the new mesh and transfer the solution are described in Section 6.3.

## 6.1 Rigid-body dynamics

The initial position and velocity of the bodies, and the initial state of the fluid is known and is advanced in time by an explicit time-marching scheme. Within each time-step, the code determines the motion of bodies before updating the fluid-dynamics.

A body is defined by boundary edges of the flow domain that are connected and, may be part of the external boundary (for example, a piston driven by expanding gas) or form an internal loop within the flow domain. Either one (translation) or three (two in translation and one in rotation) degrees of freedom are assigned to a structure depending on whether the motion is either one- or two-dimensional, respectively.

The force acting on a structure is determined by integrating the pressure along its surface. The moment acting on a structure about its centre of mass is equal to,

$$M = \sum_{\text{edges}} P S \mathbf{r} \times \hat{\mathbf{n}}, \quad (6.1)$$

where  $\mathbf{r}$  is the position vector from the centre of mass to the midpoint of an edge. Each body is assumed to be rigid and the acceleration of its centre of mass and its angular acceleration can be determined by the following equations,

$$\mathbf{a} = \frac{\mathbf{F}}{m} \quad (6.2)$$

$$\ddot{\theta} = \frac{M}{I}. \quad (6.3)$$

The velocity of the centre of mass and the angular velocity of a body is updated using,

$$\mathbf{V}_s^{n+1} = \mathbf{V}_s^n + \mathbf{a} \Delta t \quad (6.4)$$

$$\dot{\theta}_s = \dot{\theta}_s + \ddot{\theta}_s \Delta t, \quad (6.5)$$

and then, the velocities of the vertices of the mesh edges that define a structure are set to,

$$\mathbf{w} = \mathbf{V}_s + \dot{\theta}_s \hat{\mathbf{k}} \times \mathbf{r}, \quad (6.6)$$

where  $\mathbf{r}$  is the position vector from the centre of mass to the vertex.

The velocities of every vertex within the mesh can be determined after the velocities of the vertices associated with the bodies are determined. The velocities of the vertices on the boundary of the flow domain are either: (a) set permanently to zero, (b) determined by rigid-body dynamics, or (c) allowed to slide along the boundary. A smoothing operator [84] is used to determine the velocities of the internal vertices and the boundary vertices which are allowed to slide. Specifically, the velocity of a vertex is set to the average velocities of the vertices surrounding it. This process is repeated until the largest change is small,  $\frac{|\Delta w|}{w_{max}} < 0.01$ . If the motion of the structure is simple (for example, one-dimensional motion of a piston in a tube) the velocities of all vertices can be determined as an explicit function of time and position.

## 6.2 Flow solver for moving mesh

The method used to solve the Euler equations is similar to the method outlined in Chapter 2, and the differences between the two schemes are described in this section. These differences include the addition of grid velocity to the flux vector and the treatment of cell volume changes during a time-step.

The Euler equations for two dimensional unsteady compressible flows for a general moving reference frame can be written as [68],

$$\frac{\partial}{\partial t} \int_{\vartheta(t)} \mathbf{U} d\vartheta + \int_{S(t)} \mathbf{F} \cdot \hat{\mathbf{n}} dS = 0 \quad (6.7)$$

where,

$$\mathbf{U} = \begin{bmatrix} \rho \\ \rho u \\ \rho v \\ \rho E \end{bmatrix}, \quad \mathbf{F} = \begin{bmatrix} \rho(\mathbf{u} - \mathbf{w}) \\ \rho(\mathbf{u} - \mathbf{w})u + P\hat{\mathbf{i}} \\ \rho(\mathbf{u} - \mathbf{w})v + P\hat{\mathbf{j}} \\ \rho(\mathbf{u} - \mathbf{w})E + P\mathbf{u} \end{bmatrix}, \quad (6.8)$$

$\mathbf{u}$  is the fluid velocity, and  $\mathbf{w}$  is the mesh velocity. The case of  $\mathbf{w} = \mathbf{u}$  corresponds to a Lagrangian system while the case of  $\mathbf{w} = \mathbf{0}$  is Eulerian. The mesh velocities are determined from the rigid-body dynamics.

The reconstruction of the left and right edge flow states is performed in the same manner stated in Section 2.3.2, except that flow velocities relative to the edge are considered. The velocity of a cell edge is assumed to be the average velocity of its two vertices. This edge velocity will be referred to as the average edge velocity,

$$\mathbf{w}'_{\mathbf{AB}} = \frac{\mathbf{w}_{\mathbf{A}} + \mathbf{w}_{\mathbf{B}}}{2}. \quad (6.9)$$

The Riemann solver (Appendix D) can be used to determine the flow state at the moving edge. To calculate the fluxes  $\mathbf{F} \cdot \hat{\mathbf{n}}$  (Eqn. 6.7), an effective edge velocity (Eqn. 6.10) is used to describe the mesh velocity  $\mathbf{w}$ . This satisfies the Geometric Conservation Law (GCL) [82] which requires that the change in all cell volumes due to the discretised motion of the edges is the same as the change in geometric cell volumes. Only the normal component of the edge velocity affects the flux calculation and the tangential component is not considered. In Figure 6.1, the area swept by the edge AB (AA'B'B) is equal to the area swept by the edge AB (AA''B''B) with the effective edge velocity (Ambrosi *et al.* [3]),

$$\mathbf{w}_{\mathbf{AB}} = \frac{\frac{1}{2} [(\mathbf{r}_{\mathbf{B}'} - \mathbf{r}_{\mathbf{A}}) \times (\mathbf{r}_{\mathbf{A}'} - \mathbf{r}_{\mathbf{B}})]}{\Delta t S} \hat{\mathbf{n}}, \quad (6.10)$$

where  $\mathbf{r}_{\mathbf{A}}$  and  $\mathbf{r}_{\mathbf{B}}$  are the position vectors of vertices A and B,  $\Delta t$  is the change in time, and  $S$  is the length of the edge (Fig. 6.1). The vectors  $\mathbf{r}_{\mathbf{A}'}$  and  $\mathbf{r}_{\mathbf{B}'}$  are equal to,

$$\mathbf{r}_{\mathbf{A}'} = \mathbf{r}_{\mathbf{A}} + \mathbf{w}_{\mathbf{A}} \Delta t \quad (6.11)$$

$$\mathbf{r}_{\mathbf{B}'} = \mathbf{r}_{\mathbf{B}} + \mathbf{w}_{\mathbf{B}} \Delta t. \quad (6.12)$$

The orientation of  $\mathbf{r}_{\mathbf{A}}$  and  $\mathbf{r}_{\mathbf{B}}$  with respect to the normal vector is such that,

$$(\hat{\mathbf{r}}_{\mathbf{AB}}) \times \hat{\mathbf{n}} = \hat{\mathbf{k}}, \quad (6.13)$$

and  $w_n$  is positive in the direction of  $\hat{\mathbf{n}}$ .

The flow state at the edge is required to determine the fluxes for the method described above. The edge flow state cannot be determined easily when using EFM.

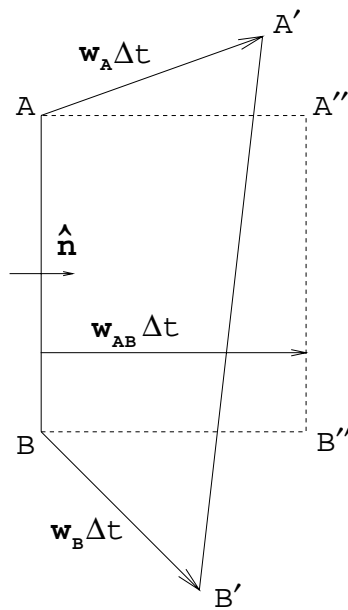


Figure 6.1: Calculation of effective edge velocity for edge AB.

To use EFM to calculate the fluxes across a moving edge without knowing the edge flow state, either the effective or the average edge velocity has to be used for the reconstruction and the flux calculation. The fluxes relative to the edge can be determined from the left and right edge flow states relative to the edge by the method described in Appendix C. The fluxes can then be transformed to the global reference frame using the following transformation (Macrossan [51]),

$$m = m' \quad (6.14)$$

$$p_x = p'_x + m w_x \quad (6.15)$$

$$p_y = p'_y + m w_y \quad (6.16)$$

$$\epsilon = \epsilon' + \frac{1}{2} m w^2 + p'_x w_x + p'_y w_y \quad (6.17)$$

where,

$$\mathbf{F} \cdot \hat{\mathbf{n}} = \begin{bmatrix} m \\ p_x \\ p_y \\ \epsilon \end{bmatrix}, \quad (6.18)$$

$$\mathbf{w} = w_x \hat{\mathbf{i}} + w_y \hat{\mathbf{j}}, \quad (6.19)$$

$w_x$  and  $w_y$  are the effective grid velocities in the global  $x$  and  $y$  directions, and  $w = |\mathbf{w}|$ . If the average edge velocity is used, the scheme may not be conservative depending on the mesh velocities and, if the effective edge velocity is used, the determination of the static fluxes may not be accurate because the determination of the fluxes is a one-dimensional problem and depends on the actual (average) normal



velocity of the edge. In the author's opinion, it is better to use the effective edge velocity and ensure that the conserved variables remain conserved.

The predictor-corrector time-stepping scheme (Eqns. 6.20 - 6.23) is used to explicitly time march the flow solution and is different from the scheme described in Section 2.3.3 because of the change in cell volume,

$$\Delta U^1 = \sum (\mathbf{F} \cdot \mathbf{S})^n \Delta t \quad (6.20)$$

$$U^1 = \frac{A^n U_n + \Delta U^1}{A^{n+1}} \quad (6.21)$$

$$\Delta U^2 = \sum (\mathbf{F} \cdot \mathbf{S})^1 \Delta t \quad (6.22)$$

$$U^{n+1} = U^2 = U^1 + \frac{1}{2} \frac{(\Delta U^2 - \Delta U^1)}{A^{n+1}}. \quad (6.23)$$

The mesh is assumed to be at level  $n$  for both calculations of the change in conserved variables (Eqns. 6.20 & 6.22). That is, the edge velocity, length and normal are the same for both stages of the time-step.

The magnitude of each time-step is limited by,

$$\Delta t = \text{minimum}(\Delta t_f, \Delta t_g) \quad (6.24)$$

where  $\Delta t_f$  is the maximum allowable change in time due to flow constraints as described in Section 2.3.3, and  $\Delta t_g$  is the maximum allowable change in time such that the length of any edge does not change by more than ten percent. Unlike the two-dimensional static mesh formulation, the magnitude of the time-step must be known before the fluxes are calculated, in order to calculate the effective edge velocity. The first change in time is specified by the user and subsequent changes in time are the maximum allowable change in time calculated during the flux calculations of the previous time-step.

### 6.3 Grid management

The deformation of the mesh caused by the movement of its boundaries may cause certain cells with the mesh to become distorted. The geometric *quality*  $q$ , of a cell [84] can be defined as,

$$q = 4\sqrt{3} \frac{A}{a^2 + b^2 + c^2} \quad (6.25)$$

where  $A$  is the area of the triangle and  $a$ ,  $b$ , and  $c$  are the lengths of the sides. For this definition, the quality of a triangle is bound between 0 (degenerate triangle) and 1 (equilateral triangle). Low quality cells can affect the accuracy of the solution [50] and are undesirable. The mesh is allowed to distort until the minimum cell quality,  $q_{min} < 0.4$ . A new mesh with a higher  $q_{min}$  is generated and the solution is transferred from the old mesh to the new. This new mesh is generated by performing the following operations on the old mesh: grid smoothing, diagonal swapping, and vertex deletion.

Mesh smoothing [84] is the process of moving each vertex in turn so that its position is equal to the average position of the vertices surrounding it (Fig. 6.2). If concave angles exist within the polygon created by the vertices surrounding the current vertex, the movement of the vertex may cause cells to overlap. This is highly undesirable, and to prevent it occurring, a vertex will not be moved if the area of the cells surrounding the vertex before it is moved, is not the same as the area after it is moved.

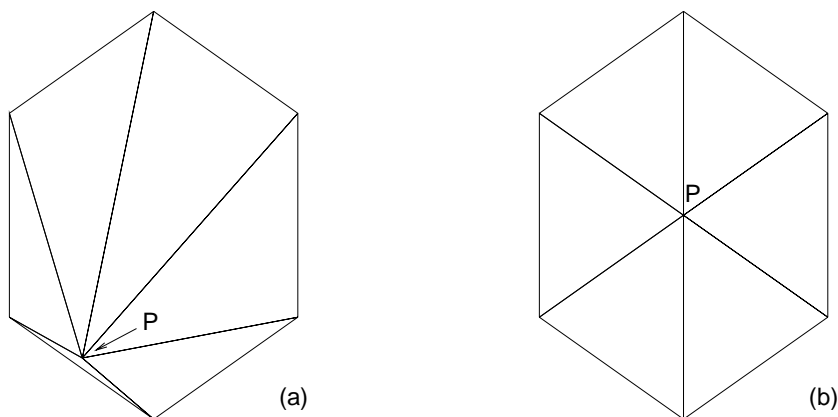


Figure 6.2: Mesh smoothing. The quality of the mesh is improved by moving vertex P to the average position of the vertices surrounding it.

Diagonal swapping [47] is another tool used to improve the quality of a mesh. Each internal edge of the mesh is examined individually. The minimum quality of the cells associated with the edge is determined. If it is lower than the minimum quality of the cells that are formed by swapping the diagonal to the other two vertices of the two cells, the diagonal is swapped (Fig. 6.3).

Vertex deletion [84] is also used to improve mesh quality. The cell with the lowest quality in the mesh is identified. If the vertex opposite the longest edge of this cell

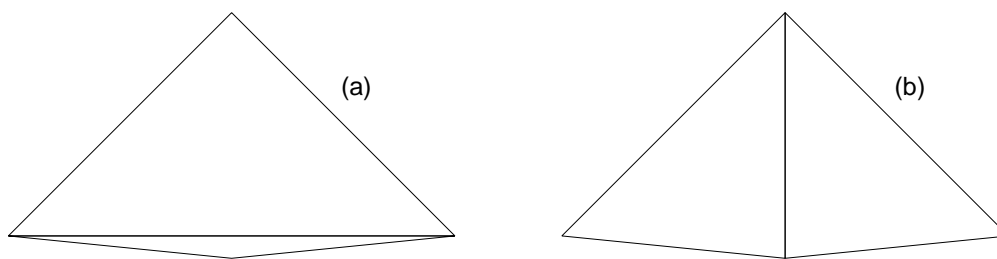


Figure 6.3: Diagonal swapping: (a) before and (b) after.

is not a permanent vertex (i.e. a vertex on the boundary where there is a sudden change in the profile, for example a corner), the vertex is deleted from the mesh. If this vertex cannot be deleted from the mesh, the vertex opposite the second longest edge of the cell is deleted. If this vertex cannot be deleted, the cell is split. It is rare for this to occur and it only occurs when boundaries of the domain become close to each other. The deletion of the vertex from the mesh creates a polygon which may have more than three sides. The polygon is triangulated by removing recursively the highest quality triangle (Fig. 6.4).

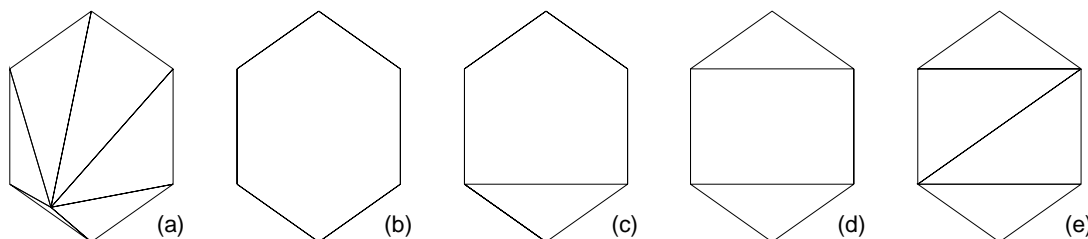


Figure 6.4: Vertex deletion.

The order in which the mesh operations were performed was determined heuristically. The remeshing procedure which performed the best in most cases is described as follows. Firstly (i) the diagonals are swapped and then the location of the vertices are smoothed and this is repeated six times. Secondly (ii) a vertex associated with the cell of the lowest quality is deleted or the cell is split. Steps (i) and (ii) are repeated until  $q_{min} > 0.6$ . An example of a new mesh that was generated from a distorted mesh is shown in Figure 6.5.

If solution-adaptive remeshing is activated, cells within the new mesh are refined until the volume of each cell is less than the volumes of the cells from the old mesh which overlaps with the new cell, or the cell volume is less than the specific minimum cell volume. The method for determining which cells from the old mesh overlap with a new cell is described in Appendix F. Now we have a new, adapted mesh. The next stage is to transfer the solution from the old mesh to the new mesh.

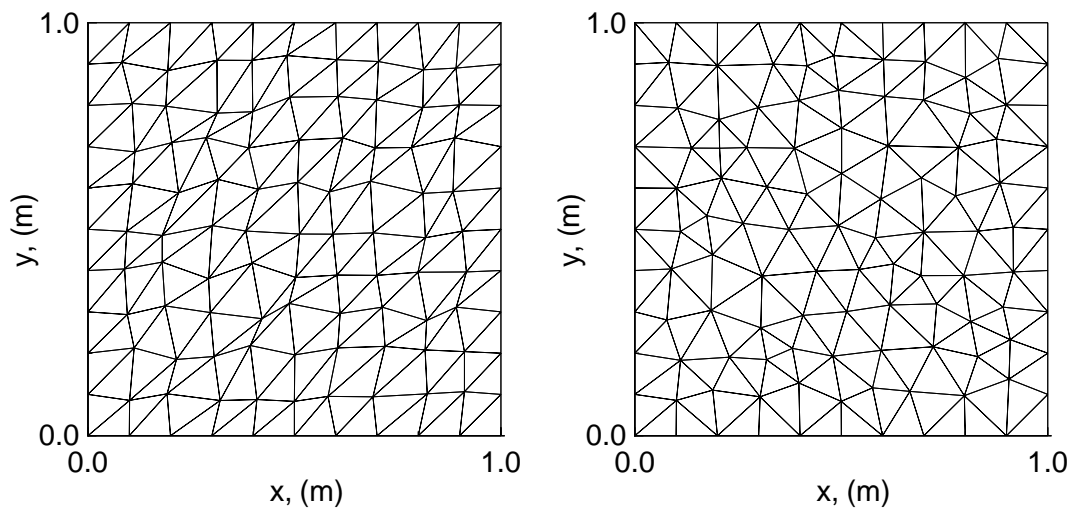


Figure 6.5: Remeshing: (a) before and (b) after. Minimum cell quality was improved from 0.373 to 0.810.

The method of Ramshaw [67] and Cline *et al.* [18] is used to transfer a solution from one arbitrary unstructured triangular mesh to another. This method assumes that the two meshes have the same boundary. The conserved quantities (mass, momentum, and total energy) in a cell of the new mesh is equal to the sum of the quantities in the intersections of the new cell with cells of the old mesh. For example, the mass in the cell ABC in Figure 6.6 is equal to the mass  $\triangle DEG \cap \triangle ABC$  plus the mass in  $\triangle EFH \cap \triangle ABC$  plus the mass in  $\triangle EGH \cap \triangle ABC$  plus the mass in  $\triangle GHI \cap \triangle ABC$ .

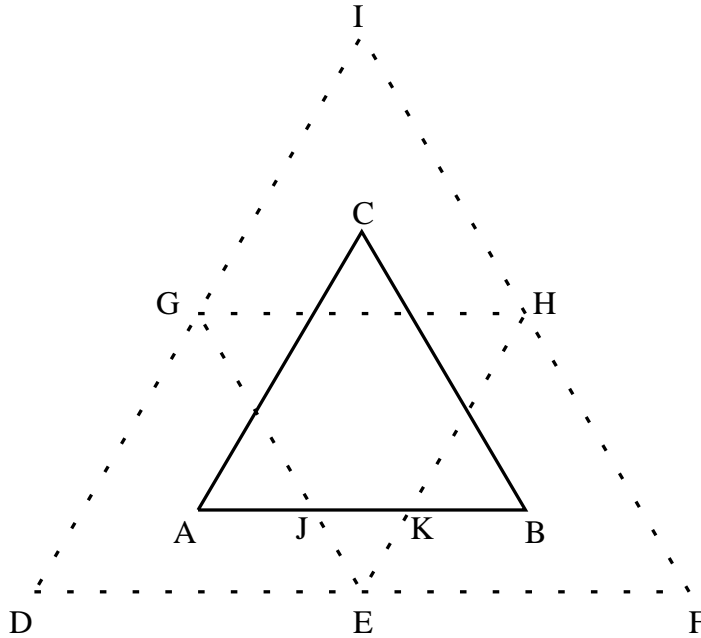


Figure 6.6: Overlapping of new mesh (solid lines) and old mesh (dashed lines).

The mass in each intersecting region is calculated by an application of Gauss' theorem (or divergence theorem). For example the mass in a cell is calculated as,

$$\int_{\vartheta} \rho(\mathbf{r}) d\vartheta = \int_S \mathbf{F} \cdot \mathbf{n} dS \quad (6.26)$$

where,

$$\nabla \cdot \mathbf{F} = \rho(\mathbf{r}). \quad (6.27)$$

It is assumed the specific conserved quantities are constant within a cell. Letting

$$\mathbf{F} = \frac{1}{2} \rho (x \hat{\mathbf{i}} + y \hat{\mathbf{j}}) \quad (6.28)$$

satisfies Equation 6.27 and the mass in a cell is equal to,

$$\frac{1}{2} \sum_{i=1}^3 \rho(x_1 y_2 - x_2 y_1) \quad (6.29)$$

where  $(x_1, y_1)$  and  $(x_2, y_2)$  are the end points of the line segment.

The contribution to the mass of the cell from a line integral along the edge of the new mesh is,

$$\frac{1}{2} \rho_0 (x_1 y_2 - x_2 y_1) \quad (6.30)$$

where  $\rho_0$  is the density in the cell of the old mesh in which the new edge lies. The contribution is added to one cell associated with the new edge and subtracted from the other cell (depending on the direction of the line integral), if the edge is internal.

The contribution to the mass of the cell from a line integral along an edge of the old mesh is,

$$\frac{1}{2} (\rho_L - \rho_R) (x_1 y_2 - x_2 y_1). \quad (6.31)$$

This integral includes contributions from both cells associated with the edge of the old mesh and is added to the new cell in which the line segment lies. Which cell is the left or right depends on the direction of the line integral.

Special treatment is required for edges of the new and old mesh that are on the same line and overlap (coincidence). It can be shown [67] that the proper treatment is to consider both integrals and add half the line integral from the old edge (Eqn. 6.31) to each of the new cells and the density along the new edge is equal to the average density of the old cells either side of the edge.

To perform the line integrals (Eqns. 6.30 & 6.31) it is necessary to know where an edge is relative to the other mesh and determine all intersections of the edge with the other mesh. The line integral along the edge AB of the new mesh in Figure 6.6 is performed in three parts: AJ, JK, and KB. The location of an edge relative to the other mesh is determined by using *Z* lines [18] (Appendix F) which zigzag through the mesh.

The *Z* lines of any arbitrary triangulation trace all edges of the mesh twice: direct segments trace over each edge once, and indirect segments trace over each edge once. To transfer the solution from the old mesh to the new mesh every *Z* line in both the old and the new mesh is traced through the other mesh and the line integrals and contributions to the new cells are evaluated along the direct segments.

It is important that if an edge is considered to be coincident with another edge from the other mesh during a trace, that both edges are also considered to be coincident

when the other edge on the other mesh is traced. If this does not occur, the solution may not be transferred correctly. To ensure that this does occur, two initial traces of the  $Z$  lines of each mesh through the other mesh are performed and a list of the edges that were identified as coincident is generated. This list is then examined before a line integral along an edge is calculated to determine if the edges will be treated as coincident edges during another trace.

After the  $Z$  lines of both meshes have been traced, the line integrals evaluated, and the contribution of mass, momentum, and total energy have been added to the new cells, the extensive quantities are divided by the cell volume to obtain the specific quantities.

## 6.4 Test cases

Three test cases were examined to verify the ability of U2DE to accurately predict the behaviour of fluid-structure interactions. The first test case is designed to check the correct implementation of the Geometric Conservation Laws (Sec. 6.2) and the time-stepping scheme. The second test case examines the ability of the code to solve the Euler equations accurately for a moving boundary problem. The last test case examines the ability of the code to solve the coupled solid-dynamic and fluid-dynamic equations accurately. The geometry and flow properties for all three test cases were treated as non-dimensional values.

### 6.4.1 Random grid motion

The first test case was used by Reggio *et al.* (1992). It verifies that mass, momentum, and energy are conserved. This will occur if the area swept by the effective normal velocity of the edge is equal to the area swept by the motion of the vertices of the edge (Sec. 6.2) and if the time-stepping scheme is correct.

For this test case the flow domain is a square (Fig. 6.7a) with a stationary fluid. The initial density and pressure throughout the domain are equal to 1.0. The internal vertices of the mesh, are assigned random velocities with the  $x$  and  $y$  components varying between  $-0.1$  and  $0.1$ . The velocity of the external vertices are set to zero. The solution is advanced in time until the quality of the mesh is unacceptable,  $q_{min} < 0.4$ . If the scheme is correct, density and pressure should remain constant and the flow velocity zero.

The solution was advanced 22 time-steps (Courant number = 0.2). MUSCL interpolation was used with the predictor-corrector time-stepping scheme and the Riemann solver was used to calculate the fluxes. The final mesh is shown in Figure 6.7 (b). The maximum change in density, momentum, or energy for all cells was  $1.998 \times 10^{-15}$ . This is close to machine precision ( $1.1 \times 10^{-16}$ ) and verifies that the code satisfies GCL. The test was repeated with the initial density of each cell equal to the  $x$  co-ordinate of the cell centre. The difference in the total mass before and after the simulation was also close to machine precision and this performance was considered adequate.

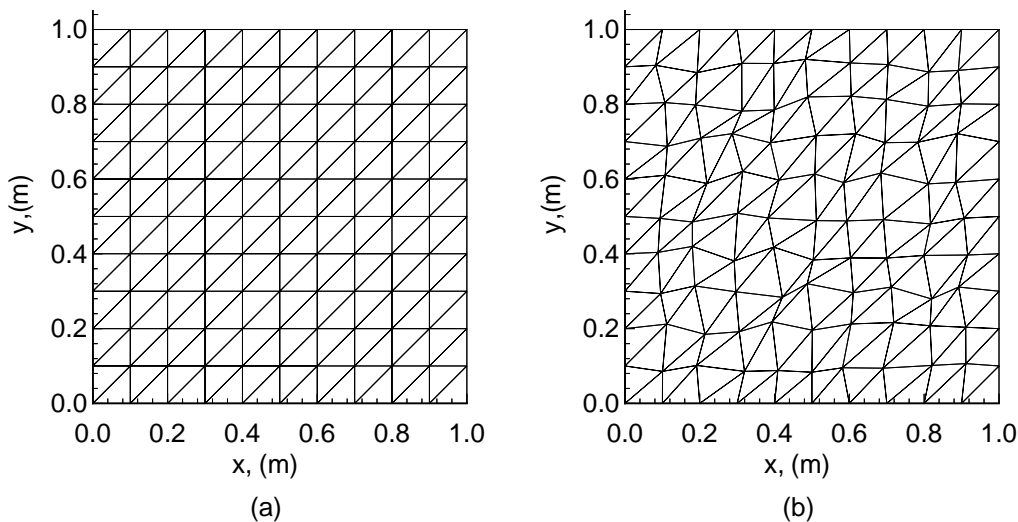


Figure 6.7: Initial (a) and final (b) meshes for random grid motion test case.

### 6.4.2 Constant velocity piston

The problem of a piston moving with a constant velocity [60, 68] in an inviscid shock tube has an analytic solution and was used to verify that the code can solve the Euler equations for a moving reference frame accurately. An initial rectangular domain (Fig. 6.10a) 1 unit long ( $x$ -direction) and 0.1 units wide ( $y$ -direction) was chosen. The piston was represented by the boundary of domain initially at  $x = 1.0$ . The initial density and pressure were set to 1.0 and the gas was initially at rest. The velocity of the piston was 1.0 (Mach number = 0.845) for the expansion case and  $-1.0$  for the compression case. The velocities of the mesh vertices were set to

$$\mathbf{w} = \frac{x}{1.0 + V_p t} \times V_p \hat{\mathbf{i}}. \quad (6.32)$$



The first- and higher-order two-dimensional solutions (Riemann solver) for the compression case are compared with the analytical solution in Figures 6.8 and 6.9. Solution-adaptive remeshing was used with the minimum volume set to  $1.0 \times 10^{-5}$  ( $\alpha = 1.0 \times 10^{-4}$ ). The initial and final meshes for the higher-order solution are displayed in Figure 6.10. Note that there is a glitch in the density profile near the piston location. The cause of the glitch is unknown and is also present in solutions from similar codes [60, 37].

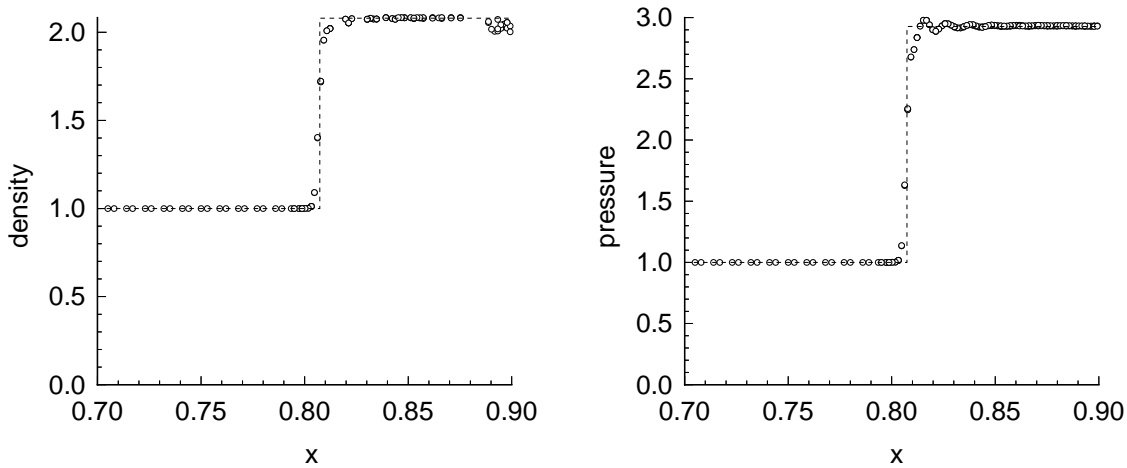


Figure 6.8: Piston compressing gas: comparison of first-order Riemann solver solution ( $\circ$ ) with analytical (dashed line) solution. Data points taken from  $0.05 < y < 0.06$ .

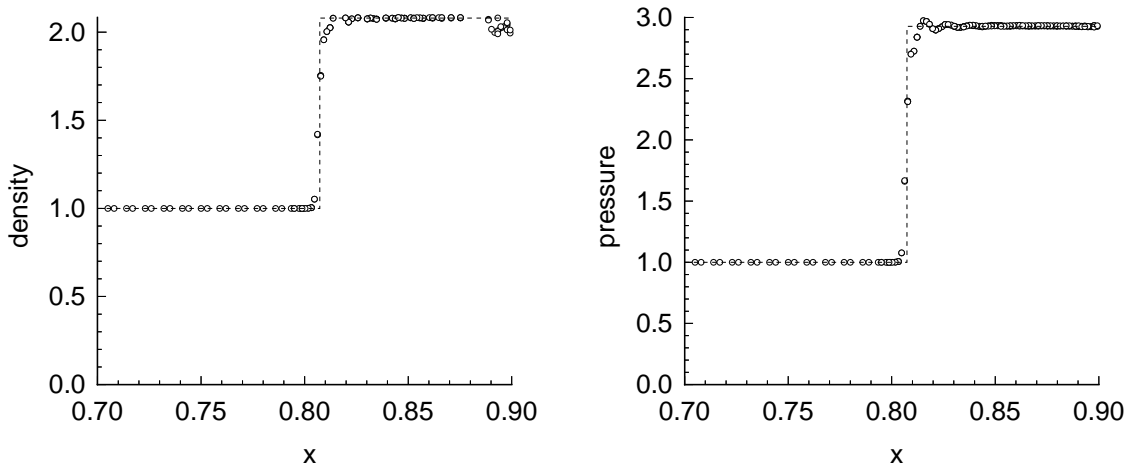


Figure 6.9: Piston compressing gas: comparison of higher-order ( $\beta = 1.0$ ) Riemann solver solution ( $\circ$ ) with analytical (dashed line) solution. Data points taken from  $0.05 < y < 0.06$ .

The two-dimensional solutions also contain oscillations near the shock. The cause

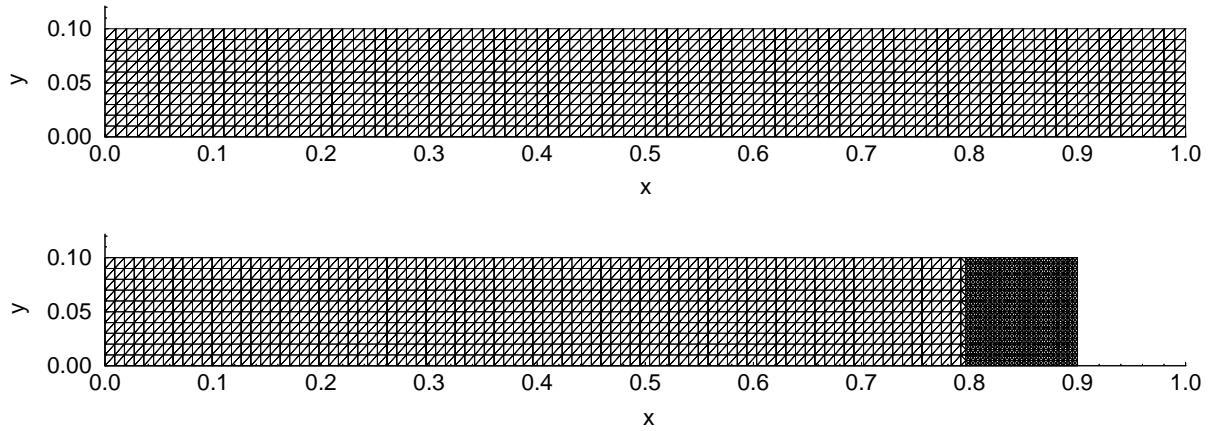


Figure 6.10: Piston compressing gas: (a) initial and (b) final meshes. Minimum area  $1 \times 10^{-5}$ ,  $\alpha = 1 \times 10^{-4}$ .

of the oscillations was investigated further by examining the solution from a one-dimensional flow solver (Appendix B). A first-order solution and higher-order solutions using two different values for the compression parameter,  $\beta$  (Sec. 2.3.1) are compared with the analytical solution in Figures 6.11–6.13. Note that the amplitude of the oscillations is greater for the solution with the higher  $\beta$  value. Increasing the compression parameter  $\beta$ , increases the levels at which the gradients are limited during interpolation. The higher the value of  $\beta$ , the higher the gradients, and the greater the height or depth of any extrema. This allows larger amplitude oscillations to exist in the solution.

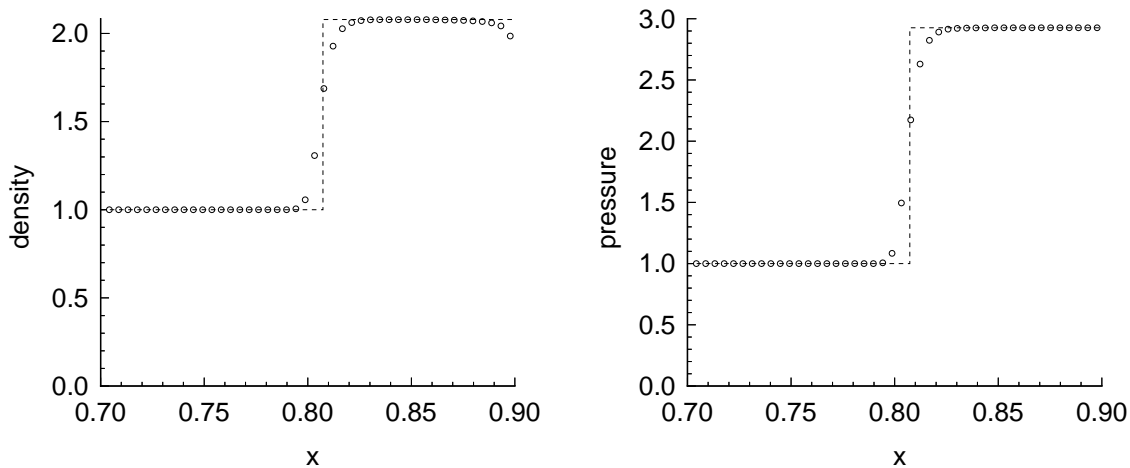


Figure 6.11: Piston compressing gas: comparison of one-dimensional Riemann solver solution (o) with analytical solution (dashed line). Interpolation was first-order.

The one-dimensional and two-dimensional solutions are different, with the two-dimensional solutions exhibiting larger oscillations. The differences between the

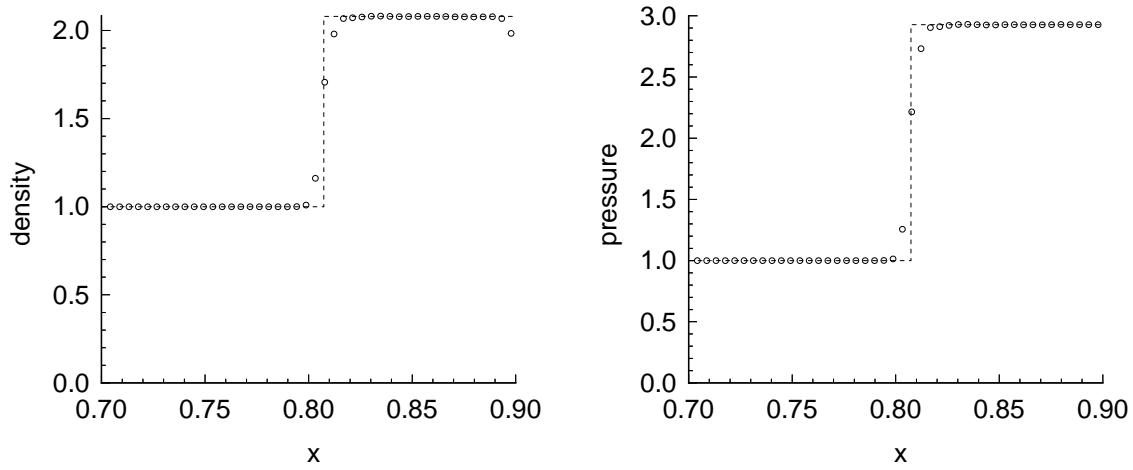


Figure 6.12: Piston compressing gas: comparison of one-dimensional Riemann solver solution (o) with analytical solution (dashed line). Compression parameter,  $\beta = 1.0$ .

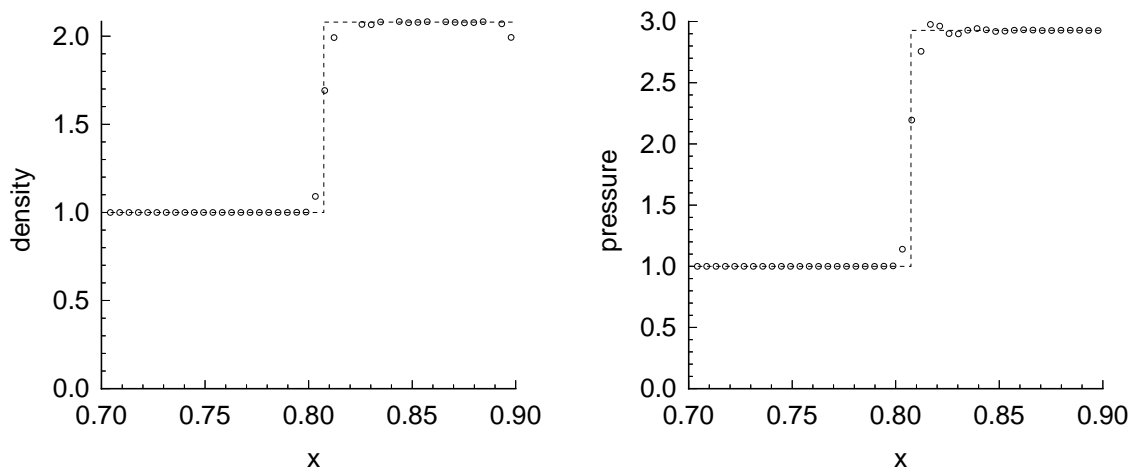


Figure 6.13: Piston compressing gas: comparison of one-dimensional Riemann solver solution (o) with analytical solution (dashed line). Compression parameter,  $\beta = 2.0$ .

two solvers for this test case are: (i) the lines along which the interpolation are performed and (ii) that some edges for the two-dimensional simulation are at 45 degrees to the flow. The non-aligned edges cause the flow to have a finite velocity in the  $y$  direction (Sec. 3.5). It is speculated that these small flow velocities in the  $y$  direction cause the oscillations because the Riemann solver exhibits low dissipation for small flow velocities. This may be related to odd-even decoupling (Sec. 3.5).

Two dimensional EFM solutions are shown in Figures 6.14 - 6.16. The oscillation at the shock are significantly less than the Riemann solver solutions. It is speculated that the extra dissipation ([51] & Sec. 3.2.4) produced by EFM suppressed the oscillations. Note that accuracy of the EFM solutions for this test case is not affected by the issues discussed in Section 6.2 because the average and the effective edge velocities are the same.

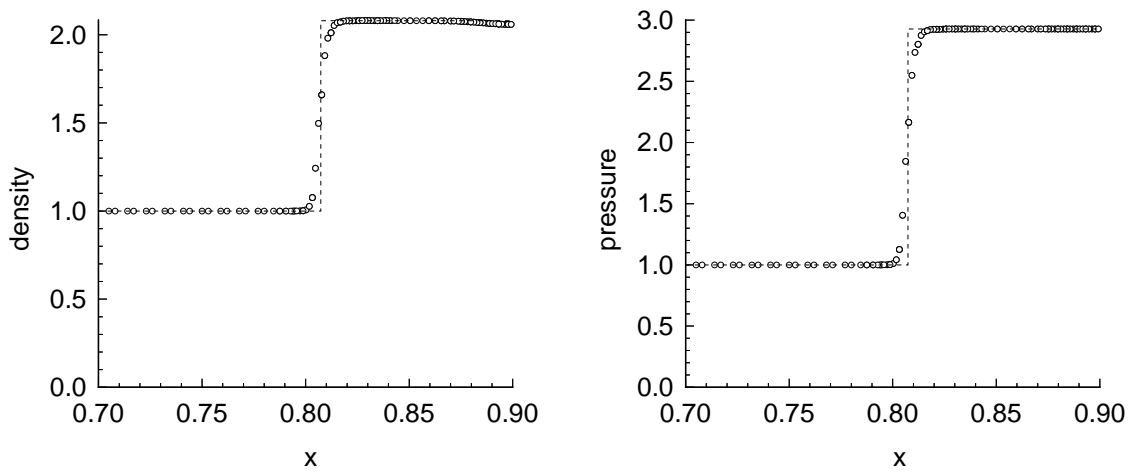


Figure 6.14: Piston compressing gas: comparison of numerical solution ( $\circ$ ) with analytical (dashed line) solution. Minimum area  $1 \times 10^{-5}$ ,  $\alpha = 1 \times 10^{-4}$ . EFM used, first-order interpolation. Data points taken from  $0.05 < y < 0.06$ .

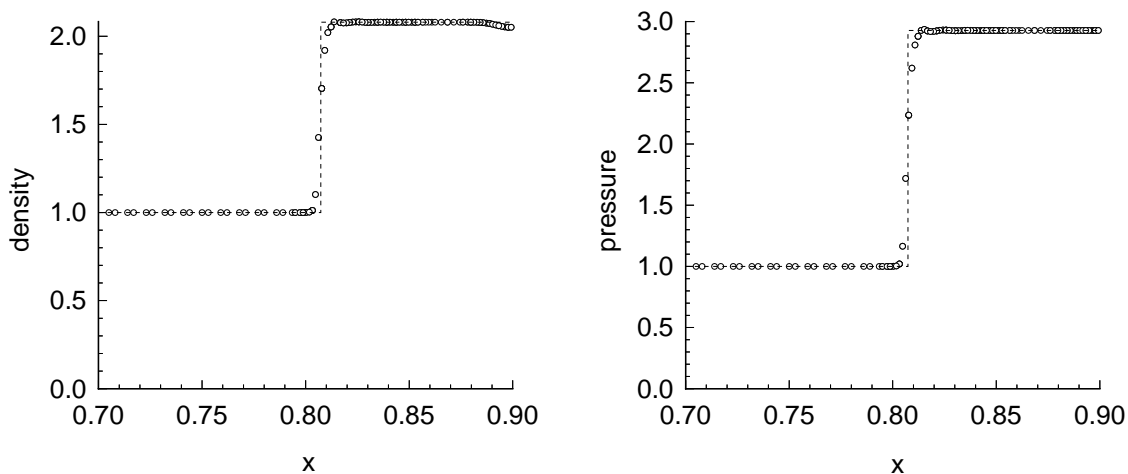


Figure 6.15: Piston compressing gas: comparison of numerical solution (o) with analytical (dashed line) solution. Minimum area  $1 \times 10^{-5}$ ,  $\alpha = 1 \times 10^{-4}$ . EFM used, higher-order interpolation ( $\beta = 1.0$ ). Data points taken from  $0.05 < y < 0.06$ .

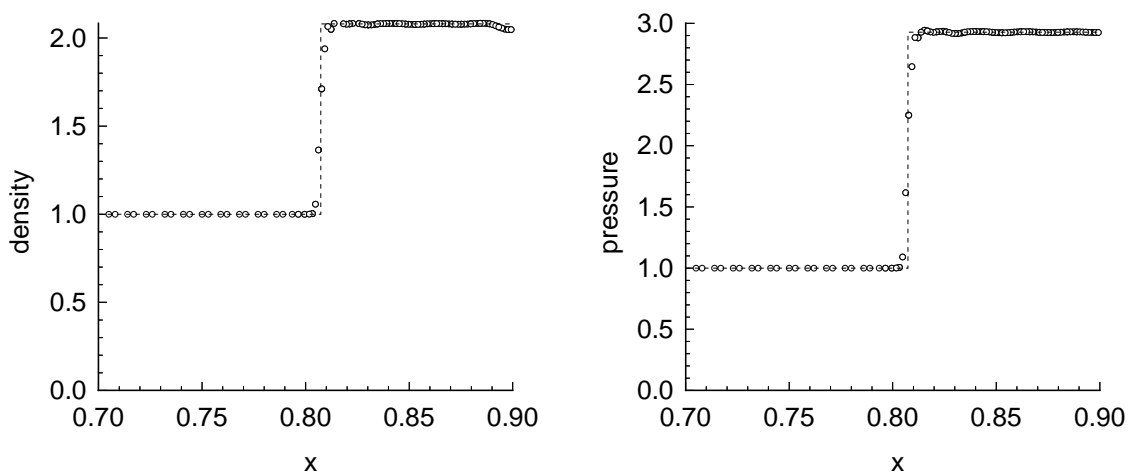


Figure 6.16: Piston compressing gas: comparison of numerical solution (o) with analytical (dashed line) solution. Minimum area  $1 \times 10^{-5}$ ,  $\alpha = 1 \times 10^{-4}$ . EFM used, higher-order interpolation ( $\beta = 2.0$ ). Data points taken from  $0.05 < y < 0.06$ .

There is little difference between the first-order and higher-order Riemann solver solutions, but the higher-order EFM solutions are *sharper* at the shock (i.e. there are fewer cells across the shock) than the first-order EFM solution. It is suspected that the oscillations in the Riemann solver solution near the shock have *turned off* the higher-order interpolation because of the action of the MINMOD function. However, the first-order Riemann solver solution is sharper than any of the EFM solutions.

Two dimensional Riemann solver solutions for the expansion case are shown in Figures 6.17 and 6.18. Solution-adaptive remeshing was used with the minimum volume set to  $1.0 \times 10^{-5}$  ( $\alpha = 1.0 \times 10^{-4}$ ). As expected, the higher-order scheme is closer to the analytical solution than the first-order scheme. No oscillations are present in the solutions, however, the glitch in the density near the piston still occurs.

A mass check was performed before and after all simulations referred to in this section, and discrepancies were close to machine precision.

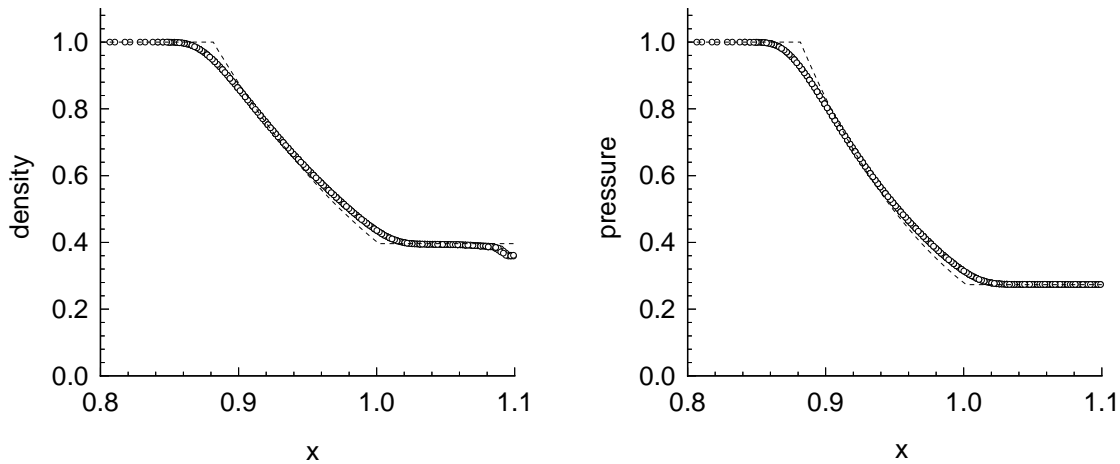


Figure 6.17: Piston expanding gas: comparison of two-dimensional Riemann solver solution ( $\circ$ ) with analytical (dashed line) solution. First-order solution. Data points taken from  $0.05 < y < 0.06$ .

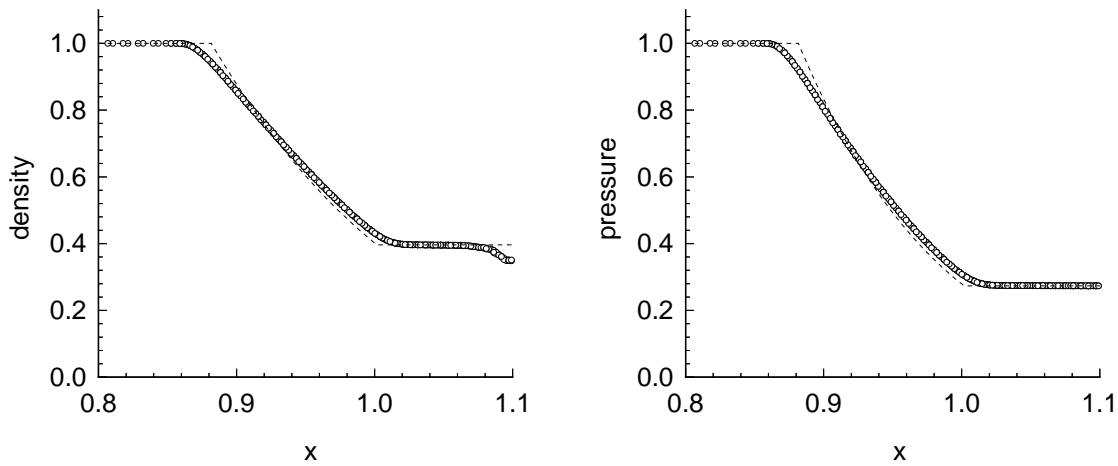


Figure 6.18: Piston expanding gas: comparison of two-dimensional Riemann solver solution (o) with analytical (dashed line) solution. Higher-order interpolation ( $\beta = 2.0$ ). Data points taken from  $0.05 < y < 0.06$ .

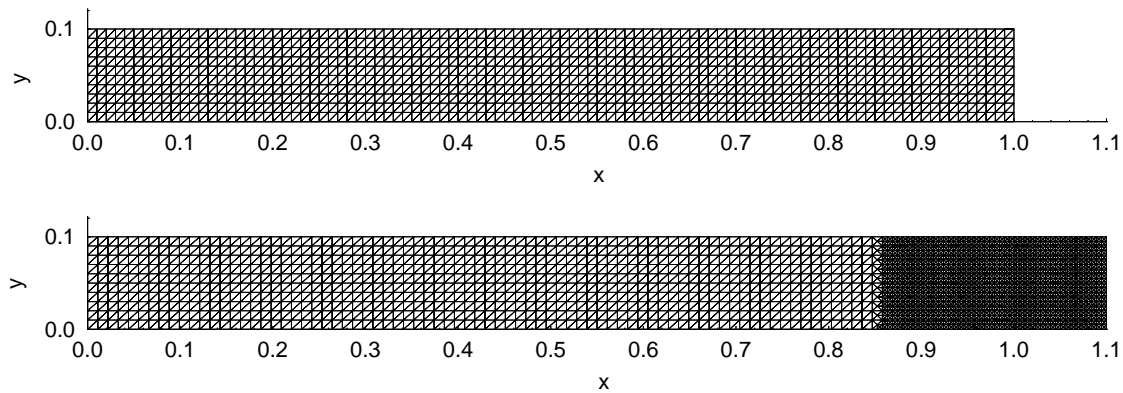


Figure 6.19: Piston expanding gas: (a) initial and (b) final meshes. Minimum area was  $1.0 \times 10^{-5}$ ,  $\alpha = 1.0 \times 10^{-4}$ .

### 6.4.3 Gas driving piston

The motion of a projectile in a tube was examined to verify the ability of the code to solve the coupled rigid-body and fluid-dynamic equations. The initial domain and flow condition are the same as the constant velocity piston problem in the previous section. The boundary initially at  $x = 1.0$  is defined as the interface between the expanding gas and the projectile. It is assumed that there is no gas in front of the projectile.

The motion of the projectile is described by Equation 6.33. As the projectile accelerates, the gas behind the projectile expands. The pressure acting on the piston can be determined by Equation 6.34. Assuming that the velocity of the gas near the piston equals the velocity of the piston, the velocity of the piston can be expressed as an explicit function of time (Eqn. 6.35).

$$\frac{d V_p}{d t} = \frac{P A}{m} \quad (6.33)$$

$$\frac{P}{P_o} = \left[ 1 - \frac{\gamma - 1}{2} \frac{u}{a_o} \right]^{\frac{2\gamma}{\gamma - 1}} \quad (6.34)$$

$$V_p = \frac{2 a_o}{\gamma - 1} \left\{ 1 - \left[ \frac{P_o t (\gamma + 1)}{2 a_o} \left( \frac{A}{m} \right) + 1 \right]^{-\frac{\gamma - 1}{\gamma + 1}} \right\} \quad (6.35)$$

Simulations were performed assuming the mass of the piston was 0.01. The Riemann solver was used to calculate the fluxes for these simulations and the Courant number was set to 0.2. The velocities of the vertices of the mesh were set explicitly as,

$$\mathbf{w} = \frac{V_p x}{x_p} \hat{\mathbf{i}}. \quad (6.36)$$

The errors associated with the velocity of the piston at time,  $t = 0.1$  ( $V_p = 0.651657$ ) for simulations with various minimum cell volumes (solution-adaptive remeshing,  $\alpha = 1.0 \times 10^{-4}$ ) are shown in Table 6.1. The errors are relatively small and converge as the minimum cell volume decreases. It appears that U2DE is solving the coupled equations accurately.

## 6.5 Summary

A code has been described that is capable of performing two-dimensional simulations where one or more rigid bodies interact with a mass of inviscid, compressible



Minimum cell volume	Final number of cells	Error
–	2000	$1.371 \times 10^{-2}$
$4.0 \times 10^{-5}$	2238	$4.686 \times 10^{-3}$
$1.0 \times 10^{-5}$	4120	$2.569 \times 10^{-3}$
$2.5 \times 10^{-6}$	10535	$1.062 \times 10^{-3}$

Table 6.1: Projectile motion: error of piston velocity versus minimum cell volume.

gas. The method used to solve the coupled rigid body motion equations and Euler equations for a moving mesh was described.

The motion of the rigid bodies causes the boundaries of the flow domain to move and the mesh is allowed to deform, while maintaining connectivity. When the minimum cell quality (Sec. 6.3) is less than 0.4, the old distorted mesh is transformed into a new, higher quality mesh. The solution is then transferred from the old mesh to the new.

It was verified that the code satisfies GCL [82] by examining solutions using a mesh with random grid motion. The ability of the code to produce accurate solutions was verified by comparing numerical solutions to analytical solutions for simple interactions, such as a projectile in a tube.

The best interpolation scheme appears to be case dependent and the same can be said for the method of flux calculation. As a general rule, try the Riemann solver first as it generates sharper (presumably more accurate if oscillation free) solutions. If oscillations are present in the solution then use EFM.

# Chapter 7

## Shock induced rupture of thin diaphragms

This chapter examines the shock induced rupture of thin diaphragms. This process occurs within many ground-based hypervelocity experimental facilities. For example, in an expansion tube (Sec. 1.1), the secondary diaphragm is thin and separates the test and acceleration gas. On arrival at the secondary diaphragm, the incident shock is partially reflected as it ruptures the diaphragm. The reflected shock stagnates some of the test gas, increasing its internal energy and the level of molecular dissociation. Significant levels of dissociation in the test gas are undesirable because it is not representative of the ambient air for actual flight. The strength of the reflected shock depends on how the diaphragm, which breaks free from the tube wall, interacts with the flow. Previous one-dimensional models [57, 93, 8] have assumed that the diaphragm mass acted as a piston or wall.

A one-dimensional code AEL1D (described in Appendix B), was used to perform simulations of the shock induced rupture of thin diaphragms, assuming the diaphragm acted as a piston (same model as Bakos & Morgan [8]). The diaphragm inertia model of Morgan & Stalker [57] was also used to describe the interaction between the diaphragm mass and the subsequent flow. Computed and experimentally determined shock trajectories were compared (Sec. 7.2) and computed pressure traces at locations 10 mm upstream and 424 mm downstream were compared with experimental pressure traces (Sec. 7.3). Both comparisons highlight the main flaw of the diaphragm inertia model; the test gas cannot penetrate the diaphragm mass.

The aim of this work was to develop models for the shock induced rupture of thin diaphragms that considered the diaphragm mass and simultaneously allows the test gas to penetrate the plane of the diaphragm. Two multi-dimensional models were examined. The first assumed that the diaphragm vaporised (Sec. 7.4) immediately after rupture. This was implemented by adding gas with the same mass as the diaphragm to a thin strip of cells at the diaphragm location. The second model assumed that the diaphragm shattered (Sec. 7.5) at rupture and introduced a number of diaphragm pieces into the flow which can be treated as rigid bodies.

Before describing the work performed for this thesis, previous work relating to secondary diaphragm rupture is now examined in detail.

## 7.1 Previous work

Morgan & Stalker [57] developed the diaphragm inertia model. It assumed that the diaphragm instantaneously sheared at the walls and flow between the reflected shock and the diaphragm mass (on the upstream side), and between the transmitted

shock and the diaphragm (on the downstream side) was uniform. This model was improved by Bakos & Morgan [8] who used the one-dimensional finite-volume code of Jacobs [38] to solve the unsteady Euler equations for the flow near the diaphragm. This model was used to predict the levels of dissociation in the test gas after it had been processed by the reflected shock and then expanded into the acceleration tube. The level of dissociation predicted was significantly lower than the levels reported by Wilson [93] who assumed that the diaphragm held fast for a specified holding time and then opened instantaneously, thus allowing a sudden expansion. The reason for lower levels was attributed to the rate of expansion which was slower for the diaphragm inertia model. This slower expansion allowed an increased rate of recombination.

Experimental work by Roberts [70] suggests that the strength of the reflected shock can be reduced by using a pre-deformed diaphragm. Experiments were performed in the TQ expansion tube facility at the University of Queensland. The facility was operated in shock tube mode with the gases either side of the secondary diaphragm having the same pressure. The test and acceleration gas were argon. The shock tube fill pressures were 1, 4, and 20 kPa. The strength of the reflected shock for the following diaphragms were measured: 13  $\mu\text{m}$  polyethylene, 25  $\mu\text{m}$  and 50  $\mu\text{m}$  cellophane and 102  $\mu\text{m}$  and 109  $\mu\text{m}$  mylar. Experiments were also performed with pre-deformed 25  $\mu\text{m}$  cellophane. The diaphragm was deformed by maintaining a pressure differential of approximately 80 % of rupture pressure (80 kPa) for 20 minutes prior to the experiment. The deformation of the diaphragm was approximately 10 mm at the centre. The comparison of the sidewall pressure 15 mm upstream for the pre-deformed diaphragm and a planar diaphragm showed that the strength of the reflected shock was considerably reduced. The shift in the effective diaphragm location for the deformed case was considered. It was also estimated that the effective opening time of the diaphragm was reduced.

Paull [62] performed a study of the PISTL expansion tube investigating disturbances in the Pitot pressure trace during the test time. The influence of secondary diaphragm was studied. Pressure traces were recorded at locations 10 mm upstream and 424 mm downstream of the secondary diaphragm (mylar) for two different diaphragm thicknesses, 127 and 6.35  $\mu\text{m}$  (Figs. 7.1 & 7.2). A reflected shock was detected on the upstream pressure trace for the heavier diaphragm but not the lighter diaphragm. Evidence of the reflected shock existing when the lighter diaphragm was used can be seen in the downstream pressure trace as the pressure rose to a level higher than the pressure behind the incident shock.

Daru & Damion [21, 22] perform axisymmetric simulations of the opening of cel-

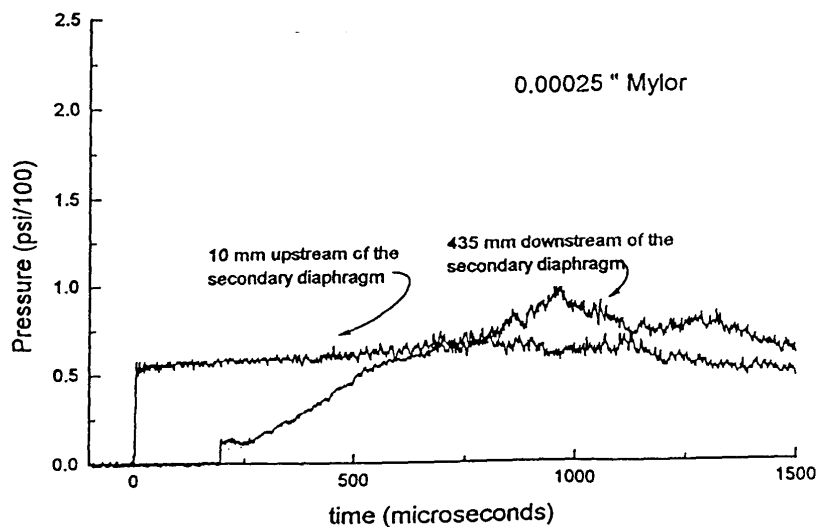


Figure 7.1: Pressure traces up and downstream of the secondary diaphragm for the PISTL expansion tube. The diaphragm was  $6.35 \mu\text{m}$  thick mylar. Taken from Paull [62].

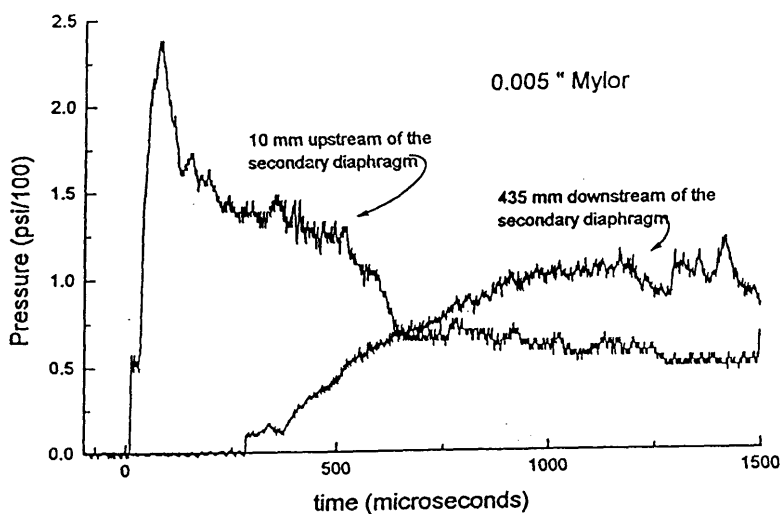


Figure 7.2: Pressure traces up and downstream of the secondary diaphragm for the PISTL expansion tube. The diaphragm was  $127 \mu\text{m}$  thick mylar. Taken from Paull [62].

lophane diaphragms in a shock tube. The diaphragm opening was assumed to be instantaneous and the initial contact surface between the two gases separated by the diaphragm was assumed to be curved. Viscous effects were not considered. Computed downstream pressure traces contained periodic perturbations and were in good agreement with experimental data.

Wilson [95] performed axisymmetric simulations of the HYPULSE expansion tube. The opening of the secondary diaphragm was assumed to be instantaneous. The simulations included finite-rate chemistry and viscous effects. Two operating conditions were examined. Test gas “nonuniformity” was found to be strongly linked to the boundary layer displacement thickness. It was also shown that non-equilibrium chemistry in the flow through the acceleration tube can have a significant effect on the shock speed. It was also concluded that the accuracy of the predictions could be improved by modelling the rupturing of the secondary diaphragm.

## 7.2 Shock trajectories

A computational and experimental study<sup>1</sup> [44] of double-diaphragm drivers for expansion tubes was performed. A double-diaphragm driver is created by adding an extra driver tube (of significant length) downstream of the initial driver section (Fig. 1.1). A heavy diaphragm separates the driver gases between the two driver tubes. In the case of an expansion tube, a light diaphragm separates the downstream driver gas and the test gas. This method can be used to drive faster shock. Note that this device has a different purpose to the classical double-diaphragm device for holding large pressure differences across two relatively weak diaphragms.

The purpose of the study was to determine the effect of heat losses and the non-ideal rupture of the light secondary diaphragm on the driver performance. Four experimental conditions were examined (Table 7.1). The secondary diaphragm was 25  $\mu\text{m}$  thick cellophane for all shots except for shot 6B where 13  $\mu\text{m}$  polyethylene was used. Incident, reflected and transmitted shock trajectories near the secondary diaphragm were experimentally determined. The reflected shock trajectories were determined from the heat transfer traces. It was argued [44] that the shock did not bifurcate and that the heat transfer traces can be used to give a true indication of the position of the reflected shock.

Experimental shock trajectories for condition 3A (Table 7.1) are plotted and com-

---

<sup>1</sup>The experimental work was performed by M. Kendall using the X1 facility at the University of Queensland and the computational work was performed by the author of this thesis.

Shot	$P_1$ (kPa)	$P_5$ (Pa)	$U_{S_1}$ (m/s)	$P_2$ (kPa)	$U_{S_2}$ (m/s)
3A	37.5	900	5900	1600	6820
3B	37.5	450	5900	1600	7780
6A	5	150	8150	410	7900
6B	5	150	7850	380	8700

Table 7.1: Experimental conditions used for double-diaphragm study. State 1 is the fill condition upstream of the diaphragm (helium). State 2 is the flow state behind the incident shock. State 5 is the fill condition downstream of the diaphragm (air). The measured incident and transmitted shock speeds are  $U_{S_1}$  and  $U_{S_2}$  respectively.

pared with trajectories computed using the one-dimensional diaphragm inertia models of Morgan & Stalker [57] and Bakos & Morgan [8] (the one-dimensional code, AEL1D, Appendix B, was used to solve the unsteady Euler equations), (Fig. 7.3). There are significant differences between the computed shock trajectories. The difference between the two models is that Morgan & Stalker approximated that the flow between the reflected shock and the diaphragm mass on the upstream side, and between the transmitted shock and the diaphragm on the downstream side is uniform. Hence, it can be concluded that this approximation can cause significant errors. However, for the reflected shock, the Morgan & Stalker model is closer to the experimental data. This may be due to compensating errors of the flow approximation and the neglected viscous effects.

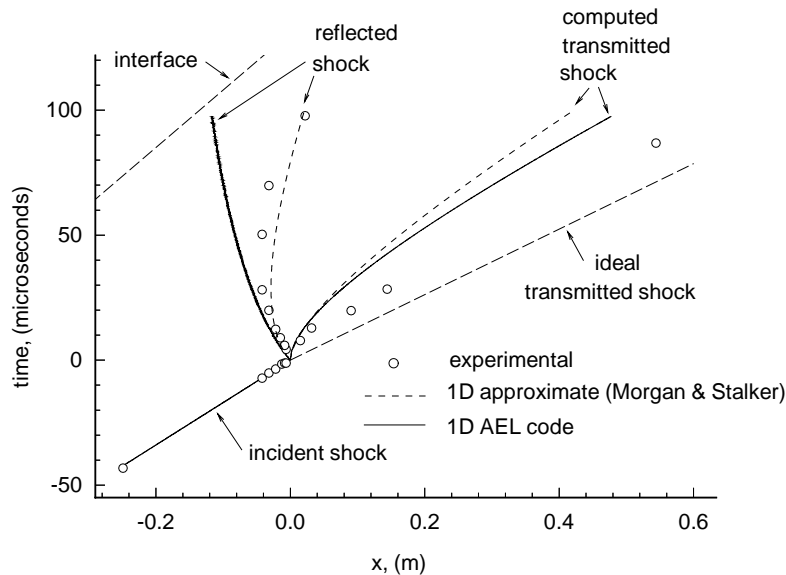


Figure 7.3: Experimentally and numerically calculated shock trajectories near the secondary diaphragm for condition 3A. The ideal transmitted shock is also shown.

Comparisons of experimentally and numerically calculated trajectories for conditions

3B, 6A and 6B are shown in Figures 7.4 – 7.6. The agreement between the computed and the experimental reflected shock trajectories for all conditions is good for the first 30 microseconds (note that the position of the experimental reflected shock is only known for 15 microseconds after the arrival of the incident shock for conditions 6A and 6B). After this time the trajectories diverge. The discrepancy is not due to the arrival of the primary driver gas interface, which arrives well after the trajectories have started to diverge. The interface position was calculated with a boundary layer mass-loss correlation [56]. Possible reasons for the discrepancy are the neglected heat losses, viscous effects, and the upstream gas cannot penetrate the diaphragm mass in the present simulation.

The temperature behind the reflected shock is high enough to cause ionisation and radiation for the conditions examined here. For example, the perfect gas temperature of helium behind the reflected shock for condition 6B is 13500 K if it is assumed that the diaphragm holds its position. The AEL1D code does not consider high temperature effects and this may be a source of error for the current model.

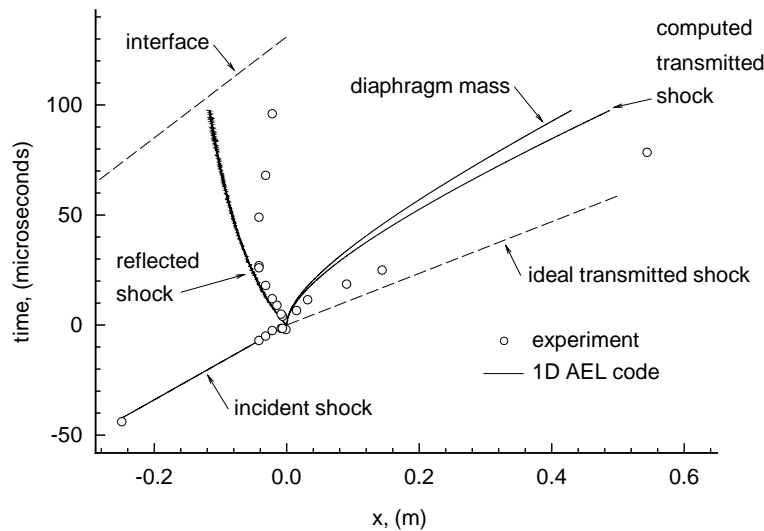


Figure 7.4: Experimentally and numerically calculated shock trajectories near the secondary diaphragm for condition 3B. The ideal transmitted shock is also shown.

The AEL1D code under-estimates the location of the transmitted shock for all conditions. This is because the upstream gas cannot penetrate the diaphragm mass for the diaphragm inertia model. A simulation was performed assuming that the mass of the diaphragm became negligible ( $1.0 \times 10^{-4}$  kg/m<sup>2</sup>), a short time ( $3.0 \mu\text{s}$ ) after the arrival of the incident shock (Fig. 7.7) The agreement between the experimental and numerical reflected shock trajectories has improved. However, the computed transmitted shock is faster than the experimental; although this is expected as vis-



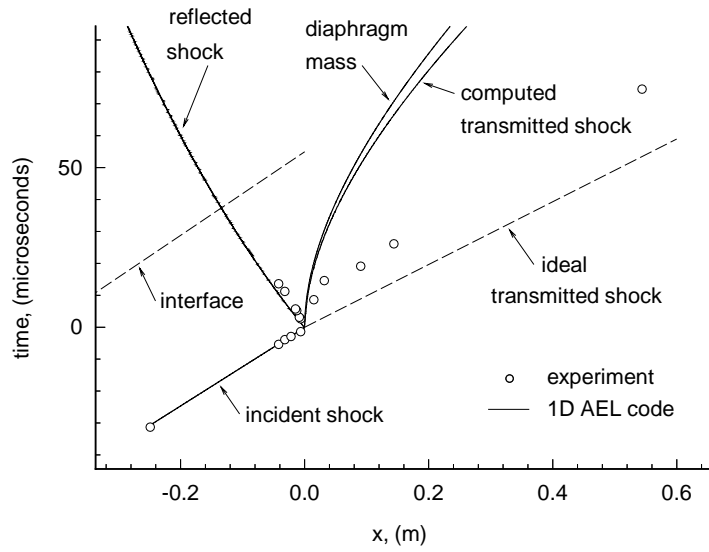


Figure 7.5: Experimentally and numerically calculated shock trajectories near the secondary diaphragm for condition 6A. The ideal transmitted shock is also shown.

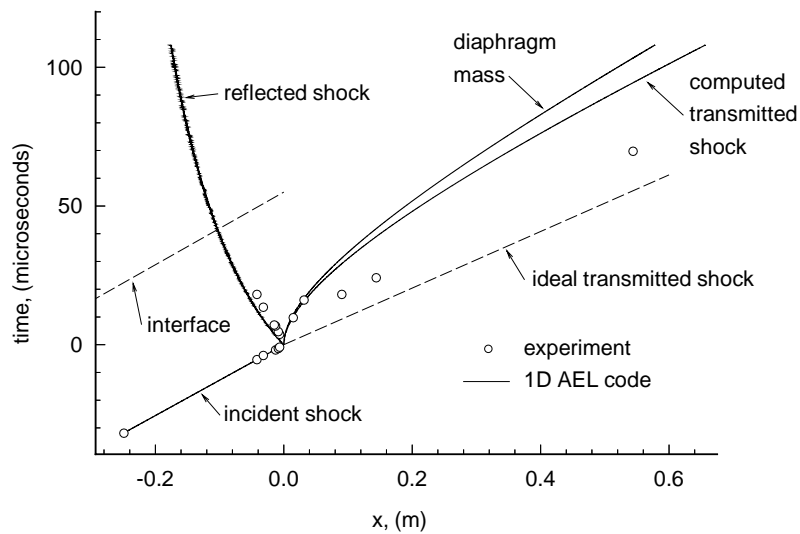


Figure 7.6: Experimentally and numerically calculated shock trajectories near the secondary diaphragm for condition 6B. The ideal transmitted shock is also shown.

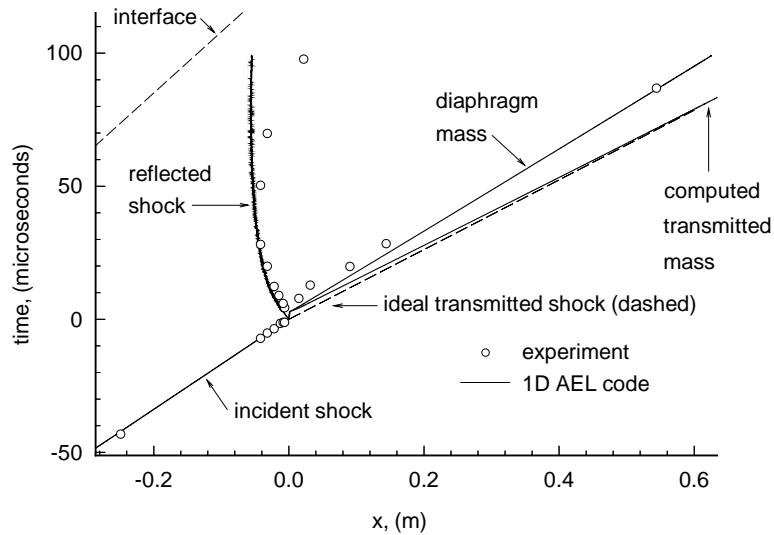


Figure 7.7: Experimentally and numerically calculated shock trajectories near the secondary diaphragm for condition 3A. The diaphragm mass was assumed to be negligible,  $3\mu\text{s}$  after rupture.

cous effects which tend to slow the transmitted shock, have been neglected. It is concluded that the diaphragm mass is behaving like a piston only for a short time after diaphragm rupture. After that time the diaphragm mass ceases to influence the flow. In Sections 7.4 and 7.5, diaphragm mass models which permit the diaphragm mass to be penetrated by the upstream gas are examined.

### 7.3 One-dimensional diaphragm inertia simulations of PISTL expansion tube

The AEL1D code was also used to perform simulations of the rupture of the secondary diaphragm within the PISTL [62] expansion tube which is located at the General Applied Science Laboratories, Ronkonkoma, New York. The diaphragm inertia model of Bakos & Morgan [8] was again used to describe the interaction between the diaphragm mass and the subsequent flow. The fill pressures of the intermediate (air) and the acceleration (air) tubes were 13.8 and 1.38 kPa respectively. The incident shock speed in the intermediate tube was assumed to be 1600 m/s giving the flow condition behind the shock as,

$$\rho = 0.823 \text{ kg/m}^3, P = 413 \text{ kPa}, u = 1400 \text{ m/s}.$$

The internal diameter of the intermediate and acceleration tubes was 89 mm. Simulations were performed for two different diaphragm thicknesses, 6.35 and 127 micrometres. The density of the diaphragm material (mylar) was assumed to be 1000

kg/m<sup>3</sup>.

The agreement between the computed and experimental pressure traces is good for the lighter diaphragm (Figs. 7.8 & 7.9) as the influence of the diaphragm mass is small and the reflected shock is weak (not visible on the upstream trace). The difference in pressure levels is due to the experimental uncertainty associated with the fill condition and the incident shock speed and, possibly, the neglected viscous effects. Note that the experimental data was obtained manually from Figures 7.1 and 7.2.

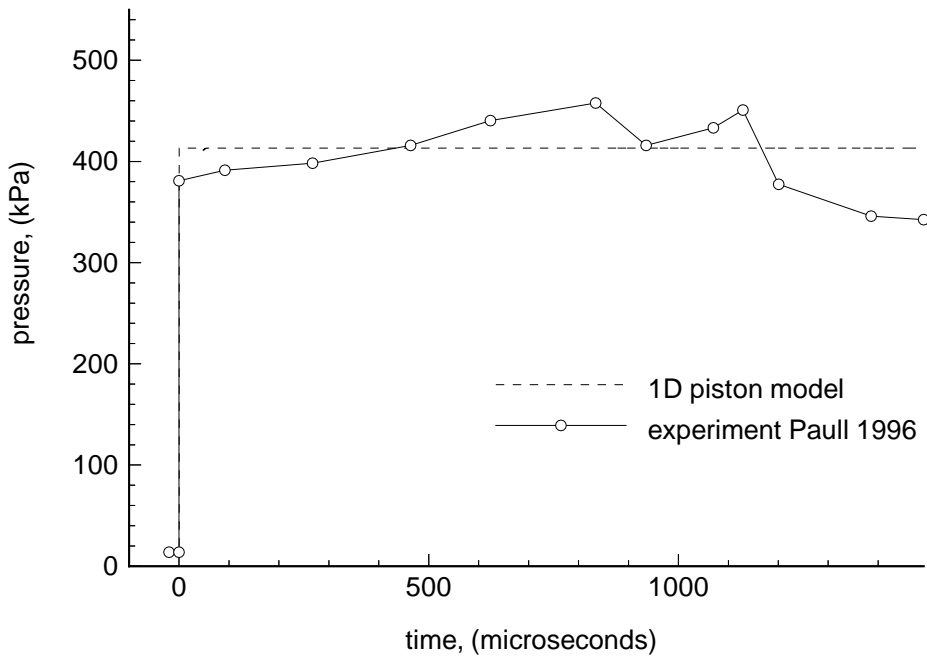


Figure 7.8: Comparison of experimental and computed pressure trace 10 mm upstream of secondary diaphragm ( $6.35 \mu\text{m}$ ) for PISTL expansion tube.

The reflected shock was stronger for the heavier diaphragm and its influence is visible in the upstream pressure trace (Fig. 7.10). The computed reflected shock was stronger than the experiment; the maximum computed pressure was 25 % higher than the experimental value and the computed reflected shock remained upstream of the pressure location for approximately 50 microseconds longer. The general shapes of the upstream traces are similar and overall the agreement is good.

There are significant differences between the computed and experimental downstream pressure trace for the heavier diaphragm (Fig. 7.11). There is a distinct pressure jump in the computed trace as the diaphragm mass passes. The jump occurs because the diaphragm mass is still accelerating and does not occur for the

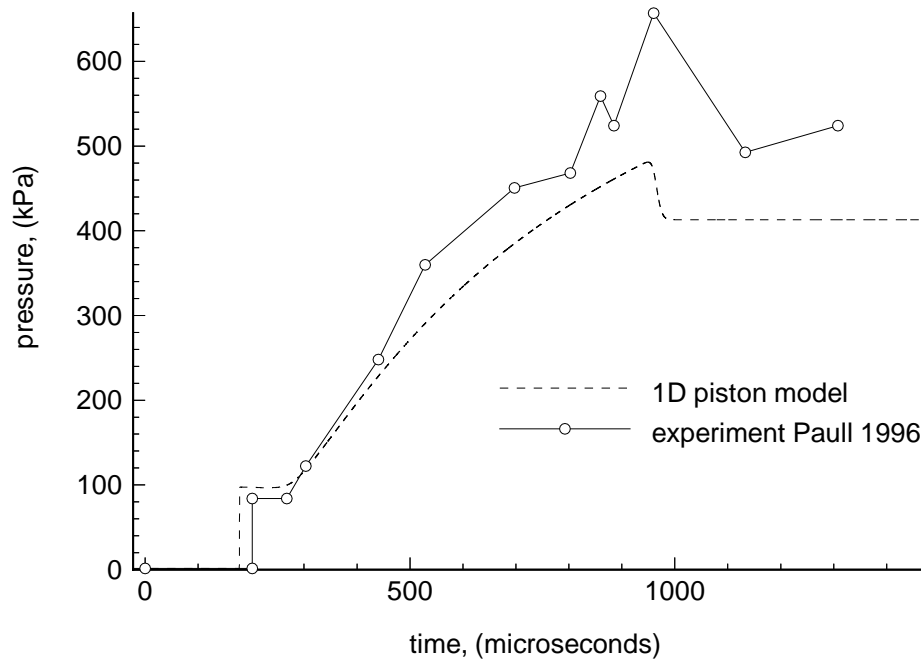


Figure 7.9: Comparison of experimental and computed pressure trace 424 mm downstream of secondary diaphragm ( $6.35 \mu\text{m}$ ) for PISTL expansion tube.

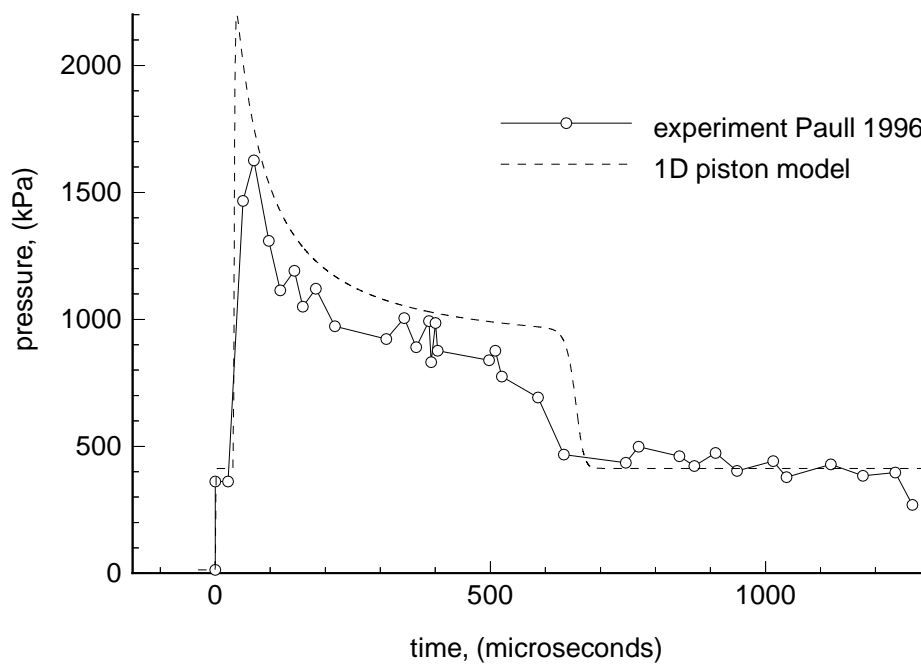


Figure 7.10: Comparison of experimental and computed pressure trace 10 mm upstream of secondary diaphragm ( $127 \mu\text{m}$ ) for PISTL expansion tube.

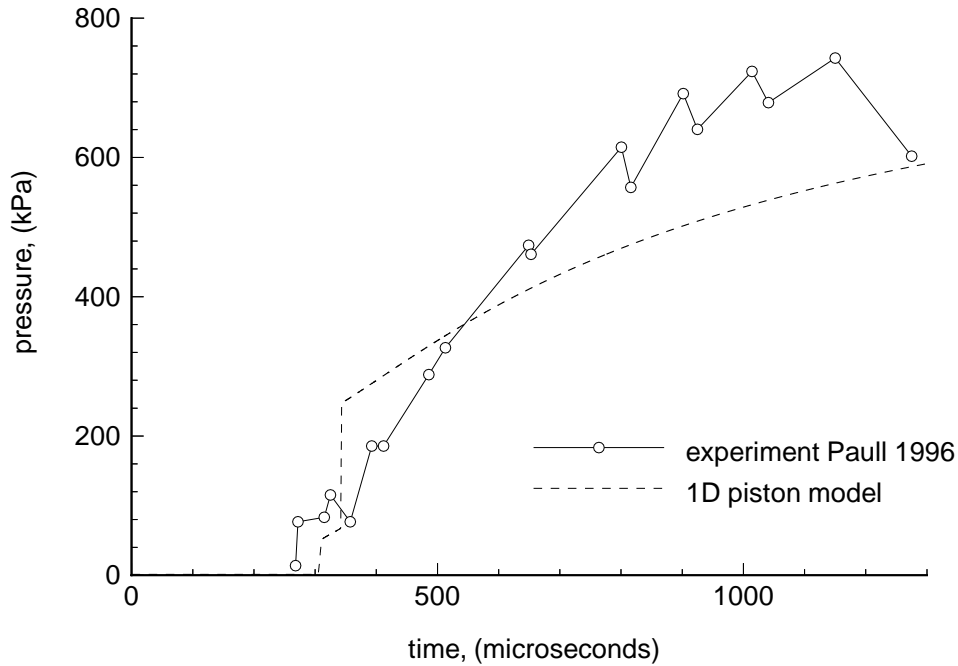


Figure 7.11: Comparison of experimental and computed pressure trace 424 mm downstream of secondary diaphragm ( $127 \mu\text{m}$ ) for PISTL expansion tube.

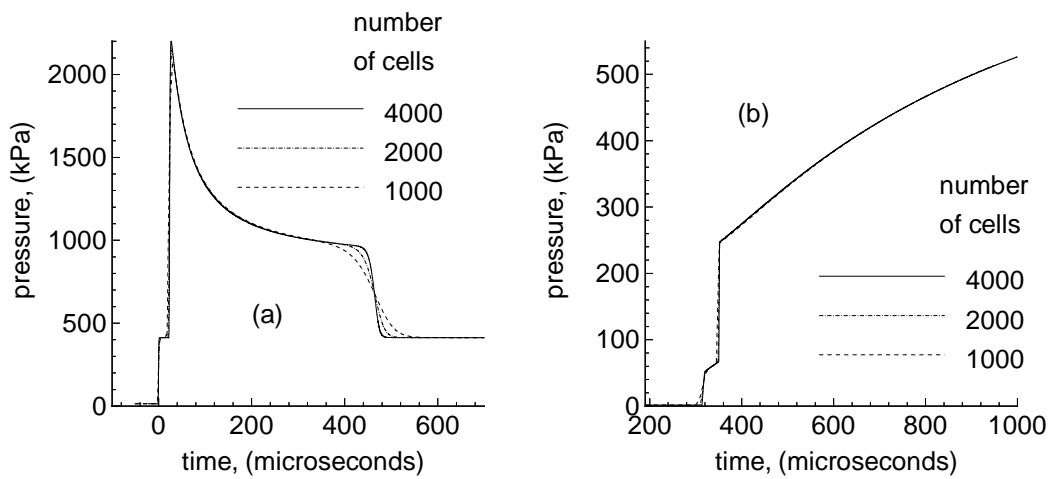


Figure 7.12: Grid convergence of solution for  $127 \mu\text{m}$  thick mylar diaphragm.

lighter diaphragm because it accelerated quickly to the same velocity of the nearby flow. It can be concluded, that the heavier diaphragm mass is not behaving like a planar piston. In Sections 7.4 and 7.5, multi-dimensional models in which the test gas is allowed to penetrate the diaphragm mass are presented.

The grid convergence of the numerical solution for the heavier diaphragm was examined (Fig. 7.12) and found to be satisfactory.

## 7.4 Vaporisation model

Axisymmetric simulations were performed of the secondary diaphragm rupture within the PISTL expansion tube. It was assumed that the diaphragm mass vaporised instantly after the arrival of the incident shock. To model the intact diaphragm, a thin strip of cells were initially ignored (similar to modelling of the opening of the primary diaphragm described in Section 4.2). The status of these cells was changed to flow cells when the pressure at the centre of the diaphragm on the upstream side exceeded 500 kPa. The initial shape of the diaphragm was assumed to be spherical with the centre of curvature lying on the axis of the tube. The initial deflection of the diaphragm was 10 mm at the centre (this was the deflection of the  $6.35 \mu\text{m}$  diaphragm for the experiments, Paull, private communication). The thickness and density of the diaphragm cells depended on the resolution of the simulation and the mass of the diaphragm as listed in Table 7.2. The initial pressure of the diaphragm cells was set to the fill pressure of the acceleration tube, hence the initial temperature of the gas representing the diaphragm mass was low.

Mesh resolution ( $\text{m}^2$ )	Diaphragm mass ( $\text{kg}/\text{m}^2$ )	Gas thickness (mm)	Gas density ( $\text{kg}/\text{m}^3$ )
$1.0 \times 10^{-5}$	0.00635	2.5253	2.5146
$2.5 \times 10^{-6}$	0.00635	1.2626	5.0292
$6.25 \times 10^{-7}$	0.00635	0.6313	10.0584
$1.0 \times 10^{-5}$	0.127	2.5253	50.292
$2.5 \times 10^{-6}$	0.127	1.2626	100.584
$6.25 \times 10^{-7}$	0.127	0.6313	201.168
$1.563 \times 10^{-7}$	0.127	0.3157	402.336
$3.906 \times 10^{-8}$	0.127	0.1578	804.672

Table 7.2: Gas *thicknesses* and densities for various diaphragm masses and mesh resolutions. The  $6.35 \mu\text{m}$  thick diaphragm corresponds to a mass/area of  $0.00635 \text{ kg}/\text{m}^2$ , while the  $127 \mu\text{m}$  diaphragm corresponds to  $0.127 \text{ kg}/\text{m}^2$ .

The time history of density contours for the lighter diaphragm is shown in Figure 7.13. The diaphragm mass is quickly pushed to the wall of the tube, allowing the test gas to penetrate it. The agreement between the computed and experimental pressure traces is good (Figs. 7.14 & 7.15), although this is expected as the influence of the diaphragm mass is small for this condition (note that the one-dimensional diaphragm inertia model also performed well for this condition).

Time histories of the density contours for the heavier diaphragm for two different mesh resolutions are shown in Figures 7.16 ( $6.25 \times 10^{-7} \text{ m}^2$ ) and 7.17 ( $3.90 \times 10^{-8} \text{ m}^2$ ). EFM was used to calculate the fluxes and the noise filter in Equation 2.24 was  $\alpha =$

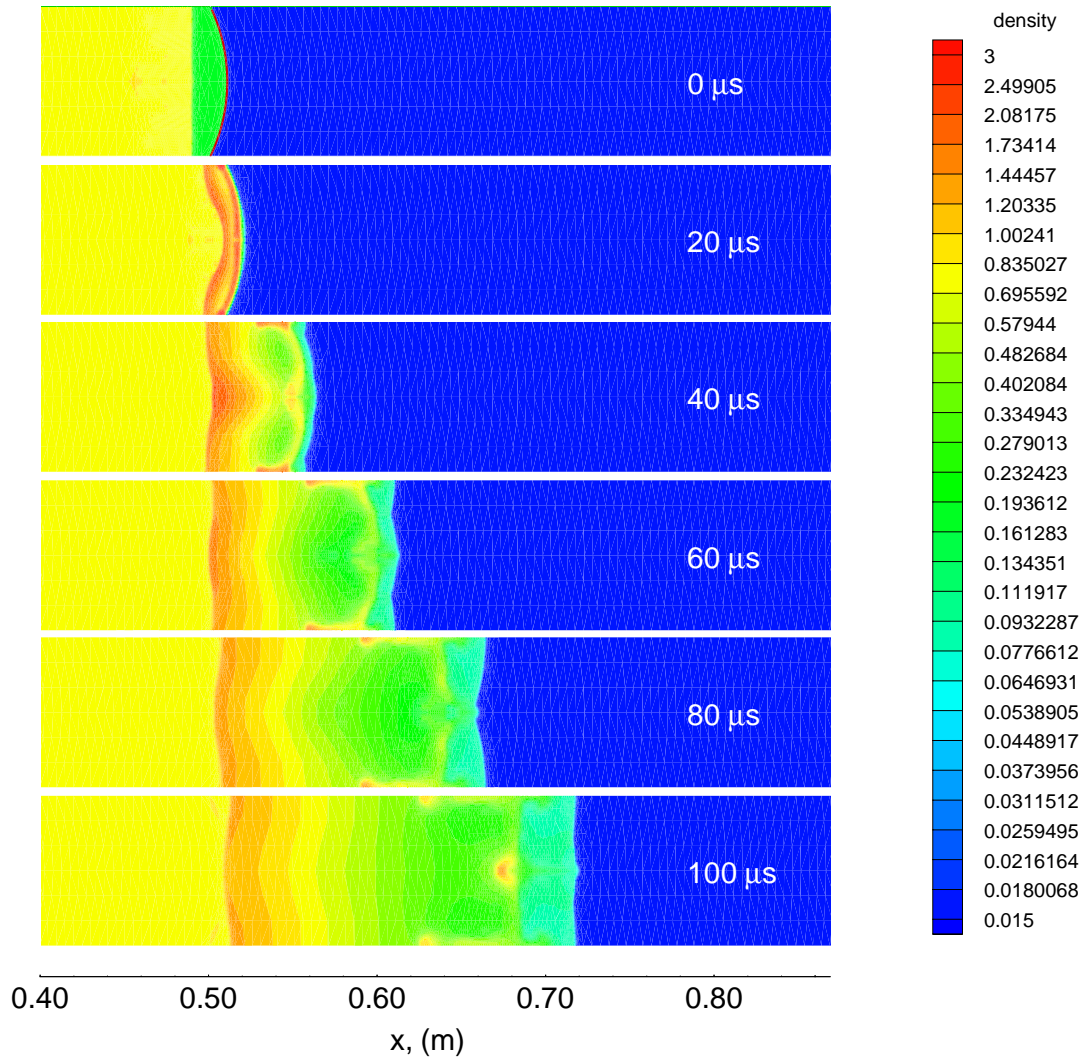


Figure 7.13: Time history of density contour for rupture of the secondary diaphragm. The diaphragm mass was  $0.00635 \text{ kg/m}^2$ . The mesh resolution was  $6.25 \times 10^{-7} \text{ m}^2$ .



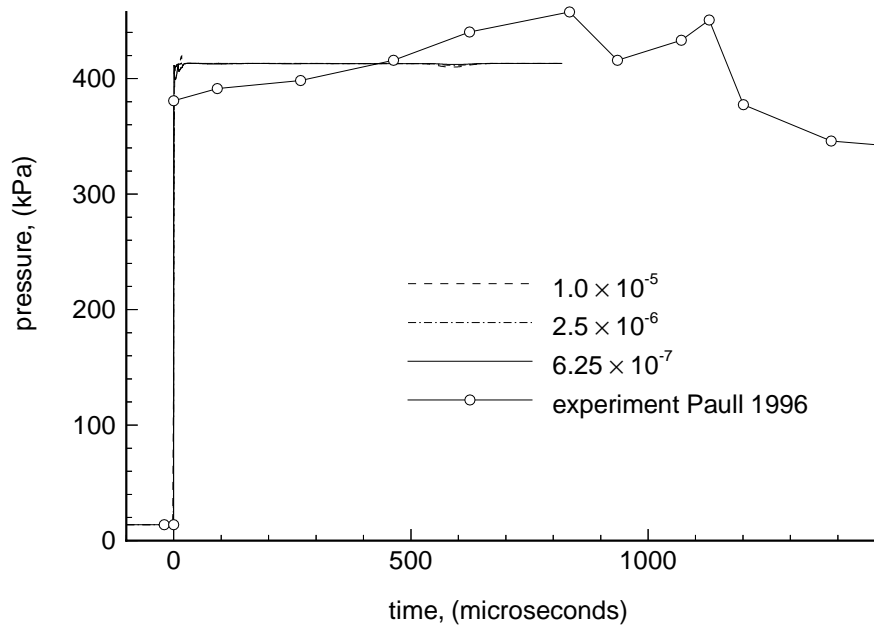


Figure 7.14: Computed and experimental upstream pressure traces (10 mm) for 6.35  $\mu\text{m}$  thick mylar diaphragm. The computed traces assume the diaphragm vaporises immediately after being struck by the incident shock. Minimum cell volumes ( $\text{m}^2$ ) for the simulations are as indicated.

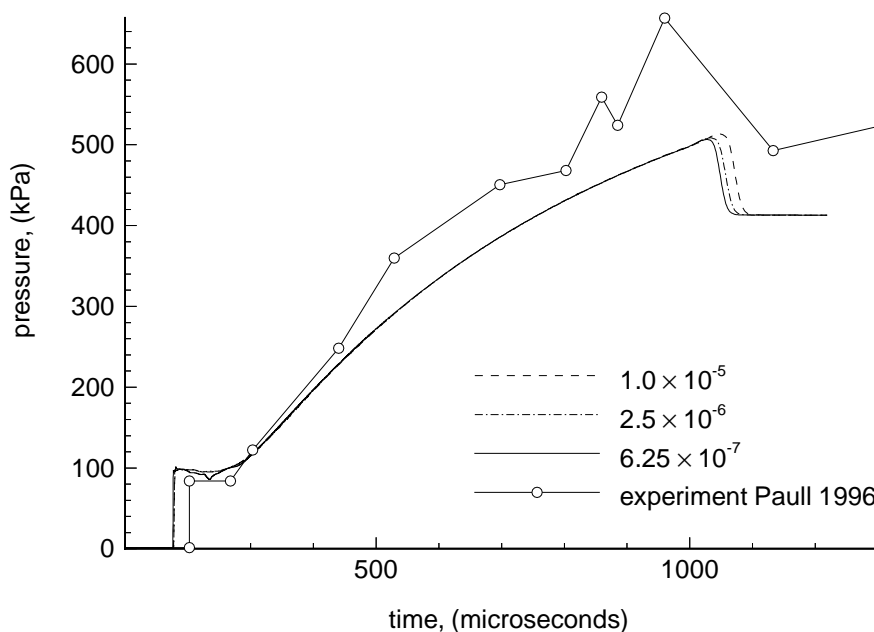


Figure 7.15: Computed and experimental downstream pressures trace (424 mm) for 6.35  $\mu\text{m}$  thick mylar diaphragm. The computed traces assume the diaphragm vaporises immediately after being struck by the incident shock. Minimum cell volumes ( $\text{m}^2$ ) for the simulations are as indicated.

0.01 for both simulations. The higher resolution simulation required 156612 CPU seconds on a SUN workstation (66.0 microseconds per cell per corrector-predictor time-step) for 800 microseconds of flow time. Note that the simulation started 280 microseconds before the incident shock arrived at the upstream pressure location (i.e. the simulation started at time  $t = -280\mu s$ ). The number of cells at time  $t = 200\mu s$  was 35965.

Comparing the two time histories (Figs. 7.16 & 7.17), it can be concluded that grid convergence was not achieved. This can also be seen in the computed downstream pressure trace (Fig. 7.19), although it does appear that grid convergence was achieved for the upstream pressure trace (Fig. 7.18). It was also difficult to achieve grid convergence for the same problem in two-dimensions (Fig. 7.20). This is probably due to numerical diffusion and the changing thickness of the diaphragm. The grid convergence for the two-dimensional model is better than the axisymmetric model. This may be due to numerical jetting (Sec. 3.2.3) or simply the nature of the axisymmetric flow. There is a significant difference between the two-dimensional and axisymmetric computations. There is a pressure jump in the downstream pressure trace from approximately 70 to 160 kPa when the time is approximately 320 microseconds in the two-dimensional result. This pressure jump is not evident in the axisymmetric result or the experimental trace. Even though grid convergence is better for the two-dimensional simulations, the axisymmetric flow model is preferred as it is closer to the physical situation.

The comparison of the computed and experimental pressure traces are shown in Figures 7.18 and 7.19. Comparing Figures 7.11 and 7.19, for the downstream pressure trace, it can be seen that the vaporisation model performs better up to  $t = 400$  microseconds. However, a jump in the computed pressure trace is still evident and occurs when the unexpanded test gas, which is trapped behind the diaphragm mass at the wall, passes the pressure location.

The strength of the reflected shock is less for the vaporisation model than the one-dimensional inertia model (Fig. 7.10), as the reflected shock passes the upstream pressure location for the second time approximately 220 microseconds earlier. Comparing Figures 7.10 and 7.18, for the upstream pressure trace, it can be seen that the one-dimensional piston model is closer to the experimental data.

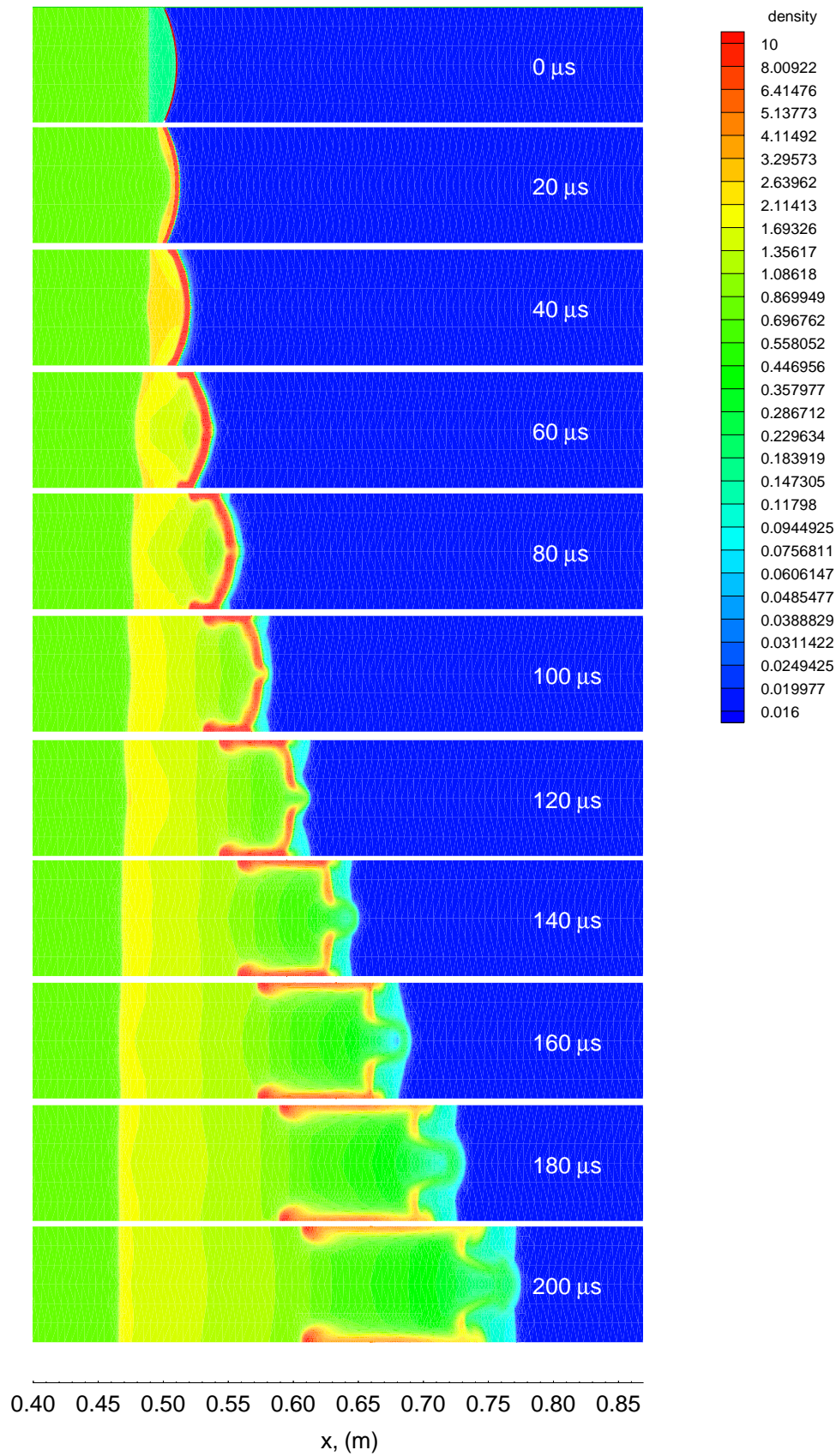


Figure 7.16: Time history of density contour for rupture of the secondary diaphragm. It is assumed that the diaphragm mass vaporises at rupture. The diaphragm mass is  $0.127 \text{ kg/m}^2$ . The mesh resolution is  $6.25 \times 10^{-7} \text{ m}^2$ .

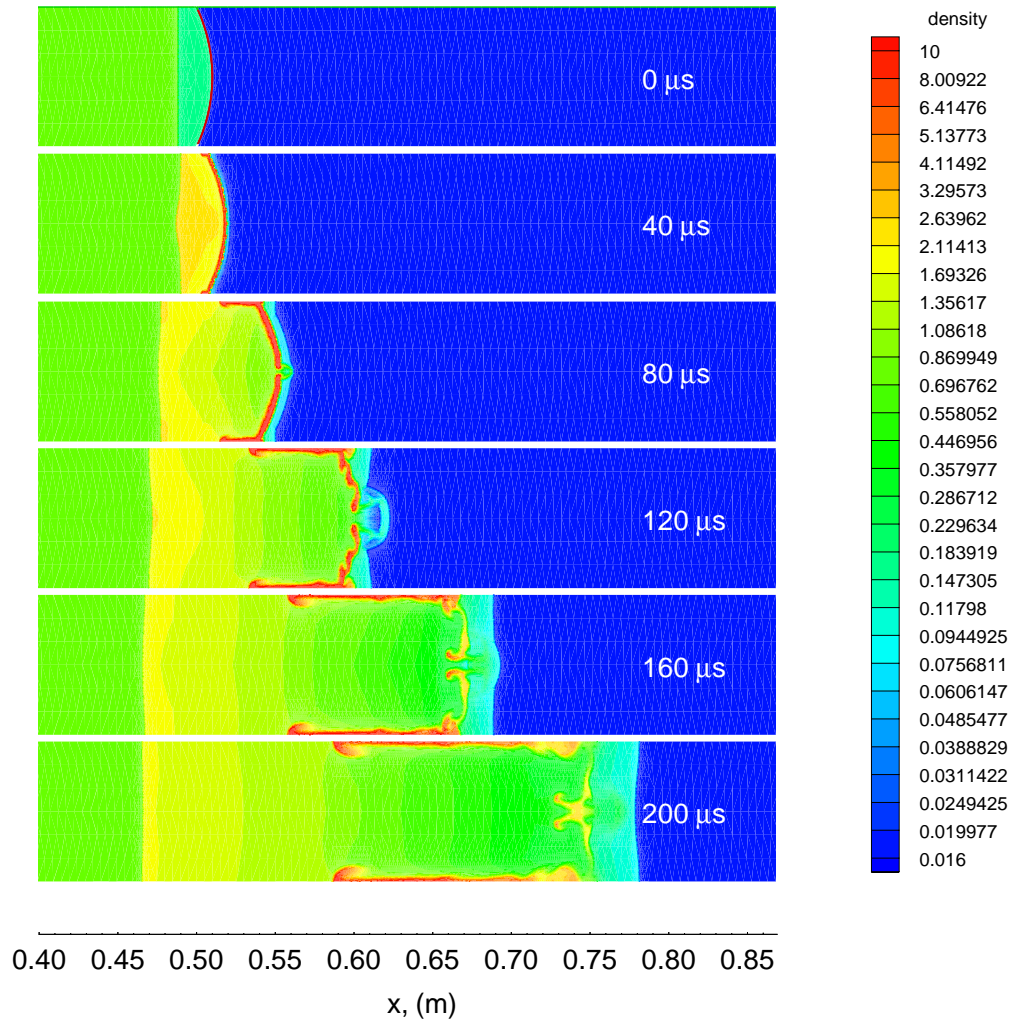


Figure 7.17: Time history of density contour for rupture of the secondary diaphragm. It is assumed that the diaphragm mass vaporises at rupture. The diaphragm mass is  $0.127 \text{ kg/m}^2$ . The mesh resolution is  $3.90 \times 10^{-8} \text{ m}^2$ .

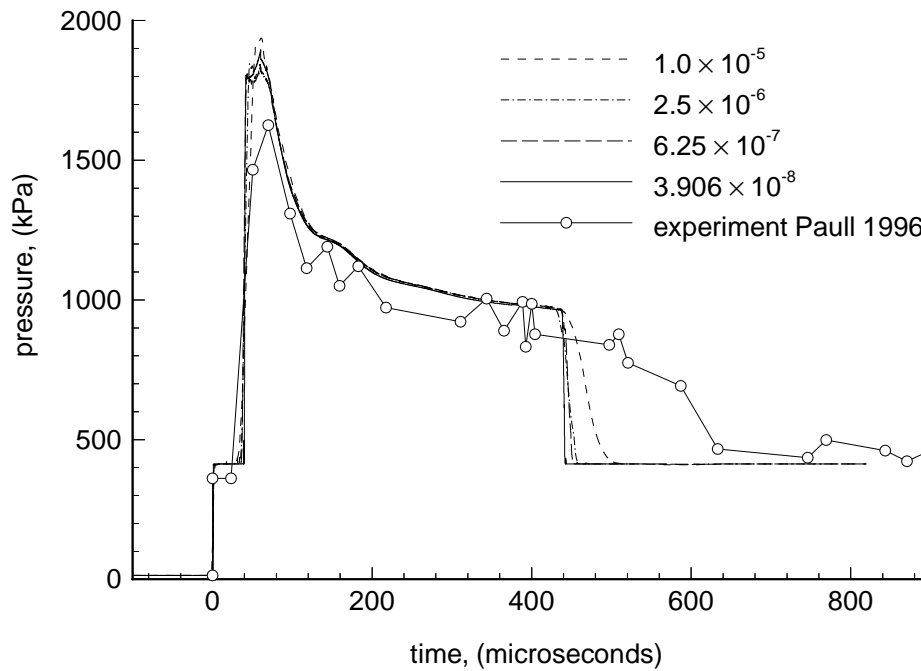


Figure 7.18: Computed and experimental upstream pressure traces (10 mm) for 127  $\mu\text{m}$  thick mylar diaphragm. The computed trace assumes the diaphragm vaporises immediately after struck by the incident shock.

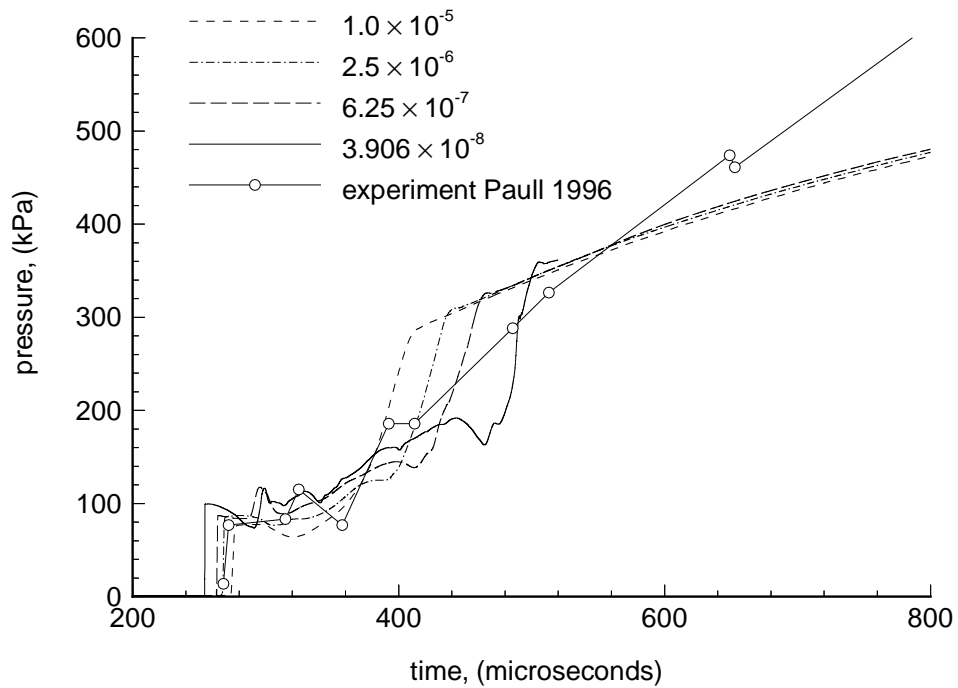


Figure 7.19: Computed and experimental downstream pressure traces (424 mm) for 127  $\mu\text{m}$  thick mylar diaphragm. The computed trace assumes the diaphragm vaporises immediately after struck by the incident shock.

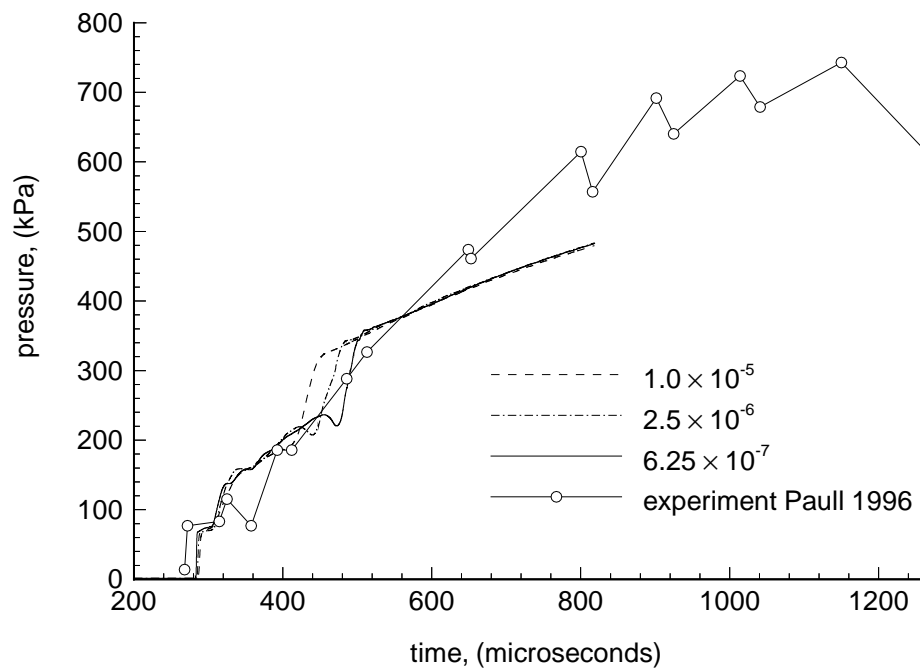


Figure 7.20: Computed and experimental downstream pressure traces (424 mm) for 127  $\mu\text{m}$  thick mylar diaphragm. It is assumed that the diaphragm mass vaporises at rupture. Two-dimensional flow is assumed.

It is speculated that the material of the heavier diaphragm does not fully vaporise during the flow time of interest. In the next section a two-dimensional model where the diaphragm does not vaporise is presented. It is assumed the diaphragm shatters into a number of solid diaphragm pieces which are swept along by the flow.

## 7.5 Fragment model

Two-dimensional simulations were performed of the secondary diaphragm rupture within the PISTL expansion tube assuming the diaphragm shatters into a number of pieces which can be treated as rigid bodies with three degrees of freedom (two in translation and one in rotation). The coupled equations for inviscid compressible flow and rigid body motion were solved by U2DE (Chapters 2 & 6).

Note that these are 2D planar simulations, and that the diaphragm pieces behave like infinitely long thin strips. This does not accurately represent the physical situation where the flow and motion of the diaphragm pieces are three-dimensional. However, performing a three-dimensional simulation of this nature would require major code development and computing resources beyond the resources available for this thesis. Nevertheless, the two dimensional model is worth investigating because it is an improvement on previous one-dimensional models.

### 7.5.1 Numerical modelling

The computational domain was a rectangle, 1.4 metres long and 0.089 metres wide and the boundary of the domain did not change during the simulation. The boundaries at  $y = 0$  and 0.089 m were treated as walls. The boundary at  $x = 0$  m was treated as an in-flow with the flow state being that same as behind the incident shock, and the boundary at  $x = 1.4$  m was treated as out-flow. A section of the initial mesh is shown in Figure 7.21. The diaphragm pieces are located between  $0.5 < x \leq 0.51$  m. Initially it was assumed the diaphragm shattered into seven pieces. Each diaphragm piece had equal mass  $m_f$ , and length,  $L = 11.125$  mm. The initial gap between each diaphragm piece was 1.39 mm. The moment of inertia of each diaphragm piece about its centre of mass is,

$$I_f = \frac{1}{12}m_f L^2. \quad (7.1)$$

The size and shape of the diaphragm pieces remained constant during a simulation.

The initial shape of the diaphragm was assumed to be circular with its centre lying

on the axis of the tube. The deflection of the centre of the diaphragm was 10 mm. The diaphragm was assumed to have a thickness of 20  $\mu\text{m}$ . The thickness of the diaphragm pieces was the same for all simulations as it was assumed that the volume displaced by the diaphragm pieces does not affect the flow development. Simulations for different diaphragm thicknesses were achieved by varying the mass of the diaphragm pieces.

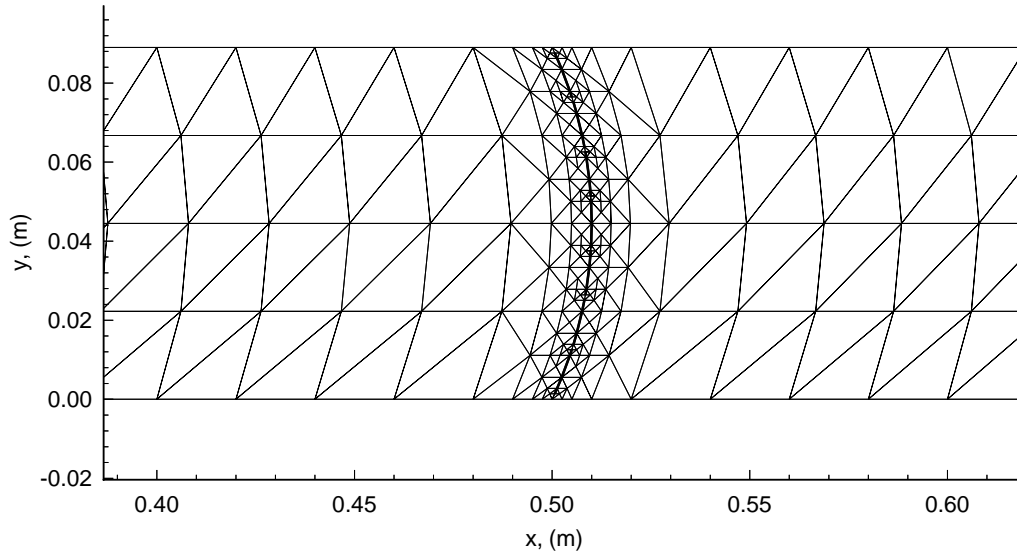


Figure 7.21: Initial mesh for diaphragm fragment model. The diaphragm pieces are represented by the thicker lines ( $0.5 < x \leq 0.51$ ).

Initially the cells representing the acceleration tube were *ignored* and hence the diaphragm behaved like an immovable wall. When the pressure of the cell immediately upstream of the diaphragm and on the wall at  $y = 0$  m exceeded 500 kPa, the diaphragm pieces were released by changing the status of the ignored acceleration tube cells to flow cells.

The diaphragm pieces were allowed to accelerate according to the fluid pressure unless they moved too close to the tube wall. A diaphragm piece was considered to have collided with the wall if one or both of its end vertices was less than 2 mm from the wall and the  $y$ -component of the velocity of the vertex was towards the wall. This prevented cells near the wall and diaphragm piece becoming unreasonably small. For the time-step during which a particle-wall collision occurred, a reaction force was applied to the diaphragm piece from the wall. The collision was assumed to be inelastic and the reaction force was such that the velocity component in the  $y$  direction of the vertex or vertices in contact become zero. The direction of the force was normal to the wall. It was decided not to add the ability to treat particle-particle collisions to the code because it would not improve the accuracy of the modelling.



If two diaphragm pieces did become close, the simulation stopped because cells near the pieces became unacceptably small. It was rare for diaphragm pieces to collide when the collisions between the particles and the walls were assumed to be inelastic.

### 7.5.2 Seven piece simulation

The time history of the density contours and diaphragm particles ( $127 \mu\text{m}$ ) are shown in Figures 7.22 - 7.25. The mesh resolution of the simulation was  $2.5 \times 10^{-6} \text{ m}^3$ . The Riemann solver was used to calculate the fluxes. The Courant number was  $\sigma = 0.3$ . The noise filter coefficient in Equation 2.24 was  $\alpha = 0.1$ . The simulation required approximately 374000 CPU seconds on a Silicon Graphics Power Challenge (94 microseconds per cell per corrector-predictor time-step) for 960 microseconds of flow time. Note that the simulation started 280 microseconds before the incident shock arrived at the upstream pressure location (i.e. the simulation started at time  $t = -280 \mu\text{s}$ ). The number of cells at time  $t = 400 \mu\text{s}$  was 27383. The mesh at 120 microseconds is shown in Figure 7.26.

The reflected shock is clearly visible in Figures 7.22 and 7.24 and travels upstream until approximately  $160 \mu\text{s}$ , and then is swept downstream. A system of shocks develop downstream of the diaphragm pieces processing the test gas, which over-expands as it jets through the gaps between the diaphragm pieces. The transmitted shock is also clearly visible as it progresses down the acceleration tube.

The initial flow and distribution of diaphragm pieces was symmetric about the axis of the tube and, it was expected that the flow and the distribution of the diaphragm pieces would remain symmetric during the simulation. However, at later times ( $t = 400 \mu\text{s}$ ) the distribution of diaphragm pieces was not symmetric. This was due to the mesh not being symmetric and the solution being grid dependent.

The comparisons of the computed and experimental pressure traces for upstream and downstream locations for both diaphragm thicknesses are shown in Figures 7.27 - 7.30.

In the simulation, the computed reflected shock for the  $127 \mu\text{m}$  thick diaphragm arrives at the upstream pressure location significantly later ( $24 \mu\text{s}$ ) than in the experiment. The reflected shock is also swept downstream considerably earlier ( $250 \mu\text{s}$ ) than for the experiment. It can be concluded that the fragment model in its current form is under-predicting the strength of the reflected shock. In fact, at this stage the vaporisation model is closer to the experimental trace. In the next two subsections, additions to the fragment model, which improve the comparison with

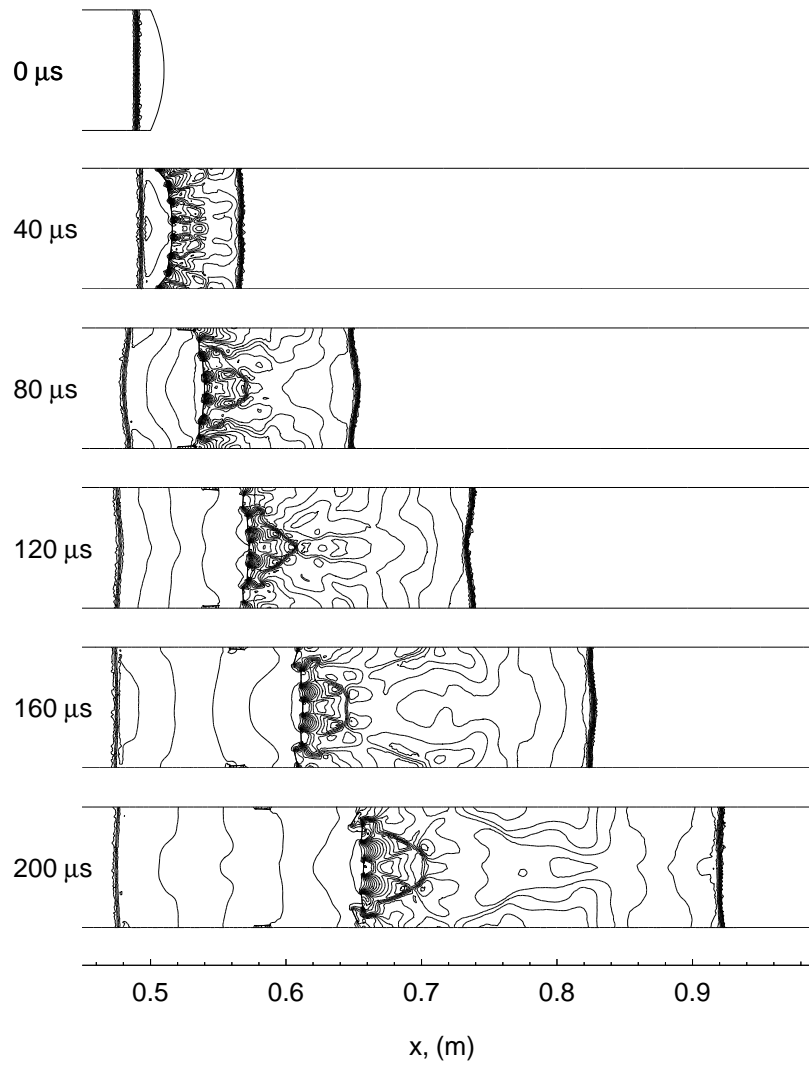


Figure 7.22: Time history (0 - 200 microseconds) of density contours for the seven piece fragment model. Diaphragm thickness is  $127 \mu\text{m}$ .

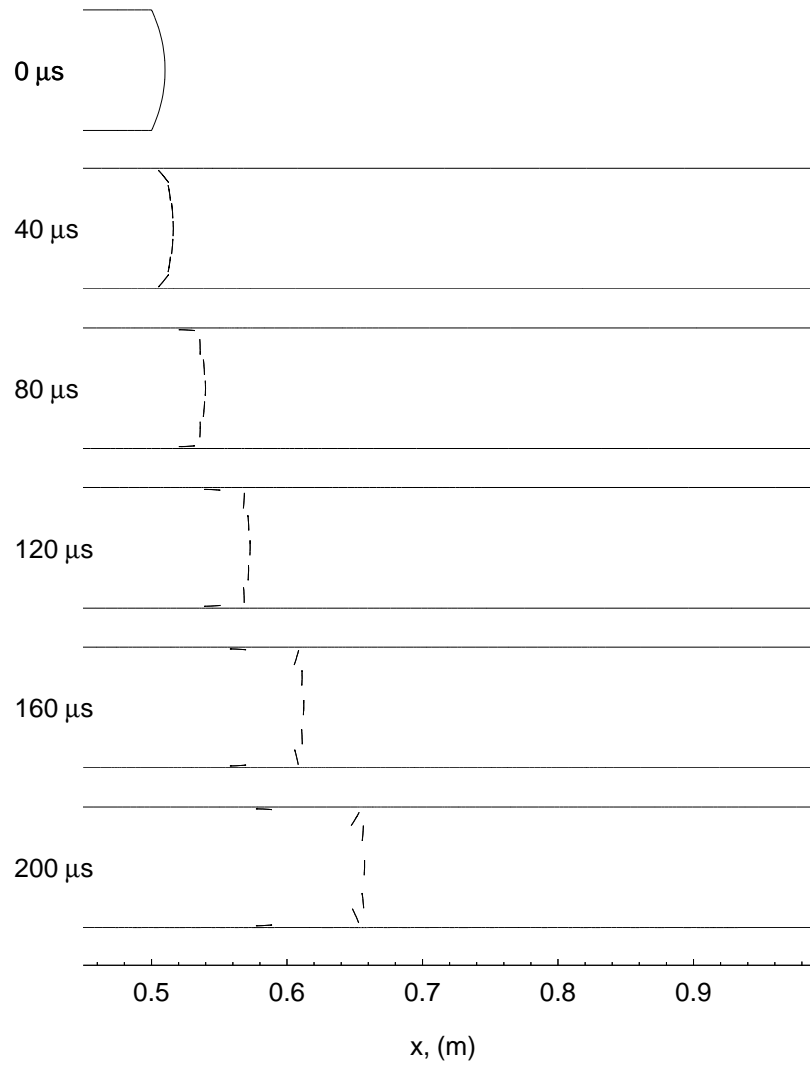


Figure 7.23: Time history (0 - 200 microseconds) of diaphragm pieces for the seven piece fragment model. Diaphragm thickness is  $127 \mu\text{m}$ .

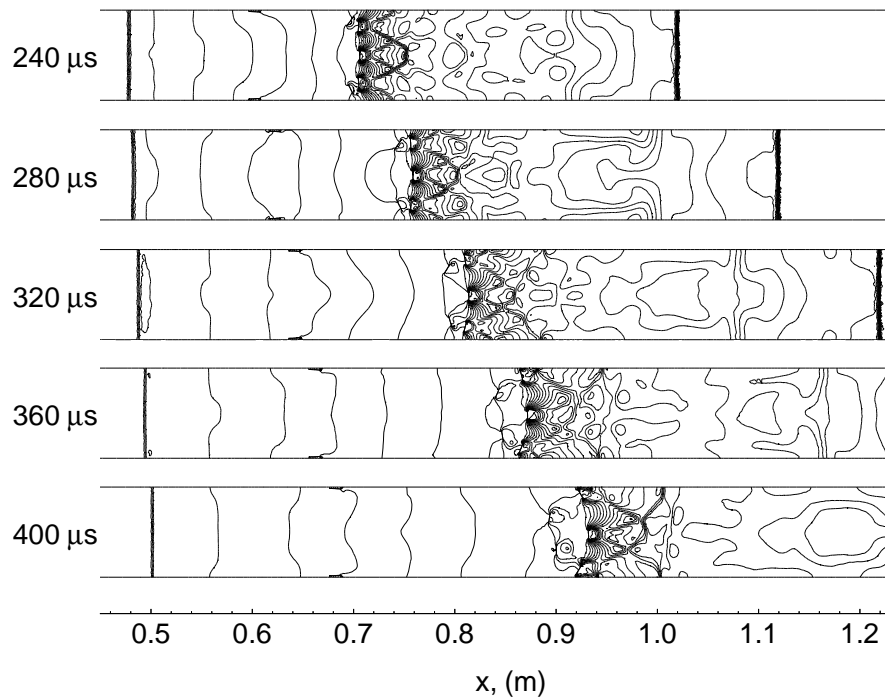


Figure 7.24: Time history (240 - 400 microseconds) of density contours for seven piece fragment model. Diaphragm thickness is  $127 \mu\text{m}$ .

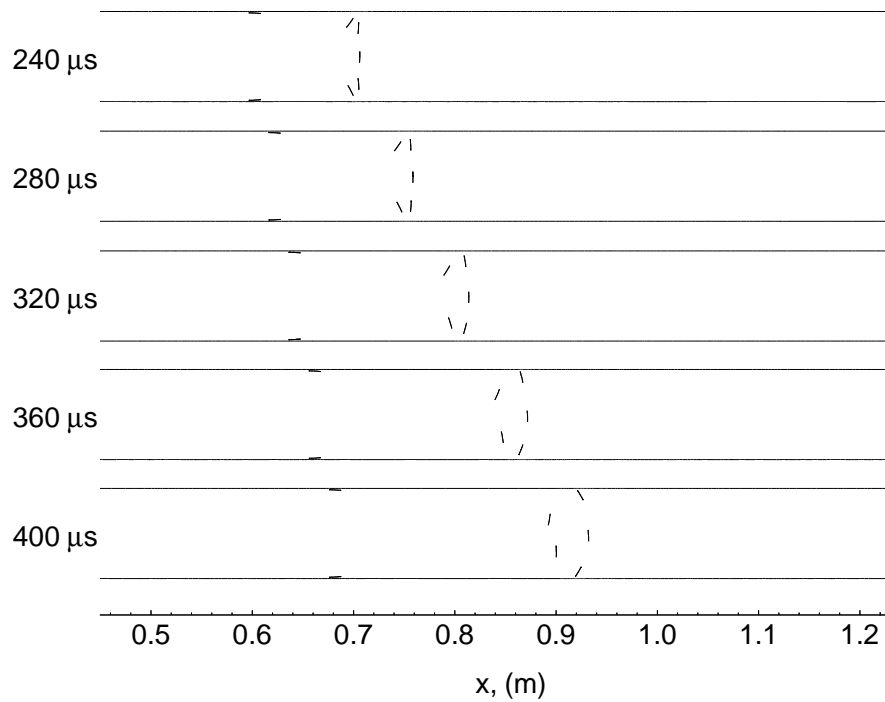


Figure 7.25: Time history (240 - 400 microseconds) of diaphragm pieces for the seven piece fragment model. Diaphragm thickness is  $127 \mu\text{m}$ .

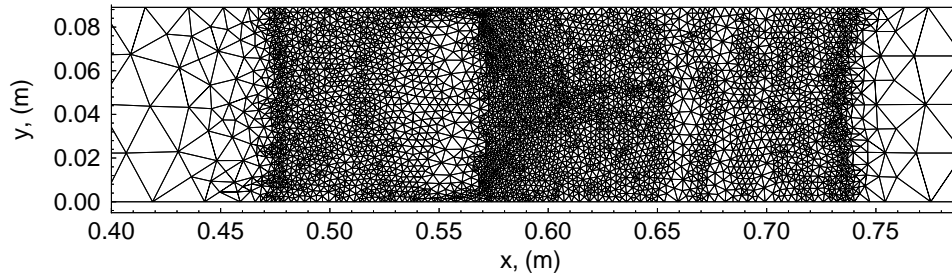


Figure 7.26: Mesh at 120 microseconds for seven piece fragment simulation. The mesh resolution is  $2.5 \times 10^{-6} \text{ m}^3$ . Diaphragm thickness is  $127 \mu\text{m}$ .

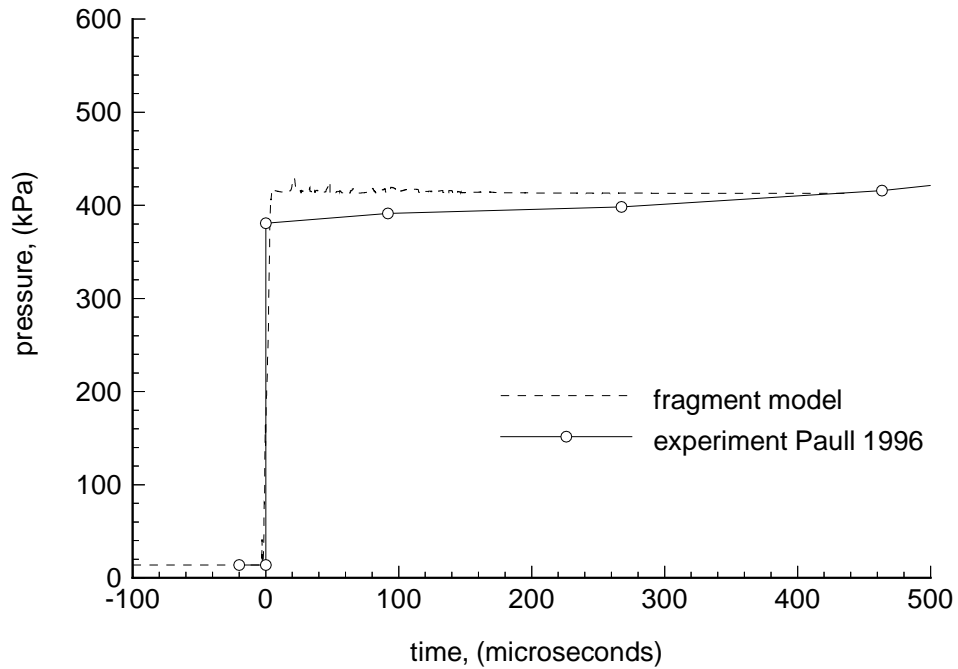


Figure 7.27: Comparison of experimental and computed (seven piece fragment model) pressure trace 10 mm upstream of secondary diaphragm. Diaphragm thickness is  $6.35 \mu\text{m}$ .

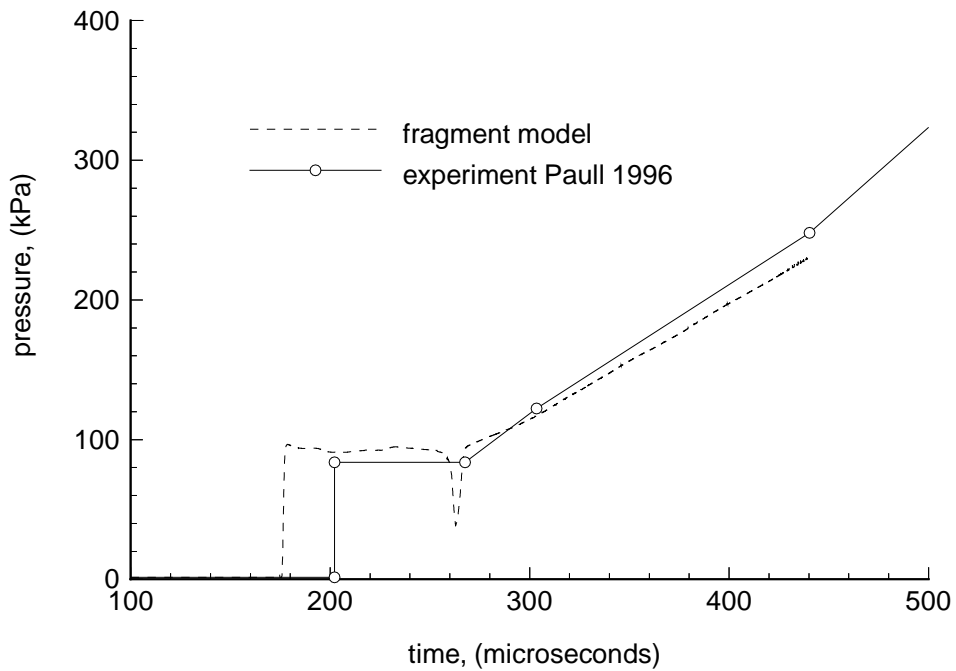


Figure 7.28: Comparison of experimental and computed (seven piece fragment model) pressure trace 424 mm downstream of secondary diaphragm. Diaphragm thickness is  $6.35 \mu\text{m}$ .

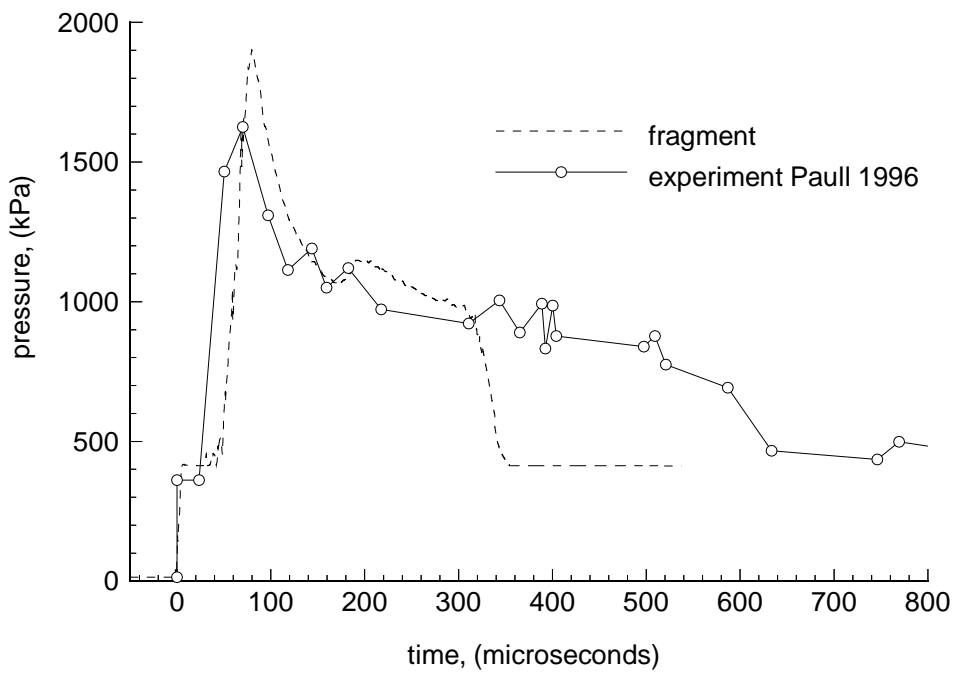


Figure 7.29: Comparison of experimental and computed (seven piece fragment model) pressure trace 10 mm upstream of secondary diaphragm. Diaphragm thickness is  $127 \mu\text{m}$ .

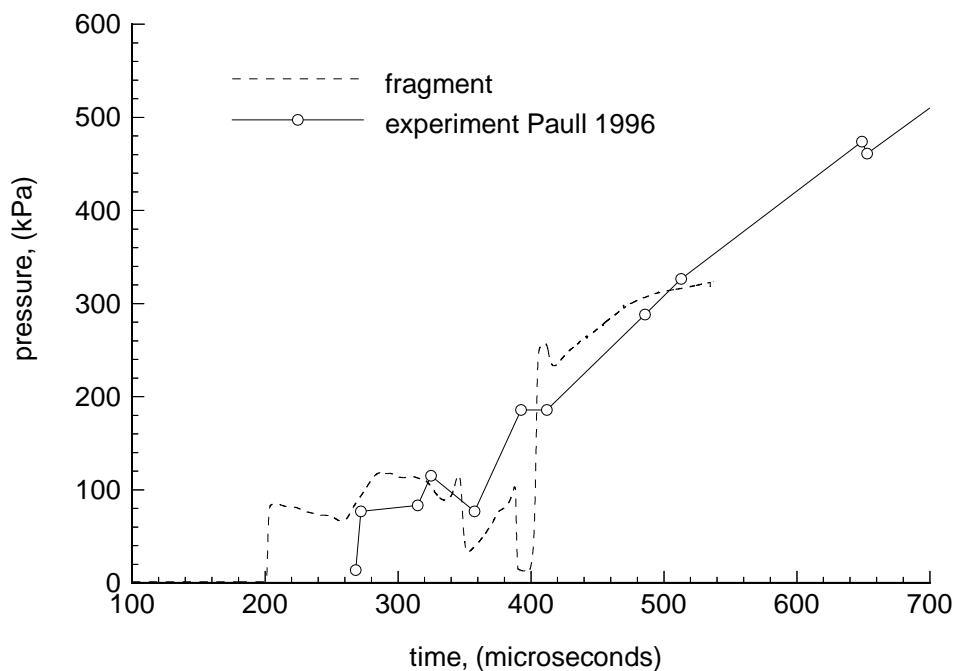


Figure 7.30: Comparison of experimental and computed (seven piece fragment model) pressure trace 424 mm downstream of secondary diaphragm. Diaphragm thickness is  $127 \mu\text{m}$ .

the experimental data will be discussed.

The computed downstream pressure traces exhibit dips ( $t \approx 260 \mu\text{s}$  for lighter diaphragm and  $t \approx 350 - 400 \mu\text{s}$  for the heavier diaphragm). This is because the test gas is over-expanding as it jets through the gaps in the diaphragm pieces. This can be seen in Figure 7.24. These dips are not present in the experimental traces. Also, the arrival of the computed transmitted shock is significantly earlier ( $25 \mu\text{s}$  for the lighter diaphragm and  $70 \mu\text{s}$  for the heavier diaphragm) than the experimental traces.

A simulation was performed assuming that the collisions between the diaphragm pieces and the wall were elastic. The time history of the density contours and diaphragm pieces are shown in Figures 7.31 and 7.32. The simulation ceased when two of the diaphragm pieces collided. Overall, there was little difference between the pressure traces for the elastic and non-elastic particle-to-wall collisions (Figs. 7.33 & 7.34).

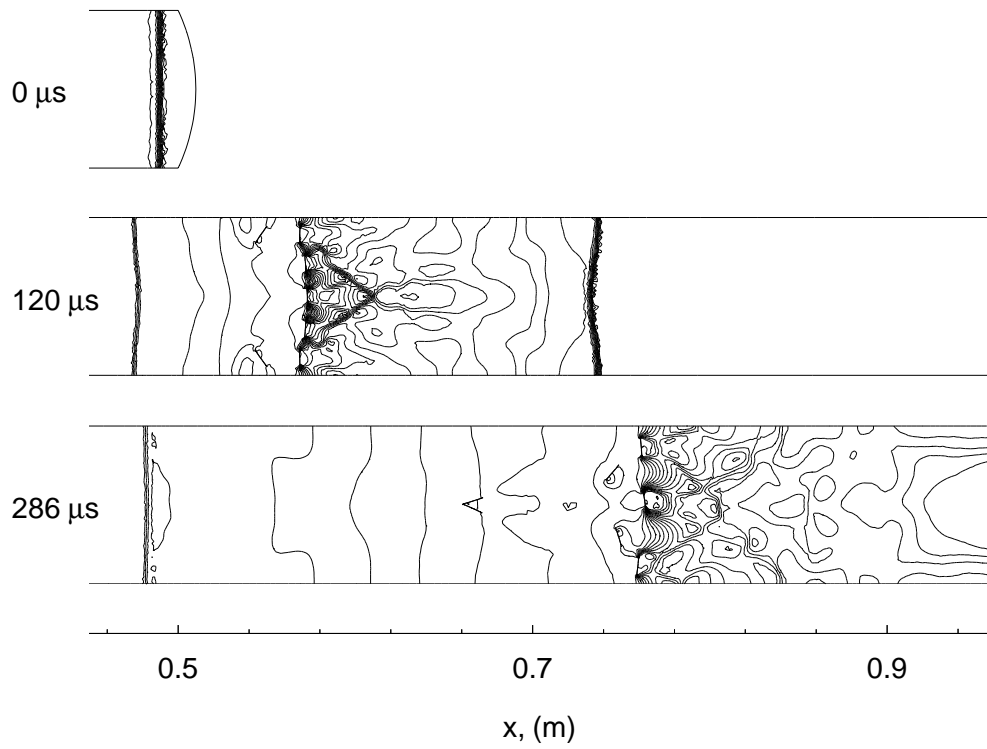


Figure 7.31: Density contours for the flow near the secondary diaphragm when collisions between diaphragm pieces and the wall are assumed to be elastic. Diaphragm thickness is  $127 \mu\text{m}$ .

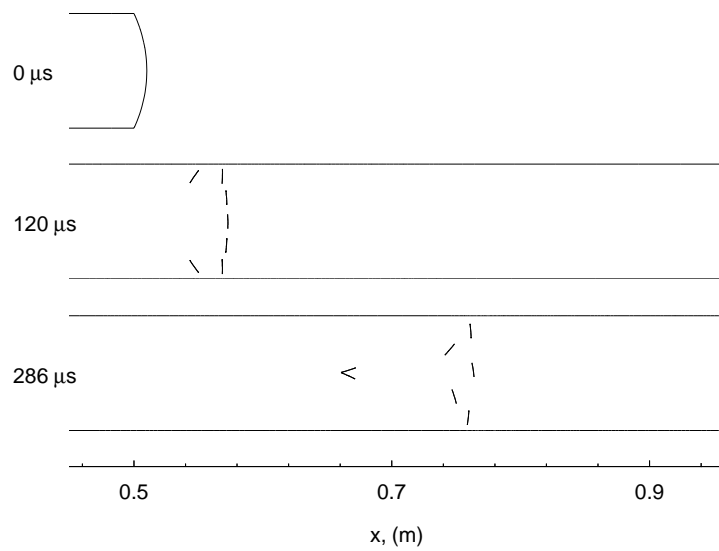


Figure 7.32: Motion of diaphragm pieces when collision between diaphragm pieces and the wall are assumed to be elastic. Diaphragm thickness is  $127 \mu\text{m}$ .



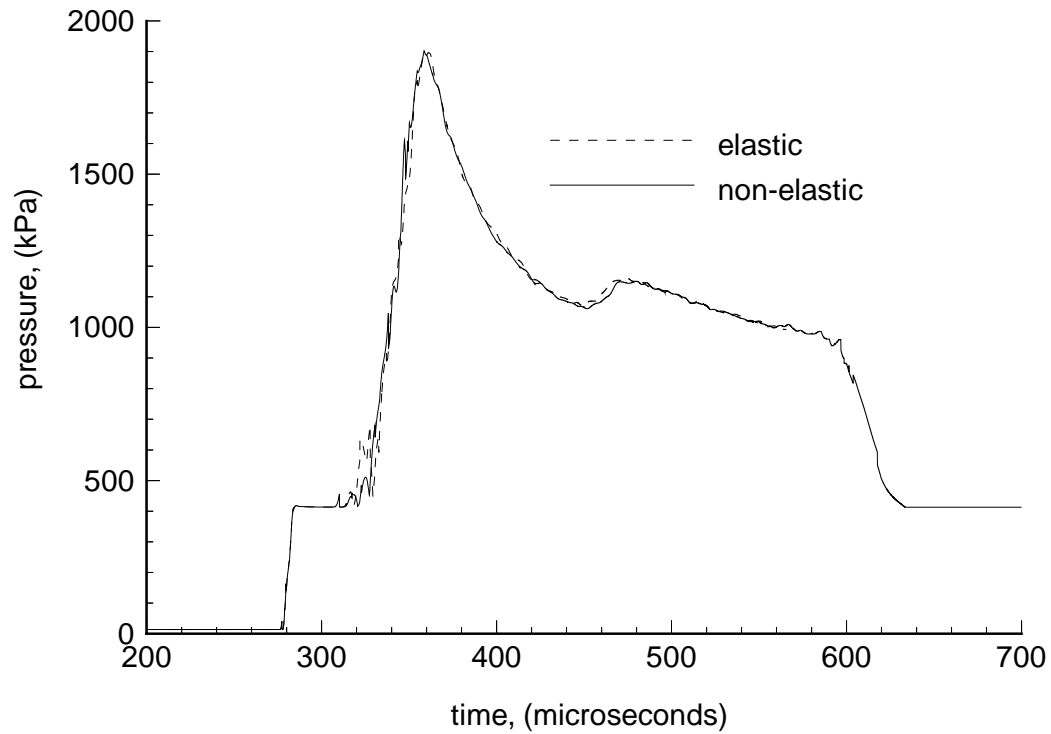


Figure 7.33: Comparison of the computed upstream pressure traces for elastic and inelastic collisions at the tube wall. Diaphragm thickness is  $6.35 \mu\text{m}$ .

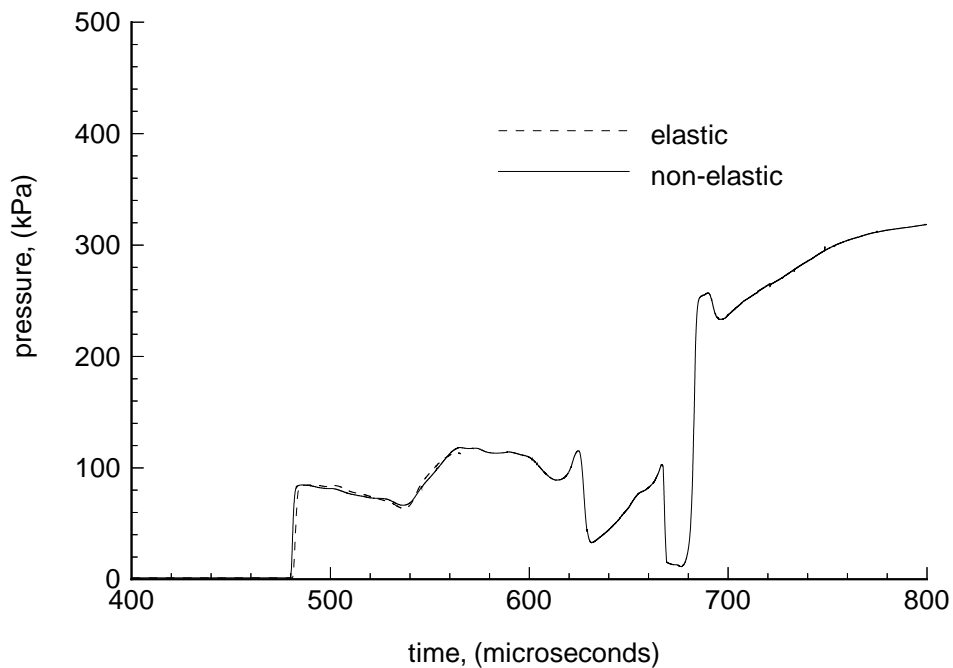


Figure 7.34: Comparison of computed downstream pressure traces for elastic and inelastic collisions at the tube wall. Diaphragm thickness is  $127 \mu\text{m}$ .

Discrepancies between the computed and experimental traces in Figures 7.27 – 7.30 may be due to the following factors: the initial deflection of the diaphragm is too large (the same initial deflection as for the axisymmetric simulations was used; hence the centre of the diaphragm mass is further downstream than for the axisymmetric case), the diaphragm is holding for a finite time after the arrival of the incident shock, the initial gaps between the diaphragm pieces are allowing the test gas to penetrate the diaphragm mass too quickly, and/or the neglected viscous effects. The next two sub-sections will examine the influence of the diaphragm holding time and the number of diaphragm pieces.

### 7.5.3 Holding model

A simulation was performed assuming the diaphragm held its position for 30 microseconds after the arrival of the incident shock and then fragmented. The results are shown in Figures 7.35 and 7.36. The strength of the reflected shock was increased by the holding time and was significantly greater than experimental results. It appears that the holding time of 30 microseconds is too large, but a good comparison between the computed and experimental upstream trace could be achieved by choosing an appropriate holding time. An additional improvement that could be made to the simulation is to allow the diaphragm to act as a curved piston for a short time before releasing the diaphragm pieces.

The holding time causes the transmitted shock to arrive at the downstream pressure gauge 25 microseconds later (compare Fig. 7.36 & 7.30). This is closer to the experimental data, however, a smaller holding time (as required to match the computed and experimental downstream pressure trace) would reduce the improvement.

### 7.5.4 Fourteen piece simulation

The effect of varying the number of diaphragm pieces was examined by performing a simulation with fourteen diaphragm pieces. The diaphragm mass was  $0.1270 \text{ kg/m}^2$ . For this particular case, the symmetry of the problem was exploited and only half of the tube was considered. The time histories of the density contours and diaphragm pieces are shown in Figures 7.37 and 7.38 respectively.

There are significant differences between the computed pressure traces for seven and fourteen pieces (Figs. 7.39 & 7.40). Firstly, the reflected shock arrives earlier at the upstream pressure gauge and is swept downstream later for the fourteen piece

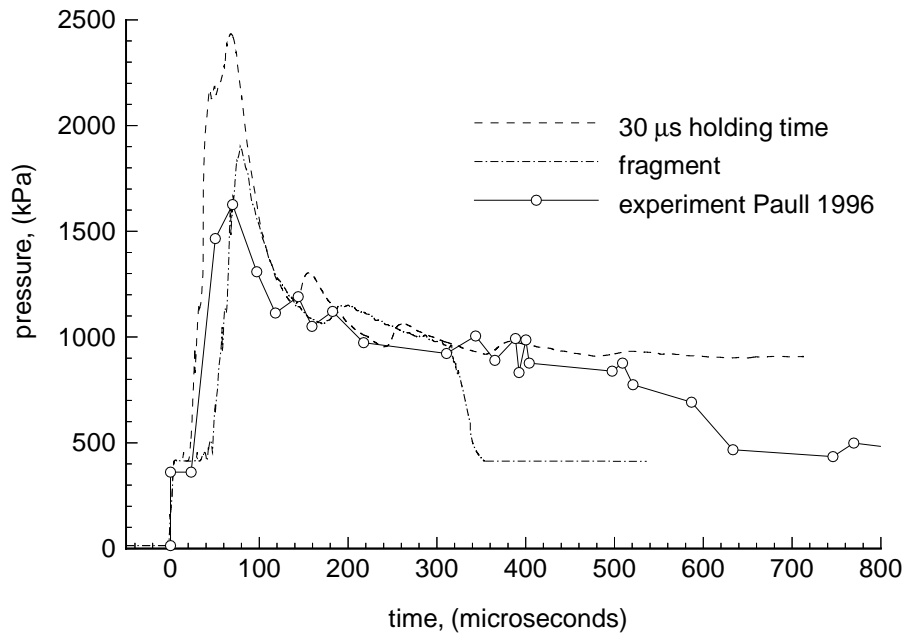


Figure 7.35: Comparison of experimental and computed upstream pressure traces for the seven piece fragment model. The diaphragm is assumed to either hold its position for 30 microseconds or break free instantly when the incident shock arrives. Diaphragm thickness is  $127 \mu\text{m}$ .

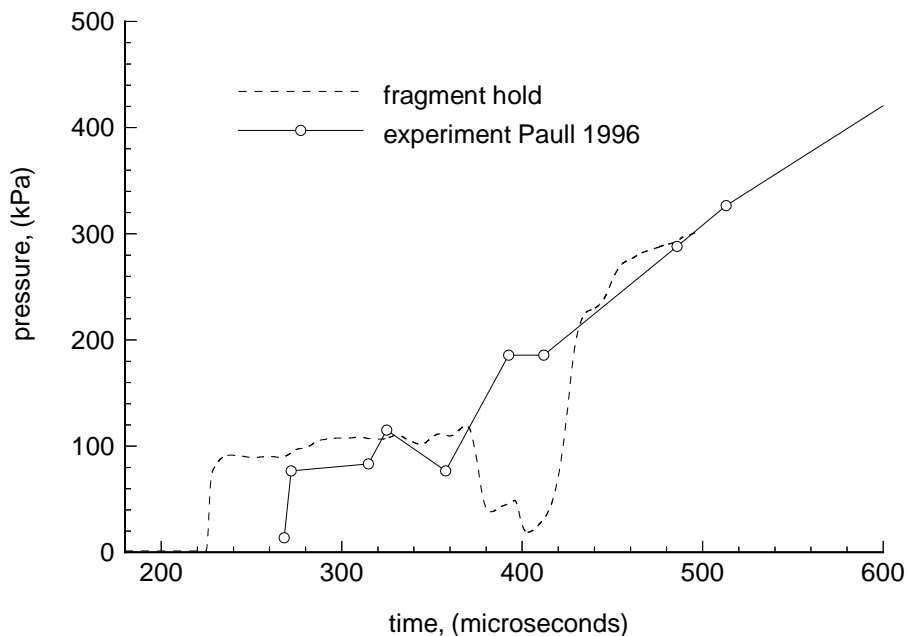


Figure 7.36: Comparison of experimental and computed downstream pressure traces for the seven piece fragment model. The diaphragm is assumed to hold its position for 30 microseconds after the arrival of the incident shock. Diaphragm thickness is  $127 \mu\text{m}$ .

model. This is closer to the experimental trace. Secondly, the size of the dips in the downstream pressure due to the test gas over-expanding are smaller for the fourteen piece model. It appears that having a greater number of gaps between the diaphragm pieces produces weaker jetting of the test gas through the diaphragm mass. Thus there is an improvement in the comparison between the computed and experimental downstream pressure traces.

The computed transmitted shock still arrived earlier than the experimental shock. Viscous effects, which were not considered, would reduce the speed of the shock and improve the comparison. If the diaphragm held its position for a finite time before rupturing (as discussed in Sec. 7.5.3) this would also delay the arrival of the incident shock.

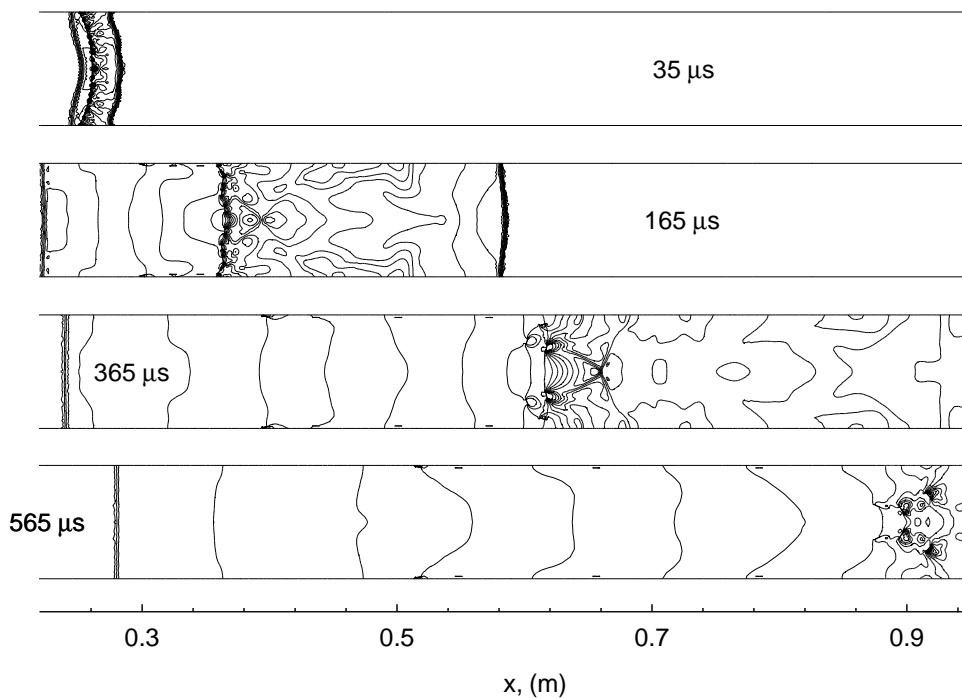


Figure 7.37: Time history of density contours for the flow near the rupture of the secondary diaphragm for the fourteen piece fragment model.

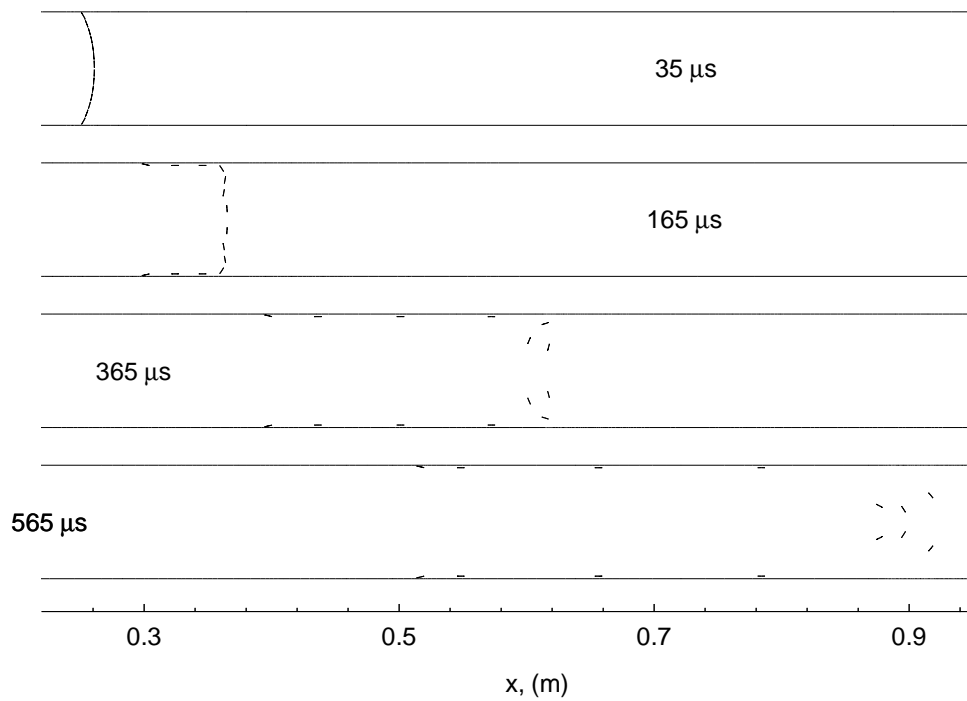


Figure 7.38: Time history of diaphragm pieces for the fourteen piece fragment model.

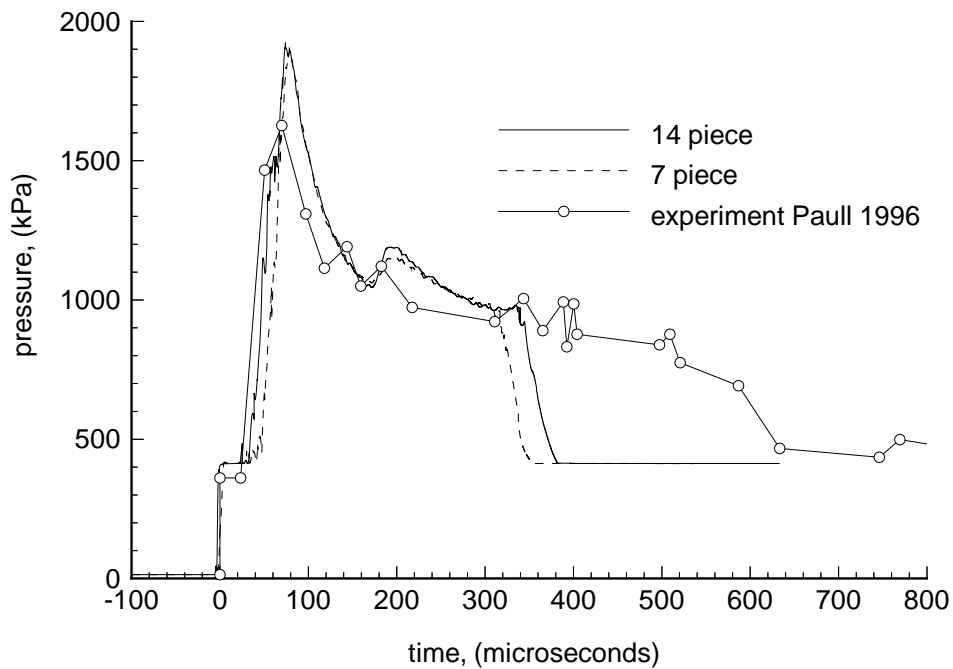


Figure 7.39: Comparison of the computed upstream pressure traces for the seven and fourteen piece fragment models.

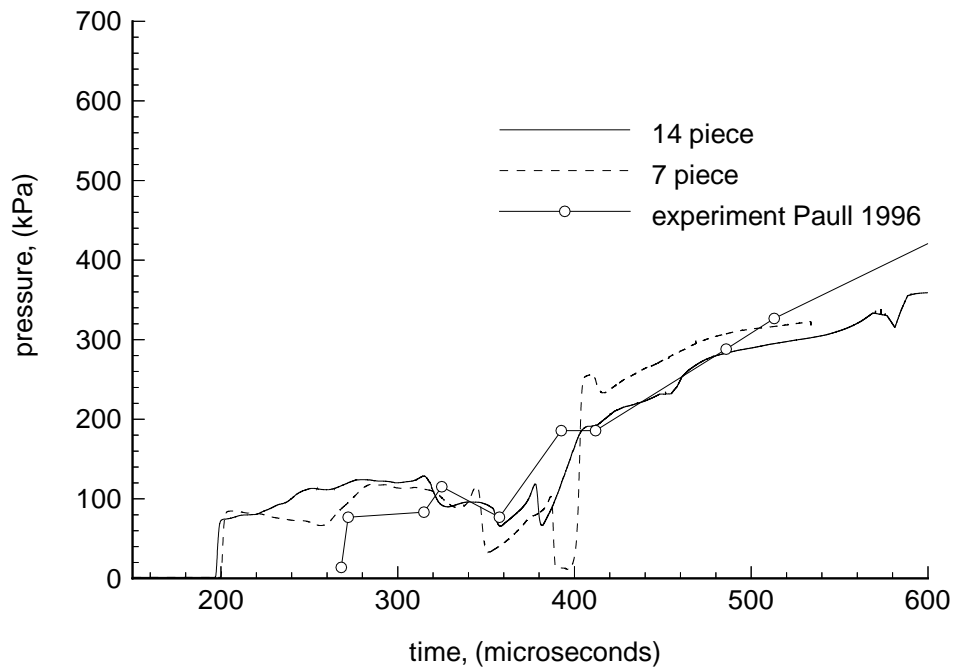


Figure 7.40: Comparison of the computed downstream pressure traces for the seven and fourteen piece fragment models.

## 7.6 Summary

This chapter examined numerical models for the shock induced rupture of thin diaphragms. The computed shock trajectories using the one-dimensional diaphragm inertia model of Bakos & Morgan [8] were compared with experimentally determined trajectories. The agreement was good for the first 30 microseconds after the arrival of the incident shock but, after that time the model did not predict the observed trajectories. The diaphragm inertia model of Bakos & Morgan was also used to compute pressure traces 10 mm upstream and 424 mm downstream of the secondary diaphragm within the PISTL expansion tube. The comparisons with the experimental traces were good except for the downstream pressure trace for a thick diaphragm. There was a distinct pressure jump as the diaphragm mass passed the pressure location that was not evident in the experimental trace. This highlights the major flaw of the diaphragm inertia model, which is that the test gas cannot penetrate the diaphragm mass. Also, the computed reflected shock was stronger than the experimental shock.

In an attempt to improve upon the Bakos & Morgan model, axisymmetric simulations of secondary diaphragm rupture within an expansion tube were performed. It was assumed that the diaphragm vaporised immediately after the arrival of the incident shock. The initial shape of the diaphragm was assumed to be spherical. The test gas pushed the diaphragm mass toward the wall of the tube and then penetrated the diaphragm mass. This model improved the comparison between the computed and experimental downstream pressure trace for the heavier diaphragm, however there was still a pressure jump as the tail of the diaphragm mass passed the pressure location. Also, the model was flawed in that the heavier diaphragm was not expected to vaporise in the short time of interest. Indeed, very recent flow visualisations by Sutcliffe & Wegener at the University of Queensland (unpublished) clearly show the diaphragm breaking into many fragments and remaining in the flow for at least one diameter downstream.

Two-dimensional simulations of secondary diaphragm rupture assuming the diaphragm shattered into many pieces (seven or fourteen) were performed. The computed downstream pressure trace for the seven piece model exhibited significant drops in pressure below the experimental value. This was due to the test gas over-expanding as it jetted through the gaps between the diaphragm pieces. The drops in pressure were significantly less for the fourteen piece model because the larger number of gaps between the diaphragm pieces reduced the strength of the jetting. A three-dimensional simulation of the diaphragm fragments would allow the gaps between the diaphragm pieces to grow larger more rapidly and hence reduce the

strength of the jetting even further.

The times when the computed reflected shocks for both the vaporisation and the fragment models are swepted downstream are earlier than the time observed in the experiment. It was shown that the comparison of the computed with the experimental reflected shock behaviour could be improved by assuming that the diaphragm held its position for a short time ( $< 30 \mu s$ ). Note that the reflected shock for the one-dimensional model (Fig. 7.10) is closer to the experimental trace than the computed traces from the two multi-dimensional models (Figs. 7.18 & 7.39). This is probably due to compensating errors: the one-dimensional model does not allow the upstream gas to penetrate causing a larger reflected shock, the diaphragm is assumed to break free immediately (no holding time) causing a weaker reflected shock, and heat transfer is not considered causing a stronger reflected shock. The maximum predicted pressures behind the reflected shocks for all the computed models are greater than the experimental value. This is probably because heat transfer was not considered in any of the models.

Unlike the other models, the agreement between the computed and experimental downstream pressure trace (424 mm) for a heavy diaphragm (127  $\mu m$ ), for the fourteen piece fragment model was good. However, the computed transmitted shock arrived 65  $\mu s$  earlier than the experimental. This is mainly due to the fact that viscous effects and the holding time of the diaphragm were not considered in the computed trace. Both of these factors would delay the arrival of the incident shock.





# Chapter 8

## Conclusions

This thesis examined the use of Computational Fluid Dynamics (CFD) to explain observed phenomena relating to diaphragm rupture within shock tubes and expansion tubes. The work has led to a better understanding of the flow within such facilities. From this understanding, better interpretation of experimental data can be achieved. The models developed could be used during the design of new facilities. Also a better understanding of the application and limitations of CFD was achieved.

In Chapter 2, the essential components of a finite-volume code, U2DE was described. U2DE is capable of solving the unsteady two-dimensional and axisymmetric Euler equations for compressible inviscid flow. The code was designed to use unstructured grids and solution-adaptive remeshing to focus computational effort in regions where the flow-field gradients were high. Solution-adaptive remeshing provided large savings (up to 97 %) in computer resources for high resolution simulations and made the simulations presented in Chapters 4 – 7 feasible on workstation class computers.

There was a considerable effort to verify that the solutions produced by U2DE were accurate. This involved the examination of well known test cases. Solutions generated by U2DE were compared with either analytical solutions or previous numerical solutions in Chapter 3. The ability of U2DE to compute the shock speed within an ideal shock tube was examined in detail. For low initial pressure ratios, the computed speed was similar to the analytical value. However, for high initial pressure ratios ( $> 1000$ ), the computed shock speed was initially overestimated but, did eventually decay to the analytical value. The main reason for the initial overestimation of the shock speed was shown to be numerical diffusion at the contact surface (CS).

Two different flux calculators were examined by this thesis: the Riemann solver and EFM. The Riemann solver was found to generate noisy solutions for some cases. The noise was due to odd-even decoupling (Sec. 3.5) caused by the low dissipation of the scheme. EFM was used for most of the simulations presented in this thesis. EFM is known to be a dissipative flow solver, however, accurate solutions were obtained through the use of solution-adaptive remeshing (a similar approach was also taken by Arora & Roe [6]). It was shown in Section 3.2.4 that the current scheme was accurately determining the shock speed for an ideal shock tube with  $P_4/P_1 \leq 1000$ .

The axisymmetric Euler solver was used to simulate the flow through a relatively slow opening diaphragm. The development of the contact surface was found to be strongly dependent on the initial pressure ratio. The higher the initial pressure ratio the greater the radial expansion, and for  $P_4/P_1 > 10$ , the temporary existence of an oblique upstream-facing shock was observed. This shock redirected the radially expanding flow parallel to the tube wall and caused the jetting of CS along the wall.

The higher the initial pressure ratio the greater the penetration of the CS along the tube wall.

The diaphragm opening time did not affect the area of the CS for the simulations with  $P_4/P_1 > 10$ . This was because the radially expanding driver gas arrived at the tube wall quickly, separating the CS from the partially opened diaphragm. If the pressure was low,  $P_4/P_1 = 10$ , the radial expansion was not strong enough to separate the CS from the partially opened diaphragm and the area of the CS was dependent on the diaphragm opening time.

The shock speed in a shock tube with a gradually opening diaphragm was examined. The maximum speed of the primary shock wave for multi-dimensional simulations exceeded the speeds predicted by previous one-dimensional theories (White [91] and Ikui *et al.* [33]) and is closer to the experimental measurements of Miller & Jones [55]. One of the mechanisms behind the increase in the shock speed is an entropy rise through the oblique shock structure which exists temporarily downstream of the diaphragm while it is opening. This mechanism is a multi-dimensional flow effect that can be captured only in two- or three-dimensional simulations. The accuracy of the diaphragm simulations was examined by performing grid convergence tests. For many cases, convergence was not convincingly demonstrated, however, the observed trends appear to be reliable.

The shock induced rupture of thin diaphragms was examined in Chapter 7. The major flaw of the previous one-dimensional diaphragm inertia model is that the upstream gas cannot penetrate the diaphragm mass. Two multi-dimensional models which allow this to occur were presented.

The first model assumed that the diaphragm vaporised immediately after the arrival of the incident shock. The computed downstream (424 mm) pressure trace using this model for a heavy diaphragm (127  $\mu\text{m}$ ) was better than the one-dimensional diaphragm inertia model, although there was a sudden rise in pressure (not evident in the experiment) as the diaphragm mass passed the pressure location.

The second model assumed that the diaphragm shattered (fragment model) into pieces (seven or fourteen) which could be treated as rigid bodies. The computed downstream pressure trace for the seven piece model exhibited significant drops in pressure below the experimental value. This was due to the test gas over-expanding as it jetted through the gaps between the diaphragm pieces. The drops in pressure were significantly less for the fourteen piece model because of the reduced strength of the expansion of the test gas. This occurred because the gaps between the diaphragm pieces became larger more rapidly. This caused the computed downstream trace to

be closer to the experimental trace than the seven piece model. There was no sudden pressure rise associated with the diaphragm mass in the downstream pressure trace for the fragment model, because the volume of the diaphragm pieces were small and the pieces were parallel to the flow.

The computed upstream (10 mm) pressure trace for the 127  $\mu\text{m}$  diaphragm for the one-dimensional diaphragm inertia model was closer to the experimental trace than the multi-dimensional models. This was probably due to the diaphragm requiring a finite time to break free from the tube wall. It was shown that holding the diaphragm for a short time ( $< 30 \mu\text{s}$ ) for the fragment model can make the computer trace closer to the experimental trace.

The work presented in this thesis has added to the body of knowledge about flows in expansion tubes and shock tubes. The main aim of the thesis was to improve the modelling of hypersonic test facilities. These models can be used to determine the flow condition in the test section during operation and as tools to design new facilities. The better the model, the closer the actual performance of the facility will be to the desired performance.

A multi-dimensional flow feature which causes the speed of the shock generated by a gradually opening diaphragm in a high performance shock tube to be higher than that predicted by one-dimensional models was identified. The flow condition behind the shock and subsequently in the test section is determined by the speed of the shock. Hence, the better the estimate of the shock speed, the better the estimate of the flow condition in the test section.

Multi-dimensional models of the rupture of the thin diaphragms were developed and compared with experimental data. The next step is to include viscous and chemistry effects. This model could then be used to estimate the flow condition in the test section.

A possible source of contamination of the test gas in reflected shock tunnels is the jetting of driver gas when the reflected shock interacts with the contact surface. Other Researchers (Chue & Itoh [17] and Wilson *et al.* [94]) have investigated this mechanism via simulation. The simulations so far have assumed that the contact surface is planar when it interacts with the shock. The work presented here can be used to predict the shape of the contact surface as a function of the operating condition, and hence may enable improved simulations of the driver gas jetting to be performed.

## 8.1 Future work

The experimental shock speeds measured by Miller & Jones [55] are higher than the computed shock speeds from the axisymmetric simulations presented in this thesis. It was shown in Section 3.2.4 that numerical diffusion at the contact surface (CS) can cause higher shock speeds. The effect of physical diffusion and turbulent mixing at the CS may account for these higher shock speeds, and could be investigated.

The petalling of the primary diaphragm during its opening (rupture) is a three-dimensional process and a three-dimensional simulation of the gas-dynamic processes that occur during the opening would be more accurate than an axisymmetric simulation. However, a three-dimensional simulation would require greater computing power and possibly parallel computing.

With respect to the numerical methods used by U2DE, fundamental problems with the axisymmetric flow solver were encountered. Numerical jetting of the solution occurred at the axis for some of the problems examined by this thesis. In Section 3.2.3 the jetting was shown to be non-physical. This problem has also been observed by Cambier [13] and Jacobs [34] and its cause is unknown. However, Cambier has speculated on the underlying mechanism (Sec. 3.2.3). The numerical jetting can be alleviated by using a mesh stretched in the radial direction. However, this is not a long term solution to the problem and there appears to be a need to improve the numerical techniques used to solve the axisymmetric Euler equations.

The numerical techniques used to solve the Euler equations are constantly improving. For example, it was shown in Section 3.1 that the recent multi-dimensional reconstruction schemes of Luo *et al.* [50] and Aftosmis *et al.* [1] appear to be more accurate than U2DE. A new flux calculator EFMO [58] claims to be robust and have low-dissipation. The performance of these new schemes should be examined if this work is to be revisited in the future.

The multi-dimensional models developed for the shock induced rupture of thin diaphragms have potential for improvement. Recent work by Kendall *et al.* [45] has shown that it is necessary to consider heat transfer to predict accurately the shock trajectories near thin diaphragms. This suggests that viscous effects (including heat transfer) should be added to the current model. The flow visualisations performed by Sutcliffe & Wegener at the University of Queensland (unpublished) could be used to validate the multi-dimensional models. Another improvement would be the development of a three-dimensional model, however, this would require major effort. The influence of turbulence on the motion of the diaphragm fragments could also

be examined. Another area for future work would be to use the multi-dimensional models to predict dissociation levels in the test gas, similar to the work of Wilson [95].

# Bibliography

- [1] M. Aftosmis, D. Gaitonde, and T. S. Tavares. Behaviour of linear reconstruction techniques on unstructured meshes. *AIAA Journal*, 33(11):2038–2049, 1995.
- [2] S. W. Akin and N. Y. Schenectady. The thermodynamic properties of helium. *Transactions. (American Society of Mechanical Engineers)*, 72:751–7, 1950.
- [3] D. Ambrosi, L. Gasparini, and L. Vigevano. Full potential and Euler solutions for transonic unsteady flow. *Aeronautical Journal*, 98(979):340 – 348, 1994.
- [4] W. K. Anderson, J. L. Thomas, and B. Van Leer. A comparison of finite volume flux vector splitting for the Euler equations. AIAA Paper 85-0122, 1985.
- [5] J. D. Anderson Jr. *Modern Compressible Flow with Historical Perspective*. Mcgraw-Hill, 1990.
- [6] M. Arora and P. L. Roe. On postshock oscillations due to shock capturing schemes in unsteady flows. *Journal of Computational Physics*, 130:25–40, 1997.
- [7] R. H. Aungier. A fast, accurate real gas equation of state for fluid dynamic analysis applications. *Journal of Fluids Engineering*, 117:277–281, 1995.
- [8] R. J. Bakos and R. G. Morgan. Chemical recombination in an expansion tube. *AIAA Journal*, 32(6):1316–9, June 1994.
- [9] J. T. Batina. Implicit upwind solution algorithms for three-dimensional unstructured meshes. *AIAA Journal*, 31(5):801–5, May 1993.
- [10] G. Ben-Dor. *Shock Waves Reflection Phenomena*. Springer-Verlag, 1992.
- [11] F. G. Blottner. Accurate Navier-Stokes results for the hypersonic flow over a spherical nosetip. *Journal of Spacecraft and Rockets*, 27(2):113–122, 1990.
- [12] D. Bogdanoff. Improvements of pump tubes for gas guns and shock tube drivers. *AIAA Journal*, 28(3):383–391, 1990.



- [13] J.-L. Cambier, S. Tokarcik, and D. K. Prabhu. Numerical simulations of unsteady flow in a hypersonic shock tunnel facility. In *AIAA 17th Aerospace Ground Testing Conference*, Nashville, TN, July 1992.
- [14] G. A. Campbell, G. M. Kimber, and D. H. Napier. Bursting of diaphragms as related to the operation of shock tubes. *Journal of Scientific Instruments*, 42:381–384, 1965.
- [15] A. Chaix, M. P. Dumitrescu, L. Z. Dumitrescu, and R. Brun. Calibration of the TCM2 conical nozzle and internal flow investigations. In *21th International Symposium on Shock Waves*, 1997.
- [16] D. R. Chapman. A perspective on aerospace CFD. *Aerospace America*, 30(2):16–9,58–9, February 1992.
- [17] R. S. M. Chue and K. Itoh. Influence of reflected-shock/boundary-layer interaction on driver-gas contamination in high-enthalpy shock tunnels. In *Proceedings of the 20th International Symposium on Shock Waves*, 1995.
- [18] M. C. Cline, J. K. Dukowicz, and F. L. Addressio. CAVEAT-GT: A general topology version of the CAVEAT code. Technical Report LA-11812-MS, Los Alamos National Laboratory, June 1990.
- [19] C. H. Cooke and K. S. Fansler. Comparison of blast waves from a shock tube. *International Journal for Numerical Methods in Fluids*, 9:9–22, 1989.
- [20] F. L. Curzon and M. G. R. Phillips. Low attenuation shock tube: driving mechanism and diaphragm characteristics. *Canadian Journal of Physics*, 49:1982–93, 1971.
- [21] V. Daru and J. P. Damion. Analysis of the flow perturbations in a shock tube due to the curvature of the diaphragm. In *19th International Symposium on Shock Waves*, 1993.
- [22] V. Daru and J. P. Damion. Influence of the curvature of the diaphragm on flow quality in shock tubes. In *20th International Symposium on Shock Waves*, pages 1527–32, 1995.
- [23] R. E. Duff. Shock-tube performance at low initial pressure. *The Physics of Fluids*, 2(2):207–216, 1959.
- [24] T. A. Edwards. The effect of exhaust plume / afterbody interaction on installed scramjet performance. NASA Technical Memorandum 101033, 1988.

- [25] H. M. Glaz, P. Colella, I. I. Glass, and R. L Deschambault. A detailed numerical, graphical, and experimental study of oblique shock wave reflections. Technical Report 285, UTIAS, University of Toronto, 1986.
- [26] J. J. Gottlieb and C. P. T. Groth. Assessment of Riemann solvers for unsteady one-dimensional inviscid flows of perfect gases. *Journal of Computational Physics*, 78:437–58, 1988.
- [27] S. W. Hammond and T. J. Barth. Efficient massively parallel Euler solver for two-dimensional unstructured grids. *AIAA Journal*, 30(4):947–952, April 1992.
- [28] B. D. Henshall. On some aspects of the use of shock tubes in aerodynamic research. Technical Report 3044, Aeronautical Research Council, 1957.
- [29] R. S. Hickman, L. C. Farrar, and J. B. Kyser. Behaviour of burst diaphragms in shock tubes. *The Physics of Fluids*, 18(10):1249–52, 1975.
- [30] C. Hirsch. *Numerical Computation of Internal and External Flows. Volume 1: Computational Methods for Inviscid and Viscous Flows*. John Wiley & Sons, 1990.
- [31] W. J. Hooker. Testing time and contact-zone phenomena in shock-tube flows. *The Physics of Fluids*, 4(12):1451–63, December 1961.
- [32] P. W. Huber. Note on hydrogen as a real-gas driver for shock tubes. *Journal of the Aeronautical Sciences*, page 269, April 1958.
- [33] T. Ikui, K. Matsuo, and M. Nagai. Investigations of the aerodynamic characteristics of the shock tubes. *Bulletin of JSME*, 12:783–792, 1969.
- [34] P. A. Jacobs. Simulations of transient flow in a shock tunnel and a high mach number nozzle. In *Fourth International Symposium on Computational Fluid Dynamics*, Davis, September 1991.
- [35] P. A. Jacobs. Single-block Navier-Stokes integrator. NASA CR-187613 ICASE Interim Report 18, 1991.
- [36] P. A. Jacobs. Approximate Riemann solver for hypervelocity flows. *AIAA Journal*, 30(10):2558–61, 1992.
- [37] P. A. Jacobs. L1d: a computer code for the quasi-one-dimensional modelling of transient-flow facilities. Technical report, WBM-Stalker Pty. Ltd., 1992. (unpublished).
- [38] P. A. Jacobs. Quasi-one-dimensional modeling of free-piston shock tunnels. AIAA Paper 93-0352, January 1993.

- [39] P. A. Jacobs. Numerical simulation of transient hypervelocity flow in an expansion tube. *Computer & Fluids*, 23(1):77–101, 1994.
- [40] I. A Johnston, S. L. Tuttle, P. A. Jacobs, and T. Shimoda. The numerical and experimental simulation of flow around the HYFLEX vehicle forebody. In *21th International Symposium on Shock Waves*, 1997.
- [41] M. T. Jones and P. E. Plassmann. Parallel algorithms for the adaptive refinement and partitioning of unstructured meshes. In *Proceedings of the 1994 SHPCC*, 1994.
- [42] D. Kamowitz. Some observations on boundary conditions for numerical conservation laws. Technical Report 88-67, Institute for Computer Applications in Science and Engineering, NASA Langley Research Center, Hampton, Virginia 23665, 1988.
- [43] M. A. Kendall, R. G. Morgan, and P. A. Jacobs. A compact shock-assisted free-piston driver for impulse facilities. *Shock Waves*, 7(4):219–30, August 1997.
- [44] M. A. Kendall, R. G. Morgan, and P. J. Petrie-Repar. A study of free-piston double-diaphragm drivers for expansion tubes. In *35th Aerospace Sciences Meeting & Exhibit*. AIAA, January 1997. AIAA Paper 97-0985.
- [45] M. A. F. Kendall, R. G. Morgan, and P. J. Petrie-Repar. Heat losses and shock-diaphragm interactions within double-diaphragm drivers. To be submitted to AIAA Journal.
- [46] G. F. Lake and N. P. Inglis. The design and manufacture of bursting disks. *Institution of Mechanical Engineers - Journal & Proceedings*, 142(4):365–78, February 1940.
- [47] C. L. Lawson. *Software for c1 Interpolation*. Academic Press, New York, 1977.
- [48] R. Löhner. An adaptive finite element scheme for transient problems in CFD. *Computer Methods in Applied Mechanics and Engineering*, 61:323–338, 1987.
- [49] R Löhner. Adaptive remeshing for transient problems. *Computer Methods in Applied Mechanics and Engineering*, 75:195–214, 1989.
- [50] H. Luo, J. D. Baum, and R. Löhner. An improved finite volume scheme for compressible flows on unstructured grids. In *33rd Aerospace Sciences Meeting and Exhibits*, Reno, Nevada, January 1995. AIAA Paper 95-0348.
- [51] M. N. Macrossan. The equilibrium flux method for the calculation of flows with non-equilibrium chemical reactions. *Journal of Computational Physics*, 80(1):204 – 231, January 1989.

- [52] E. R. Mallett. *A Numerical Study of Hypersonic Leeward Flow over the Delta Wing of the Hermes Spacecraft using a Parallel Architecture Supercomputer*. PhD thesis, University of Queensland, 1993.
- [53] D. J. Mee. Uncertainty analysis of conditions on the test section of the T4 shock tunnel. Technical Report 4/93, Mechanical Engineering Department, University of Queensland, St. Lucia Brisbane, Australia., 1993.
- [54] U. B. Mehta. Aerospace plane design challenge: Credible computations. *Journal of Aircraft*, 30(4):519–25, 1993.
- [55] C. G. Miller III and J. J. Jones. Incident shock-wave characteristics in air, argon, carbon dioxide, and helium in a shock tube with unheated helium driver. Technical Report TN D-8099, NASA, Langley Research Center Hampton, Va. 23665, December 1975.
- [56] H. Mirels. Test time in low pressure shock tubes. *Physics of Fluids*, 6:1201–15, 1963.
- [57] R. G. Morgan and R. J. Stalker. Double diaphragm driven free piston expansion tube. In *18th International Symposium on Shock Waves*, 1991.
- [58] J.-M. Moschetta and D. I. Pullin. A robust low diffusive kinetic scheme for the Navier-Stokes/Euler equations. *Journal of Computational Physics*, 133:193–204, 1997.
- [59] H. T. Nagamatsu, R. E. Geiger, and R. E. Sheer Jr. Hypersonic shock tunnel. *ARS Journal*, 29(5):332–340, 1959.
- [60] B. Nkonga and H. Guillard. Godunov type method on non-structured meshes for three-dimensional moving boundary problems. *Computer Methods on Applied Mechanics and Engineering*, 113:183–204, 1994.
- [61] E. Outa, K. Tajima, and K. Hayakawa. Shock tube flow influence by diaphragm opening (two-dimensional flow near the diaphragm). In *10th International Symposium on Shock Waves and Shock Tubes*, pages 312–9, 1975.
- [62] A. Paull. Report on the commissioning of the expansion tube, PISTL. Technical report, Hypersonic Airbreathing Propulsion Branch of NASA Langley Research Center, 1996.
- [63] J. Probert, O. Hassan, J. Peraire, and K. Morgan. An adaptive finite element method for transient compressible flows. *International Journal for Numerical Methods in Engineering*, 32:1145–1159, 1991.

- [64] D. I. Pullin. Direct simulation methods for compressible inviscid ideal-gas flow. *Journal of Computational Physics*, 34(2):231–244, February 1979.
- [65] J. J. Quirk. An alternative to unstructured grids for computing gas dynamic flows around arbitrarily complex two-dimensional bodies. *Computers & Fluids*, 23(1):125–142, 1994.
- [66] J. J. Quirk. A contribution to the great Riemann solver debate. *International Journal for Numerical Methods in Fluids*, 18:555–574, 1994.
- [67] J. D. Ramshaw. Conservative rezoning algorithm for generalized two-dimensional meshes. *Journal of Computational Physics*, 59:193–9, 1985.
- [68] M. Reggio and J. Y. Trépanier. Numerical simulation of the gas flow in a circuit-breaker. *International Journal for Numerical Methods in Engineering*, 34:607 – 18, 1992.
- [69] L. F. Richardson. The approximate arithmetical solution by finite differences of physical problems involving differential equations, with an application to the stresses in a masonry dam. *Transactions of the Royal Society of London, Series A*, 210:307–357, 1910.
- [70] G. T. Roberts. Influence of secondary diaphragms on flow quality in expansion tubes. Technical Report 1/93, Department of Mechanical Engineering, University of Queensland, 1993.
- [71] A. Roshko and D. Baganoff. A novel device for bursting shock-tube diaphragms. *The Physics of Fluids*, 4(11):1445–6, November 1961.
- [72] E. M. Rothkopf and W. Low. Diaphragm opening process in shock tubes. *The Physics of Fluids*, 17(6):1169–73, 1974.
- [73] E. M. Rothkopf and W. Low. Shock formation distance in a pressure driven shock tube. *The Physics of Fluids*, 19(12):1885–88, 1976.
- [74] N. Satofuka. A numerical study of shock formation in cylindrical and two-dimensional shock tubes. Technical Report 451, ISAS, University of Tokyo, June 1970.
- [75] C. J. S. M. Simpson, T. R. D. Chandler, and K. B. Bridgman. Effect on shock trajectory of the opening time of diaphragms in a shock tube. *The Physics of Fluids*, 10(9):1894–1896, September 1967.
- [76] G. A. Sod. A survey of several finite difference methods for systems of nonlinear hyperbolic conservation laws. *Journal of Computational Physics*, 27(1):1–31, 1978.

- [77] R. J. Stalker. Development of a hypervelocity wind tunnel. *Aeronautical Journal*, 76:374–84, June 1972.
- [78] R. J. Stalker. Hypervelocity aerodynamics with chemical nonequilibrium. *Annual Review of Fluid Mechanics*, 21:37–60, 1989.
- [79] K. Takayama and O. Inoue. Shock wave diffraction over a 90 degree sharp corner – Posters presented at 18th ISSW. *Shock Waves*, 1:301–312, 1991.
- [80] G. I. Taylor. The instability of liquid surfaces when accelerated in a direction perpendicular to their planes I. *Proceedings of the Royal Society of London Series A*, 201:192–196, 1950.
- [81] G. I. Taylor and J. W. Maccoll. The air pressure on a cone moving at high speed I. *Proceedings of the Royal Society of London Series A*, 139:278–311, 1933.
- [82] P. D. Thomas and C. K. Lombard. Geometric conservation law and its application to flow computations on moving grids. *AIAA Journal*, 20:1030, 1979.
- [83] E. F. Toro. Direct Riemann solvers for the time-dependent Euler equations. *Shock Waves*, 1:75–80, 1995.
- [84] J. Y. Trépanier, M. Reggio, M. Paraschivoiu, and R. Camarero. Unsteady Euler solutions for arbitrarily moving bodies and boundaries. *AIAA Journal*, 31(10):1869–76, October 1993.
- [85] R. L. Trimpi. A preliminary theoretical study of the expansion tube, a new device for producing high-enthalpy short-duration hypersonic gas flows. Technical Report TR-133, NASA, 1962.
- [86] N. Uchiyama and O. Inoue. Shock wave/vortex interaction in a flow over 90-deg sharp corner. *AIAA Journal*, 33(9):1740–2, September 1995.
- [87] E. I. Vasil’ev and E. V. Danil’chuk. Numerical solution of the flow formation problem for a shock tube with transverse diaphragm removal. *Izvestiya AN SSSR. Mekhanika Zhidkosti i Gaza*, 2:147–154, 1994.
- [88] V. Venkatakrishnan. Perspective on unstructured grid flow solvers. *AIAA Journal*, 34(3):533–547, March 1996.
- [89] J. C. T. Wang and G. F. Widhopf. A high-resolution TVD finite volume scheme for the Euler equations in conservation form. *Journal of Computational Physics*, 84:145–173, 1989.

- [90] K. J. Weilmuenster, P. A. Gnoffo, and F. A. Greene. Navier-Stokes simulations of Orbiter aerodynamic characteristics including pitch trim and bodyflap. *Journal of Spacecraft and Rockets*, 31(3):355–66, 1994.
- [91] D. R. White. Influence of diaphragm opening time on shock-tube flows. *J. Fluid Mech.*, 4:585–599, 1958.
- [92] J. D. Whitfield, G. D. Norfleet, and W. Wolny. Status of research on a high performance shock tunnel. Technical Report AEDC-TR-65-272, U.S. Air Force, May 1966.
- [93] G. J. Wilson. Time-dependent quasi-one dimensional simulations of high enthalpy pulse facilities. Technical Report 92-5096, AIAA Paper, December 1992.
- [94] G. J. Wilson, S. P. Sharma, and W. D. Gillespe. Time-dependent simulations of reflected-shock/boundary layer interaction. In *31st Aerospace Sciences Meeting & Exhibit*, 1993.
- [95] G. J. Wilson and M. A. Sussman. Numerical simulations of the flow in the HYPULSE expansion tube. Technical Report 110357, NASA Technical Memorandum, 1995.
- [96] Y. Yamaki and J. R. Rooker. Experimental investigation of circular, flat, grooved, and plain steel diaphragms bursting into a 30.5-centimeter-square section. Technical Report TM X-2549, NASA, 1972. (cited by Miller & Jones, 1975).
- [97] D. Zeitoun, R. Brun, and M.-J. Valetta. Shock-tube flow computation including the diaphragm and boundary-layer effects. In *Proceedings of the 12th International Symposium on Shock-Tubes and Waves*, pages 180–186, 1979.

# Appendix A

## Redlich-Kwong EOS for helium



The Redlich-Kwong equation [7] of state (Eqn. A.1) can be used to describe accurately the behaviour of helium at the conditions of interest ( $P = 35$  MPa,  $T = 342$  K) in Chapters 4 and 5.

$$P = \frac{\rho R T}{1 - b \rho} + \frac{\rho^2 a(T)}{1 + b \rho} \quad (\text{A.1})$$

$$a(T) = a_0 T_R^{-0.03} \quad (\text{A.2})$$

$$T_R = \frac{T}{T_c} \quad (\text{A.3})$$

$$T = \frac{E - \frac{\rho}{2}(u^2 + v^2)}{C_v} \quad (\text{A.4})$$

where  $a_0 = 226.20 \text{ m}^5/\text{kg s}^2$ ,  $b = 4.1648 \times 10^{-3} \text{ m}^3/\text{kg}$ ,  $C_v = 3115.6 \text{ J/kg K}$ ,  $R = 2077 \text{ J/kg K}$  and  $T_c = 5.3\text{K}$ . A comparison of the Redlich-Kwong equation of state with other equations of state and actual experimental data is shown in Figure A.2.

Note that  $C_v$  was assumed to be constant. This assumption is not valid when the temperature is less than 25 K (Fig. A.1) or when the gas has ionized significantly ( $T > 6000$  K). For the simulations presented in Chapters 4 and 5, the maximum temperature was less than 3000 K. However, for the simulations with high initial pressure ratios ( $P_4/P_1 \leq 1000$ ) the minimum temperature was less than 25 K immediately downstream of the expansion at the centre of the tube.

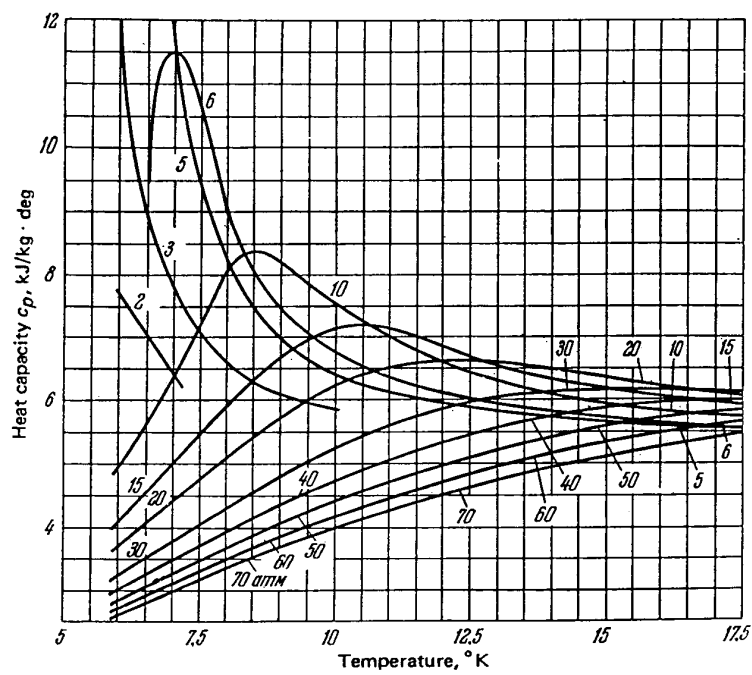


Figure A.1: Heat capacity of helium as a function of temperature at different pressures.

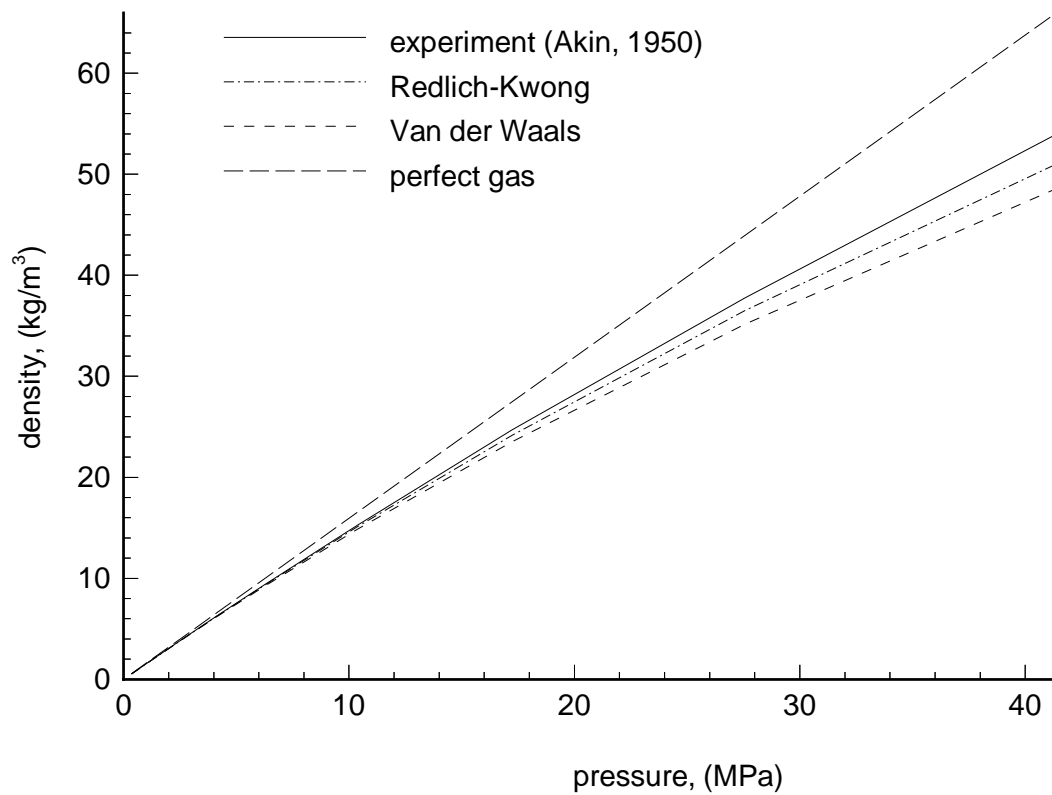


Figure A.2: Comparison of Redlich-Kwong equation of state with other equations of state and experimental data [2] at  $T = 310.9$  K.

# Appendix B

## One-dimensional Euler solver

This appendix describes AEL1D, a *C* program which numerically solves the one-dimensional arbitrary Eulerian-Lagrangian equations for inviscid compressible flow. The code was used to examine the performance of the two-dimensional code, U2DE (Sec. 6.4.2) and obtain solutions for the diaphragm inertia model (Sec. 7.2)

The one-dimensional arbitrary Euler-Lagrangian equations can be written,

$$\frac{\partial}{\partial t} \int_{\vartheta(t)} \mathbf{U} \, d\vartheta + \int_{S(t)} \mathbf{F} \, dS = 0 \quad (\text{B.1})$$

where

$$\mathbf{U} = \begin{bmatrix} \rho \\ \rho u \\ \rho E \end{bmatrix}, \quad \mathbf{F} = \begin{bmatrix} \rho(u-w) \\ \rho(u-w)u + P \\ \rho(u-w)E + P u \end{bmatrix} \quad (\text{B.2})$$

where  $u$  is the speed of the fluid and,  $w$  is the speed of the mesh. The case of  $w = u$  corresponds to a Lagrangian system while the case of  $w = 0$  is Eulerian.

The code uses the same approach to solving the Euler equations as the two-dimensional code U2DE, described in Chapter 2. Each cell is assumed to have a cross-sectional area of  $1.0 \text{ m}^2$ . The known initial solution is explicitly advanced in time. The left- and right-edge flow state are determined using MUSCL reconstruction (Sec. 2.3.1) from the flow states of the four cells nearest the edge (Fig. B.1). The magnitude of the time-step is calculated in the same manner described in Section 2.3.3 with the length scale equal to the width of the cell.

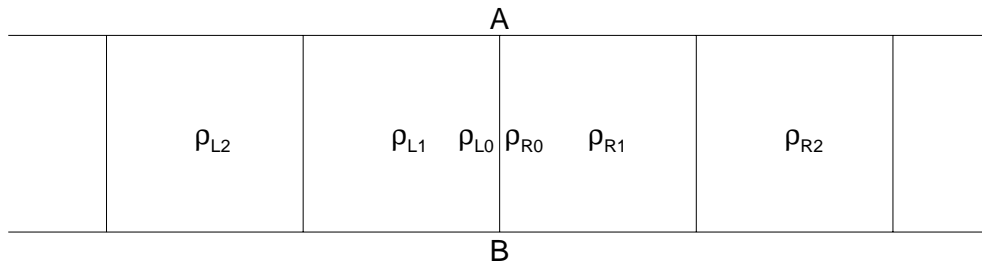


Figure B.1: Cell centred flow states required to determine the left and right flow states at edge AB.

## B.1 Thin diaphragm simulations

AEL1D was used to perform simulations of the shock induced rupture of a thin diaphragm in a tube assuming the diaphragm inertia model of Bakos & Morgan [8]. For these simulations the upstream and downstream sections of the tube were treated as separate domains (Fig. B.2). This allowed the gases either side of the diaphragm to be different. The diaphragm mass was located between the last cell of the intermediate tube and the first cell of the acceleration tube and the motion of the diaphragm mass was determined from the pressure either side of the diaphragm.

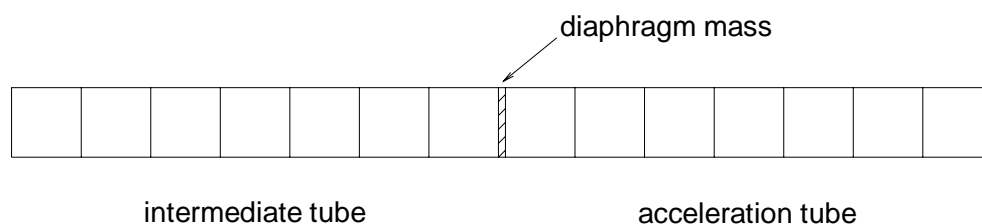


Figure B.2: Schematic of thin diaphragm simulations.



# Appendix C

## Equilibrium Flux Method



The Equilibrium Flux Method (EFM) can be used to estimate the fluxes of mass, momentum and energy at an interface separating gases at different flow states. The two flow states are now referred to as the left ( $\rho_L, V_{Ln}, V_{Lp}, P_L$ ) and right ( $\rho_R, V_{Rn}, V_{Rp}, P_R$ ) flow states. The subscript  $n$  refers to the direction normal to the interface and  $p$  refers to the tangential direction. The positive direction of  $n$  is from left to right. It is assumed that the gases either side of the interface are at equilibrium and that Boltzmann's distribution can be used to describe the distribution of molecular velocities of the gases, that is, the number of molecules having velocities in the range  $\mathbf{v}$  to  $\mathbf{v} + d\mathbf{v}$  is,

$$dN(\mathbf{v}) = \frac{N\beta^3}{\pi^{3/2}} e^{-\beta^2 v^2} d\mathbf{v} \quad (\text{C.1})$$

where

$$\beta = \sqrt{\frac{m}{2kT}}, \quad (\text{C.2})$$

$N$  is the total number of molecules,  $m$  is the mass of a molecule,  $k = 1.38 \times 10^{-23}$  J/K (Boltzmann's constant), and  $T$  is the temperature of the gas.

The flux of the quantity  $Q$  across a surface is equal to,

$$\langle n Q V_n \rangle = \iiint_{-\infty}^{\infty} n Q \frac{dN(\mathbf{v})}{N} v_n d\mathbf{v} \quad (\text{C.3})$$

where  $n$  is the number of molecules per unit volume. By setting  $Q = m$ , the flux of mass from the left state in the positive  $n$  direction is equal to,

$$\langle n m V_n \rangle^+ = \rho_L \int_0^{\infty} \frac{\beta_L}{\pi^{1/2}} v_n \exp\{-\beta_L^2 (v_n - V_{Ln})^2\} dv_n \quad (\text{C.4})$$

$$= W^+ \rho_L V_{Ln} + D^+ \frac{\rho_L}{\beta_L} \quad (\text{C.5})$$

where,

$$W^+ = \frac{1}{2}(1 + \text{erf}(\beta_L V_{Ln})) \quad (\text{C.6})$$

$$D^+ = \frac{1}{2\pi^{1/2}} \exp(-(\beta_L V_{Ln})^2) \quad (\text{C.7})$$

and,

$$\text{erf}(s) = \frac{2}{\sqrt{\pi}} \int_0^s \exp(-t^2) dt. \quad (\text{C.8})$$

Similarly the flux of molecules from the right state in the negative normal direction is equal to,

$$\langle n m V_n \rangle^- = W^- \rho_R V_{Rn} + D^- \frac{\rho_R}{\beta_R}, \quad (\text{C.9})$$

where,

$$W^- = \frac{1}{2}(1 - \text{erf}(\beta_R V_{Rn})) \quad (\text{C.10})$$

$$D^- = -\frac{1}{2\pi^{1/2}} \exp(-(\beta_R V_{Rn})^2). \quad (\text{C.11})$$

The fluxes of momentum and energy (Eqns. C.12 - C.14) can be found by letting  $Q = m V_n$ ,  $m V_p$ , and  $\frac{1}{2}m V^2$ .

$$\begin{aligned} \langle n m V_n V_n \rangle &= W^+(\rho_L V_{Ln} V_{Ln} + P_L) + D^+(\rho_L V_{Ln} / \beta_L) + \\ &W^-(\rho_R V_{Rn} V_{Rn} + P_R) + D^-(\rho_R V_{Rn} / \beta_R) \end{aligned} \quad (\text{C.12})$$

$$\begin{aligned} \langle n m V_p V_n \rangle &= W^+(\rho_L V_{Lp} V_{Ln}) + D^+(\rho_L V_{Lp} / \beta_L) + \\ &W^-(\rho_R V_{Rp} V_{Rn}) + D^-(\rho_R V_{Rp} / \beta_R) \end{aligned} \quad (\text{C.13})$$

$$\begin{aligned} \langle n \frac{1}{2} m V_n^2 V_n \rangle &= W^+(\rho_L V_{Ln} (\frac{1}{2} V_{Ln}^2 + \frac{\gamma P_L}{(\gamma - 1) P_L})) + \\ &D^+(\frac{\rho_L}{\beta_L} \{ \frac{1}{2} V_{Ln}^2 + \frac{P_L}{(\gamma - 1) P_L} \}) + \\ &W^-(\rho_R V_{Rn} (\frac{1}{2} V_{Rn}^2 + \frac{\gamma P_R}{(\gamma - 1) P_R})) + \\ &D^-(\frac{\rho_R}{\beta_R} \{ \frac{1}{2} V_{Rn}^2 + \frac{P_R}{(\gamma - 1) P_R} \}) \end{aligned} \quad (\text{C.14})$$

If a perfect gas is assumed, the only thermodynamic property required is the ratio of the specific heats  $\gamma$ , giving

$$P = \rho e (\gamma - 1) \quad (\text{C.15})$$

$$\beta = \sqrt{\frac{\rho}{2P}}. \quad (\text{C.16})$$



# Appendix D

## Riemann solver

The fluxes of mass, momentum, and energy at the interface between two cells can be estimated by assuming that the flow state within the cells is constant and that the cells are separated by an imaginary diaphragm which is instantly removed. The fluxes are determined from the flow state at the interface ( $x = 0$ ). This problem is the same as the ideal shock tube problem described in Section 3.2. This appendix describes a three stage approximate solver similar to schemes described by Gottlieb & Groth [26] and Jacobs [35]. The multi-dimensional fluxes are determined by solving the one-dimensional problem using the flow velocities normal to the interface. The transverse flow velocity at the interface is assumed to be the transverse velocity of the upwind cell.

## D.1 Stage 1

The first stage assumes that all the waves are isentropic, and a solution can be determined explicitly as,

$$P^* = P_L \left[ \frac{(\gamma - 1)(\bar{U}_L - \bar{U}_R)}{2a_L(1 + Z)} \right]^{\frac{2\gamma}{\gamma-1}} \quad (\text{D.1})$$

$$u^* = \frac{\bar{U}_L Z + \bar{U}_R}{1 + Z} \quad (\text{D.2})$$

$$\bar{U}_L = u_L + \frac{2a_L}{\gamma - 1} \quad (\text{D.3})$$

$$\bar{U}_R = u_R - \frac{2a_R}{\gamma - 1} \quad (\text{D.4})$$

$$Z = \frac{a_R}{a_L} \left( \frac{P_L}{P_R} \right)^{\frac{\gamma-1}{2\gamma}} \quad (\text{D.5})$$

$$a_L = \sqrt{\frac{\gamma P_L}{\rho_L}} \quad (\text{D.6})$$

$$a_R = \sqrt{\frac{\gamma P_R}{\rho_R}} \quad (\text{D.7})$$

where  $P^* = P_2 = P_3$  and  $u^* = u_2 = u_3$ .

In the exceptional situation of  $(\bar{U}_L - \bar{U}_R) < 0$ , it is assumed that a (near) vacuum has formed at the cell interface and all interface flow properties are set to minimum values.

## D.2 Stage 2

The solution is improved by considering any shock waves that may exist. If  $P^*$  is greater than  $1.5P_L$  or  $1.5P_R$ , the estimate of  $P^*$  is improved by four Newton-Raphson steps of the form,

$$P_{n+1}^* = P^* - F_n \left( \frac{dF_n}{dP^*} \right)^{-1}, \quad (\text{D.8})$$

where,

$$F_n = u_L^*(P_n^*) - u_R^*(P_n^*), \quad (\text{D.9})$$

and,

$$u_L^* = \begin{cases} u_L - \frac{a_L}{\gamma} \left[ \frac{P^*}{P_L} - 1 \right] \left[ \frac{\gamma+1}{2} \frac{P^*}{P_L} + \frac{\gamma-1}{2} \right]^{\frac{-1}{2}} & : P^* \geq P_L \\ u_L - \frac{2a_L}{\gamma-1} \left[ \left[ \frac{P^*}{P_L} \right]^{\frac{\gamma-1}{2\gamma}} - 1 \right] & : P^* < P_L \end{cases} \quad (\text{D.10})$$

$$u_R^* = \begin{cases} u_R + \frac{a_R}{\gamma} \left[ \frac{P^*}{P_R} - 1 \right] \left[ \frac{\gamma+1}{2} \frac{P^*}{P_R} + \frac{\gamma-1}{2} \right]^{\frac{-1}{2}} & : P^* \geq P_R \\ u_R + \frac{2a_R}{\gamma-1} \left[ \left[ \frac{P^*}{P_R} \right]^{\frac{\gamma-1}{2\gamma}} - 1 \right] & : P^* < P_R. \end{cases} \quad (\text{D.11})$$

## D.3 Stage 3

The last stage is to determine the flow state at the interface. Firstly, the intermediate densities and the speeds of the left and right waves are determined.

If  $P^* > P_L$ , the left wave is assumed to be a shock and the density is obtained from the Rankine-Hugoniot relation,

$$\rho_L^* = \rho_L \left[ \frac{(\gamma+1)P^* + (\gamma-1)P_L}{(\gamma+1)P_L + (\gamma-1)P^*} \right]. \quad (\text{D.12})$$

The velocity of left wave is given by,

$$ws_L = u_L - \left[ \frac{(\gamma+1)P_L}{2\rho_L} \left( \frac{P^*}{P_L} + \frac{\gamma-1}{\gamma+1} \right) \right]^{\frac{1}{2}}. \quad (\text{D.13})$$

If the left-moving wave is an expansion, the speed of sound of the intermediate left state is equal to,

$$a_L^* = \frac{(U_L - u_L^*)(\gamma-1)}{2} \quad (\text{D.14})$$

and the density is equal to,

$$\rho_L^* = \frac{P \gamma}{a_L^2}. \quad (\text{D.15})$$

The velocity of the left-moving wave is given by,

$$ws_L = u_L - a_L. \quad (\text{D.16})$$

The intermediate density and wave speed associated with the right wave are determined in a similar manner.

The interface flow state is determined using the logic described in Figure D.1. If an expansion fan straddles the interface, the flow state is interpolated from the flow states either side of the expansion fan assuming that the flow properties are linear functions of the flow velocity.

if ( $u^* > 0$ ) then

The contact surface has moved to the right.

The interface state is determined from the  $L$  and  $L^*$  states.

if ( $ws_L \geq 0$ ) then

All waves have moved to the right.

The interface state is equal to  $L$ .

else

if ( $P^* > P_L$ )

The left wave is shock.

The interface state is equal to  $L^*$ .

else

The left is an expansion fan.

if ( $u_L^* - a_L^* > 0$ )

The expansion fan straddles the interface.

Interpolate the interface state from  $L$  and  $L^*$ .

else

The expansion fan is to the left of the interface.

The interface state is equal to  $L^*$ .

else

The contact surface has moved to the left.

The interface state is determined from the  $R$  and  $R^*$  states in a similar manner.

Figure D.1: Interpolation logic for the Riemann solver

# Appendix E

## Exact one-dimensional flow solver



This appendix describes the equations for flow in an ideal shock tube (Sec. 3.2) when the gas is non-perfect. The flow behind the shock can be determined by considering the conservation of mass, momentum and energy,

$$(\rho_2 - \rho_1)U_s = \rho_2 u_2 - \rho_1 u_1 \quad (\text{E.1})$$

$$(\rho_2 u_2 - \rho_1 u_1)U_s = P_2 + \rho_2 u_2^2 - P_1 + \rho_1 u_1^2 \quad (\text{E.2})$$

$$\left[ \rho_2 \left( e_2 + \frac{u_2^2}{2} \right) - \rho_1 \left( e_1 + \frac{u_1^2}{2} \right) \right] U_s = \rho_2 u_2 \left( e_2 + \frac{p_2}{\rho_2} + \frac{u_2^2}{2} \right) - \rho_1 u_1 \left( e_1 + \frac{p_1}{\rho_1} + \frac{u_1^2}{2} \right) \quad (\text{E.3})$$

where  $U_s$  is the speed of the shock.

The flow behind the tail of the expansion can be found using Equations E.4 – E.6.

$$u_3 = u_4 + \int_{p_4}^{p_3} \frac{dp}{\rho a} \quad (\text{E.4})$$

$$a = \sqrt{\left. \frac{\partial P}{\partial \rho} \right|_s} \quad (\text{E.5})$$

$$\frac{d\rho}{de} = \frac{\rho^2}{P} \quad (\text{E.6})$$

Equation E.6 comes from assuming the flow is isentropic.

Closure of these equations is achieved by the equation of state (Eqn. E.7) and the fact that the pressures and flow velocities either side of the contact surface are equal, that is  $u_2 = u_3$  and  $p_2 = p_3$ .

$$p = f(\rho, e) \quad (\text{E.7})$$

# Appendix F

## *Z* lines

This appendix describes the  $Z$  lines of an unstructured mesh of triangular cells. The  $Z$  lines are used to aid the transfer of a solution from one mesh to another.

Consider the mesh shown in Figure F.1. Two  $Z$  lines starting from edge AB are shown as dashed lines. The  $Z$  line in Figure F.1(a) starts at A and moves to vertex B. From vertex B the  $Z$  line continues along the edge which is the first edge (BC) in the clockwise direction of edge AB pivoted about vertex B. From vertex C the  $Z$  line continues along the edge which is the first edge (CD) in the counter-clockwise direction of edge BC pivoted about vertex C. The line continues along the edges turning alternatively clockwise then counter-clockwise. The  $Z$  line finishes when it reaches an edge on the boundary. Two  $Z$  lines commence from every edge on the boundary.

Each  $Z$  line contains *direct* and *indirect* segments. The direct segments are counter-clockwise from the preceding edge and indirect segments are clockwise from the preceding edge (Fig. F.2). The  $Z$  lines of any arbitrary triangulation trace all edges of the mesh twice. Direct segments trace over each edge once, and indirect segments trace over each edge once. It is this feature of  $Z$  lines which is exploited during the solution transfer.

Not all  $Z$  lines commence at the boundary of the mesh. A  $Z$  line may commence at an internal edge and return to that edge forming a loop. The loop is only closed when a segment of the same type (direct or indirect) returns to the start of the loop. If the loop returns to the starting edge and is of a different type, the loop will continue past the starting edge eventually returning with the same type of segment, to the starting edge.

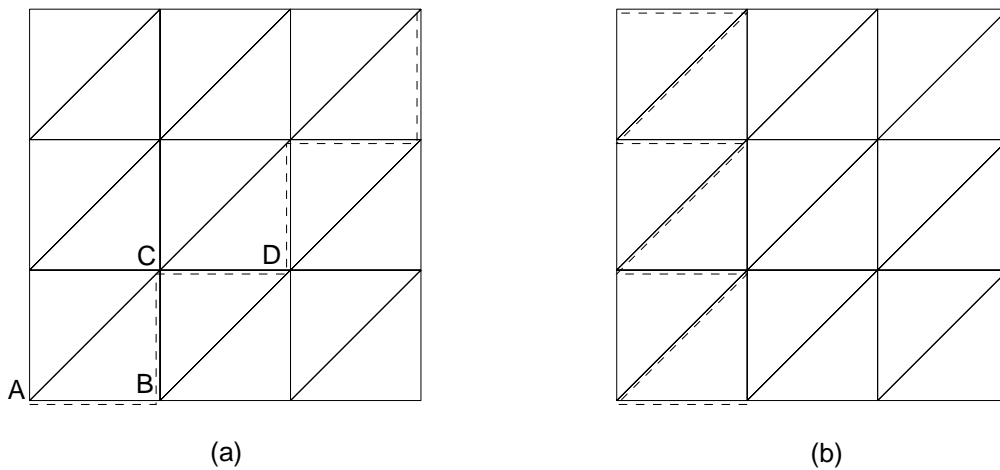


Figure F.1: Two  $Z$  lines (dashed) starting from the same edge.

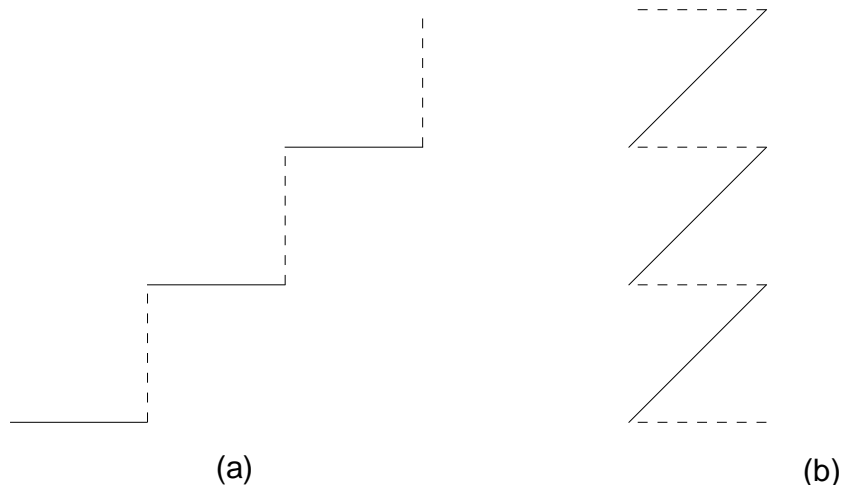


Figure F.2: Direct (solid) and indirect (dashed) segments of the  $Z$  lines shown in Figure F.1.

The location of the first vertex of a  $Z$  line on the other mesh has to be found before the trace can begin. If a  $Z$  line starts at a boundary edge, the trace must start either on a boundary vertex or a boundary edge of the other mesh. If a  $Z$  line starts on an internal edge (any edge within a  $Z$  loop) the trace will start either on an internal vertex, or on an internal edge, or in a cell. From the first vertex of the  $Z$  line the next intersection with the other mesh or the end of the current segment of the  $Z$  line is found (whichever comes first) and, if the current segment is a direct segment, the line integral is evaluated and the contributions are added to the new cells. This process of tracing along the  $Z$  line and determining the next intersection or end of the segment continues until the end of the  $Z$  line is reached.

Two geometric searches are used to determine the locations of the intersections with the other mesh. The first search examined the relation between a vertex and a cell. The vertex can be either in the cell, or on an edge of the cell, or on a vertex of the cell, or outside the cell. The second search examines two line segments. The line segment can either intersect at a point on both line segments which is not one of the endpoints, or intersect at one of the endpoints, or intersect at two of the endpoints, or not intersect.

The current location of a tracing  $Z$  line can either be on a vertex, or on an edge or in a cell of the other mesh. If on a vertex, the relation of the end point of the current edge of the  $Z$  line (in the direction of the trace) to the cells surrounding the vertex is determined. If the end point is outside all the cells, the relationship between the current edge and the edges of the polygon formed by the surrounding cells is examined. If the current location of the tracing  $Z$  line is within a cell of the

other mesh, the relationship between the current edge and the edges of the cell is examined. If no intersection can be found, the current edge must lie within the cell. If the location of the tracing  $Z$  line is on an edge, the relationship between the end point of the current edge and the cells associated with the edge is examined. If the point is outside the cells, the current edge must intersect with one of the other edges of the cells.

Sometimes while tracing a  $Z$  line on the other mesh, the next intersection cannot be found and the tracing line becomes *stuck*. This usually occurs because a vertex on the old mesh and the new mesh are very close but not close enough ( $1.0 \times 10^{-10}$ ) to be considered the same point by the geometric procedures (is a point in a cell?, does a line segment intersect with another line segment?). To overcome this problem, the vertex of the new mesh is moved so that it has exactly the same co-ordinates as the vertex on the old mesh. The relative distance a vertex is moved is small and the change in the cell quality is small.